



THESIS / THÈSE

DOCTOR OF SCIENCES

Towards artificial photosynthesis

heterogenized molecular complexes for CO₂ electroreduction and optimization of perovskite solar cells

Pugliese, Silvia

Award date:
2022

Awarding institution:
University of Namur
Université de Paris IV-Sorbonne

[Link to publication](#)

General rights

Copyright and moral rights for the publications made accessible in the public portal are retained by the authors and/or other copyright owners and it is a condition of accessing publications that users recognise and abide by the legal requirements associated with these rights.

- Users may download and print one copy of any publication from the public portal for the purpose of private study or research.
- You may not further distribute the material or use it for any profit-making activity or commercial gain
- You may freely distribute the URL identifying the publication in the public portal ?

Take down policy

If you believe that this document breaches copyright please contact us providing details, and we will remove access to the work immediately and investigate your claim.



Sorbonne Université

Université de Namur

Ecole doctorale de Chimie
moléculaire de Paris-Centre (ED406)

Faculté de Sciences
Département de Chimie

*Laboratoire de Chimie des Processus
Biologiques*

*Laboratoire de Chimie des Matériaux
Inorganiques*

CNRS UMR 8229 Collège de France, Paris

**Towards artificial photosynthesis: heterogenized
molecular complexes for CO₂ electroreduction and
optimization of perovskite solar cells**

Par Silvia Pugliese

Thèse de doctorat de Chimie

Dirigée par Pr. Marc Fontecave et Pr. Bao-Lian Su

Présentée et soutenue publiquement le 25 avril 2022 (Date provisionnelle)

Devant un jury composé de :

Pr. Christel Laberty-Robert, Professeure à Sorbonne Université	Examinatrice
Dr. Elodie Anxolabéhère-Mallart, Directrice de recherche à l'Université de Paris	Rapporteur
Pr. Yann Garcia, Professeur à l'Université Catholique de Louvain	Rapporteur
Dr. Luca Fusaro, Directeur de recherche à l'Université de Namur	Examineur
Pr. Antoni Llobet, Professeur à l'Institut Catalan d'Investigation Chimique	Examineur
Pr. Damien Debecker, Professeur à l'Université Catholique de Louvain	Examineur
Pr. Bao-Lian Su, Professeur à l'Université de Namur	Directeur de thèse
Pr. Marc Fontecave, Professeur au Collège de France	Directeur de thèse
Pr. Alain Krief, Professeur émérite à l'Université de Namur	Membre Invité

List of Figures and schemes

Figure 1.1 Comparison between energy density and normalized energy density (number of e ⁻ needed to convert CO ₂ to such product) of a series of unbranched alcohols. ^[14]	3
Figure 1.2 Overview of the most important chemical products from two-step CO ₂ conversion through CO electroreduction and their fields of application. ^[17]	4
Figure 1.3 SEM images for a) Zn dendrite catalyst ^[29] and b) electrochemically deposited Bi-thin film. ^[28]	6
Figure 1.4 Reported active sites in heterogeneous electrocatalysts for CO ₂ RR. ^[43]	8
Figure 1.5 Structure of the catalyst (protoporphyrin IX cobalt chloride, left) and preparation of chemically grafted cobalt porphyrins on carbon nanotubes (right). ^[94]	13
Figure 1.6 a) Schematic representation of the molecularly dispersed NiPc on the side-walls of CNTs and b) Long-term operation of molecularly dispersed NiPc-OMe at -150 mA cm ⁻² . ^[99]	14
Figure 1.7 From homogeneous to heterogeneous catalysis: the optimization of the catalyst starts at the homogeneous level. The support brings to the hybrid system additional benefits such as extensive surface areas and improved mass transport and electron transfer. Modified from Sun et al. ^[88]	18
Figure 1.8 a) Structure of cyclam showing two equatorial N-H fragments establishing H bonds with the lone pairs of the adjacent nitrogen atoms ^[116] and b) packing diagram for cyclam showing the intermolecular hydrogen bonded columnar arrays and intramolecular hydrogen bonding. ^[115]	20
Figure 1.9 Configurations of metal-cyclam complexes. ^[126]	21
Figure 1.10 First mechanism proposed by Sauvage and coworkers for the electroreduction for CO ₂ to CO catalyzed by [Ni(cyclam)] ²⁺ . ^[134]	22
Figure 1.11 Molecular structures of 1 , 2 and 3 as described by Lu and collaborators. ^[137]	24
Figure 1.12 Preparation of [Ni(cyclam)] ²⁺ -PALA ^[145]	25
Figure 1.13 Crystal structures of [Ni-propargyl-cyclam] ²⁺ (1), [Ni-pentynyl-cyclam] ²⁺ (2) and [Ni-hexynyl-cyclam] ²⁺ (3). ^[149]	26
Figure 1.14 a) CVs of 1mM [Ni(Cyclam)pyrene] ²⁺ (top) and [Ni(Cyclam)] ²⁺ (bottom) in 0.1M TBAPF ₆ in MeCN with 10% water using a GC electrode; 100mV/s under N ₂ (black) and CO ₂ (red) and b) electrolysis data from a [Ni(Cyclam)pyrene] ²⁺ GDE used in 0.5 M KHCO ₃ with a CO ₂ flow rate of 20 ml min ⁻¹ . ^[151]	28

Figure 1.15 CVs of aqueous solutions (0.1 M NaClO ₄ and 0.035 M NaHCO ₃ , pH 6.2) under CO ₂ on a GC disk electrode (a) without and (c) with 1 mM [Ni(cyclam)] ²⁺ , and on a Hg-Au disk electrode (b) without and (d) with 1 mM [Ni(cyclam)] ²⁺ (Scan rates 100 mV s ⁻¹). ^[162]	33
Figure 1.16 From left to right, drawings of the two primary isomers of [Ni(cyclam)] ²⁺ , <i>trans</i> -I and <i>trans</i> -III, present in solution at equilibrium; the C-RRSS-isomer of [Ni(HTIM)] ²⁺ ; [Ni(MTC)] ²⁺ having a trans-cyclohexane. ^[157]	35
Figure 1.17 structure of the Complexes studied by Cook and collaborators. ^[160,161]	37
Figure 1.18 Optimized geometries of (A) <i>trans</i> -I with the four N-H pointing towards Hg, (B) <i>trans</i> -I with no N-H pointing towards Hg or (C) <i>trans</i> -III [Ni(cyclam)] ⁺ on an Hg surface. Hydrogens on amine groups are highlighted in red. ^[171]	39
Figure 1.19 Architecture of the bias-free perovskite–BiVO ₄ PEC tandem device for syngas production proposed by Reisner et al. ^[179]	41
Figure 1.20 Representative architectures for PSCs: a) mesoscopic, and b) thin film.	42
Figure 1.21 Scheme of the carrier dynamics at interfaces in PSCs. ^[185]	43
Figure 1.22 Summary of movements throughout the 3-year PhD project.	46
Figure 1.23 eSCALED dream team. From left to right, top row: Robin, Silvia, Van, Karell, Ignasi, Oli, Saeed. Bottom row: Afridi, Bruno, Andrew, Dome, Ludo, Andy, Diogo.	47
Figure 2.1 Crystal structure representation of the cation part of complex 1 . Ellipsoids are drawn with 30% probability. All hydrogen atoms are omitted for the sake of clarity. (a) <i>R,S,S,R trans-1</i> (from crystallization in MeCN); (b) <i>S,S,S,S cis-1</i> (from crystallization in DMF). Only one of the enantiomers is shown in both cases.....	60
Figure 2.2 Cyclic voltammograms of complex 1 (black, dashed and dotted), [Ni(cyclam)] ²⁺ (red), ligand (L1 , blue). Conditions: DMF with 0.1M TBAPF ₆ as the electrolyte, under Ar and at room temperature. Concentrations were 1 mM for all species. Scan rate 100 mV s ⁻¹	62
Figure 2.3 Cyclic voltammograms of 1 mM complex 1 (black) and 1 mM [Ni(Cyclam)] ²⁺ (red). Conditions: DMF with 0.1M TBAPF ₆ as the electrolyte, under Ar and at room temperature. Scan rate 100 mV s ⁻¹	62
Figure 2.4 Cyclic voltammograms of 1 mM complex 1 (dotted), 1 mM [Ni(Cyclam)] ²⁺ (red) and 1mM complex 1 in presence of AgPF ₆ (black and mauve). Conditions: DMF with 0.1M TBAPF ₆ as the electrolyte, under Ar and at room temperature. Scan rate 100 mV s ⁻¹	63
Figure 2.5 (a) CV of 1 mM complex 1 (DMF with 0.1M TBAPF ₆ as the electrolyte, under Ar and at room temperature) at different scan rates and (b) plot of the cathodic peak current at -2.28 V as a function of the square root of the scan rates.....	64
Figure 2.6 CV of complex 1 (1 mM) in Ar-saturated (red) and CO ₂ -saturated (black) DMF with 0.1M TBAPF ₆ at room temperature. Scan rate 100 mV s ⁻¹	65

Figure 2.7 CVs of 1 (1 mM) in DMF with 0.1M TBAPF ₆ and increasing concentrations of H ₂ O under CO ₂ (a) and under Ar (b) at room temperature. Scan rate 100 mV s ⁻¹ . Same colors have been used for the same H ₂ O concentrations in both figures.	65
Figure 2.8 (a) CVs of 1 (1 mM) in DMF with 0.1M TBAPF ₆ and H ₂ O 2M under CO ₂ and under Ar at room temperature compared with a blank (absence of complex 1). Scan rates 100 mV s ⁻¹ . (b) Controlled-potential electrolysis at - 2.39 V vs. Fc ⁺ /Fc ⁰ under the same conditions.....	66
Figure 2.9 SEM images of 1 /MWCNT/GDL electrode (a) before and (b) after 4h CPE.	68
Figure 2.10 XPS survey spectrum of 1 /MWCNT/GDL electrode (a), high resolution XPS spectra of N1s (b), Ni 2p and F auger (c).....	68
Figure 2.11 (a) CV of 1 /MWCNT/GDL (acetonitrile with 0.1M TBAPF ₆ as the electrolyte, under Ar and at room temperature) at different scan rates and (b) plot of the anodic peak current at -2.28 V as a function of the square root of the scan rates.	69
Figure 2.12 (a) LSV of 1 /MWCNT/GDL (black) and MWCNT/GDL (dotted) in acetonitrile with TBAPF ₆ 0.1 M and H ₂ O 1% under CO ₂ . Scan rate 10 mV s ⁻¹ . (b) Controlled Potential Electrolysis using 1 /MWCNT/GDL as the electrode at different potentials under the same conditions. (c) Faradaic yields for CO and H ₂ after 20 min electrolysis at different potentials.	70
Figure 2.13 Controlled-Potential Electrolysis at -2.54 V vs. Fc ⁺ /Fc ⁰ using 1 -MWCNT/GDL in acetonitrile with 0.1M TBAPF ₆ and 1% H ₂ O. Inset: Faradaic yields for CO and H ₂ after 4h electrolysis.....	71
Figure 2.14 X-ray photoelectron spectra of 1 /MWCNT/GDL electrode after long-term electrolysis of CO ₂ in acetonitrile with 0.1M TBAPF ₆ and 1% H ₂ O. XPS survey spectrum (a), high resolution XPS spectra of N1s (b), Ni 2p and F Auger (c).	72
Figure 2.15 (a) LSVs of 1 /MWCNT/GDL in MeCN with 3 v% (dotted) and 5 v% water (solid) with TBAPF ₆ 0.1 M under CO ₂ or Ar. Scan rate 10 mV s ⁻¹ . (b) Controlled Potential Electrolysis using 1 /MWCNT/GDL at different potentials under the same conditions. (c) Faradaic yields for CO and H ₂ after 20 min electrolysis at different potentials under the same conditions with 1 /MWCNT/GDL.	73
Figure 2.16 (a) LSVs of 1 /MWCNT/GDL (black and red) and MWCNT/GDL (dotted) in water with KHCO ₃ 0.1 M under CO ₂ or Ar. Scan rate 50 mV s ⁻¹ . (b) Controlled Potential Electrolysis using 1 /MWCNT/GDL at different potentials under the same conditions. (c) Faradaic yields for CO and H ₂ after 20 min electrolysis at different potentials under the same conditions with 1 /MWCNT/GDL.	74
Figure A2.1 ¹ H NMR (400 MHz, 25°C, CDCl ₃) of 4	86
Figure A2.2 ¹ H NMR (400 MHz, 25°C, CDCl ₃) of L1	87
Figure A2.3 UV-Vis spectrum of complex 1 (25°C, DMF).....	87
Figure A2.4 CVs of <i>cis</i> - 1 (pink crystals) and <i>trans</i> - 1 (purple crystals) 1 mM in DMF with 0.1M TBAPF ₆ under Ar (a) and under CO ₂ (b) at room temperature. Scan rate 100 mV s ⁻¹	88

Figure A2.5 CVs of **1** (1 mM) in DMF with 0.1M TBAPF₆ and increasing concentrations of TFE under CO₂ (a) and under Ar (b) at room temperature. Scan rate 100 mV s⁻¹. Same colors have been used for the same TFE concentrations in both figures. 88

Figure A2.6 a) Controlled-Potential Electrolysis at -2.54 V vs. Fc⁺/Fc⁰ of MWCNT/GDL in acetonitrile with 0.1M TBAPF₆ and 1% H₂O under CO₂. Inset: Faradaic yields for CO and H₂ after 20 min electrolysis; b) Controlled-Potential Electrolysis at -2.54 V vs. Fc⁺/Fc⁰ of **1**/MWCNT/GDL in acetonitrile with 0.1M TBAPF₆ and 1% H₂O under Ar. Inset: LSV of **1**/MWCNT/GDL in acetonitrile with TBAPF₆ 0.1 M and H₂O 1% under CO₂ (black) and Ar (red). Scan rates 10 mV s⁻¹. 89

Figure 3.1 Cyclic voltammograms of complex **2** (black and dotted), [Ni(cyclam)]²⁺ (red), ligand (**L2**, blue). Conditions: DMF with 0.1M TBAPF₆ as the electrolyte, under Ar and at room temperature. Concentrations were 1 mM for all species. Scan rate 100 mV s⁻¹. 100

Figure 3.2 a) CV of 1 mM complex **2** (DMF with 0.1M TBAPF₆ as the electrolyte, under Ar and at room temperature) at different scan rates and b) plot of the cathodic peak current at -2 V and the anodic peak current at -1.9V as a function of the square root of the scan rates. 101

Figure 3.3 CV of complex **2** (1 mM) in Ar-saturated (red and dotted red) and CO₂-saturated (black and dotted black) DMF with 0.1M TBAPF₆ at room temperature with no H₂O added and in the presence of H₂O 2M. Scan rate 100 mV s⁻¹ 102

Figure 3.4 CVs of **2** (1 mM) in DMF with 0.1M TBAPF₆ and increasing concentrations of H₂O under CO₂ (a) and under Ar (b) at room temperature. Scan rate 100 mV s⁻¹. Same colors have been used for the same H₂O concentrations in both figures. 103

Figure 3.5 (a) CVs of **2** (1 mM) in DMF with 0.1M TBAPF₆ and H₂O 2M under CO₂ and under Ar at room temperature compared with a blank (absence of complex **2**). Scan rates 100 mV s⁻¹. (b) Controlled-potential electrolysis at -2.38 and -2.28 V vs. Fc⁺/Fc⁰ under the same conditions, in the presence of complex **2** (green, black) and at -2.38 V in the absence of complex **2** (red). (c) Controlled-Potential Electrolysis at -2.38 V vs. Fc⁺/Fc⁰ in the presence of **2** under the same conditions, and relative faradaic yields for CO and H₂ after 2h electrolysis. 104

Figure 3.6 XPS survey spectrum of **2**/MWCNT/GDL electrode (a), high resolution XPS spectra of N1s (b), Ni 2p (c). 105

Figure 3.7 (a) CV of **2**/MWCNT/GDL (acetonitrile with 0.1M TBAPF₆ as the electrolyte, under Ar and at room temperature) at different scan rates. 106

Figure 3.8 (a) LSV of **2**/MWCNT/GDL (black and red) and MWCNT/GDL (dotted) in acetonitrile with TBAPF₆ 0.1 M and H₂O 1% under CO₂ or Ar. Scan rate 10 mV s⁻¹. (b) Controlled Potential Electrolysis using **2**/MWCNT/GDL as the electrode at different potentials under the same conditions. (c) Faradaic yields for CO and H₂ after 20 min electrolysis at different potentials under the same conditions with **2**/MWCNT/GDL. 107

Figure 3.9 Controlled-Potential Electrolysis at -2.23 V vs. Fc⁺/Fc⁰ using **2**-MWCNT/GDL in acetonitrile with 0.1M TBAPF₆ and 1% H₂O. Inset: Faradaic yields for CO and H₂ during electrolysis. 108

Figure 3.10 (a) LSVs of **2**/MWCNT/GDL in acetonitrile with TBAPF₆ 0.1 M and H₂O 1 v% (red, black) or 10 v% (green, blue) under CO₂ or Ar. Scan rate 10 mV s⁻¹. (b) Controlled

Potential Electrolysis using **2**/MWCNT/GDL as the electrode at different potentials under the same conditions and H₂O 1% (black) or 10% (blue). Inset: faradaic yields for CO and H₂ after 20 min electrolysis at different water concentrations..... 109

Figure 3.11 (a) LSVs of **2**/MWCNT/GDL (black and red) and MWCNT/GDL (dotted) in water with KHCO₃ 0.1 M under CO₂ or Ar. Scan rate 50 mV s⁻¹. (b) Controlled Potential Electrolysis using **2**/MWCNT/GDL as the electrode at different potentials under the same conditions. (c) Faradaic yields for CO and H₂ after 20 min electrolysis at different potentials under the same conditions with **2**/MWCNT/GDL. (d) Controlled Potential Electrolysis using **2**/MWCNT/GDL (black) compared to MWCNT/GDL (blue) at -0.8 V under the same conditions. 110

Figure 3.12 Controlled-Potential Electrolysis at -0.8 V vs. RHE using **2**/MWCNT/GDL in water with 0.1M KHCO₃ and a CO₂ flow rate of 5 ml/min. Faradaic yields for CO and H₂ during the same experiment..... 111

Figure A3.1 Controlled-Potential Electrolysis at -2.13V vs. Fc⁺/Fc⁰ using MWCNT/GDL in acetonitrile with 0.1M TBAPF₆ and 1% H₂O. Inset: Faradaic yields for CO and H₂ after 20min electrolysis..... 131

Figure A3.2 SEM images of **2**/MWCNTs/GDL electrode a) before and b) after 4h electrolysis. 131

Figure A3.3 Comparison of CVs of 1 mM complex **2** and complex **1** (DMF with 0.1M TBAPF₆, under Ar and at room temperature, scan rate 100 mV s⁻¹). 132

Figure A3.4 Comparison of CVs of 1 mM complex **2** and complex **1** (DMF with 0.1M TBAPF₆ and H₂O 2M, under Ar or CO₂ and at room temperature, scan rate 100 mV s⁻¹). 133

Figure A3.5 FT-IR spectrum of **5** (powder) 134

Figure A3.6 ¹H NMR (400 MHz, 50°C, CDCl₃) of **5** 135

Figure A3.7 ¹³C NMR (101 MHz, 55 °C, CDCl₃) of **5**. 135

Figure A3.8 FT-IR spectrum of 1-pyrenemethylamine (blue) and its hydrochloride salt (brown) (powders)..... 136

Figure A3.9 ¹H NMR (400 MHz, 25°C, CDCl₃) of 1-Pyrenemethylamine 137

Figure A3.10 FT-IR spectrum of **6** (powder) 138

Figure A3.11 ¹H NMR (400 MHz, 50°C, CDCl₃) of **6** 139

Figure A3.12 FT-IR spectrum of **L2** (powder) 139

Figure A3.13 ¹H NMR (400 MHz, 25°C, CDCl₃) of **L2**..... 140

Figure A3.14 2D HMBC NMR (101 MHz, 400 MHz, 25°C, CDCl₃) of **L2**..... 141

Figure A3.15 ¹³C NMR (101 MHz, 25 °C, CDCl₃) of **L2**. 142

Figure A3.16 2D HSQC NMR (101 MHz, 400 MHz, 25°C, CDCl₃) of **L2**..... 143

Figure A3.17 MS (ESI) report for L2	144
Figure A3.18 UV-Vis spectrum of complex 2 (25°C, MeOH)	145
Figure A3.19 FT-IR spectrum of 7 (powder)	146
Figure A3.20 ¹ H NMR (400 MHz, 25°C, CDCl ₃) of 7	147
Figure A3.21 ¹³ C NMR (101 MHz, 25 °C, CDCl ₃) of 7	148
Figure A3.22 FT-IR spectrum of 8 (powder)	149
Figure A3.23 ¹ H NMR (400 MHz, 25°C, CDCl ₃) of 8	149
Figure A3.24 ¹³ C NMR (101 MHz, 25 °C, CDCl ₃) of 8	150
Figure A3.25 FT-IR spectrum of 9 (powder)	151
Figure A3.26 ¹ H NMR (400 MHz, 25°C, CDCl ₃) of 9	152
Figure A3.27 ¹³ C NMR (101 MHz, 25 °C, CDCl ₃) of 9	153
Figure A3.28 FT-IR spectrum of bis-aminal (powder)	154
Figure A3.29 ¹³ C NMR (101 MHz, 25 °C, CDCl ₃) of bis-aminal	154
Figure 4.1 wide-angle X-ray diffraction XRD pattern for sample 1	158
Figure 4.2 N ₂ pysisorption isotherm (a) and pore size distribution (b) BJH adsorption for sample 1	159
Figure 4.3 SEM (a) and TEM (b, c) images for material 1	160
Figure 4.4 wide-angle X-ray diffraction XRD pattern for sample 2	161
Figure 4.5 N ₂ pysisorption isotherm (a) and pore size distribution (b) BJH adsorption for sample 2	162
Figure 4.6 SEM (a,b) and TEM (c) images for material 2	163
Figure 4.7 a) SEM image of PS nanospheres and b) DLS analysis (mean diameter 270 nm).	164
Figure 4.8 a) SEM image of PS- <i>s</i> -PAA nanospheres and b) DLS analysis (mean diameter 290 nm).	165
Figure 4.9 a) SEM image of IO-TiO ₂ material and b) picture of several glass substrates on which IO-TiO ₂ was deposited (green reflex).	166
Figure 4.10 Architecture of the PSCs used in this work, with a focus on the different mesoporous TiO ₂ scaffolds tested as ETL.	166

Figure 4.11 SEM cross sections of a) IO-TiO ₂ synthesized on FTO+ compact TiO ₂ before the print of the successive layers; b,c) IO-TiO ₂ synthesized on FTO+ compact TiO ₂ after the screen print of the successive layers (ZrO ₂ , Carbon).	171
Figure 4.12 <i>J-V</i> parameters obtained from reverse (black) and forward (red) scans of the PSCs made by adding different wt% of ~300 nm PS- <i>s</i> -PAA nanospheres within the meso-TiO ₂ layer.	174
Figure 4.13 <i>J-V</i> parameters obtained from reverse (black) and forward (red) scans of the PSCs made by adding different wt% of ~300 nm PS nanospheres within the meso-TiO ₂ layer.....	175
Figure 4.14 <i>J-V</i> curves of the champion PSCs, based on the reference TiO ₂ nanoparticles + 5 wt% 300 nm-sized PS nanospheres in forward and reverse scan directions (compared to the bare reference).....	176
Figure 4.15 <i>J-V</i> parameters obtained from reverse (black) and forward (red) scans of the PSCs made by adding different wt% of ~180 nm PS nanospheres within the m-TiO ₂ layer.	177
Figure 4.16 Meso-TiO ₂ layers for the sample PS- <i>s</i> -PAA 300 nm 20 wt % a) before and c) after firing. Meso-TiO ₂ layers for PS 180 nm 20 wt % b) before and d) after firing.	178
Figure 4.17 SEM cross sections of meso-TiO ₂ layer for PS- <i>s</i> -PAA 300 nm a) 20 wt % and b) 50 wt % ; meso-TiO ₂ layer for PS 180 nm a) 20 wt % and b) 50 wt %	179
Figure 4.18 Nyquist plots of PSCs based on reference cells (SN101 to 103), vs. m-TiO ₂ layers with with 10 wt% 180 nm-sized PS nanospheres (SN201 to 204).....	180
Figure A4.1 SEM images of the m-TiO ₂ layer made with the reference TiO ₂ nanoparticles (Nanoxide T/SP m-TiO ₂ produced by Solaronix SA). Above, top view; Below, cross-section view.	190
Figure A4.2 SEM image of the m-TiO ₂ layer made with material 1 . Cross-section view....	191
Figure A4.3 a) SEM image of PS nanospheres and b) DLS analysis (mean diameter 175 nm).	191
Scheme 2.1 Synthesis of complex 1 . Conditions: (i) ClCH ₂ COCl, NEt ₃ , CH ₂ Cl ₂ ; (ii) K ₂ CO ₃ , KI (cat.), MECN; (iii) NiCl ₂ ·6H ₂ O, EtOH.	59
Scheme 3.1 Synthesis of complex 2 . Conditions: (i) Boc ₂ O, dioxane, H ₂ O, RT, 72h, 83% , Na ₂ CO ₃ ; (ii) EDC-HCl, DMAP, DCM, RT, 5h, 93%; (iii) TFA, DCM, RT, o/n, KOH, H ₂ O, 100%; (iv) DMF, NiCl ₂ ·6H ₂ O, 2h, 49%.	98
Scheme 3.2 Synthesis of complex 3 . Conditions: (i) Tosyl chloride, CHCl ₃ , RT, 6h, 83%; (ii) DMM, DMF, reflux o/n, 77%; (iii) LiAlH ₄ , THF, 0°C to RT 4h, 90%; (iv) PBr ₃ , DCM, 0°C to reflux, 12h; (synthetic steps from (iv) to (vii) are in progress).	113
Scheme 4.1 Synthethic process for crystalline anatase nanoparticles, 1 . ^[22]	157

Scheme 4.2 Synthesis pathway for the formation of spherical-shaped TiO₂ nanoparticles (2).^[23]
..... 160

List of Tables

Table 1.1 Selected CO ₂ reduction processes and the corresponding redox potentials (pH 7 in aqueous solution vs NHE, 25 °C, 1 atmosphere gas pressure, and 1 M for the other solutes). ^[8]	2
Table 1.2 Representative structures of molecular catalysts for the CO ₂ RR.....	8
Table 1.3 Representative heterogenized molecular catalysts for the CO ₂ RR, with a focus on pyrene-modified catalysts.	16
Table 1.4 Summary of CO ₂ reduction results after 1 h in a) MeCN or b) DMF for the flow cell and H-cell. ^[150]	27
Table 1.5 Overview of the [Ni(Cyclam)] ²⁺ based catalysts described so far, either in homogeneous or in heterogeneous conditions. *TON and TOF values were calculated based on the number of the catalyst molecules in the diffusion layer.....	28
Table A2.1 XPS analysis of the functionalized 1 /MWCNT/GDL electrode.	89
Table A2.2 Crystallographic data for compounds <i>trans-1</i> and <i>cis-1</i>	92
Table A2.3 Selected bond lengths and angles in crystal structures. Distance and angles are measured with DIAMOND software.	94
Table 4.1 J-V parameters obtained from reverse and forward voltage sweeps of the prepared PSCs with m-TiO ₂ made of 1 , 2 , or IO-TiO ₂ . Maximum values (average values of at least 5 different devices between brackets).	167

Acronyms

^{13}C NMR	Carbon-13 Nuclear Magnetic Resonance
^1H NMR	Proton Nuclear Magnetic Resonance
APS	Ammonium Persulfate
BET	Brunauer–Emmett–Teller
BJH	Barrett–Joyner–Halenda
Boc₂O	di- <i>tert</i> -butyl dicarbonate
CO₂RR	CO ₂ Reduction Reaction
COF	Covalent Organic Framework
CPE	Controlled Potential Electrolysis
CV	Cyclic Voltammogram
DFT	Density-Functional Theory
DLS	Dynamic Light Scattering
DMAP	Dimethylaminopyridine
DMM	Dimethyl Malonate
DSSC	Dye-Sensitized Solar Cell
EDC	1-ethyl-3-(3-dimethylaminopropyl)carbodiimide
EIS	Electrochemical Impedance Spectroscopy
EISA	Evaporation-Induced Self Assembly
EPG	Edge-Plane Graphite
eSCALED	European School on Artificial Leaf: Electrodes & Devices
ESI	Electrospray Ionization
ETL	Electron Transporting Layer
Fc	Ferrocene
FE	Faradaic Efficiency
FF	Fill Factor
FTO	Fluorine-Doped Tin Oxide
FY	Faradaic Yield
GC	Glassy Carbon Gc
GDE	Gas Diffusion Electrode
GDL	Gas Diffusion Layer
HER	Hydrogen Evolution Reaction

HOPG	Highly Oriented Pyrolytic Graphite
HTM	Hole Transporting Material
IEA	International Energy Agency
IO-TiO₂	Inverse-Opal TiO ₂ Materials
IR	Infrared (spectroscopy)
JCPDS	Joint Committee On Powder Diffraction Standards
J_{sc}	Short Circuit Current Density
KPS	Potassium Persulfate
LSV	Linear Sweep Voltammogram
MeCN	Acetonitrile
MOF	Metal Organic Framework
MS	Mass Spectroscopy
MWCNT	Multi Walled Carbon Nanotube
NHE	Normal Hydrogen Electrode
PALA	Polyallylamine
PCE	Power Conversion Efficiency
PCET	Proton Coupled Electron Transfer
PCs	Phtalocyanines
PEC	Photoelectrochemical Cell
PEDOT	Poly 3,4-Ethylenedioxythiophene
Ps	Porphyrines
PS	Polystyrene
PSC	Perovskite Solar Cell
PS-<i>s</i>-PAA	Polystyrene- <i>statistical</i> -polyacrylic acid
PV-EC	Photovoltaics-Electrochemical Cell
RH	Relative Humidity
RHE	Reference Hydrogen Electrode
RP-HPLC	Reversed-Phase High-performance Liquid Chromatography
R_s	Series Resistance
R_{sh}	Shunt Resistance
RVC	Reticulated Vitreous Carbon
SDS	Sodium Dodecylsulfate
SEM	Scanning Electron Microscopy

SHE	Standard Hydrogen Electrode
SPANI	Sulphonated Polyaniline
TBAPF₆	Tetrabutylammonium Hexafluorophosphate
TEM	Transmission Electron Microscopy
TFA	Trifluoroacetic acid
TFE	Trifluoroethanol
TFE	2,2,2-Trifluoroethanol
TIPO	Titanium Isopropoxide
TOF	Turnover Frequency
TON	Turnover Number
TPPs	Tetraphenylporphyrins
UPPA	Université de Pau et des Pays de l'Adour
V_{oc}	Open Circuit Voltage
XPS	X-Ray Photoelectron Spectroscopy
XRD	X-Ray Diffraction

List of Publications

List of publication concerning this PhD thesis:

S. Pugliese, N. T. Huan, A. Krief, B. L. Su, Y. Li, M. Fontecave, Selective CO₂ electroreduction in aqueous conditions with a heterogenized C-substituted Ni cyclam catalyst, *in preparation*.

S. Pugliese, N. T. Huan, J. Forte, D. Grammatico, S. Zanna, B. L. Su, Y. Li, M. Fontecave, Functionalization of Carbon Nanotubes with Nickel Cyclam for the Electrochemical Reduction of CO₂, *ChemSusChem*, **2020**, *13*, 6449–6456. Chapter 2 of this thesis was adapted with minor alterations from this publication.

D. Grammatico, H. N. Tran, Y. Li, **S. Pugliese**, L. Billon, B. L. Su, M. Fontecave, Immobilization of a Molecular Re Complex on MOF-derived Hierarchical Porous Carbon for CO₂ Electroreduction in Water/Ionic Liquid Electrolyte, *ChemSusChem*, **2020**, *13*, 6418–6425.

Table of Contents

List of Figures and schemes.....	i
List of Tables.....	ix
Acronyms	x
List of Publications.....	xiii
Table of Contents	xiv
Chapter 1 Introduction.....	1
1.1 CO ₂ as a valuable commodity and CO ₂ electroreduction	1
1.2 Catalysts for CO ₂ electroreduction.....	5
1.2.1 Heterogeneous and homogeneous catalysts	5
1.2.2 Heterogenization of molecular catalysts	11
1.3 The case of [Ni(cyclam)] ²⁺	19
1.3.1 Homogeneous and heterogeneous CO ₂ RR catalyzed by [Ni(cyclam)] ²⁺	21
1.3.2 Understanding the mechanism of CO ₂ RR catalyzed by [Ni(cyclam)] ²⁺	32
1.4 Towards artificial photosynthesis: coupling an electrolyzer with a photovoltaic device	40
1.4.1 Solar-powered CO ₂ electroreduction	40
1.4.2 Increasing the power conversion efficiency of perovskite solar cells.....	42
1.5 The eSCALED framework and scope of the project.....	45
1.5.1 Objectives of the present project	48
1.6 References	49
Chapter 2 Functionalization of Carbon Nanotubes with Nickel Cyclam for the Electrochemical Reduction of CO₂	57
2.1 Introduction	57
2.2 Results	58
2.2.1 Complex 1 synthesis and characterization	58
2.2.2 CO ₂ reduction catalyzed by complex 1 in homogeneous conditions	64
2.2.3 Immobilization of complex 1: preparation of the hybrid electrode, characterization, and CO ₂ electroreduction	67
2.2.4 CO ₂ electroreduction in aqueous conditions	73
2.3 Discussion	74
2.4 Conclusion.....	77
2.5 Experimental Section	78
2.6 References	84
2.7 Appendix	86
Chapter 3 Selective CO₂ electroreduction in aqueous conditions with a heterogenized C-substituted Ni cyclam catalyst.....	96
3.1 Introduction	96
3.2 Results	98
3.2.1 Synthesis of Complex 2.....	98
3.2.2 Homogeneous electrochemical studies of complex 2	100
3.2.3 Heterogenization of complex 2, electrodes characterization, and CO ₂ reduction .	104
3.2.4 Electroreduction of CO ₂ catalyzed by 2/MWCNTs/GDL in water.....	109

3.2.5 Complex 1 and complex 2: a comparison	111
3.2.6 Synthesis of complex 3	113
3.3 Discussion	114
3.4 Conclusion.....	117
3.5 Experimental Section	119
3.6 References	129
3.7 Appendix	131
Chapter 4 Increasing the performance of mesoscopic printable perovskite solar cells by modifying the meso-TiO₂ layer morphology.....	155
4.1 Introduction	155
4.2 Results and Discussion.....	157
4.2.1 Synthesis of mesoporous TiO ₂ materials	157
4.2.2 Synthesis of polymeric nanospheres and inverse-opal TiO ₂	163
4.2.3 Fabrication of perovskite solar cells with modified mesoscopic TiO ₂ layer.....	166
4.2.4 Photovoltaic parameters and characterization of the modified perovskite solar cells	168
4.3 Conclusion.....	181
4.4 Experimental section	183
4.5 References	188
4.6 Appendix	190
Chapter 5 Conclusions and future perspectives	192
5.1 References	197

Chapter 1 Introduction

1.1 CO₂ as a valuable commodity and CO₂ electroreduction

While nowadays most of the focus on CO₂ is on its contribution to climate change, carbon dioxide can also be seen as an important commercial input to a range of products and services.

If just a few decades ago most of the processes that involved direct or indirect conversion of CO₂ were just starting to see the light of day,^[1] at the present time the interest of the scientific community is growing at an exponential pace,^[2] together with the advancements in different CO₂ utilization pathways. Lately, the International Energy Agency (IEA) released a study^[3] that identifies the most promising categories of CO₂-derived products and services that are attracting significant global interest, in terms of cost, maturity of the technology and amount of recycled carbon dioxide. Thus, CO₂ is used in biological processes, to enrich the growing environment in algae production and boost crop yields in greenhouses cultivations. It can be used in the production of building materials (concrete), or as a raw material in its constituents (cement and construction aggregates). CO₂ can be converted to a wide range of carbon-containing substances, such as chemicals, including synthetic rubbers, plastics, or fibers. Finally, it can be used to produce fuels that are in use today, including methane, methanol, gasoline and aviation fuels.

On this regard, the electrochemical conversion of CO₂ to fuel and feedstocks, i.e. the CO₂ reduction reaction (CO₂RR), is a very dynamic and promising field of research.^[3,4] The idea of producing substances that can be used directly or as intermediates for the production of other fuels by means of CO₂ and renewable energy could be an efficient way to tackle two of the biggest issues of the Anthropocene era, i.e., global warming and energy demand.^[5]

The reduction of CO₂, a notoriously inert molecule, is not a trivial process. Multiple electron reduction of CO₂ involves the generation of a radical anion, CO₂^{•-}.^[6] This species is bent, conversely to the neutral CO₂ molecule, which is linear. The large reorganization energy is what makes the thermodynamic potential for the reduction of CO₂ so unfavorably negative (-1.90 V vs NHE at pH 7 in aqueous solution at 25°C under 1 atm gas pressure).^[7] Fortunately, proton coupled multiple-electron reductions of CO₂ are easier than single electron reductions, as thermodynamically more stable molecules are produced. Thus, the electroreduction of CO₂ can

proceed at more favorable potentials via one-, two-, four-, six-, even eight-electron reduction pathways (Table 1.1).

Reduction process	Potential (V)
$\text{CO}_2 + \text{e}^- \rightarrow \text{CO}_2^{\cdot-}$	-1.9
$\text{CO}_2 + 2\text{H}^+ + 2\text{e}^- \rightarrow \text{CO} + \text{H}_2\text{O}$	-0.53
$\text{CO}_2 + 2\text{H}^+ + 2\text{e}^- \rightarrow \text{HCOOH} + \text{H}_2\text{O}$	-0.61
$\text{CO}_2 + 4\text{H}^+ + 4\text{e}^- \rightarrow \text{HCHO} + \text{H}_2\text{O}$	-0.48
$\text{CO}_2 + 6\text{H}^+ + 6\text{e}^- \rightarrow \text{CH}_3\text{OH} + \text{H}_2\text{O}$	-0.38
$\text{CO}_2 + 8\text{H}^+ + 8\text{e}^- \rightarrow \text{CH}_4 + 2\text{H}_2\text{O}$	-0.24

Table 1.1 Selected CO₂ reduction processes and the corresponding redox potentials (pH 7 in aqueous solution vs NHE, 25 °C, 1 atmosphere gas pressure, and 1 M for the other solutes).^[8]

However, to manage proton coupled multiple-electron processes is a huge challenge kinetically.^[8] The key problem is the assembly of nuclei and/or the rearrangement of chemical bonds, which require an additional driving force (the overpotential, η_{cat} , i.e. the energy beyond the thermodynamically determined reduction potential needed to drive the reaction).^[9] Another challenge related to CO₂ electroreduction is the presence of competing hydrogen evolution reaction (HER), a side-reaction that especially in aqueous media occurs at similar potentials and at appreciable catalytic rates.^[10] The presence of a catalyst that can direct the sequences of steps necessary for converting CO₂, with low kinetic barriers and scarce affinity for HER, is crucial.^[11]

The way catalysts lower the activation barrier and influence the selectivity of CO₂RR resides in the possibility for bond-forming interactions (chemisorption) prior to electron transfer. This leads to low values for η_{cat} and opens the way to different reduction pathways. Typically, one or a mixture of products can be obtained, as the selectivity of catalysts depends on the nature of catalyst itself, but also on additional parameters e.g., nature of solvent and supporting electrolyte, as well as temperature, pressure, and so on.^[9]

The main C₁ products that can be obtained with the CO₂RR include carbon monoxide, formic acid or formate, formaldehyde, methanol, and methane. Oxalic acid or oxalate, ethanol, ethylene are the main C₂ products. The formation of higher-order (C₃₊) hydrocarbons, such as propanol, has also been observed.^[12] Considering the economic perspectives of CO₂RR, it comes natural to wonder what would be the best tradeoff between energy demand, product

selectivity and product market value, that makes certain products more attractive as a target than others.

From a fuel perspective, the amount of energy that can be stored in a given product increases with the number of C atoms, therefore the logical reasoning supports production of longer-chain carbon products. However, the direct conversion of CO₂ to such long-chained products requires several proton coupled multiple-electron processes, which involves high amounts of energy, highly complex reaction pathways and (for the moment) poor selectivities.^[13] Taking as example a series of non-branched alcohols, a recent study^[14] shows that while the volumetric and gravimetric energy density increase with chain length, the energy density normalized to the number of electrons transferred decreases (**Figure 1.1**). Additionally, when the catalyst is poorly selective, the costs of separation of the product from a mixture can be prohibitive.

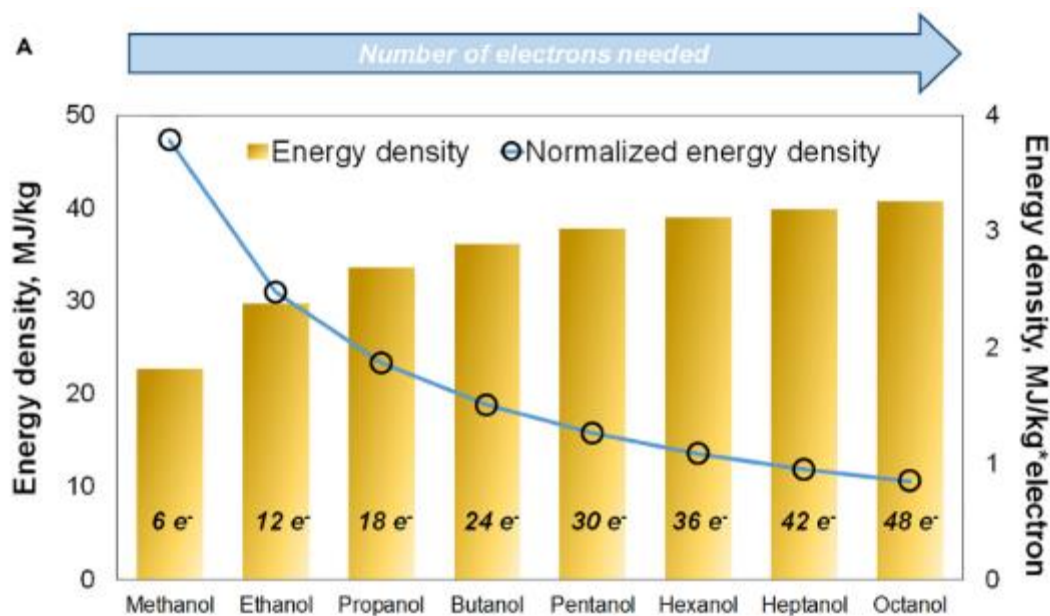


Figure 1.1 Comparison between energy density and normalized energy density (number of e^- needed to convert CO₂ to such product) of a series of unbranched alcohols.^[14]

Consequently, while pursuing the search for a catalyst that is extremely efficient and selective for specific higher-carbon products, a viable strategy consists in focusing on the catalysis of single-carbon products, such as CO and HCOOH, which have the double advantage of being able to be upgraded into more energy dense products and be used as building blocks for the production of several chemicals.

For example, CO has high relevance for the chemical industry.^[15] It is considered the most important C₁-building block and is intensively used in large industrial processes, such as Fischer-Tropsch synthesis of hydrocarbons and Monsanto/Cativa acetic acid synthesis. CO is one of the most economically viable targets as demonstrated from techno-economic analysis^[16] that take into account the costs of CO₂, electricity, separation, capital and maintenance, operation and the known product selectivity for the CO₂RR process. Interestingly, CO electroreduction using CO₂- derived CO is becoming very attractive, thanks to the possibility to generate several products like ethylene and acetate/acetic acid or even specialty chemicals (Figure 1.2).^[17]

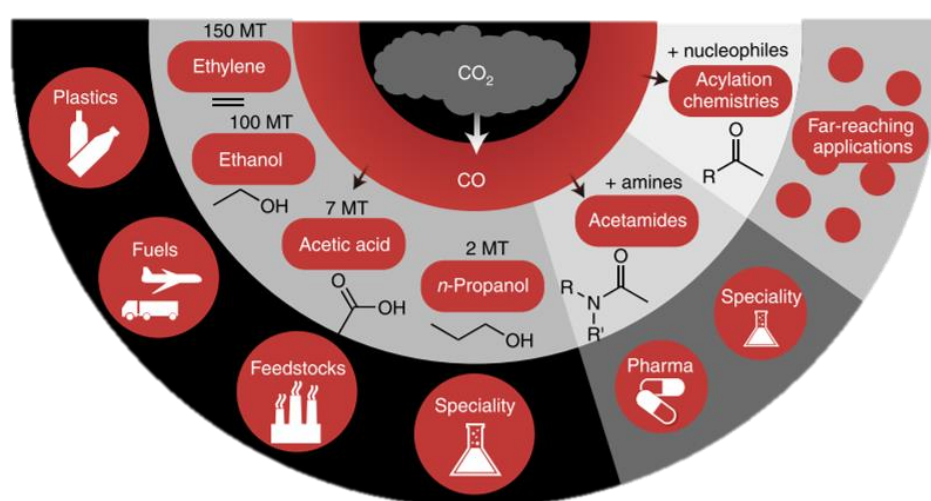


Figure 1.2 Overview of the most important chemical products from two-step CO₂ conversion through CO electroreduction and their fields of application.^[17]

Formic acid could be directly used as a feedstock for fuel cells and as a precursor for manufacturing value-added chemicals such as formate esters, methanol, and other carboxylic acids and derivatives.^[18] Other applications include cleaning, textile industry, and antiseptics.^[19] More importantly, catalyzed formic acid dehydrogenation^[20] is now making formic acid attractive as hydrogen carrier, due to its liquid phase under ambient conditions, low flammability and toxicity. Producing this important energy carrier via electrochemical CO₂ reduction can lower carbon emissions and make formic acid a carbon neutral liquid fuel.^[21]

The CO₂RR can be either homogeneously or heterogeneously catalyzed. While heterogeneous catalysts are generally materials that constitute the cathode itself, homogeneous catalysts are molecularly defined compounds that act as a “shuttle” between the cathode and the substrate to be reduced, and are dissolved in the electrolyte solution. Some of the most relevant metrics to

evaluate a CO₂RR catalyst include the faradaic yield (FY) (the product selectivity of the reaction), the already mentioned overpotential η_{cat} , and the current density at which it can operate (i.e., the rate of reaction). Additionally, turnover frequency (TOF), and turnover number (TON) are very important parameters to compare the activity of different catalysts; while the TON is calculated by dividing the moles of desired product formed by the number of catalytic active sites, the TOF is calculated by dividing the TON by the reaction time (and gives a more accurate idea of the efficiency of the catalyst).

In the next section, the most representative heterogeneous and homogeneous catalysts will be presented, along with their strengths and weaknesses for the CO₂RR process. Heterogenization of molecular catalysts will also be introduced, as a way to circumvent downsides and at the same time combine the strengths of both approaches.

1.2 Catalysts for CO₂ electroreduction

1.2.1 Heterogeneous and homogeneous catalysts

The first studies of catalyzed electrochemical CO₂ reduction focused primarily on heterogeneous catalysts, namely polycrystalline monometallic catalysts,^[22] because they are structurally simple, robust and easy to handle, which makes them attractive candidates for fundamental studies. Thus, it was demonstrated that some metals are selective for CO (e.g., Au, Ag, and Zn), formate (e.g., Sn, In, and Pb), or hydrogen (e.g., Fe, Ni, and Pt) production. Among all the monometallic catalysts, Cu exhibits a unique catalytic ability to produce a wide range of CO₂ reduction products, including CO, formate, ethanol, and ethylene.^[22–25]

Because the catalytic activity of heterogeneous catalysts is usually proportional to the number of surface active sites, during the years efforts have been made to improve the efficiency of bulk monometals with nanostructuring.^[26] Researchers have thus managed to create a plethora of nano-architected electrode materials^[26–29] exhibiting enormous promise to achieve high-performance CO₂ reduction (besides having, in some cases, also beautiful structures (**Figure 1.3**)).

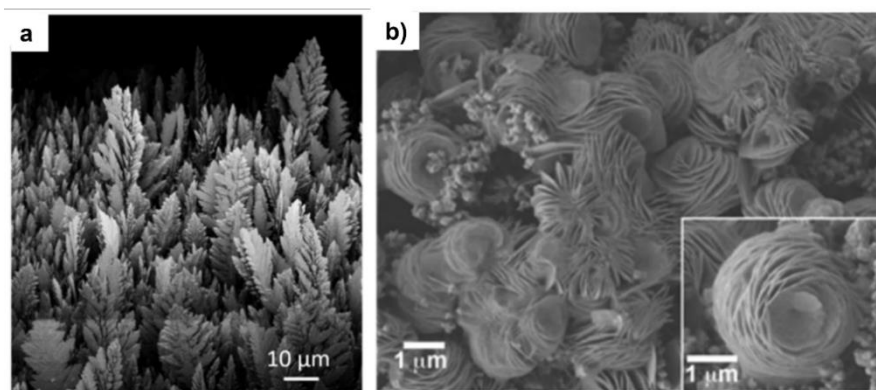


Figure 1.3 SEM images for a) Zn dendrite catalyst^[29] and b) electrochemically deposited Bi-thin film.^[28]

Besides poly- or mono-crystalline monometallic catalysts, ion-modified metallics or bimetallics have also been recently demonstrated as promising catalysts for CO₂ reduction.^[30] Among these, Cu-Sn catalysts have attracted attention due to the high selectivity for CO evolution in aqueous conditions (FY values up to 94% over a potential range of -0.75 V to -0.9 V vs RHE),^[31] good activity, and stability.^[32] The intentional oxidation or reduction of metallic electrodes is also frequently employed to create active surface sites for CO₂RR. The anodic oxidation of Sn nanoparticles to SnO₂ has been demonstrated to generate a very selective catalyst in aqueous NaHCO₃ solutions, with maximum faradaic yields for formate production of > 93%.^[33,34] Organic functionalization of metal catalysts has been recently explored to tune product selectivity.^[35,36]

Non-metallic materials have also been used as a heterogeneous catalyst. Carbon nanofibers, as a metal-free and non-precious catalyst, exhibits exceptionally high current densities (~13 times higher than bulk Ag) for the conversion of CO₂ to CO (at -0.573 V versus SHE).^[37] Heteroatom-doped graphitic carbon materials, in particular nitrogen-doped carbon N-C, or metal and nitrogen doped carbon M-N-C, with M= Fe, Co, and Ni showed the most promising performances.^[38] Ni-N-C electrodes could provide CO partial current densities above 200 mA cm² and stable FY for CO around 85% for up to 20 hours in aqueous conditions.^[39] Lately, a flexible and self-supported single-atom nickel-decorated porous carbon membrane catalyst was presented by He and collaborators.^[40] This membrane was used as a gas diffusion electrode reaching industrially relevant carbon monoxide production with 308.4 mA cm⁻² partial current density and 88% Faradaic efficiency for up to 120 h.

While heterogeneous catalysts have demonstrated exceptional results in CO₂ reduction to C₁ products, future efforts focus on the development of efficient electrocatalysts to reduce CO₂ to more value-added chemicals, such as C₂–C₄ products. Selective formation of C₃₊ products and beyond is challenging as the catalytic sites need to bind key intermediates tightly enough to allow the next C–C coupling, and additionally avoid all side reactions that are more thermodynamically and kinetically favorable and lead to C₁- C₂ species.^[41] Cu is the foremost metal capable of C–C coupling reactions, and hence CO₂ conversion to products with two or more carbon atoms.^[42]

CO₂RR research with heterogeneous catalysts has progressed from initial metal screening to improving reaction kinetics and active sites through facet engineering, interface catalysis, defects introduction, alloying, and lastly through single-atom catalysts.^[43] Relatively facile design represents one of the attractive features of heterogeneous catalysts, as materials can be optimized and engineered. In particular, over the past few decades efforts in nanostructuring of materials gave rise to 0D quantum dots, nanoparticles, and clusters, 1D nanotubes and nanowires, 2D nanoplates and layers, and 3D multi-component nanostructures.^[44] On the other hand, although intricate and efficient architectures may now be relatively easy to obtain, they can be delicate, and morphology can undergo changes during catalysis.^[45]

At the same time, since most mass transfer processes occur on the surface of heterogeneous catalysts, the inactivity of the sites inside the material limit their overall performance.^[46] Such a different behavior between surface and interior atoms also makes the mechanistic investigations difficult. Thus, elucidation of the mechanisms of heterogeneous catalysis towards CO₂RR is a difficult task, given the number and the complexity of possible active sites in such materials (**Figure 1.4**). This, in return, slows down rational design and tailoring of the properties of catalysts.

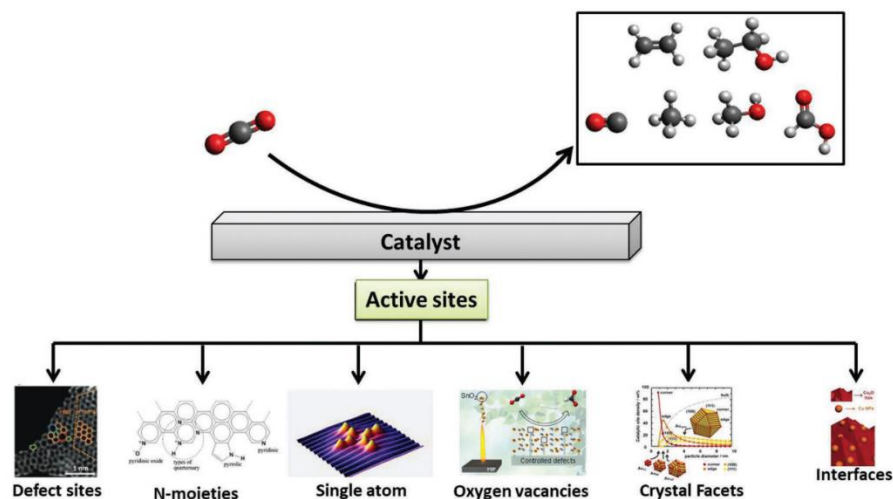
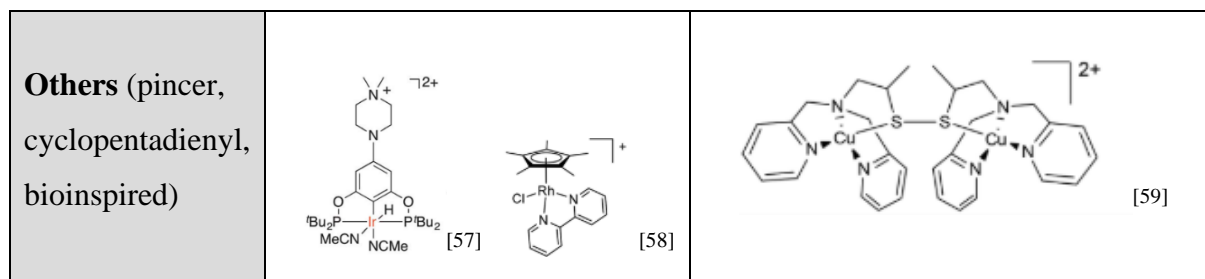


Figure 1.4 Reported active sites in heterogeneous electrocatalysts for CO₂RR.^[43]

The first homogeneous electrocatalysts were reported in the 70s by Tamaru and coworkers,^[47] and later by Toshima and collaborators,^[48,49] who investigated the electrocatalytic behaviour of complexes of phthalocyanines (MPCs) and porphyrins (MPs, where M = Co, Ni, Cu, Fe) as CO₂ reduction catalysts. There now exists a wide range of known molecular catalysts, including those based on noble (e.g., Ru, Ir, and Re) metals.^[9] Research is now devoting particular attention to earth-abundant metals (e.g., Co, Ni, Fe, Mn, and Cu), for obvious environmental reasons.^[50] Along with different metals, several classes of ligands have been investigated^[51] (Table 1.2).

Table 1.2 Representative structures of molecular catalysts for the CO₂RR.

Metal / Ligand	Rare	Earth Abundant
Macrocycle	---	
Bipy-Poly-pyridine		



PCs and Ps display a rich redox chemistry because of their 18 π -electron arrangement. Savéant and co-workers extensively studied this class of catalysts, especially substituted Fe tetraphenylporphyrins (TPPs), which are among the most active homogenous catalysts for CO₂ to CO conversion in aprotic solvents (DMF, MeCN).^[60] For example, CO faradaic yield above 90% through 50 million turnovers over 4 hours of electrolysis at low overpotential (0.465 V), with no observed degradation^[61] was obtained through the introduction of phenolic groups in all ortho and ortho' positions of the of the TPP phenyl groups. Through their work, the group provided incommensurable advances in the field, with rigorous deciphering of mechanisms and catalyst benchmarking,^[62,63] highlighting the influence of ligand modifications in the trade-off between activity and overpotential.^[64]

Along with PCs and Ps, the first high current efficiencies and TONs were found in Co and Ni tetraazamacrocycles.^[65] In particular, [Ni(cyclam)]²⁺ became known as one of the first homogeneous catalyst to selectively reduce CO₂ to CO in aqueous conditions.^[66] An in-depth analysis of this catalyst will be provided in the following sections. Interestingly, Co was found to be efficient for the selective reduction of CO₂ to formate in combination with other ligands. A series of monometallic cyclopentadienylcobalt complexes were reported to produce formic acid in mixtures of DMF and water, with faradaic efficiencies of ~90 % at moderate overpotentials (500–700 mV).^[67]

In 1984, Lehn's group reported the electrocatalytic reduction of CO₂ by the use of a Re(bipy)(CO)₃Cl (bipy = 2,2' - bipyridine) complex.^[68] This rhenium complex selectively reduced CO₂ to CO at a potential of 1.49 V vs. SCE using a 9:1 DMF-H₂O solution. Since then, bi- and poly-pyridyl transition metal complexes have become one of the more thoroughly studied classes of molecular catalysts towards CO₂ reduction to date.^[69] As a cheaper alternative to the analogue Re catalyst, Deronzier and collaborators^[70] reported that [Mn(bpy)(CO)₃Br] in the presence of water could produce only CO with a faradaic efficiency of almost 100%. This first finding was followed by several noteworthy contributions, in particular from Kubiak and

collaborators, who investigated the related $[\text{Mn}(\text{bpy-}t\text{Bu})(\text{CO})_3\text{Br}]$ with respect to type and concentration of the proton source, as well as ligand modifications in this class of catalysts,^[55] providing as well some mechanistic insights.^[71]

It is worth noting that the great majority of described molecular catalysts are known to operate in organic solvents, with the addition of only small percentages of either water or a weak organic acid, to provide a source of protons. While this is mostly because of the poor solubility of the complexes in aqueous solution, the use of organic solvents minimizes parasitic hydrogen evolution, which would be much more evident in a proton rich environment like water. Nonetheless, some notable examples exist: Brookhart and collaborators described a water-soluble Ir pincer catalyst, selective for formate (93% FY) at -1.41 V vs NHE in 0.1 M NaHCO_3 with 1% MeCN added.^[72] The substitution of the four paraphenyl hydrogens by trimethylammonio groups in the FeTPP mentioned before afforded a water-soluble catalyst that converted CO_2 to CO with ~90% FY in 0.1 M KCl at -0.97 V vs. NHE.^[73] A Ru^{II} polypyridyl carbene complex gave a FY of 66% for CO production when employed in 0.1 M NaHCO_3 at -1.2 V vs NHE.^[74]

As could be seen from the above mentioned examples, tuning the primary and secondary coordination spheres of a molecular catalyst by manipulating the chelating environment represents a powerful advantage in homogenous catalysis. The selectivity of a catalyst can be significantly increased through subtle chemical modifications of the steric and electronic effects of the ligands.^[75,76]

Another advantage of molecular catalysts is that their structures can be readily characterized by conventional spectroscopy and X-ray crystallography. Their catalytic sites are therefore clearly exposed and identifiable. This allows for a prompt understanding of catalytic reaction mechanisms and benchmarking of the catalysts. Several common techniques can be successfully employed, such as spectroelectrochemistry, stopped-flow UV-Vis spectroscopy, *in situ* IR spectroscopy, *in situ* NMR spectroscopy and *in situ* MS.^[77,78]

Homogeneously catalyzed CO_2 reduction typically involves a two-electron reduction of CO_2 to either CO or formate. C_2 or C_{2+} products can rarely be obtained,^[79] due to the intrinsic nature of molecular catalysts, i.e. possessing only one “isolated” active site, making the formation of several C-C bonds difficult, if not impossible. Efforts to tackle this problem have resulted,

among others, in dinuclear metal complexes,^[80] as the synergistic effect between two metals can trigger a variety of chemical transformations by binding and activating small molecules, just as metalloenzymes do in nature. Biological systems are indeed a huge source of inspiration in homogeneous CO₂ reduction,^[81] and that is why several syntheses of bio-inspired molecular catalysts that can replicate the active site of various biomolecules have been proposed.^[82–84]

Nevertheless, products separation and stream recycle is more efficient in heterogeneous conditions than in homogeneous. The usually non-recyclable character of homogeneous catalysts, as well as their general shorter lifetimes,^[85] impedes their application in industrial utilization, despite their excellent selectivity and tunability.

1.2.2 Heterogenization of molecular catalysts

Associating a molecular catalyst to a conductive substrate could lead to new, efficient catalytic systems. Under supported conditions, transfer of electrons from the electrode to the catalyst are faster, as the distances are minimized, and diffusion limitations are by-passed.^[86] The heterogenization can make a complex active in a solvent where the complex normally is not soluble, e.g., water.

Other major benefits include facilitated separation of catalyst and products (liquid or gaseous) and lower amount of catalyst needed compared to homogeneous conditions, two important requirements from a point of view of practical applications, notably for the design and development of industrially relevant electrolyzers.^[87] Additionally, if the catalysts are well dispersed onto the surface of a substrate, the physical confinement can prevent unwanted deactivation induced by aggregations or dimerizations.^[88]

Several heterogenization methods have been proposed.^[84–88] Considering the interactions between the molecular catalyst and the target surface, these methods can be grouped into three main categories: covalent, non-covalent, and periodic interactions. **Table 1.3** provides an overview of the performances of a selection of heterogenized molecular electrocatalysts for the CO₂RR.

Covalent grafting of a molecular catalyst can proceed via either chemical or electrochemical reactions. The catalyst ligand and/or the substrate are thus modified with functionalizations

such as diazonium, amine, alkynyl, phosphonic acid, and then reacted to form the desired bonds. Classical organic reactions, such as C-C or C-N coupling reactions, or click chemistry reactions, have been successfully employed.^[91]

Initial attempts employed 2D substrates, such as glassy carbon^[91,92], however such a strategy permitted to graft only a monolayer of catalyst on the surface, which resulted in poor loadings and therefore poor performances. Current densities and selectivity for the CO₂RR could be increased significantly with the use of highly porous substrates. This was the case for a Fe porphyrin (with six pendant –OH groups in ortho and ortho' positions on three of the phenyl rings and one carboxylic acid group in the para position of the fourth phenyl), which was heterogenized on multi walled carbon nanotubes (MWCNTs) via an amide linkage, and then deposited on a glassy carbon electrode.^[93] Electrolysis was performed in aqueous conditions at –1.06 V vs SHE, corresponding to 510 mV overpotential. After 1 hour, CO was selectively produced with 90% catalytic selectivity; after 3h, the selectivity slightly decreased to 80%.

Another very effective strategy, which involved the heterogenization of a cobalt porphyrin with the metal centers directly grafted onto carbon nanotubes, was proposed by Han and collaborators.^[94] To synthesize the grafted catalysts, protoporphyrin IX cobalt chloride was refluxed with hydroxyl-functionalized carbon nanotubes (containing 3.06 wt.% hydroxyls) in ethanol with additional triethylamine. A covalent bond between Co and a surface O atom was formed in the process (which produced HCl that was removed by triethylamine through the formation of a triethylamine hydrochloride salt, **Figure 1.5**). Impressive current densities (up to 25 mA cm⁻²) and almost quantitative FYs for CO were obtained when running electrolysis at -0.60 V vs. RHE in 0.5 M NaHCO₃ solution, which makes this system one of the best performing examples of heterogenized molecular catalyst available to date.

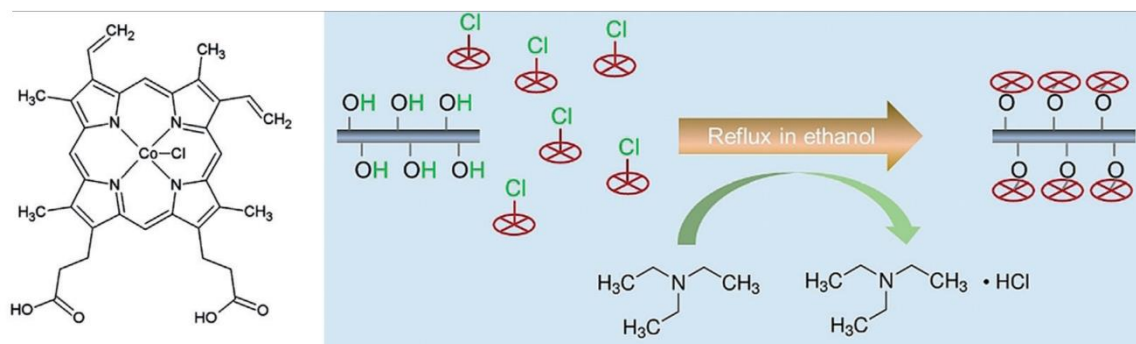


Figure 1.5 Structure of the catalyst (protoporphyrin IX cobalt chloride, left) and preparation of chemically grafted cobalt porphyrins on carbon nanotubes (right).^[94]

π - π interactions are widely accepted to be an efficient method to immobilize metal complexes onto a substrate via non-covalent interactions. This approach requires the metal complexes used to be highly aromatic, with delocalized electrons, in order to facilitate the interaction with a substrate, and to permit electron transfer as a result. Ligands such as porphyrin- or phthalocyanine-derivatives are perfectly suited for such applications.

Among the catalysts that have received the most benefit through this type of heterogenization, Co complexes, especially CoPCs and CoPs, have been extensively studied and are able to provide excellent performances in aqueous media on the surfaces of MWCNTs.^[95,96] Berlinguette and collaborators^[97] reported that a commercially available CoPC immobilized on a gas diffusion layer could form CO with >95% selectivity at current densities of 150 mA cm⁻² in a flow cell (a zero-gap membrane reactor, in tandem with a nickel foam oxygen evolution reaction catalyst). The same CoPC lasted merely 10 hours at 10 mA cm⁻² in a batch-type electrolysis cell, while it could undergo electrolysis for >100 hours in a flow cell.

In 2018, Robert and coworkers^[98] heterogenized a Co^{II} quaterpyridine complex [Co(qpy)]²⁺ on MWCNTs. Typical catalyst loading was 10⁻⁸–10⁻⁹ mol cm⁻², and the material was drop-cast either onto glassy carbon or porous carbon paper. At -0.48 V vs. RHE, a high and stable current density of 6.3 mA cm⁻² was obtained during 3.5 h, with 100% FY for CO.

Zhou and coworkers^[99] designed a series of nickel phthalocyanine molecules supported on carbon nanotubes as molecularly dispersed electrocatalysts. By tuning the pendant groups on the phthalocyanine ligand, they could obtain extremely selective catalysts (nearly 100% FY for CO). Additionally, π -stacking interactions were confirmed to be a valid strategy, as

demonstrated by the stability of the system during electrolysis at 150 mA cm^{-2} current density for 40h (**Figure 1.6**).

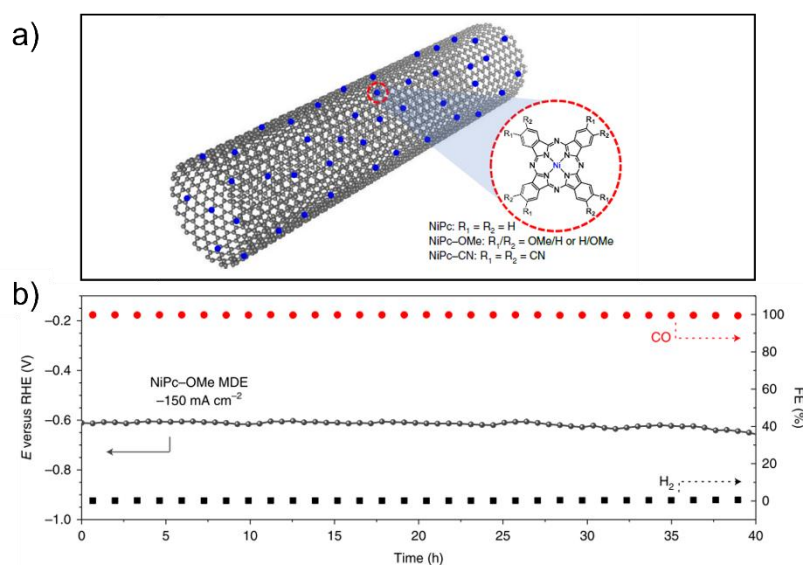


Figure 1.6 a) Schematic representation of the molecularly dispersed NiPc on the side-walls of CNTs and b) Long-term operation of molecularly dispersed NiPc-OMe at -150 mA cm^{-2} .^[99]

For bipyridine or macrocycles with a relatively low content of delocalized structure, a conjugated fragment like pyrene can be appended to the ligands.^[100] One of the first reports that employed this strategy was proposed by Gray and coworkers in 2013.^[101] Two well-known molecular complexes, $[\text{Cp}^*\text{Rh}(\text{phen})\text{Cl}]\text{Cl}$ (phen = 1,10-phenanthroline) and $[\text{Re}(\text{bpy})(\text{CO})_3\text{Cl}]$, were modified with two pyrene groups. The modified complexes were mixed with carbon black and further deposited on highly oriented pyrolytic graphite (HOPG). While the Rh complex was found very active for proton reduction, the modified Re complex proved to be catalytically active in a CO_2 saturated acetonitrile solution, with a CO faradaic yield of 70% and a TON of 58 (1.25 h electrolysis), at a very negative potential of -1.93 V vs SHE. While the performance of the electrodes was not exceptional, the novelty of the strategy encouraged other groups to test the same approach with other modified complexes.

Brookhart and collaborators proposed, in 2014,^[102] an Ir pincer dihydride complex modified with a pyrene and immobilized onto carbon nanotubes, which were further deposited onto a gas diffusion electrode (GDE) and finally coated with a polyethylene glycol overlayer. Formic acid was obtained with high yield (up to 96%). Noteworthy, the stability of the so-made electrodes, the high turnover numbers (ca. 54000) and turnover frequencies (15 s^{-1}).

Shortly thereafter, Maurin and Robert^[103] heterogenized a pyrene-appended iron triphenyl porphyrin bearing six pendant OH groups on the phenyl rings in all ortho and ortho' positions on carbon nanotubes, and successively deposited it on GC. Electrolysis in aqueous conditions at a potential of -1.03 V vs NHE (480 mV overpotential) was run for 3 h. During this period, the current remained very stable and excellent selectivity for CO was obtained.

An example of pyrene modified *fac*-[MnBr(bpy)(CO)₃] (bpy= 2,2'-bipyridine) was proposed by Reisner and coworkers.^[104] The complex was anchored on MWCNTs and then on glassy carbon. Interestingly, it was found that, depending on the loading of the catalyst on the substrate, the selectivity for the CO₂RR could be tuned towards either CO (at high catalyst concentrations) or HCOOH (at low concentrations). UV-vis and surface-sensitive IR spectroelectrochemical techniques were used to elucidate this change in selectivity.

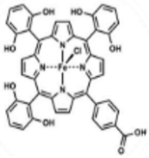
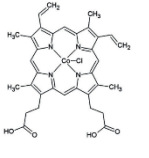
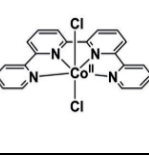
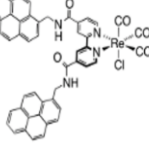
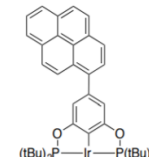
Lately, Warren and coworkers reported the heterogenization of another rhenium^I diimine complex.^[105] ClRe(CO)₃QuBIm-pyr was dropcasted on a edge-plane graphite (EPG) working electrode. The pyrene-modified complex shows activity in H₂O, with CO as the primary reduction product, albeit at modest FY after 1h of controlled potential electrolysis (CPE).

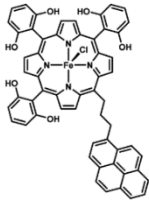
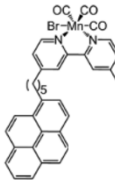
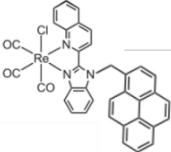
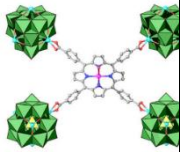
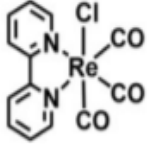
The third method to immobilize molecular catalysts is to incorporate the catalysts into 3D structured frameworks, such as covalent organic or metal organic frameworks (COFs or MOFs, respectively) and other polymers. The diversity of possible metal precursor and organic linkers leads to a huge variety of MOFs in terms of structure and chemical composition.^[106] Generally, these materials present high porosity, which is an advantage in terms of transport and exposure of the active sites. Additionally, when the framework is conducting, there is no need for additional support material. Noble metals such as Re and Ag, as well as earth abundant metals like Fe, Co, Ni, Cu and Zn have been investigated in this kind of materials.^[107]

Lan and co-workers^[108] prepared Co-polyoxometalate-metalloporphyrin organic frameworks and tested the electrocatalytic properties toward the CO₂RR in 0.5 M KHCO₃ electrolyte, obtaining remarkable FY (99%, highest in reported MOFs) for CO production. The cobalt in Co-porphyrin was proposed as a favorable active site whereas the polyoxometalate served as electron-rich aggregates and efficiently promote electronic transport.

Polymer-based supports have been also employed in the CO₂RR for the incorporation of molecular complexes. Lately, the complex *fac*-[Re(bpy)(CO)₃Cl] was dispersed in a polymer ion gel of acrylamide with imidazolium moieties, in order to make the catalyst operate in aqueous conditions. Electrolysis for 6h at -0.68 V vs. RHE produces CO with over 90 % FY. The selectivity, however, diminishes with time to 50% FY over 24h.

Table 1.3 Representative heterogenized molecular catalysts for the CO₂RR, with a focus on pyrene-modified catalysts.

Catalyst	Loading	Medium	Support/Working electrode/type of heterogenization	E (V)	FY(%)	TON (CO)	TOF (CO)	Electrolysis time (h)	Ref.
	6.4 · 10 ⁻⁹ mol cm ⁻²	NaHCO ₃ 0.5 M (pH 7.3)	MWCNTs/GC/covalent	-1.06 vs SHE	80% CO	750	178 h ⁻¹	3	[93]
	84.8 · 10 ⁻⁹ mol cm ⁻²	NaHCO ₃ 0.5 M	MWCNTs/Carbon paper/covalent	-0.60 vs RHE	98% CO	60000	1.37 s ⁻¹	12	[94]
	8.5 · 10 ⁻⁹ mol cm ⁻²	NaHCO ₃ 0.5 M	MWCNTs/GC/noncovalent	-0.48 vs RHE	100% CO	89095	5.45 s ⁻¹	4.5	[98]
	26 · 10 ⁻⁹ mol cm ⁻²	MeCN 0.1 M NBu ₄ PF ₆	Carbon black/HOPG/noncovalent	-2.3 vs Fc ⁺ /Fc ⁰	70% CO	58	-	1.25	[109]
	3.8 · 10 ⁻⁹ mol cm ⁻²	0.5 M LiClO ₄ , 0.1M NaHCO ₃ , 1% v/v MeCN	MWCNTs/GDE/noncovalent	-1.4 vs NHE	83% HCOO ⁻	54200	15.1 s ⁻¹	1	[72]

	2.4 10^{-8} mol cm^{-2}	NaHCO_3 0.5 M	MWCNTs/GC/ noncovalent	-1.03 vs NHE	96% CO	432	144 h^{-1}	3	[103]
	30 10^{-9} mol cm^{-2}	0.5 M KHCO_3	MWCNTs/GC/ noncovalent	-1.1 vs SHE	25% CO , 8% HCOOH , 59% H_2 (HCO OH)	1400 (CO) 460 (HCO OH)	-	8	[104]
	2.26 10^{-10} mol cm^{-2}	0.5 M KHCO_3	EPG/ noncovalent	-1.32 vs NHE	65% CO , 35% H_2	-	-	1	[105]
	1 mg cm^{-2}	0.5 M KHCO_3	Carbon cloth	-0.8 vs RHE	99% CO	-	1656 h^{-1}	36	[108]
	0.75 to 2.2 μmol cm^{-2}	0.1 M KOH + 0.1 M K_2CO_3	Polymer ion gel/Carbon cloth	-0.68 vs RHE	50% CO	76	-	24	[110]

All in all, whether homogeneous or heterogeneous, a good catalyst for the reduction of CO_2 must have certain characteristics to be able to reach the market and avoid being forgotten in a drawer of the laboratory. High activity under small overpotentials is necessary to minimize the cost of electricity. High selectivity towards the desired chemicals is fundamental to avoid postreaction separation. High stability for long-term applications, and minimum production capital cost have a great relevance in the industrial field.

We have seen above how the immobilization of molecular catalysts has been a valid approach to help them reach industrial requirements. In many cases, in fact, they have demonstrated excellent selectivity as well as good stability and current densities. This is the result of the synergistic combination of tools that are typical of either homogeneous or heterogeneous catalysis and originate from the most diverse scientific fields. Thus, before its immobilization,

the complex can be optimized thanks to synthetic approaches and *in situ* or *in operando* characterization techniques, that are able to reveal not only the structure, but also the catalytic mechanism, in a feedback loop of redesigns that can lead to maximize the intrinsic activity of the catalyst (**Figure 1.7**, left).

In parallel, nanostructuring and surface engineering, which are typical tools of heterogeneous catalysis, have achieved impressive results. Starting from one or two-dimensional materials it is possible to design hierarchical materials with very high surface areas and multiple levels of porosity, reminiscent of the natural structures of leaves, among others (**Figure 1.7**, right).

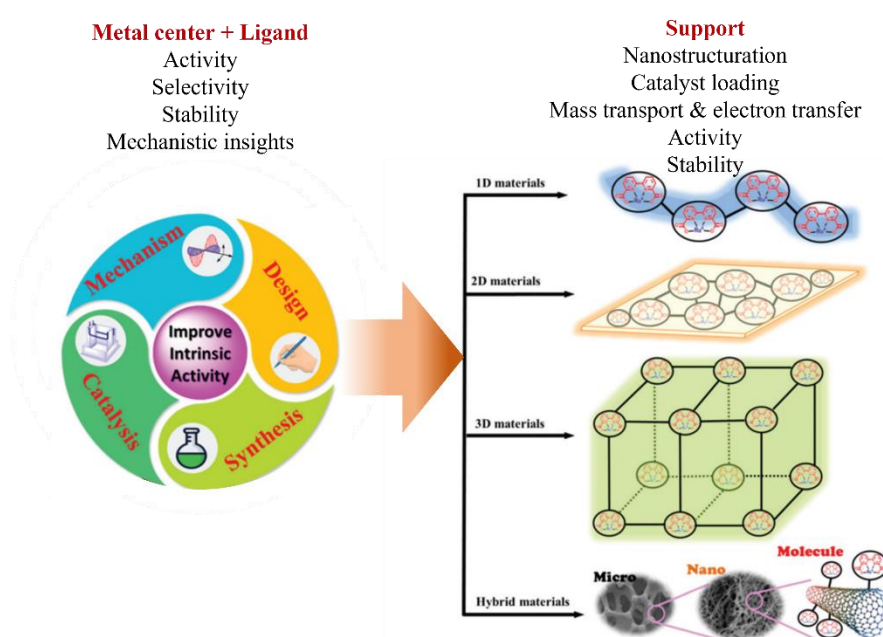


Figure 1.7 From homogeneous to heterogeneous catalysis: the optimization of the catalyst starts at the homogeneous level. The support brings to the hybrid system additional benefits such as extensive surface areas and improved mass transport and electron transfer. Modified from Sun et al.^[88]

However, building structures with multiple variables, such as hybrid electrodes, also necessarily introduces additional levels of complexity. An effective heterogenization of the molecular complexes is still challenging, as each strategy presents some key issues. Physically adsorbed molecular catalysts easily suffer from electrode surface detachment owing to the weakness of such interaction forces.^[89] Additionally, it is difficult to control the catalyst loading and dispersion, since π - π and/or electrostatic interactions are much less specific than chemical bonding. Excessive catalyst stacking may hinder both the mass transport of CO_2 and electron transfer processes.^[86] Covalent heterogenization may minimize these issues, however it

requires the design of an additional reaction that adds complexity and increases the cost of the process.^[111] As the immobilized complexes could undergo different catalytic mechanisms when they are in the heterogeneous phase, deep characterization of hybrid electrodes is required; however, since molecular catalysts are generally immobilized with rather low loading amounts, the characterization of such catalysts is particularly challenging with traditional techniques, due to the limited signal response.^[87]

Nonetheless, the field of CO₂R is rapidly evolving, with more efficient and selective systems, together with more advanced analytical methods. The recent implementation of molecular catalysts into flow cells and electrolyzers that could operate at large current densities^[95] represents the proof that this approach can give rise to exciting new perspectives in the near future.

1.3 The case of [Ni(cyclam)]²⁺

Cyclam (1,4,8,11-tetraazacyclotetradecane) is a macrocycle that presents four secondary amines and at 25°C is a solid, with the appearance of a white fluffy needle-like crystalline powder. Its synthesis was first proposed in 1937 by Van Alpen,^[112,113] who firstly synthesized the linear tetramine (1,4,8,11-tetraazaundecane). By reacting it with an excess of 1,3-dibromopropane in ethanol in the presence of potassium carbonate he then isolated the macrocycle.

It was immediately noticed that, conversely to other tetramine macrocycles, cyclam presented an unusual stability.^[114] When the crystal structure of cyclam was determined, it was shown that four intramolecular bonds are present, which involve two N-H fragments, interacting with the lone pairs of the two adjacent nitrogen atoms (**Figure 1.8a**). Such arrangement confers to cyclam some peculiar properties, besides the ability of forming beautiful hydrogen bonded assembled columns, when crystallized from CHCl₃-hexane (**Figure 1.8b**).^[115]

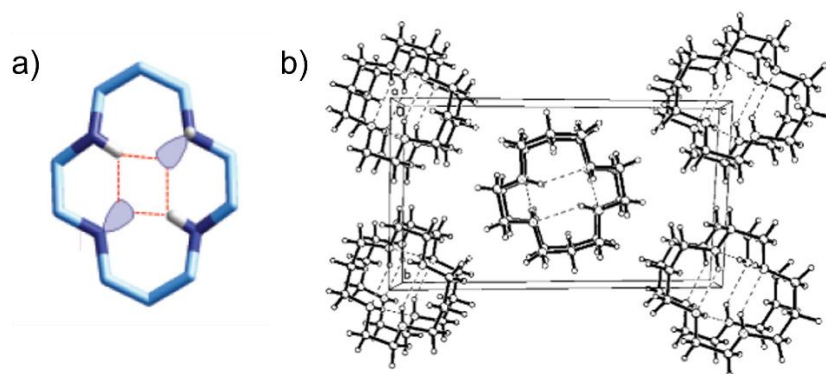


Figure 1.8 a) Structure of cyclam showing two equatorial N–H fragments establishing H bonds with the lone pairs of the adjacent nitrogen atoms^[116] and b) packing diagram for cyclam showing the intermolecular hydrogen bonded columnar arrays and intramolecular hydrogen bonding.^[115]

Owing to the good nucleophilicity of the sp^3 -hybridized nitrogen atoms, ligands can be directly attached to the amine functionalities on the ring via N-alkylation or N-acylation. But the special feature that has probably made this cyclic tetramine interesting in many different scientific fields is the ability to bind very strongly to transition metal cations: cyclam forms exceptionally stable complexes because it is perfectly “preorganized and preoriented” for including and establishing strong interactions with those 3d metals that experience the highest ligand field stabilization from a tetragonal coordination geometry.^[116,117] This special ability, which has been object of study for several years now,^[118] has been called the “macrocyclic effect”.^[119]

It was in 1965 when Bosnich, Poon and Tobe^[120] reported the first complexes of 1,4,8,11-tetraazacyclotetradecane (with Co^{III}), which they named cyclam (from cycl[ic] [tetr]am[ine]). During their experiments they observed that each nitrogen in the cyclam molecule, when coordinated, represented an asymmetric center, thus giving rise to five distinct non-enantiomeric combinations which they named as *trans*-I to *trans*-V, depending on the direction in which the N-H bond points (**Figure 1.9**). By solving the X-ray structure of the first $[Ni(cyclam)Cl_2]$ complex^[121] and comparing it with their initial qualitative assessments made with Dreiding stereomodels, they also concluded that the most stable configurations should be *trans*-I and *trans*-III. Hundreds of XRD structures of cyclam complexes in the following years confirmed these hypotheses: Donnelly and Zimmer analyzed all the nickel complexes containing the cyclam backbone in the Cambridge Structural Database (CSD), and found that the most commonly found configuration is the most stable configuration, *trans*-III.^[122] Similar results were found for Cu^{II} cyclam complexes,^[123] isolated for the first time in 1969.^[119]

Experimentally, it was found that for $[\text{Ni}(\text{cyclam})]^{2+}$ the *trans*-I and *trans*-III complexes are the only isomers present in any significant concentration in solution.^[124] The equilibrium concentrations of the *trans*-I and *trans*-III isomers were reported to be roughly 15 and 85% respectively in aqueous solution based on ^1H NMR data.^[125]

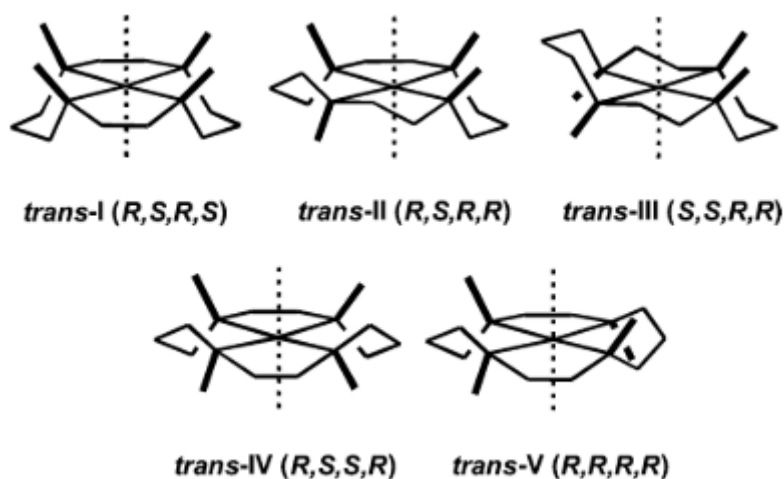


Figure 1.9 Configurations of metal-cyclam complexes.^[126]

For decades, different $[\text{Ni}(\text{cyclam})]^{2+}$ complexes were described and isolated^[127,128]. This class of complexes have been widely studied for CO_2RR , and for several years they were considered among the best catalysts for the electroreduction of CO_2 . Other uses of $[\text{Ni}(\text{cyclam})]^{2+}$ include application as catalysts for oxidation and reduction reactions. Electrocatalytic reduction of aldehydes and ketones was studied using a Ni^{II} tetraazamacrocyclic complex-modified graphite felt electrode.^[129] Another interesting use is for electrochemical CO_2 sensing applications. In 2001 Jacquinet and Hauser proposed to use $[\text{Ni}(\text{cyclam})]^{2+}$ for a gas sensing device capable of detecting CO_2 directly in the gas phase.^[130] $[\text{Ni}(\text{cyclam})]^{2+}$ has also been investigated because of its cytotoxic and antimicrobial properties.^[131] Another use is single redox couple in non-aqueous redox flow batteries.^[132] Ni cyclam has also been heterogenized on ITO glass for water oxidation.^[133]

1.3.1 Homogeneous and heterogeneous CO_2RR catalyzed by $[\text{Ni}(\text{cyclam})]^{2+}$

It was at the beginning of the 80s that Fisher and Eisenberg employed tetraazamacrocyclic complexes of Co and Ni as electrocatalysts for CO_2 reduction,^[65] but it was in 1984 that

Sauvage and coworkers demonstrated for the first time that $[\text{Ni}(\text{cyclam})]^{2+}$ could be used as a very efficient electrocatalyst for the reduction of CO_2 .^[66] The experiments were conducted by using a mercury drop electrode in CO_2 saturated solutions of KNO_3 (0.1 M) containing the electrocatalyst ($1.7 \cdot 10^{-4}$ M). At -1 V vs. NHE, the velocity of the reaction was remarkable (turnover frequency ca. 18 h^{-1} and overall turnover numbers ca. 102), as well as the selectivity for CO production (99% average faradaic efficiency).

Three years later, the same group proposed the first mechanism of $[\text{Ni}(\text{cyclam})]^{2+}$ catalyzed CO_2 reduction, along with the analysis of several factors affecting the efficiency and the selectivity of the process itself.^[134] By varying the amount of electrocatalyst they found that (i) the intensity of the catalytic peak under CO_2 was only weakly dependent on the concentration of the nickel complex and (ii) the influence of the catalyst concentration on the velocity of CO generation was not very important. With these observations they hypothesized that the concentration of $[\text{Ni}(\text{cyclam})]^{2+}$ in the bulk was not rate determining, but that on the contrary, interface reactions were very important, due to the presence of adsorbed species on the electrode. Additionally, in an attempt to identify the intermediates present during the catalytic process, they analyzed the electronic spectrum of the solution during the course of the electrolysis and observed an unknown, green species forming, which they suggested being Ni^I carbonyl complexes. Their proposition for the mechanism of CO_2RR catalyzed by $[\text{Ni}(\text{cyclam})]^{2+}$ is depicted in **Figure 1.10**

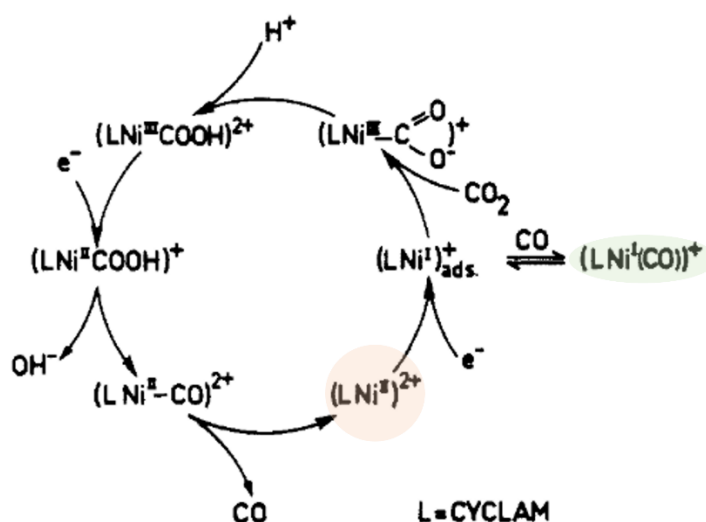


Figure 1.10 First mechanism proposed by Sauvage and coworkers for the electroreduction for CO_2 to CO catalyzed by $[\text{Ni}(\text{cyclam})]^{2+}$.^[134]

Thus, the initial step would be the reduction of the Ni^{II} complex and the strong adsorption of Ni^I product on the electrode surface. Ni^I would then react with CO₂, forming a Ni^{III} complex that gets protonated and reduced and after the expulsion of OH⁻ forms a Ni^{II} carbonyl complex only weakly bound to CO. After CO expulsion, the starting Ni^{II} compound is regenerated. Additionally, they suggest, after a few cycles several of the catalytic species in the scheme may be in equilibrium with their carbonylated analogues, especially Ni^I cyclam. In particular, the latter could greatly affect the efficiency of the catalytic process for two reasons. First, it was observed that Ni^I carbonyl complex was much more stable in DMF than in H₂O. Fast decomposition of this intermediate with liberation of CO providing rapid regeneration of the catalyst could explain the efficiency of the electrocatalytic process in water. Secondly, Ni^I carbonyl complexes might be electroreduced more easily than the corresponding noncarbonylated species.

Sauvage and collaborators^[135] successively compared the catalytic activity of cyclam and biscyclam as they had the intuition that the two coordination sites of the dimetallic compound might be close enough to interact simultaneously with small molecules or their reduction products, leading to potentially different reaction pathways than cyclam. Importantly, coupling reactions were envisioned, leading to C₂ compounds. The experiments, however, were disappointing. The electrocatalytic behavior of [Ni(cyclam)]₂⁴⁺ was not markedly different from that of [Ni(cyclam)]²⁺, if not worse. No coupling products could be obtained under the experimental conditions.

The idea of multinuclear tetraazacyclotetradecane complexes was later brought forward by Lee et al. who tested a trinuclear macrocyclic [Ni(cyclam)]₂²⁺ derivative for CO₂RR.^[136] The synthesized trinuclear complex exhibited a much more anodic Ni^{II}/Ni^I reduction potential than the mononuclear parent, however, even if CO was the only one product detected, the catalytic efficiency as well as the turnover number (water, Hg pool electrode, -1.6 V vs SCE) were lower than that of [Ni(cyclam)]²⁺.

A different biscyclam structure was later tested by Lu and collaborators.^[137] In their approach, two [Ni(cyclam)]²⁺ were connected by a phenyl group (**Figure 1.11, 1**) and the activity of this derivative was compared to the mononuclear counterpart (**2**) and to another dinuclear [Ni(cyclam)]₂²⁺ complex (**3**) with a larger separation between two Ni^{II} catalytic centers. **1** showed excellent catalytic activity and selectivity for electrocatalytic reduction of CO₂ to CO in MECN/H₂O (v/v = 4:1) solution, with Faradaic efficiency of 95%, and TON and TOF values

of 4.1×10^6 and 190 s^{-1} , respectively. These values were much higher than those of **2** and **3** under the same conditions. The group sought further elucidations for the high catalytic activity by DFT calculations and suggested a mechanism for the CO_2RR reduction catalyzed by **1**, in which only one of the two Ni^{I} centers would bind to CO_2 and complete the catalytic process, while the other Ni center would help the stabilization of the intermediate state by through-space interactions.

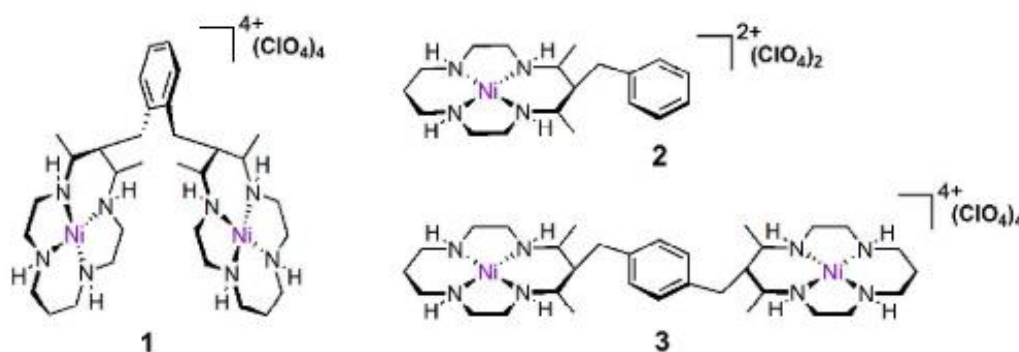


Figure 1.11 Molecular structures of **1**, **2** and **3** as described by Lu and collaborators.^[137]

The pioneering work of Sauvage and collaborators also brought them to be among the first to attempt the heterogenization of $[\text{Ni}(\text{cyclam})]^{2+}$ on polymeric substrates. In 1987 they synthesized a C-substituted cyclam molecule bearing a pendant pyrrole unit, in order to create, via electropolymerization, an electroactive film incorporating a $[\text{Ni}(\text{cyclam})]^{2+}$ derivative.^[138] Despite the innovative idea, the modified polypyrrole film did not lead to redox processes involving the $\text{Ni}^{\text{II}}/\text{Ni}^{\text{I}}$ couple, preventing its use in electroreductive reactions. Similar results were obtained by other groups when N-substituted cyclam derivatives with a pendant pyrrole unit or a thiophene one were assessed for their ability to form conductive films on GC electrodes in MeCN.^[139–141]

Other polymers investigated in relation to the heterogenization of $[\text{Ni}(\text{cyclam})]^{2+}$ include sulphonated polyaniline (SPANI)^[142] and poly(3,4-ethylenedioxythiophene) (PEDOT),^[143,144] which, however, showed electrocatalytic activity only towards oxidative processes.

A successful heterogenization on a polymer backbone was presented by Saravanakumar et al.^[145] who linked a polyallylamine (PALA) polymer via the axial coordination of pyridine to $[\text{Ni}(\text{cyclam})]^{2+}$ (**Figure 1.12**). CPE with $[\text{Ni}(\text{cyclam})]^{2+}$ -PALA supported on glassy carbon was run for 24h in aqueous solution (-0.78 V vs. Ag/AgCl). CO was detected as a major product at

a FY of 92% during the initial 6 h electrolysis, which dropped to 88% at 12 h and 79% at 24 h. Interestingly, the electrocatalytic reduction of CO₂ was run at the calculated thermodynamic potential for conversion of CO₂ to CO (-0.78 V vs. Ag/AgCl, at pH 8 in aqueous solution). The authors hypothesized this positive potential shift could be due to (i) the axial coordination of the pyridine unit and the π -acceptor property of the aromatic pyridine ring and (ii) the interaction of the free amines of the PALA polymer, which increase the solubility in aqueous solution and stabilize the reduced state of the metal center.

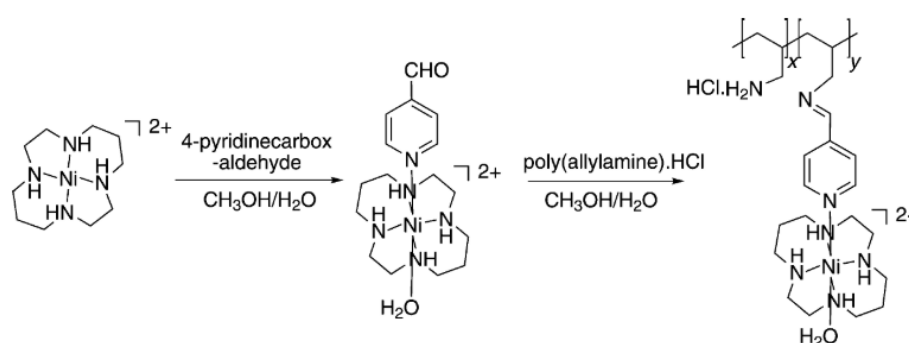


Figure 1.12 Preparation of $[\text{Ni}(\text{cyclam})]^{2+}$ -PALA^[145].

Besides polymeric substrates, several groups have investigated the heterogenization of $[\text{Ni}(\text{cyclam})]^{2+}$ directly on glassy carbon supports. In 1992, Fujihira and coworkers successfully deposited a layer of a $[\text{Ni}(\text{cyclam})]^{2+}$ complex N-substituted with a long alkyl chain (22 C) on a glassy carbon electrode, but did not perform electrolysis with the so-formed electrode.^[146]

A few years after, Kaden and collaborators incorporated a series of methyl-substituted derivatives of cyclam onto electrodes via different methods,^[147] either via incorporation into Nafion coatings, or by forming a monolayer of catalyst on the surface of the electrode (e.g. Langmuir–Blodgett technique). Most efficient catalysis was observed with electrodes covered by monolayers of the cyclam complex modified with a pyridine side group, and in particular, when the catalyst molecules were oriented with their alkyl chains towards the substrate and the macrocyclic head-group towards the solution.

Kubiak and collaborators^[148] synthesized three new alkynyl-cyclam ligands as well as new nickel complexes, namely $[\text{Ni}(\text{propargyl-cyclam})]^{2+}$ (**Figure 1.13, 1**), $[\text{Ni}(\text{pentynyl-cyclam})]^{2+}$ (**2**) and $[\text{Ni}(\text{hexynyl-cyclam})]^{2+}$ (**3**). Anodic electrografting through terminal alkynes resulted in the formation of alkynyl radicals, which reacted with the surface of a GC electrode. The covalent linkage resulted in a monolayer of catalyst deposited, with a surface coverage of 1.28

10^{-10} mol cm^{-2} . Heterogeneous CO_2 reduction experiments were carried out in 0.1 M TBAPF₆/MeCN solution with 20% water as a proton source. When held at -2.4 V vs Fc⁺/Fc⁰ for 1 h, the average FY was determined to be 89% for H₂ and 7% for CO. CPE for homogenous Ni-alkynyl cyclams were carried out at the same conditions with average FE 54% for CO and 39% for H₂.

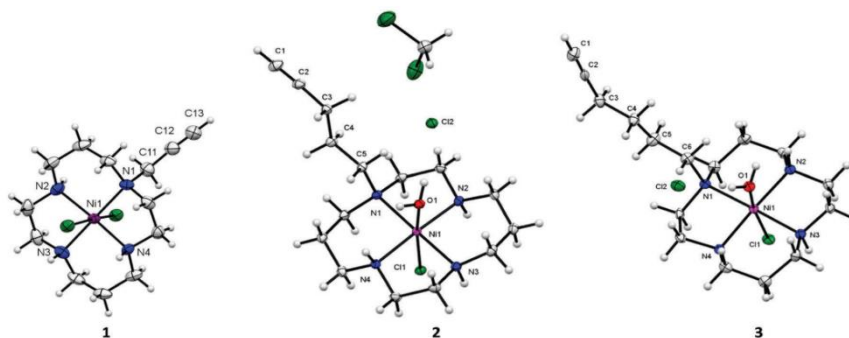


Figure 1.13 Crystal structures of [Ni-propargyl-cyclam]²⁺ (1), [Ni-pentynyl-cyclam]²⁺ (2) and [Ni-hexynyl-cyclam]²⁺ (3).^[149]

The most recent achievements with [Ni(cyclam)]²⁺ as a catalyst for CO₂RR involve its use in a flow cell and its heterogenization on MWCNTs/gas diffusion electrodes.

Machan and collaborators^[150] tried for the first time to catalyze the reduction of CO₂ by [Ni(cyclam)]²⁺ in a flow cell. The authors chose a nonaqueous flow configuration (either MeCN or DMF), in which CO₂ was reduced at the cathode in the presence of ammonium hexafluorophosphate (or other salts) as electrolyte and proton donor, and ferrocene was used as the sacrificial electron donor at the anode side. The performance of the flow configuration was evaluated by analyzing the influence of solvent, applied cell potential, catalyst concentration, proton donor and flow rates. More importantly, the same experiments were carried out with a “classic” H-shape cell, for comparison. The results showed that (i) with a representative catalyst loading of 10 mM [Ni(cyclam)]²⁺ and 0.5 M NH₄PF₆ electrolyte in MeCN, the flow cell can reach current densities close to 50 mA cm^{-2} at -2.2 V vs Fc⁺/Fc⁰; (ii) selectivity for CO is kept, especially in DMF, where no H₂ was detected at potentials lower than -1.9 V; (iii) NH₄⁺ was the best sacrificial proton donor for CO₂ reduction in the flow configuration, better than phenol, TFE or H₂O and (iv) for all the tests, the flow cell proved to be better than the H-shape cells in the same conditions (**Table 1.4**). Finally, even if the initial current densities for the flow cell were quite satisfactory, during the experiments they dropped significantly. As the authors

suggested, the major issue was the poor stability of $[\text{Ni}(\text{cyclam})]^{2+}$ in a CO-rich environment, especially at large overpotentials, due to the generation of an inactive CO adduct.

Table 1.4 Summary of CO₂ reduction results after 1 h in a) MeCN or b) DMF for the flow cell and H-cell.^[150]

a)	E_{applied} (V)	proton donor (0.5 M)	J (mA·cm ⁻²)	FE(CO) (%)	FE(H ₂) (%)	CO production rate (mL·h ⁻¹)	TON (CO)
	1.4 ^b	NH ₄ PF ₆	1.2	8	64	0.2	0.04
	1.5 ^b	NH ₄ PF ₆	1.9	60	32	2.4	0.5
	1.6 ^b	NH ₄ PF ₆	5.6	83	7	9.8	2.2
	1.6 ^c	NH ₄ PF ₆	0.24	13	84	8.0 × 10 ⁻²	0.2
	1.7 ^b	NH ₄ PF ₆	12.7	83	4	22.1	4.9
	1.8 ^b	NH ₄ PF ₆	18.9	80	5	31.8	7.0
	1.8 ^c	NH ₄ PF ₆	0.58	30	71	0.4	0.8
	2.0 ^b	NH ₄ PF ₆	27.4	70	15	40.3	9.1
	2.2 ^b	NH ₄ PF ₆	37.9	60	23	41.6	9.1
	1.6 ^b	AcOH	3.3	71	9	6.9	1.1
	1.6 ^b	PhOH	3.2	97	0	6.7	1.4
	1.6 ^b	TFE	2.0	91	0	4.2	0.8
	1.6 ^b	H ₂ O	1.8	77	0	3.7	0.7

b)	E_{applied} (V)	J (mA·cm ⁻²)	FE (CO) (%)	FE (H ₂) (%)	TON (CO)
	1.5 ^b	0.2	34	0	0.03
	1.6 ^b	1.0	80	0	0.4
	1.7 ^b	3.5	82	0	1.4
	1.8 ^b	6.4	80	0	2.4
	1.8 ^c	0.24	71	30	1.45
	1.9 ^b	8.3	73	4	2.8
	2.0 ^b	11.4	65	16	3.4
	2.2 ^b	14.7	54	35	3.7

All experiments in a two-electrode configuration with cathode and anode electrodes made of graphite felt (SIGRACELL, GFD4.6 EA, 4.6 mm thickness, 5 cm² area), Fc as a sacrificial electron donor.
^bFlow configuration conditions: three layers Celgard film; 8.0 mL min⁻¹ flow rate; 10 mM of $[\text{Ni}(\text{cyclam})]^{2+}$, 0.5 M added NH₄PF₆ as electrolyte and proton donor, 0.1 M Fc. ^cH-Cell conditions: 1 mM catalyst; chambers separated by porous glass frit; convection from stir-bar in anode and cathode chambers, 0.04 M Fc.

Very recently, during the course of our studies, Cowan and coworkers synthesized a pyrene-modified $[\text{Ni}(\text{cyclam})]^{2+}$ complex for its noncovalent heterogenization on a gas diffusion electrode.^[151] The ligand accounts for a N-functionalized cyclam ring and a pyrene function, which are separated by a 4-carbon chain. CPE in aqueous conditions was tested at -1.4 V versus a Ag/AgCl. Both the current and selectivity towards CO₂ decrease over 140 minutes of use, with increased levels of H₂ production occurring at longer times (**Figure 1.14**, b). The authors underlined that loss from the surface, not poisoning, was the primary cause of the loss of selectivity to CO production.

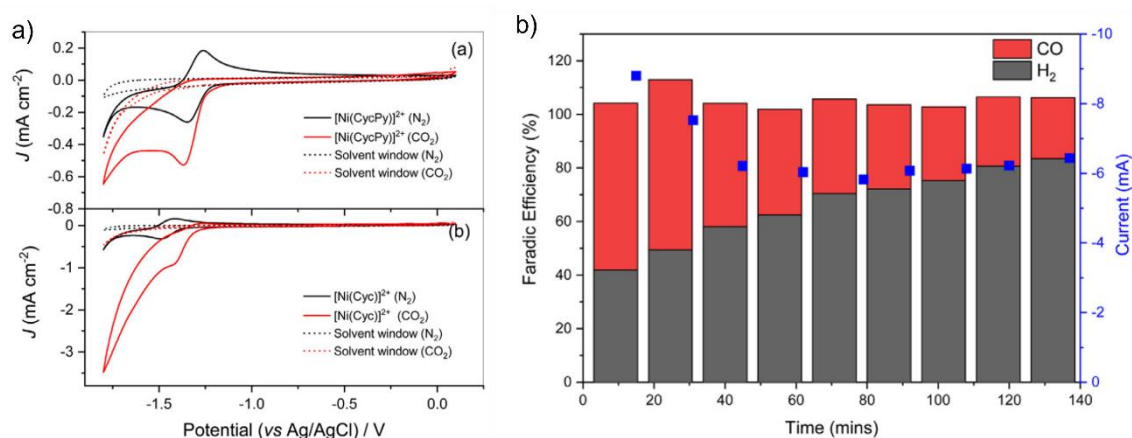
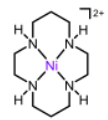
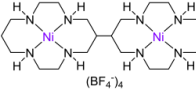
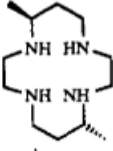
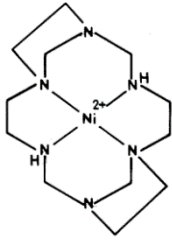
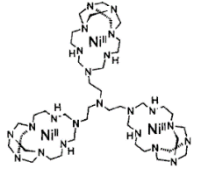
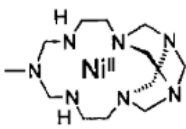


Figure 1.14 a) CVs of 1mM $[\text{Ni}(\text{Cyclam})\text{pyrene}]^{2+}$ (top) and $[\text{Ni}(\text{Cyclam})]^{2+}$ (bottom) in 0.1M TBAPF₆ in MeCN with 10% water using a GC electrode; 100mV/s under N₂ (black) and CO₂ (red) and b) electrolysis data from a $[\text{Ni}(\text{Cyclam})\text{pyrene}]^{2+}$ GDE used in 0.5 M KHCO₃ with a CO₂ flow rate of 20 ml min⁻¹.^[151]

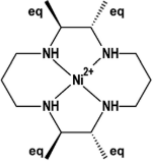
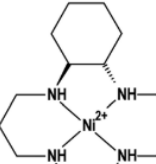
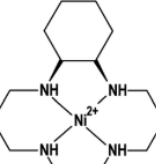
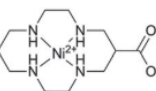
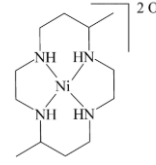
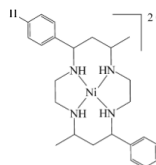
Table 1.5 provides an overview of the $[\text{Ni}(\text{Cyclam})]^{2+}$ based catalysts described so far, either in homogeneous (different experimental conditions such as electrolyte, working electrode and so on) or in heterogeneous condition.

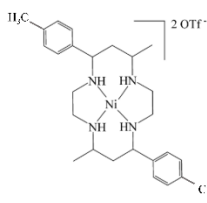
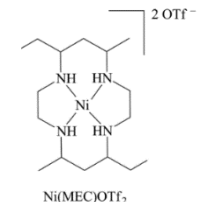
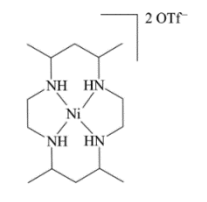
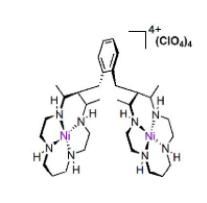
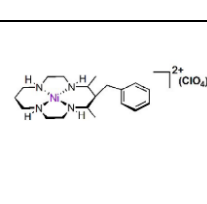
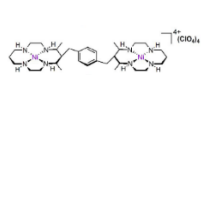
Table 1.5 Overview of the $[\text{Ni}(\text{Cyclam})]^{2+}$ based catalysts described so far, either in homogeneous or in heterogeneous conditions. *TON and TOF values were calculated based on the number of the catalyst molecules in the diffusion layer.

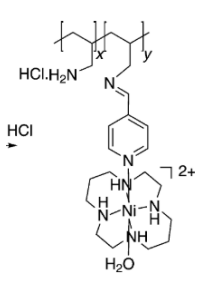
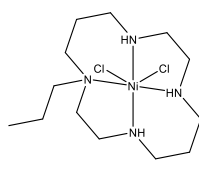
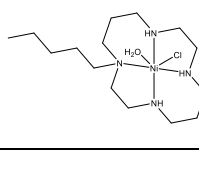
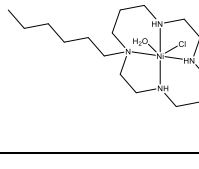
Catalyst	Loading/ Catalyst concentration	Medium	Working electrode	E (V)	FY (%)	TON (CO)	TOF (CO)	Electrolysis time (h)	Ref
HOMOGENEOUS									
	1.7 10 ⁻⁴ M	H ₂ O (KNO ₃ 0.1 M)	Hg drop	-1 vs NHE	99% CO	102	18	-	[66]
	2 10 ⁻⁴ M	DMF NaClO ₄ 0.1 M	Hg	-1.6 vs SCE	36% CO, 27% HCOO ⁻	-	-	6.67	[135]
	1 mM	0.1 M KCl	GC	-1.3 vs NHE,	90% CO (-1.3V), 90% CO,	-	-	1	[152]

				-1.6 vs NHE	20% H ₂ (-1.6V)				
	3 10 ⁻⁶ M	0.1 M NaClO ₄ (pH = 2)	Hg pool	-0.99 V vs NHE	13% CO, 73% H ₂	45	-	1	[153]
	-	BMIImBF ₄	GC	-1.4 vs Fc ⁺ /Fc ⁰	95.2% CO	2.19	0.73	4	[154]
	-	0.1M KCl (pH =10)	Sn disk	-1.4 vs SHE	2% CO, 35% H ₂	-	-	0.5	[159]
	2 10 ⁻⁴ M	DMF NaClO ₄ 0.1 M	Hg	-1.6 vs SCE	22% CO, 13% HCOO ⁻	-	-	6	[135]
	5 10 ⁻⁶ M	0.1 M KCl	Hg	-	90% CO	-	-	4	[155]
	1 mmol/dm ³	10% DMF– H ₂ O (LiClO ₄ 0.1 mol/dm ³)	Hg	-1.6 vs SCE	75% CO	-	-	5	[156]
	1.0 10 ⁻³ M	MeCN/ H ₂ O (9:1, v/v) 0.1M NaClO ₄	Hg pool	-1.6 vs SCE	96.2% CO	2.6	-	0.5	[136]
	1.0 10 ⁻³ M	MeCN/ H ₂ O (9:1, v/v) 0.1M NaClO ₄	Hg pool	-1.6 vs SCE	95.3% CO	3.9	-	0.5	[136]

Chapter 1

	50 μ M	0.1M NaClO ₄ , (pH=5)	Hg pool	-0.96 vs NHE	88% CO	-	-	1h	[157]
	50 μ M	0.1M NaClO ₄ , (pH=5)	Hg pool	-0.96 vs NHE	88% CO	-	-	1h	[157]
	50 μ M	0.1M NaClO ₄ , (pH=5)	Hg pool	-0.96 vs NHE	92% CO	-	-	1h	[157]
	10 ⁻⁴ M	0.1M NaClO ₄	Hg-Au amalgam	-1.4 vs Ag/ AgCl	88% CO	5.3	-	1h	[158]
	3 10 ⁻⁶ M	0.1M NaClO ₄ (pH = 2)	Hg pool	-0.99 vs NHE	66% CO, 15% H ₂	591	-	1h	[153]
	0.5 mM	20% MeCN/ H ₂ O, 0.08M NBu ₄ PF ₆	Reticulated vitreous carbon (RVC)	-1.7 vs Fc ⁺ /Fc ⁰	10.3% CO, 53.4% H ₂	0.64	-	0.5	[160]
	0.5 mM	20% MeCN/ H ₂ O, 0.08M NBu ₄ PF ₆	RVC	-1.7 vs Fc ⁺ /Fc ⁰	80% CO, 7.3% H ₂	4.5	-	0.5	[160]

	0.5 mM	20% MeCN/ H ₂ O, 0.08M NBu ₄ PF ₆	RVC	-1.7 vs Fc ⁺ /Fc ⁰	29.1% CO, 44.1% H ₂	0.25	-	0.5	[160]
	0.5 mM	20% MeCN/ H ₂ O, 0.08M NBu ₄ PF ₆	RVC	-1.76 vs Fc ⁺ /Fc ⁰	57% CO, 16% H ₂	7.3	14.5	0.5	[161]
	0.5 mM	20% MeCN/ H ₂ O, 0.08M NBu ₄ PF ₆	RVC	-1.76 vs Fc ⁺ /Fc ⁰	66% CO, 15% H ₂	7.7	15.2	0.5	[161]
	0.5 mM	MeCN/ H ₂ O (v/v 4:1), 0.1M TBAPF ₆	GC	-1.16 vs NHE	95% CO	*4.1 10 ⁶	* 190	6	[137]
	0.5 mM	MeCN/ H ₂ O (v/v 4:1), 0.1M TBAPF ₆	GC	-1.16 vs NHE	62% CO	*1.1 10 ⁵	*5	6	[137]
	0.5 mM	MeCN/ H ₂ O (v/v 4:1), 0.1M TBAPF ₆	GC	-1.16 vs NHE	25% CO	*9.2 10 ⁴	*4.2	6	[137]
HETEROGENEOUS									

	2 mg mL ⁻¹ Ni(cyclam) -PALA	50 mM tris buffer (pH = 8)	glassy carbon rod	-0.78 vs Ag/ AgCl	92% CO	-	-	6h	[145]
	1.28 · 10 ⁻¹⁰ mol cm ⁻²	MeCN/ 20% H ₂ O	Tokai glassy carbon	-2.4 vs Fc ⁺ /Fc ⁰	7% CO, 87% H ₂	-	-	1h	[149]
	1.28 · 10 ⁻¹⁰ mol cm ⁻²	MeCN/ 20% H ₂ O	Tokai glassy carbon	-2.4 vs Fc ⁺ /Fc ⁰	8% CO, 89% H ₂	-	-	1h	[149]
	1.28 · 10 ⁻¹⁰ mol cm ⁻²	MeCN/ 20% H ₂ O	Tokai glassy carbon	-2.4 vs Fc ⁺ /Fc ⁰	7% CO, 91% H ₂	-	-	1h	[149]

1.3.2 Understanding the mechanism of CO₂RR catalyzed by [Ni(cyclam)]²⁺

The initial studies by Sauvage and coworkers^[66] brought to light interesting aspects of the catalytic reactivity of [Ni(cyclam)]²⁺ that needed to be understood. The proposed mechanism was still in a speculative stage, and at the same time the role of the adsorbed species, as well as the formation of Ni^I-CO adducts, was still not clear.

Hirata et al. analyzed aqueous [Ni(cyclam)]²⁺ solutions in detail by cyclic voltammetry, polarography and electrocapillarity, under N₂, CO or CO₂.^[162,163] By comparing the effect of using either a GC electrode or a Hg-Au amalgam one, they could observe that both [Ni(cyclam)]²⁺ and [Ni(cyclam)]⁺ species adsorbed on Hg, however [Ni(cyclam)]⁺ adsorbed more strongly. The adsorbed [Ni(cyclam)]⁺ ([Ni(cyclam)]⁺_{ad}) was produced at less negative potentials than [Ni(cyclam)]⁺ in solution, giving rise to an adsorption prewave (which was observed as well by Sauvage and co-workers during their experiments). [Ni(cyclam)]⁺_{ad} was much more active for CO₂ reduction than the [Ni(cyclam)]⁺ in the bulk, and it did not behave as if it was a surface bound mediator, but rather as if it was a surface catalytic site as a part of the electrode. Finally, [Ni(cyclam)]⁺_{ad} reacted with the electrogenerated CO to form an inactive

carbonyl complex. Importantly, the efficiency for CO₂ reduction on GC was found to be much lower, both in terms of current density and catalytic current onset potential, compared to Hg-Au (Figure 1.15).

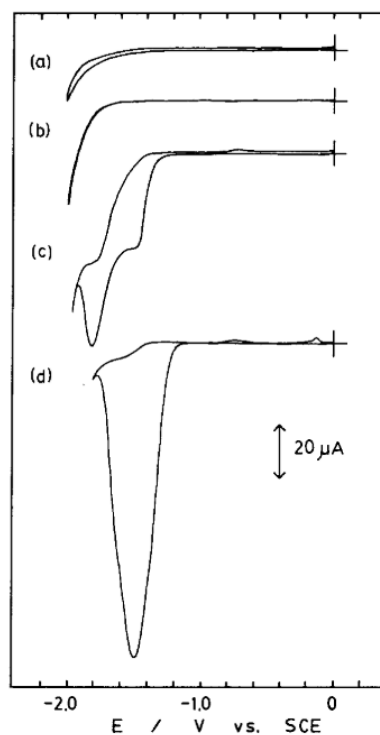


Figure 1.15 CVs of aqueous solutions (0.1 M NaClO₄ and 0.035 M NaHCO₃, pH 6.2) under CO₂ on a GC disk electrode (a) without and (c) with 1 mM [Ni(cyclam)]²⁺, and on a Hg-Au disk electrode (b) without and (d) with 1 mM [Ni(cyclam)]²⁺ (Scan rates 100 mV s⁻¹).^[162]

Successively, Balasz and Anson^[164] suggested that the production of [Ni(cyclam)]⁺_{ad} could only be generated by a very strong chemical interaction between the adsorbed complex and the mercury surface. One of the novelties of this research was to consider, for the first time, that solutions of [Ni(cyclam)]²⁺ are known to contain several configurational isomers of the complex, and that one of the isomers present in small amounts could be responsible for the reductive adsorption. Additionally, when the adsorbed complex was oxidatively desorbed, these structural rearrangements were apparently retained. The authors hypothesized that a strong binding with the Hg surface could be achieved by forcing the larger Ni^I center out of the macrocyclic plane to some extent. The resulting adsorbed complex, which would bind CO as a ligand when serving as a CO₂ reduction catalyst, would have a coordination geometry closer to octahedral.

One year later the same lab published an expansion of the previous study, focusing on the role of CO.^[165] The authors tried to explain the origin of the decrease in the catalytic current for the reduction of CO₂, which in the previous studies was mainly attributed to the desorption of [Ni(cyclam)]⁺_{ad} upon its reaction with CO. Conversely, the authors support the interpretation based on passivation of the electrode surface by an insoluble precipitate generated during the catalyzed reduction of CO₂. This precipitate, containing Ni⁰, cyclam and CO, would probably interfere with the adsorption of the catalyst, or with coordination of CO₂ to the adsorbed catalyst, [Ni(cyclam)]⁺_{ad}.

This passivation theory was confirmed by a successive study^[166] in which a Ni^{II} tetraazamacrocyclic complex very similar to [Ni(cyclam)]²⁺ was investigated by cyclic and stripping dc voltammetry. Comparative studies performed in solutions saturated with CO or CO₂ in the presence of the catalyst revealed the transformation of [Ni(cyclam)]⁺_{ad} into the carbonyl compound with the Ni in its zero-valent form.

Further information to understand the catalytic mechanism of [Ni(cyclam)]²⁺ came with the beginning of systematic studies on the effect of ligand modifications. Also in this case, Sauvage was the first to indicate that (i) steric factors might be determinant, and if the metal center is hindered, it might react with a small substrate like a proton, making the process less specific with respect to reduction of CO₂, and (ii) introduction of modifications at the periphery of the complex could drastically decrease the CO to H₂ ratio in the gas produced.^[66]

Successive efforts from several groups thus focused on a quite comprehensive study on the effect of N- or C-methylation and alkylation on modified [Ni(cyclam)]²⁺ (in aqueous solution, using mercury electrodes).^[155,156,163,167] Cyclic voltammograms found that generally, C-alkylated cyclams were behaving very similarly to standard [Ni(cyclam)]²⁺. In some cases, the catalytic wave under CO₂ was starting at more positive potentials and the catalytic current was higher than [Ni(cyclam)]²⁺. During CPE, some of these C- substituted catalysts produced more CO than the unmodified parent complex under the same experimental conditions.

For the N-substituted cyclams, the Ni^{II}/Ni^I reduction peaks under N₂ were generally found at more positive potentials than for [Ni(cyclam)]²⁺, with a positive shift increase with the number of N-substitutions. Under CO₂, however, not only the catalytic wave was starting at more negative potentials, but also the catalytic current was smaller than for the unmodified complex.

This was reflected in the selectivity, as the N-substituted cyclams were the ones that produced more H_2 in general.

It was now clear that structural differences played an important role in selectivity and adsorption onto the mercury electrode. Fujita and collaborators^[157] greatly contributed to the study of the effects of C-substitution (and more generally, of the catalytic mechanism of $[Ni(cyclam)]^{2+}$) by challenging experimental data with DFT calculations. A series of C-substituted cyclams was investigated, and it was found that two of them were better catalysts than $[Ni(cyclam)]^{2+}$, namely $[Ni(HTIM)]^{2+}$ and $[Ni(MTC)]^{2+}$ (**Figure 1.16**).

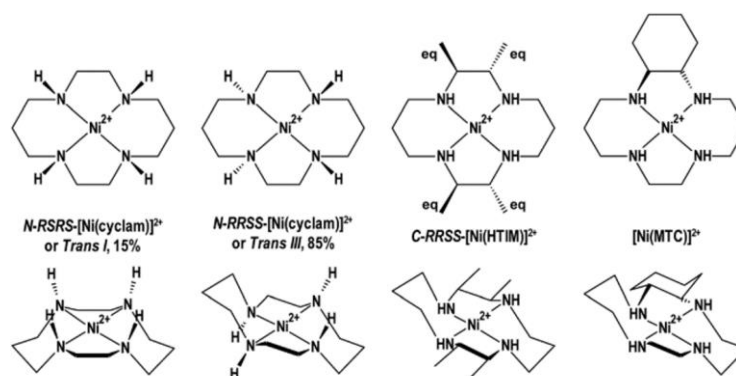


Figure 1.16 From left to right, drawings of the two primary isomers of $[Ni(cyclam)]^{2+}$, *trans-I* and *trans-III*, present in solution at equilibrium; the $C-RRSS$ -isomer of $[Ni(HTIM)]^{2+}$; $[Ni(MTC)]^{2+}$ having a *trans*-cyclohexane.^[157]

Based on DFT calculations using a continuum solvent model, they argued that the *trans-I* isomer, which is approximately 15% at equilibrium, was likely to be the preferred geometric isomer of $[Ni(cyclam)]^{2+}$ for forming an adduct with CO_2 .^[157] It was thus possible that the geometric isomerization occurring upon adsorption of the catalyst complex was due to conversion of the most abundant *trans-III* isomer to the *trans-I* isomer.

Thus, the exceptional catalytic activity of the $C-RRSS-[Ni(HTIM)]^{2+}$ and $[Ni(MTC)]^{2+}$ macrocycles could be due to the almost flat geometry around the Ni center, that (i) allowed an appropriate distance for the Ni-Hg interaction, (ii) accommodated well a CO_2 adduct (stabilised by H-bond formation), and (iii) promoted electron donation from the methyl groups to the Ni center to produce a strong interaction with CO_2 .

In the same year, Froehlich and Kubiak examined the homogeneous CO_2 reduction activity of $[Ni(cyclam)]^{2+}$ at an inert electrode material, glassy carbon, while underlining the lack of reports studying CO_2 reduction on other electrode surfaces than Hg. CPE was carried out in

aqueous conditions at -1.30 V vs NHE for 1 h and the faradaic efficiency was calculated to be 90% for CO (no H₂ was detected) with an average current density of 2.8 mA cm⁻². As the great majority of the previous studies stated that the portion of catalyst that was not adsorbed on the Hg was inactive for CO₂ reduction, these results renewed the hope for this catalyst to be used with more benign materials.

For this reason, studies on the effect of ligand modifications were carried on, this time at a GC electrode. Ren and coworkers presented the synthesis and electrochemical characterization on GC of several derivatives with pendant aryl and/or alkyl groups on the macrocycle (**Figure 1.17, 1 to 6**).^[160,161] The effect of substituents with electron withdrawing properties (such as **3**) was assessed. Interestingly, the trend in reduction potentials did not seem to match the intuition that, in a set of analogous complexes, the species bearing the most electron withdrawing substituent would have the least negative reduction potential for Ni^{II} to Ni^I under Ar. Instead, the opposite trend was observed; **3** had the most negative reduction potential followed by **1**, then **4**, and finally, **2**. Additionally, under CO₂, complex **3** was found to be inactive, while complex **1** was the most active between the aryl-substituted cyclams. CPE in water demonstrated that **1**, **5** and **6** were outperforming [Ni(cyclam)]²⁺ in terms of both the selectivity and TON for CO production under the same conditions. To explain these findings, the author suggested that the electron deficiency of **1** relative to **2** and **4** was the predominant cause. Thus, **1** could be at an ideal level of electron deficiency such that the Ni^I species is sufficiently electron-rich to bind and reduce CO₂, but not electron-rich enough to bind CO strongly (and thus inhibit catalysis). A second reason was ascribed to the fact that **1** was found in solution as a high-spin octahedral species while **2** and **4** were present as square-planar, diamagnetic species. Hence, upon reduction to Ni^I, orbital rearrangement must occur from the square-planar state to allow for binding of CO₂ as a fifth ligand for **2** and **4**, whereas **1** could circumvent this energy barrier.

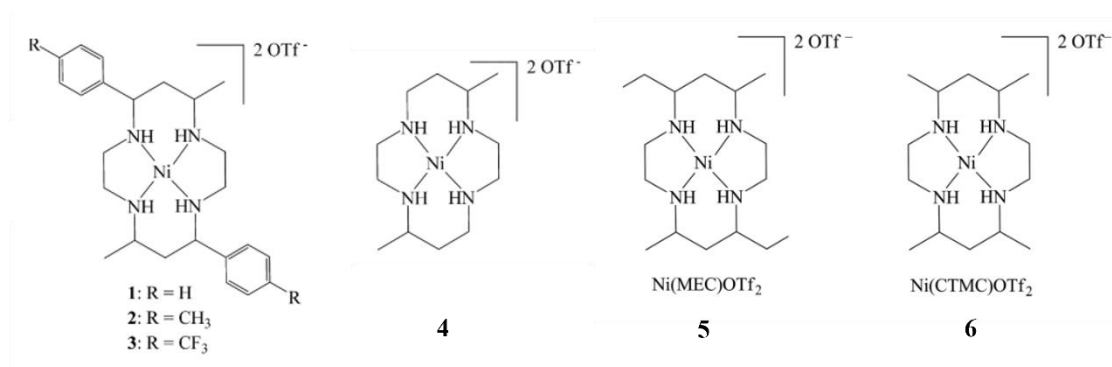


Figure 1.17 structure of the Complexes studied by Cook and collaborators.^[160,161]

Finally, the best catalysts overall, **5** and **6**, suggested a trend of increasing catalytic ability with reduction in steric bulk of the electronically donating carbon substituents, highlighting the importance of easily accessible axial catalytic sites.

The first computational-only study on the mechanism of CO₂RR catalyzed by [Ni(cyclam)]²⁺ was proposed in 2014 by Song et al.^[168]. They confirmed that CO₂ reduction by [Ni(cyclam)]⁺ proceeded via an inner-sphere electron-transfer mechanism,^[169] and the formation of a CO₂ adduct was undoubtedly the initial step of the catalytic cycle. Consequently, they analyzed the possible geometric and electronic structures of the CO₂ adduct. Between *trans*-I and *trans*-III, *trans*-I cyclam afforded marginally more stable CO₂ complexes regardless of the CO₂ coordination modes, as already anticipated by Fujita and collaborators. In contrast to the cyclam conformations, the distinct CO₂ binding modes had a significant influence on the relative stability of the investigated CO₂ adducts. During the geometry optimizations, all the structures rearranged to the binding mode in which CO₂ was coordinated to the Ni^I center by the carbon atom. In this stage, they observed bending of the coordinated CO₂ ligand, elongation of the C–O bonds, and a π -backdonation interaction that was ascribed to metal-to-ligand electron transfer. This implied that the first electron reduction of CO₂ was partially accomplished at this stage. For the catalytic process to proceed, they individuated the most feasible pathway to be concerted proton coupled electron transfer (PCET). The species formed after this PCET was described as a high-spin Ni^{II} center bound to a carboxylate anion (⁻CO₂H). At this point, breaking of one of the C–O bonds would generate a molecule of water, leaving a Ni^{II}-CO species, which could either directly release CO or easily accept another electron. In the latter case, a Ni^I-CO species would be generated, which would eventually release CO and close the catalytic cycle.

This insightful mechanism description had some fundamental implications. First, the Ni^{I} species is a potent nucleophile and its formation is the reason for the overpotential of the whole process (hence, a strategy to reduce it involves stabilizing Ni^{I}). Secondly, one may argue that free CO can readily recombine with Ni^{I} and poison the catalysts, but the authors suggest that this is highly unlikely because of the limited solubility in water of CO (27.6 mg/L) compared with that of CO_2 (1.5 g/L). Nevertheless, the accumulation of $\text{Ni}^{\text{I}}\text{-CO}$ may happen, as it was experimentally observed. Finally, an effective proton source is of paramount importance for the mechanism to proceed at a high pace.

In parallel with these findings, Froehlich and Kubiak^[170] observed considerable amounts of nickel carbonyl products, $[\text{Ni}(\text{cyclam})(\text{CO})]^+$ and $\text{Ni}(\text{CO})_4$, via IR spectroelectrochemistry while performing the electroreduction of CO_2 at a GC electrode. The magnitude of the binding constant to $[\text{Ni}(\text{cyclam})]^+$ for CO was shown to be ~ 100 times the corresponding value for CO_2 . Thus, the authors argued that $[\text{Ni}(\text{cyclam})]^+$ would preferentially react with any CO in solution and become deactivated toward reaction with CO_2 , and at more negative potentials the $[\text{Ni}(\text{cyclam})(\text{CO})]^+$ formed would be further reduced to generate Ni^0 carbonyl products including $\text{Ni}(\text{CO})_4$. They also experimentally proved their hypothesis by adding another Ni complex, $[\text{Ni}(\text{TMC})]^{2+}$ (TMC = 1,4,8,11-tetramethyl-1,4,8,11-tetraaza-cyclotetradecane) as a CO scavenger in the electrolyte solution together with $[\text{Ni}(\text{cyclam})]^{2+}$. CVs in 1:4 water:MeCN showed that the addition of $[\text{Ni}(\text{TMC})]^{2+}$ lead to a substantial increase (up to 10 times) in the catalytic current observed under CO_2 .

Another important contribution on the understanding of the role of Hg electrodes was given by Wu and coworkers,^[171] who focused on the thermodynamics and kinetics of CO binding to the reactive intermediate $[\text{Ni}(\text{cyclam})]^+$ adsorbed on Hg or Zn electrode surfaces. After having ruled out a first hypothesis that the liquid nature of Hg could play a role in the enhanced catalysis, they proceeded to determine which conformer of $[\text{Ni}(\text{cyclam})]^+$ and $[\text{Ni}(\text{cyclam})(\text{CO})]^+$ was the predominant upon adsorption on a Hg electrode.

Their calculations showed that *trans*-III $[\text{Ni}(\text{cyclam})]^+$ was more stable on the Hg surface than the other conformers (**Figure 1.18, C**). The same trend applied to $[\text{Ni}(\text{cyclam})(\text{CO})]^+$. By the analysis of the adsorption energies for the *trans*-III conformer on Hg and Zn (**Figure 1.18**), the authors found that the most probable interaction mode between the *trans*-III species and the Hg electrode surface was through dispersive interactions, with the hydrogen atoms on the N atoms of the cyclam ligand pointing towards the Hg surface as the most likely contributors to the

adsorption (given the very short range of such interactions). The absence of this interaction with Zn was attributed to the fact that Hg has many more electrons than Zn that can significantly enhance the induced- dipole-induced- dipole interaction.

Finally, *trans*-III [Ni(cyclam)(CO)]⁺ showed a facilitated CO desorption kinetics on an Hg surface, in comparison to [Ni(cyclam)(CO)]⁺ on Zn and free [Ni(cyclam)(CO)]⁺ (**Figure 1.18**), which was indicative of weaker CO binding to the Ni center. The explanation to this last finding was found in previous studies of the [Ni(cyclam)(CO)]⁺ structure,^[168,170] which emphasized the necessity for the bending out of square planar geometry to achieve a highly stable CO adduct. Between *trans*-I and *trans*-III, the *trans*-I isomer had a much more favorable CO binding energy relative to the *trans*-III. This was because the *trans*-I isomer was more flexible and better suited for out of plane distortions.

The conclusion was clear: the interaction with the Hg surface brings the Ni macrocycle to adopt the *trans*-III conformation, which in turns significantly reduces the CO binding affinity, thus enhancing the CO₂RR.

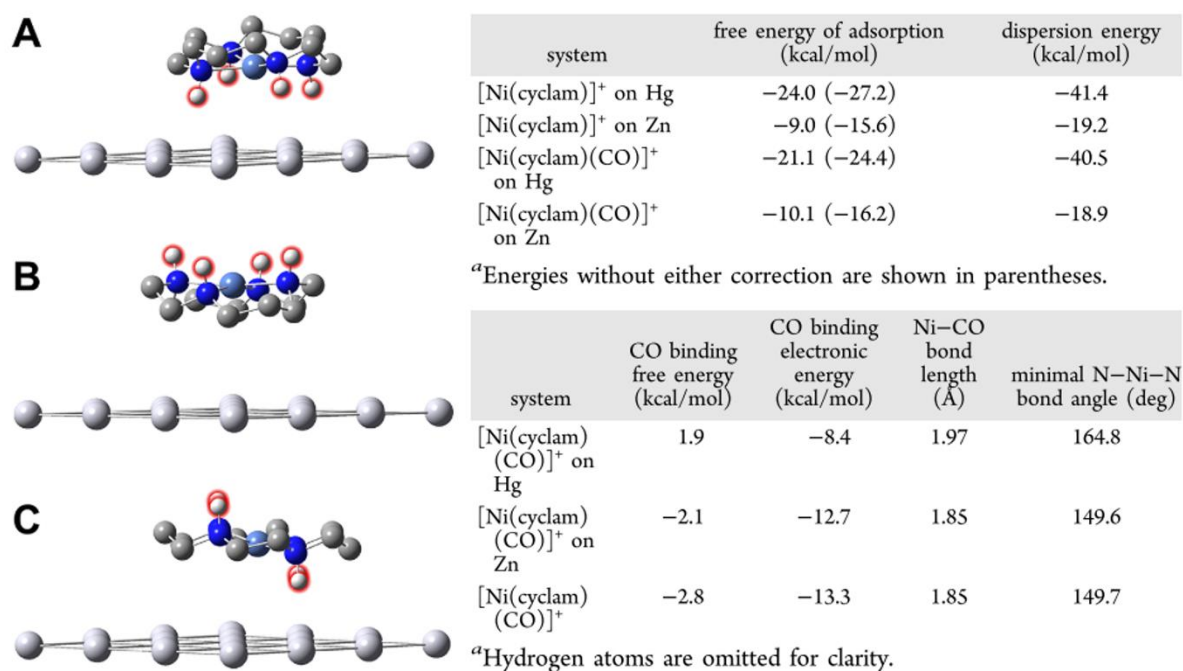


Figure 1.18 Optimized geometries of (A) *trans*-I with the four N-H pointing towards Hg, (B) *trans*-I with no N-H pointing towards Hg or (C) *trans*-III [Ni(cyclam)]⁺ on an Hg surface. Hydrogens on amine groups are highlighted in red.^[171]

1.4 Towards artificial photosynthesis: coupling an electrolyzer with a photovoltaic device

1.4.1 Solar-powered CO₂ electroreduction

The field of artificial photosynthesis, in which solar light is the driving force for the conversion of CO₂ and H₂O to chemical fuels, was pioneered by the work of Fujishima and Honda in the 70s;^[172,173] thereafter, it has been largely dominated by research on the reduction of water into hydrogen and its oxidation into oxygen.^[174] Despite its thermodynamic and kinetic challenges, the research on solar-powered CO₂ reduction devices has increased, in parallel to the development of selective and efficient catalysts.^[175]

Considering only the proposed approaches for bias-free CO₂ reduction devices, two main different architectures can be identified: photoelectrochemical cells (PEC) cells and coupled photovoltaics-electrochemical cells (PV-EC).^[176] In the PEC architecture, light absorbing materials such as semiconductors and catalytically active materials are generally embedded onto electrodes, within a single device.^[177,178] However, although theoretically a semiconductor could drive overall CO₂ reduction, usually solar photovoltaics, e.g. perovskite solar cells, are employed as a power source to speed up the process.^[176]

Among the most notable examples, Reisner and coworkers proposed one of the first PEC cells incorporating MWCNTs and a molecular catalyst (a commercially available Co porphyrin) as the device cathode.^[179] The cathode was interfaced with inverse-structure perovskite solar cells (PSCs) and the photoanode was based on BiVO₄ with a previously reported Co water oxidation catalyst (**Figure 1.19**). All was assembled in a back-to-back tandem device, immersed in aqueous electrolyte solution under CO₂ bubbling, and illuminated with solar light simulators (1.5 G, 100 mW cm⁻², 1 sun). Long-term stability tests revealed that the cell could operate at photocurrents higher than 100 μA cm⁻² for 67 h under no applied bias. The devices presented solar-to-H₂ and solar-to-CO conversion efficiencies of 0.06 and 0.02%, respectively, and was able to operate in neutral pH solution. Following this line, the same lab proposed another version of the PEC cell, this time employing a Cu₉₆In₄ alloy with a unique dendritic foam morphology as cathode material.^[180]

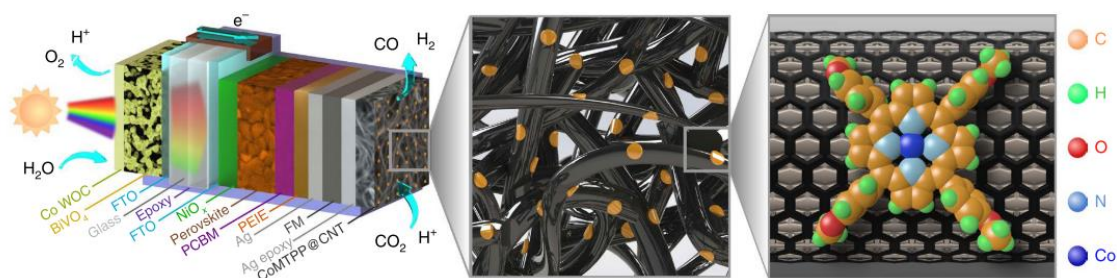


Figure 1.19 Architecture of the bias-free perovskite–BiVO₄ PEC tandem device for syngas production proposed by Reisner et al.^[179]

Challenges of the PEC approach, despite the great results obtained so far, are (i) the complexity in the research of compatible materials, i.e., some materials cannot be arbitrarily combined to form a viable integrated system, as they do not operate under mutually compatible conditions. (ii) the geometry chosen can have a major impact on the total system efficiency, due to losses associated with electrical resistances and chemical transport processes.^[181] Solar-to-fuel efficiencies are still too low to make such devices competitive.

On the contrary, coupling photovoltaic with electrolyzers in PV-EC devices (while maintaining the devices separated), represent one of the most mature technology, as the state of the art in both devices can be employed.^[181] The advantage of this route is the flexibility in the design of PV and electrocatalyst pairs. Components can be individually optimized and then combined together to enable the best overall performance.^[182]

In 2015, Graetzel and collaborators^[183] introduced an innovative approach using three series-connected perovskite solar cells, coupled to an electrolyzer (oxidized Au for the cathode, IrO₂ as the anode and 0.5M NaHCO₃ as the electrolyte). The study was also one of the first demonstrations of extended, stable operation of perovskite photovoltaics under a real load. The results were excellent: the series connected PSCs produced an open-circuit voltage of 3.1 V and a short-circuit current density of 6.15 mA cm⁻²; the reaction was driven for more than 18 h with minimal changes in the current density, demonstrating the excellent stability of not only the anode and cathode, but also of the three-perovskite photovoltaics. The solar-to-CO efficiency achieved exceeded 6.5%.

Today, the most efficient reported PV-EC devices utilize tandem GaInP/GaAs or triple junction GaInP/GaInAs/Ge solar cells, which are able to provide current densities up to 14 mA cm⁻².^[176]

In the near future, however, application of cheap and stable solar cells such as Si or perovskites will become relevant for industrial applications.

In particular, the power conversion efficiency (PCE) of metal halide perovskite solar cells has been continuously improved from 3.8% in 2009 to recently over 25%.^[184] This development was incredibly fast compared to other photovoltaic technologies, making PSCs a very promising platform for the future of solar energy generation, as well as bias-free CO₂RR. As such, research on PSCs today aims to decrease production costs, while maximizing efficiency and, most importantly, stability and durability of these devices.

1.4.2 Increasing the power conversion efficiency of perovskite solar cells

Perovskite solar cells take advantage of the optical and electronic properties of perovskites, crystalline materials with large light absorption coefficients, long photocarrier lifetime, and long diffusion lengths.^[185] Thus, in a PSC, the heart of the device is the perovskite material itself, which is generally embedded or in close contact with a hole transporting material (HTM) and an electron transporting layer (ETL), used to separate the generated holes and electrons and shuttle them more efficiently to the anode and the cathode, respectively.

Depending on their architectures, perovskite solar cells can be divided into two main groups: those which feature a mesoscopic scaffold of oxide nanoparticles like TiO₂ that hosts the perovskite material, and those in which this layer is not present and a film of perovskite is sandwiched between a TiO₂ compact layer and a HTM. These types of cells are called mesoscopic cells and thin film cells, respectively (**Figure 1.20**). Regardless of the architecture, the TiO₂ material, an n-type semiconductor, works as an ETL.

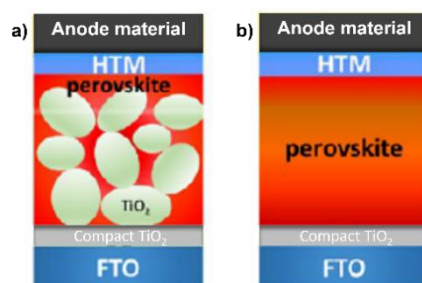


Figure 1.20 Representative architectures for PSCs: a) mesoscopic, and b) thin film.

TiO₂ extracts photoelectrons which are generated in the perovskite absorber layer and delivers them to the cathode electrode. Consequently, parameters like electron extraction efficiency and electron collection efficiency in PSCs are greatly influenced by the ETL. Besides device performance, the challenges of PSCs such as the hysteresis phenomenon and their instability also intimately correlate with the ETL. [185]

Figure 1.21 schematically depicts the general principle of a PSC with a p-i-n junction structure. After light absorption, an electron is promoted from the valence to the conduction band of the perovskite material, leaving a hole behind. In the ideal case, the photogenerated electron should be carried through the TiO₂ (a typical ETL) until it reaches the FTO (Fluorine-doped Tin Oxide, a typical cathode material); likewise, the photogenerated hole should be carried through the HTM until it reaches the Au anode. Thus, the desirable carrier dynamics at interfaces are labeled as paths **1,2** and **3**. At the same time, however, several undesired events take place, such as photocarrier recombination (like **4**, radiative recombination, **5**, nonradiative recombination, and **6,7,8** interface recombination) and trapping in defect states (**9**) at interfaces. These unwanted pathways deteriorate device performances and contribute to the emergence of the hysteresis phenomenon.

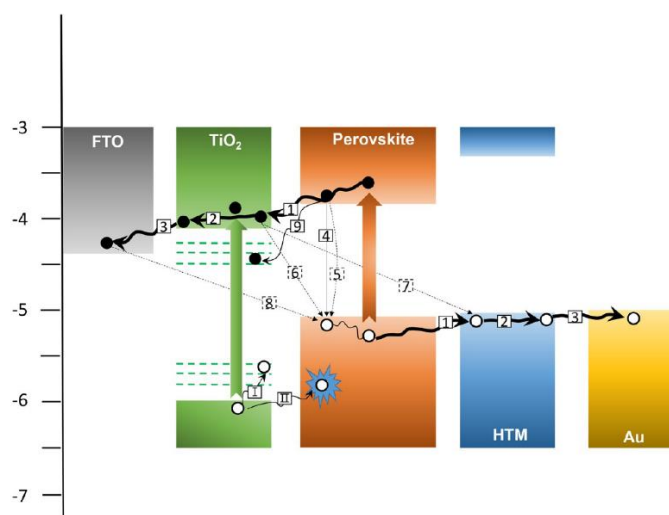


Figure 1.21 Scheme of the carrier dynamics at interfaces in PSCs. [185]

Generally, an ideal photovoltaic device should possess minimum series resistance (R_s), which relates to photocarrier collection, and maximum shunt resistance (R_{sh}) for inhibiting photocarrier recombination, leading to maximum current (J_{sc}) and open circuit voltage (V_{oc}), respectively. Additionally, the fill factor (FF) increases with reducing R_s and enlarging R_{sh} . The

morphology of the ETL can affect all these parameters. For example, a fast transportation of electrons, and a full contact with both the perovskite absorber film and the collector electrode facilitate interface transfer and bulk transportation of photoelectrons and, therefore, reduce R_s . The morphology itself could also contribute to inhibit interface recombination, thus resulting in large R_{sh} .

Hence, rational design the HTM layer, but most importantly the perovskite layer and the ETL (the interface between the two, where most of the recombination events take place) is thus crucial for the construction of high-performance PSCs.

TiO₂ has been widely investigated in photocatalytic systems and sensitized photovoltaic solar cells because of its thermal and chemical stability, low cost, suitability of band alignments, high photocatalytic activities, and easy fabrication.^[186] Due to this versatility, several strategies have been put in place to improve the TiO₂ scaffold in mesoscopic PSCs. Three types of modifications have been investigated: morphological, doping, and synthesis of composites.^[185] While in the last two cases the chemical composition of the materials is modified, the first case only accounts for physical modifications in the nanostructure of the materials and could then be considered as a valid, cheap option to improve TiO₂ ETLs.

Mesoporous layers of anatase TiO₂ particles with sizes around 25 nm and thickness of around 600 nm have proven to be efficient ETLs and are an excellent starting point for morphological improvements.^[187] When optimizing the morphology, one problem to overcome is the trade-off between large pores, to have maximum perovskite filling and big perovskite crystals, and high surface area, to maximize the contact between perovskites and TiO₂.

With an eye at the costs, one of the most economical approaches is to introduce polymeric nanospheres as a mold to improve the efficiency of the cell, as the addition of the nanospheres provides an additional level of porosity which increases the active surface area and the contact with the perovskite crystals. The nanospheres act as a frame that generates cavities and additional porosity once the TiO₂ particles cohere and the polymeric nanosphere is eliminated. When the nanospheres are organized in an ordered fashion, they generate the so-called opal and inverse opal TiO₂ materials.^[188–190]

However, to date, the inverse opal m-TiO₂ layer is generally fabricated following a time- and material-consuming fashion, which makes it difficult to reproduce and scale up.^[188,191]

Additionally, most of the so-called inverse opal materials reported do not always present a high degree of order and periodicity, as the substrate used (generally fluorine-doped tin oxide, FTO) is rough, and the formation of periodic ordered inverse opal structure is very challenging.^[192] As a result, complicated syntheses lead to materials that only partially exhibit the desired optical properties typical of photonic crystals.

On the other hand, the nanospheres can be added arbitrarily to the TiO₂ particles, so to generate a controlled but disordered porosity. This implies the generation of ETLs that would not have specific optical properties, but would feature high stability, cohesion, and very easily tunable porosity, depending on the amount and the dimension of the nanospheres added.^[193]

Over the years, different types of materials have been used to manufacture PSCs, and there have been several modifications and improvements in the architectures and precursors used.^[184] For example, if at the beginning of their study PSCs relied on precious materials such as gold or silver as anodes, it was discovered that carbon materials could be efficiently used instead.^[194] Thus, PSCs that were cheaper and easier to manufacture and that today are classified under the name of fully printable, carbon-based perovskite solar cells, started to have a relevance on the market.^[195] These solar cells have lower PCEs, but have the advantage of being easy to manufacture, having more environmentally friendly materials, and generally having better stability than their more expensive counterparts.^[196] The term “fully printable” refers to the fact that these devices can be fully fabricated and assembled via printing techniques (e.g. inkjet, screen-print).

Improving the ETL of fully printable perovskite solar cells (i.e. already commercially viable PSCs) through inexpensive methods such as morphological modifications described above, can be a way to improve the PCE of such devices while keeping the costs down. High efficiency and low cost will make these devices viable for artificial photosynthesis applications in the future.

1.5 The eSCALED framework and scope of the project

“eSCALED” is a project financed by the European Union's Horizon 2020 research and innovation program. Its name stands for “European School on Artificial Leaf: Electrodes & Devices”. The goal of this project, which is inspired by nature, is to create an artificial leaf

operating on the principle of photosynthesis. Its objective is to produce solar fuels from solar energy, H₂O and CO₂, in stable and storable chemical form.

Furthermore, the project has a double ambition: advancing the research on artificial photosynthesis while training future researchers. Thus, fourteen PhD students (**Figure 1.23**) had the opportunity to go beyond the traditional academic frame, thanks to partnerships between the public research entities and the companies of the eSCALED consortium. eSCALED project brings together 11 internationally recognized research groups, including UNamur, Collège de France, Uppsala University, ICIQ, CEA, UStuttgart, UEindhoven, but also companies like Solaronix, Eurecat, Riva Batteries. Each of the fourteen PhDs of the eSCALED program is associated to 2 complementary universities awarding the PhD co-diploma and leads his/her own subject of research in several laboratories of at least three different countries (with at least one secondment in industry).

Each student involved in this project will eventually contribute to the creation of the final device thanks to their research. The artificial leaf will include a photovoltaic device to capture sunlight and transform it into electricity to power an electrolyzer, where fuels and oxygen will be formed at the cathodic and anodic sides, respectively. The project will bring novelties in using cheap and earth-abundant materials, developing new catalysts for CO₂RR and new membranes. Nanostructured porous electrodes will be functionalised with active sites for the targeted reactions.

The present PhD project had Collège de France and UNamur as its main research entities. As part of the training, three secondments were planned: two months at the Université de Pau et des Pays de l'Adour (UPPA), four months at the Swiss company Solaronix, and two months in Uppsala University, Sweden. Because of the abrupt sanitary crisis, the secondment in Sweden was cancelled. The movements throughout 3 years of PhD are summarized in **Figure 1.22**.

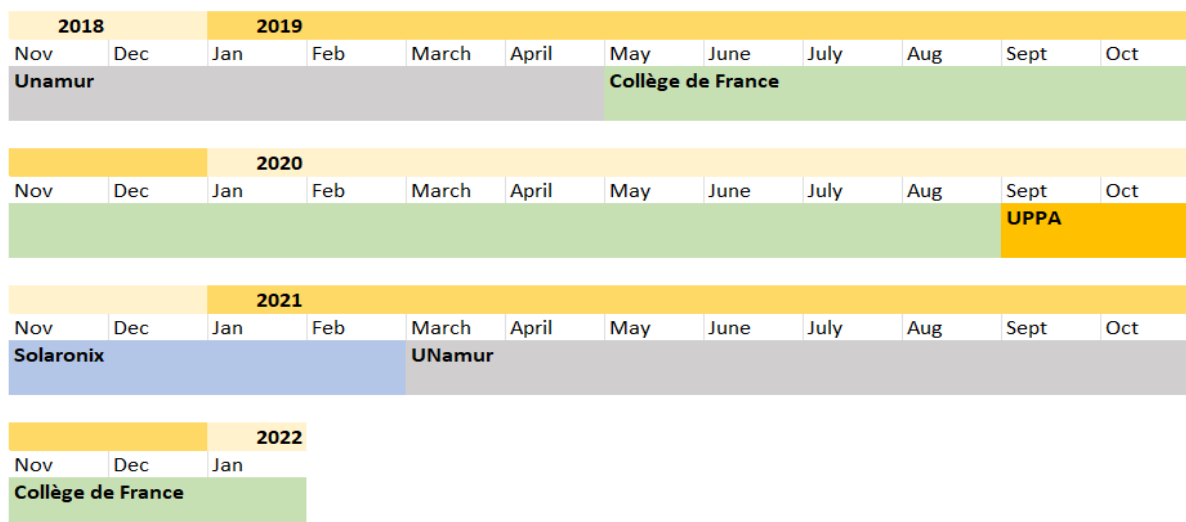


Figure 1.22 Summary of movements throughout the 3-year PhD project.

From the scientific research point of view, the project was very challenging in terms of organization (especially during the pandemic). In spite of this, the periodical meetings, the training sessions, the presentations and the valuable feedback obtained from all eSCALED participants allowed us, the PhD students, not only to grow as researchers, but also to have a significant network of european contacts (and friends!) at the end of the project.



Figure 1.23 eSCALED dream team. From left to right, top row: Robin, Silvia, Van, Karell, Ignasi, Oli, Saeed. Bottom row: Afridi, Bruno, Andrew, Dome, Ludo, Andy, Diogo.

1.5.1 Objectives of the present project

Within the eSCALED framework, the objective of the present project was to develop efficient electrodes for the electrocatalytic reduction of CO₂. More specifically, the aim was to obtain CO₂-reducing molecular catalysts in pure and active form and integrate these catalysts into nanostructured porous scaffolds. These so-formed hybrid materials would then be assayed as electrodes for the CO₂RR, and possibly used as cathodes in the final eSCALED artificial leaf.

Thus, Chapter 2 describes our results within the subject. Initially, we decided to synthesize a new [Ni(cyclam)]²⁺ complex and heterogenize it on the surface of MWCNTs, to generate new hybrid electrodes. When this was achieved, we focused on the amelioration of the performance of the catalyst, with the aim of increasing its selectivity and stability towards the production of CO in water. Chapter 3 describes this work, which ended up by the achievement of another modified [Ni(cyclam)]²⁺ catalyst, more selective than the previous one, especially in aqueous medium.

Besides the work on cathodes for the CO₂RR, the project also involved working with the Swiss company Solaronix, to improve the performance of the perovskite solar cells that will be used in the final device.

This study is described in Chapter 4, where we tried to answer the question: can we improve the performance of commercially available carbon-based monolithic perovskite solar cells in a simple and cost-effective way? To do so, we have modified the morphology of the meso-TiO₂ scaffold to increase the efficiency of such devices. We initially synthesized and fully characterized a range of mesoporous TiO₂ nanomaterials with different morphological features and we introduced them into the solar cells. Successively, we have adopted an even more viable strategy by introducing different degrees of porosity into state-of-the-art nanoparticle based TiO₂ scaffolds. The latter strategy proved effective, leading to more efficient devices.

1.6 References

- [1] X. Xiaoding, J. A. Moulijn, *Energy and Fuels*, **1996**, *10*, 305–325.
- [2] C. Hepburn, E. Adlen, J. Beddington, E. A. Carter, S. Fuss, N. Mac Dowell, J. C. Minx, P. Smith, C. K. Williams, *Nature*, **2019**, *575*, 87–97.
- [3] International Energy Agency, *Energy Rep.*, **2019**, 86.
- [4] Q. Zhu, *Clean Energy*, **2019**, *3*, 85–100.
- [5] G. A. Ozin, *Adv. Mater.*, **2015**, *27*, 1957–1963.
- [6] R. Z. Zhang, B. Y. Wu, Q. Li, L. Le Lu, W. Shi, P. Cheng, *Coord. Chem. Rev.*, **2020**, *422*, 1–28.
- [7] W. H. Koppenol, J. D. Rush, *J. Phys. Chem.*, **1987**, *91*, 4429–4430.
- [8] E. E. Benson, C. P. Kubiak, A. J. Sathrum, J. M. Smieja, *Chem. Soc. Rev.*, **2009**, *38*, 89–99.
- [9] R. Francke, B. Schille, M. Roemelt, *Chem. Rev.*, **2018**, *118*, 4631–4701.
- [10] P. Saha, S. Amanullah, A. Dey, *Acc. Chem. Res.*, **2022**, *55*, 134–144.
- [11] J. M. Savéant, *Chem. Rev.*, **2008**, *108*, 2348–2378.
- [12] Y. Y. Birdja, E. Pérez-Gallent, M. C. Figueiredo, A. J. Göttle, F. Calle-Vallejo, M. T. M. Koper, *Nat. Energy*, **2019**, *4*, 732–745.
- [13] P. De Luna, C. Hahn, D. Higgins, S. A. Jaffer, T. F. Jaramillo, E. H. Sargent, *Science (80-.)*, **2019**, *364*, DOI 10.1126/science.aav3506.
- [14] O. S. Bushuyev, P. De Luna, C. T. Dinh, L. Tao, G. Saur, J. van de Lagemaat, S. O. Kelley, E. H. Sargent, *Joule*, **2018**, *2*, 825–832.
- [15] D. U. Nielsen, X. M. Hu, K. Daasbjerg, T. Skrydstrup, *Nat. Catal.*, **2018**, *1*, 244–254.
- [16] S. Verma, B. Kim, H. R. M. Jhong, S. Ma, P. J. A. Kenis, *ChemSusChem*, **2016**, *9*, 1972–1979.
- [17] M. Jouny, G. S. Hutchings, F. Jiao, *Nat. Catal.*, **2019**, *2*, 1062–1070.
- [18] S. Moret, P. J. Dyson, G. Laurenczy, *Nat. Commun.*, **2014**, *5*, 1–7.
- [19] L. Fan, C. Xia, P. Zhu, Y. Lu, H. Wang, *Nat. Commun.*, **2020**, *11*, DOI 10.1038/s41467-020-17403-1.
- [20] K. Mori, Y. Futamura, S. Masuda, H. Kobayashi, H. Yamashita, *Nat. Commun.*, **2019**, *10*, 1–10.
- [21] J. Eppinger, K. W. Huang, *ACS Energy Lett.*, **2017**, *2*, 188–195.
- [22] Y. Hori, K. Kikuchi, S. Suzuki, *Chem. Lett.*, **1985**, *14*, 1695–1698.
- [23] E. Boutin, M. Wang, J. C. Lin, M. Mesnage, D. Mendoza, B. Lassalle-Kaiser, C. Hahn, T. F. Jaramillo, M. Robert, *Angew. Chemie*, **2019**, *131*, 16318–16322.
- [24] Y. Hori, K. Kikuchi, A. Murata, S. Suzuki, *Chem. Lett.*, **1986**, *15*, 897–898.
- [25] Y. Hori, A. Murata, R. Takahashi, *J. Chem. Soc. Faraday Trans. 1 Phys. Chem. Condens. Phases*, **1989**, *85*, 2309–2326.
- [26] Q. Lu, J. Rosen, F. Jiao, *ChemCatChem*, **2015**, *7*, 38–47.
- [27] Q. Lu, J. Rosen, Y. Zhou, G. S. Hutchings, Y. C. Kimmel, J. G. Chen, F. Jiao, *Nat.*

- Commun.*, **2014**, 5, 3242.
- [28] J. L. Dimeglio, J. Rosenthal, *J. Am. Chem. Soc.*, **2013**, 135, 8798–8801.
- [29] J. Rosen, G. S. Hutchings, Q. Lu, R. V. Forest, A. Moore, F. Jiao, *ACS Catal.*, **2015**, 5, 4586–4591.
- [30] M. Amin Farkhondehfal, J. Zeng (from the edited volume *Electrocatalysis*), IntechOpen, **2021**.
- [31] J. Zeng, K. Bejtka, W. Ju, M. Castellino, A. Chiodoni, A. Sacco, M. A. Farkhondehfal, S. Hernández, D. Rentsch, C. Battaglia, C. F. Pirri, *Appl. Catal. B Environ.*, **2018**, 236, 475–482.
- [32] S. Sarfraz, A. T. Garcia-Esparza, A. Jedidi, L. Cavallo, K. Takanabe, *ACS Catal.*, **2016**, 6, 2842–2851.
- [33] K. Bejtka, J. Zeng, A. Sacco, M. Castellino, S. Hernández, M. A. Farkhondehfal, U. Savino, S. Ansaloni, C. F. Pirri, A. Chiodoni, *ACS Appl. Energy Mater.*, **2019**, 2, 3081–3091.
- [34] S. Zhang, P. Kang, T. J. Meyer, *J. Am. Chem. Soc.*, **2014**, 136, 1734–1737.
- [35] J. Wang, F. Zhang, X. Kang, S. Chen, *Curr. Opin. Electrochem.*, **2019**, 13, 40–46.
- [36] P. T. Smith, E. M. Nichols, Z. Cao, C. J. Chang, *Acc. Chem. Res.*, **2020**, 53, 575–587.
- [37] B. Kumar, M. Asadi, D. Pisasale, S. Sinha-Ray, B. A. Rosen, R. Haasch, J. Abiade, A. L. Yarin, A. Salehi-Khojin, *Nat. Commun.*, **2013**, 4.
- [38] D. M. Koshy, S. Chen, D. U. Lee, M. B. Stevens, A. M. Abdellah, S. M. Dull, G. Chen, D. Nordlund, A. Gallo, C. Hahn, D. C. Higgins, et al., *Angew. Chemie Int. Ed.*, **2020**, 59, 4043–4050.
- [39] T. Möller, W. Ju, A. Bagger, X. Wang, F. Luo, T. Ngo Thanh, A. S. Varela, J. Rossmeisl, P. Strasser, *Energy Environ. Sci.*, **2019**, 12, 640–647.
- [40] H. Yang, Q. Lin, C. Zhang, X. Yu, Z. Cheng, G. Li, Q. Hu, X. Ren, Q. Zhang, J. Liu, C. He, *Nat. Commun.*, **2020**, 11.
- [41] C. Long, X. Li, J. Guo, Y. Shi, S. Liu, Z. Tang, *Small Methods*, **2019**, 3.
- [42] D. Karapinar, C. E. Creissen, J. G. Rivera De La Cruz, M. W. Schreiber, M. Fontecave, *ACS Energy Lett.*, **2021**, 6, 694–706.
- [43] R. Daiyan, W. H. Saputera, H. Masood, J. Leverett, X. Lu, R. Amal, *Adv. Energy Mater.*, **2020**, 10.
- [44] T. Ouyang, S. Huang, X. T. Wang, Z. Q. Liu, *Chem. - A Eur. J.*, **2020**, 26, 14024–14035.
- [45] D. D. Zhu, J. L. Liu, S. Z. Qiao, *Adv. Mater.*, **2016**, 28, 3423–3452.
- [46] W. Ren, C. Zhao, *Natl. Sci. Rev.*, **2020**, 7, 7–9.
- [47] S. Meshitsuka, M. Ichikawa, K. Tamaru, *J. Chem. Soc. Chem. Commun.*, **1974**, 158–159.
- [48] K. Takahashi, K. Hiratsuka, H. Sasaki, S. Toshima, *Chem. Lett.*, **1979**, 8, 305–308.
- [49] K. Hiratsuka, K. Takahashi, H. Sasaki, S. Toshima, *Chem. Lett.*, **1977**, 6, 1137–1140.
- [50] E. Boutin, L. Merakeb, B. Ma, B. Boudy, M. Wang, J. Bonin, E. Anxolabéhère-Mallart, M. Robert, *Chem. Soc. Rev.*, **2020**, 49, 5772–5809.
- [51] S. Gonell, A. J. M. Miller, *Carbon Dioxide Electroreduction Catalyzed by Organometallic Complexes*, Elsevier Inc., **2018**.

- [52] L. Chen, Z. Guo, X. G. Wei, C. Gallenkamp, J. Bonin, E. Anxolabéhère-Mallart, K. C. Lau, T. C. Lau, M. Robert, *J. Am. Chem. Soc.*, **2015**, *137*, 10918–10921.
- [53] C. Costentin, S. Drouet, M. Robert, J.-M. Savéant, *Science (80-.)*, **2012**, *338*, 90–94.
- [54] P. Kang, Z. Chen, A. Nayak, S. Zhang, T. J. Meyer, *Energy Environ. Sci.*, **2014**, *7*, 4007–4012.
- [55] J. M. Smieja, M. D. Sampson, K. A. Grice, E. E. Benson, J. D. Froehlich, C. P. Kubiak, *Inorg. Chem.*, **2013**, *52*, 2484–2491.
- [56] N. Elgrishi, M. B. Chambers, V. Artero, M. Fontecave, *Phys. Chem. Chem. Phys.*, **2014**, *16*, 13635–13644.
- [57] P. Kang, S. Zhang, T. J. Meyer, M. Brookhart, *Angew. Chemie - Int. Ed.*, **2014**, *53*, 8709–8713.
- [58] C. Caix, S. Chardon-Noblat, A. Deronzier, *J. Electroanal. Chem.*, **1997**, *434*, 163–170.
- [59] R. Angamuthu, P. Byers, M. Lutz, A. L. Spek, E. Bouwman, *Science (80-.)*, **2010**, *327*, 313–315.
- [60] L. Rotundo, R. Gobetto, C. Nervi, *Curr. Opin. Green Sustain. Chem.*, **2021**, *31*, 100509.
- [61] F. Franco, C. Cometto, L. Nencini, C. Barolo, F. Sordello, C. Minero, J. Fiedler, M. Robert, R. Gobetto, C. Nervi, *Chem. - A Eur. J.*, **2017**, *23*, 4782–4793.
- [62] C. Costentin, M. Robert, J. M. Savéant, *Chem. Soc. Rev.*, **2013**, *42*, 2423–2436.
- [63] C. Costentin, M. Robert, J. M. Savéant, *Acc. Chem. Res.*, **2015**, *48*, 2996–3006.
- [64] I. Azcarate, C. Costentin, M. Robert, J. M. Savéant, *J. Am. Chem. Soc.*, **2016**, *138*, 16639–16644.
- [65] B. Fisher, R. Eisenberg, *J. Am. Chem. Soc.*, **1980**, *102*, 7361–7363.
- [66] M. Beley, J. P. Collin, R. Ruppert, J. P. Sauvage, *J. Chem. Soc. - Ser. Chem. Commun.*, **1984**, *2*, 1315–1316.
- [67] S. Roy, B. Sharma, J. Pécaut, P. Simon, M. Fontecave, P. D. Tran, E. Derat, V. Artero, *J. Am. Chem. Soc.*, **2017**, *139*, 3685–3696.
- [68] J. Hawecker, J. M. Lehn, R. Ziessel, *J. Chem. Soc. Chem. Commun.*, **1984**, 328–330.
- [69] N. Elgrishi, M. B. Chambers, X. Wang, M. Fontecave, *Chem. Soc. Rev.*, **2017**, *46*, 761–796.
- [70] M. Bourrez, F. Molton, S. Chardon-Noblat, A. Deronzier, *Angew. Chemie - Int. Ed.*, **2011**, *50*, 9903–9906.
- [71] M. D. Sampson, A. D. Nguyen, K. A. Grice, C. E. Moore, A. L. Rheingold, C. P. Kubiak, *J. Am. Chem. Soc.*, **2014**, *136*, 5460–5471.
- [72] P. Kang, S. Zhang, T. J. Meyer, M. Brookhart, *Angew. Chemie Int. Ed.*, **2014**, *53*, 8709–8713.
- [73] C. Costentin, M. Robert, J. M. Savéant, A. Tatin, *Proc. Natl. Acad. Sci. U. S. A.*, **2015**, *112*, 6882–6886.
- [74] P. Kang, Z. Chen, A. Nayak, S. Zhang, T. J. Meyer, *Energy Environ. Sci.*, **2014**, *7*, 4007–4012.
- [75] M. Das Bairagya, R. J. Bujol, N. Elgrishi, *Chem. - A Eur. J.*, **2020**, DOI 10.1002/chem.201904499.
- [76] N. Elgrishi, M. B. Chambers, M. Fontecave, *Chem. Sci.*, **2015**, *6*, 2522–2531.

- [77] E. S. Rountree, B. D. McCarthy, T. T. Eisenhart, J. L. Dempsey, *Inorg. Chem.*, **2014**, *53*, 9983–10002.
- [78] K. J. Lee, N. Elgrishi, B. Kandemir, J. L. Dempsey, *Nat. Rev. Chem.*, **2017**, *1*, 0039.
- [79] A. J. A. Barrett, B. F. M. Brunner, C. P. L. Cheung, D. C. P. Kubiak, E. G. L. Lee, F. C. J. Miller, G. K. M. Waldie, H. A. Zhanaidarova, Chapter 1: Approaches to Controlling Homogeneous Electrochemical Reduction of Carbon Dioxide, in *RSC Energy Environ. Ser.*, **2021**, pp. 1–66.
- [80] J. W. Wang, D. C. Zhong, T. B. Lu, *Coord. Chem. Rev.*, **2018**, *377*, 225–236.
- [81] I. Gamba, *Bioinorg. Chem. Appl.*, **2018**, *2018*, DOI 10.1155/2018/2379141.
- [82] A. Mouchfiq, T. K. Todorova, S. Dey, M. Fontecave, V. Mougel, *Chem. Sci.*, **2020**, *11*, 5503–5510.
- [83] T. Fogeron, P. Retailleau, M. Gomez-Mingot, Y. Li, M. Fontecave, *Organometallics*, **2019**, *38*, 1344–1350.
- [84] Y. Li, M. Gomez-Mingot, T. Fogeron, M. Fontecave, *Acc. Chem. Res.*, **2021**, *54*, 4250–4261.
- [85] Y. Cheng, P. Hou, X. Wang, P. Kang, *Acc. Chem. Res.*, **2022**, DOI 10.1021/acs.accounts.1c00614.
- [86] C. Sun, R. Gobetto, C. Nervi, *New J. Chem.*, **2016**, *40*, 5656–5661.
- [87] L. Sun, V. Reddu, A. C. Fisher, X. Wang, *Energy Environ. Sci.*, **2020**, *13*, 374–403.
- [88] B. Zhang, L. Sun, *Chem. Soc. Rev.*, **2019**, *48*, 2216–2264.
- [89] X. M. Hu, S. U. Pedersen, K. Daasbjerg, *Curr. Opin. Electrochem.*, **2019**, *15*, 148–154.
- [90] B. Zhang, L. Sun, *Chem. Soc. Rev.*, **2019**, *48*, 2216–2264.
- [91] N. Elgrishi, S. Griveau, M. B. Chambers, F. Bedioui, M. Fontecave, *Chem. Commun.*, **2015**, *51*, 2995–2998.
- [92] A. Zhanaidarova, C. E. Moore, M. Gembicky, C. P. Kubiak, *Chem. Commun.*, **2018**, *54*, 4116–4119.
- [93] A. Maurin, M. Robert, *Chem. Commun.*, **2016**, *52*, 12084–12087.
- [94] M. Zhu, J. Chen, L. Huang, R. Ye, J. Xu, Y. Han, *Angew. Chemie*, **2019**, *131*, 6667–6671.
- [95] Y. Wu, Z. Jiang, X. Lu, Y. Liang, H. Wang, *Nature*, **2019**, *575*, 639–642.
- [96] X. Zhang, Z. Wu, X. Zhang, L. Li, Y. Li, H. Xu, X. Li, X. Yu, Z. Zhang, Y. Liang, H. Wang, *Nat. Commun.*, **2017**, *8*, DOI 10.1038/ncomms14675.
- [97] S. Ren, D. Joulié, D. Salvatore, K. Torbensen, M. Wang, M. Robert, C. P. Berlinguette, *Science (80-.)*, **2019**, *365*, 367–369.
- [98] M. Wang, L. Chen, T.-C. Lau, M. Robert, *Angew. Chemie*, **2018**, *130*, 7895–7899.
- [99] X. Zhang, Y. Wang, M. Gu, M. Wang, Z. Zhang, W. Pan, Z. Jiang, H. Zheng, M. Lucero, H. Wang, G. E. Sterbinsky, et al., *Nat. Energy*, **2020**, *5*, 684–692.
- [100] S. Pugliese, N. T. Huan, J. Forte, D. Grammatico, S. Zanna, B. L. Su, Y. Li, M. Fontecave, *ChemSusChem*, **2020**, *13*, 6449–6456.
- [101] J. D. Blakemore, A. Gupta, J. J. Warren, B. S. Brunshwig, H. B. Gray, *J. Am. Chem. Soc.*, **2013**, *135*, 18288–18291.

- [102] P. Kang, S. Zhang, T. J. Meyer, M. Brookhart, *Angew. Chemie Int. Ed.*, **2014**, *53*, 8709–8713.
- [103] A. Maurin, M. Robert, *J. Am. Chem. Soc.*, **2016**, *138*, 2492–2495.
- [104] B. Reuillard, K. H. Ly, T. E. Rosser, M. F. Kuehnel, I. Zebger, E. Reisner, **2017**, DOI 10.1021/jacs.7b06269.
- [105] S. Sinha, A. Sonea, W. Shen, S. S. Hanson, J. J. Warren, *Inorg. Chem.*, **2019**, *58*, 10454–10461.
- [106] P. Shao, L. Yi, S. Chen, T. Zhou, J. Zhang, *J. Energy Chem.*, **2020**, *40*, 156–170.
- [107] C. Zhao, X. Dai, T. Yao, W. Chen, X. Wang, J. Wang, J. Yang, S. Wei, Y. Wu, Y. Li, *J. Am. Chem. Soc.*, **2017**, *139*, 8078–8081.
- [108] Y. R. Wang, Q. Huang, C. T. He, Y. Chen, J. Liu, F. C. Shen, Y. Q. Lan, *Nat. Commun.*, **2018**, *9*, DOI 10.1038/s41467-018-06938-z.
- [109] J. D. Blakemore, A. Gupta, J. J. Warren, B. S. Brunshwig, H. B. Gray, *J. Am. Chem. Soc.*, **2013**, *135*, 18288–18291.
- [110] S. Sato, B. J. McNicholas, R. H. Grubbs, *Chem. Commun.*, **2020**, *56*, 4440–4443.
- [111] M. Zhu, R. Ye, K. Jin, N. Lazouski, K. Manthiram, *ACS Energy Lett.*, **2018**, *3*, 1381–1386.
- [112] J. van Alphen, *Recl. des Trav. Chim. des Pays-Bas*, **1937**, *56*, 836–840.
- [113] J. van Alphen, *Recl. des Trav. Chim. des Pays-Bas*, **1937**, *56*, 344–350.
- [114] H. Stetter, K. -H Mayer, *Chem. Ber.*, **1961**, *94*, 1410–1416.
- [115] S. Airey, A. Drljaca, M. J. Hardie, C. L. Raston, *Chem. Commun.*, **1999**, 1137–1138.
- [116] L. Fabbrizzi, A Lifetime Walk in the Realm of Cyclam, in *Macrocycl. Supramol. Chem.*, John Wiley & Sons, Ltd, Chichester, UK, **2016**, pp. 165–199.
- [117] A. Evers, R. D. Hancock, *Inorganica Chim. Acta*, **1989**, *160*, 245–248.
- [118] E. Kimura, *Tetrahedron*, **1992**, *48*, 6175–6217.
- [119] D. K. Cabbiness, D. W. Margerum, *J. Am. Chem. Soc.*, **1969**, *91*, 6540–6541.
- [120] B. Bosnich, C. K. Poon, M. L. Tobe, *Inorg. Chem.*, **1965**, *4*, 1102–1108.
- [121] B. Bosnich, R. Mason, P. J. Pauling, G. B. Robertson, M. L. Tobe, *Chem. Commun.*, **1965**, *346*, 97.
- [122] M. A. Donnelly, M. Zimmer, *Inorg. Chem.*, **1999**, *38*, 1650–1658.
- [123] M. Bakaj, M. Zimmer, *J. Mol. Struct.*, **1999**, *508*, 59–72.
- [124] E. K. Barefield, J. S. Summers, D. G. Van Derveer, A. Bianchi, E. J. Billo, P. J. Connolly, P. Paoletti, *Inorg. Chem.*, **1986**, *25*, 4197–4202.
- [125] D. T. Pierce, T. L. Hatfield, E. Joseph Billo, Y. Ping, *Inorg. Chem.*, **1997**, *36*, 2950–2955.
- [126] X. Liang, P. J. Sadler, *Chem. Soc. Rev.*, **2004**, *33*, 246–266.
- [127] L. Prasad, A. McAuley, *Acta Crystallogr. Sect. C Cryst. Struct. Commun.*, **1983**, *39*, 1175–1177.
- [128] E. J. Billo, *Inorg. Chem.*, **1981**, *20*, 4019–4021.
- [129] Y. Kashiwagi, C. Kikuchi, F. Kurashima, J. I. Anzai, *J. Organomet. Chem.*, **2002**, *662*,

9–13.

- [130] P. Jacquinet, P. C. Hauser, *Electroanalysis*, **2003**, *15*, 1437–1444.
- [131] M. Al-Bari, M. Chowdhury, M. Hossen, M. Hossain, C. Zakaria, M. Islam, *J. Appl. Sci. Res.*, **2007**, *3*, 1251–1261.
- [132] H. S. Kim, T. Yoon, J. Jang, J. Mun, H. Park, J. H. Ryu, S. M. Oh, *J. Power Sources*, **2015**, *283*, 300–304.
- [133] Y. J. Leem, K. Cho, K. H. Oh, S. H. Han, K. M. Nam, J. Chang, *Chem. Commun.*, **2017**, *53*, 3454–3457.
- [134] M. Beley, J. P. Collin, R. Ruppert, J. P. Sauvage, *J. Am. Chem. Soc.*, **1986**, *108*, 7461–7467.
- [135] J. P. Collin, A. Jouaiti, J. P. Sauvage, *Inorg. Chem.*, **1988**, *27*, 1986–1990.
- [136] E. Y. Lee, D. Hong, H. W. Park, M. P. Suh, *Eur. J. Inorg. Chem.*, **2003**, *2003*, 3242–3249.
- [137] L. M. Cao, H. H. Huang, J. W. Wang, D. C. Zhong, T. B. Lu, *Green Chem.*, **2018**, *20*, 798–803.
- [138] J. P. Collin, J. P. Sauvage, *J. Chem. Soc. Chem. Commun.*, **1987**, 1075–1076.
- [139] E. Sable, H. Handel, M. L’Her, *Electrochim. Acta*, **1991**, *36*, 15–17.
- [140] E. Simon, E. Sablé, H. Handel, M. L’Her, *Electrochim. Acta*, **1999**, *45*, 855–863.
- [141] G. King, S. J. Higgins, N. Price, *Analyst*, **1992**, *117*, 1243–1246.
- [142] F. Vilchez, S. Gutierrez-Granados, A. Alatorre Ordaz, L. Galicia, P. Herrasti, *J. Electroanal. Chem.*, **2008**, *614*, 8–14.
- [143] F. Mouffouk, A. Demetriou, S. J. Higgins, R. J. Nichols, *Inorganica Chim. Acta*, **2006**, *359*, 3491–3496.
- [144] K. Maksymiuk, M. Puszcz, K. Szewczyk, A. Michalska, *J. Solid State Electrochem.*, **2011**, *15*, 2369–2376.
- [145] D. Saravanakumar, J. Song, N. Jung, H. Jirimali, W. Shin, *ChemSusChem*, **2012**, *5*, 634–636.
- [146] U. Akiba, Y. Nakamura, K. Suga, M. Fujihira, *Thin Solid Films*, **1992**, *210–211*, 381–383.
- [147] A. Jarzebińska, P. B. Rowiński, I. Zawisza, R. Bilewicz, L. Siegfried, T. Kaden, *Anal. Chim. Acta*, **1999**, *396*, 1–12.
- [148] A. Zhanaidarova, C. E. Moore, M. Gembicky, C. P. Kubiak, *Chem. Commun.*, **2018**, *54*, 4116–4119.
- [149] A. Zhanaidarova, C. E. Moore, M. Gembicky, C. P. Kubiak, *Chem. Commun.*, **2018**, *54*, 4116–4119.
- [150] C. Jiang, A. W. Nichols, J. F. Walzer, C. W. Machan, *Inorg. Chem.*, **2020**, *59*, 1883–1892.
- [151] F. Greenwell, G. Neri, V. Piercy, A. J. Cowan, *Electrochim. Acta*, **2021**, *392*, 139015.
- [152] J. D. Froehlich, C. P. Kubiak, *Inorg. Chem.*, **2012**, *51*, 3932–3934.
- [153] G. Neri, I. M. Aldous, J. J. Walsh, L. J. Hardwick, A. J. Cowan, *Chem. Sci.*, **2016**, *7*, 1521–1526.

- [154] J. Honores, D. Quezada, M. García, K. Calfumán, J. P. Muenza, M. J. Aguirre, M. C. Arévalo, M. Isaacs, *Green Chem.*, **2017**, *19*, 1155–1162.
- [155] E. Fujita, J. Haff, R. Sanzenbacher, H. Elias, *Inorg. Chem.*, **1994**, *33*, 4627–4628.
- [156] M. Aulice Scibioh, P. V Ragini, S. Rani, V. R. Vijayaraghavan, B. Viswanathan, Reduction of CO₂ by nickel (II) macrocycle catalyst at HMDE, in *Proc. Indian Acad. Sci. Chem. Sci.*, **2001**, pp. 343–350.
- [157] J. Schneider, H. Jia, K. Kobiro, D. E. Cabelli, J. T. Muckerman, E. Fujita, *Energy Environ. Sci.*, **2012**, *5*, 9502–9510.
- [158] G. Neri, J. J. Walsh, C. Wilson, A. Reynal, J. Y. C. Lim, X. Li, A. J. P. White, N. J. Long, J. R. Durrant, A. J. Cowan, *Phys. Chem. Chem. Phys.*, **2015**, *17*, 1562–1566.
- [159] M. Murase, G. Kitahara, T. M. Suzuki, R. Ohta, *ACS Appl. Mater. Interfaces*, **2016**, *8*, 24315–24318.
- [160] T. D. Cook, S. F. Tyler, C. M. McGuire, M. Zeller, P. E. Fanwick, D. H. Evans, D. G. Peters, T. Ren, *ACS Omega*, **2017**, *2*, 3966–3976.
- [161] B. L. Mash, A. Raghavan, T. Ren, *Eur. J. Inorg. Chem.*, **2019**, *2019*, 2065–2070.
- [162] M. Fujihira, Y. Hirata, K. Suga, *J. Electroanal. Chem. Interfacial Electrochem.*, **1990**, *292*, 199–215.
- [163] M. Fujihira, Y. Nakamura, Y. Hirata, U. Akiba, K. Suga, *Denki Kagaku oyobi Kogyo Butsuri Kagaku*, **1991**, *59*, 532–539.
- [164] G. B. Balazs, F. C. Anson, *J. Electroanal. Chem.*, **1992**, *322*, 325–345.
- [165] G. B. Balazs, F. C. Anson, *J. Electroanal. Chem.*, **1993**, *361*, 149–157.
- [166] K. Bujno, R. Bilewicz, L. Siegfried, T. Kaden, *Electrochim. Acta*, **1997**, *42*, 1201–1206.
- [167] J. Costamagna, G. Ferraudi, J. Canales, J. Vargas, *Coord. Chem. Rev.*, **1996**, *148*, 221–248.
- [168] J. Song, E. L. Klein, F. Neese, S. Ye, *Inorg. Chem.*, **2014**, *53*, 7500–7507.
- [169] C. A. Kelly, E. L. Blinn, N. Camaioni, M. D’Angelantonio, Q. G. Mulazzani, *Inorg. Chem.*, **1999**, *38*, 1579–1584.
- [170] J. D. Froehlich, C. P. Kubiak, *J. Am. Chem. Soc.*, **2015**, *137*, 3565–3573.
- [171] Y. Wu, B. Rudsteyn, A. Zhanaidarova, J. D. Froehlich, W. Ding, C. P. Kubiak, V. S. Batista, *ACS Catal.*, **2017**, *7*, 5282–5288.
- [172] T. Inoue, A. Fujishima, S. Konishi, K. Honda, *Nature*, **1979**, *277*, 637–638.
- [173] A. Fujishima, T. N. Rao, D. A. Tryk, *J. Photochem. Photobiol. C Photochem. Rev.*, **2000**, *1*, 1–21.
- [174] C. Bozal-Ginesta, J. R. Durrant, *Faraday Discuss.*, **2019**, *215*, 439–451.
- [175] A. Kumar, V. Hasija, A. Sudhaik, P. Raizada, Q. Van Le, P. Singh, T. H. Pham, T. Y. Kim, S. Ghotekar, V. H. Nguyen, *Chem. Eng. J.*, **2022**, *430*, 133031.
- [176] C. E. Creissen, M. Fontecave, *Adv. Energy Mater.*, **2020**, 2002652.
- [177] Y. J. Jang, I. Jeong, J. Lee, J. Lee, M. J. Ko, J. S. Lee, *ACS Nano*, **2016**, *10*, 6980–6987.
- [178] C. Li, T. Wang, B. Liu, M. Chen, A. Li, G. Zhang, M. Du, H. Wang, S. F. Liu, J. Gong, *Energy Environ. Sci.*, **2019**, *12*, 923–928.
- [179] V. Andrei, B. Reuillard, E. Reisner, *Nat. Mater.*, **2020**, *19*, 189–194.

- [180] M. Rahaman, V. Andrei, C. Pornrungrroj, D. Wright, J. J. Baumberg, E. Reisner, *Energy Environ. Sci.*, **2020**, *13*, 3536–3543.
- [181] J. R. McKone, N. S. Lewis, H. B. Gray, *Chem. Mater.*, **2014**, *26*, 407–414.
- [182] J. Wu, Y. Huang, W. Ye, Y. Li, *Adv. Sci.*, **2017**, *4*, DOI 10.1002/advs.201700194.
- [183] M. Schreier, L. Curvat, F. Giordano, L. Steier, A. Abate, S. M. Zakeeruddin, J. Luo, M. T. Mayer, M. Grätzel, *Nat. Commun.*, **2015**, *6*, 1–6.
- [184] P. Roy, N. Kumar Sinha, S. Tiwari, A. Khare, *Sol. Energy*, **2020**, *198*, 665–688.
- [185] C. Zhen, T. Wu, R. Chen, L. Wang, G. Liu, H.-M. Cheng, *ACS Sustain. Chem. Eng.*, **2019**, *7*, 4586–4618.
- [186] O. Ola, M. M. Maroto-Valer, *J. Photochem. Photobiol. C Photochem. Rev.*, **2015**, *24*, 16–42.
- [187] Z. hui Liu, S. Bi, G. liang Hou, C. zhan Ying, X. jia Su, *J. Power Sources*, **2019**, *430*, 12–19.
- [188] Z. Liu, L. Wu, X. Wang, Q. Xu, Y. Hu, K. Meng, G. Chen, *Nanoscale*, **2020**, *12*, 8425–8431.
- [189] A. Maho, M. Lobet, N. Daem, P. Piron, G. Spronck, J. Loicq, R. Cloots, P. Colson, C. Henrist, J. Dewalque, *ACS Appl. Energy Mater.*, **2021**, *4*, 1108–1119.
- [190] X. Chen, S. Yang, Y. C. Zheng, Y. Chen, Y. Hou, X. H. Yang, H. G. Yang, *Adv. Sci.*, **2015**, *2*, 1–6.
- [191] R. Zhang, D. Shen, M. Xu, D. Feng, W. Li, G. Zheng, R. Che, A. A. Elzatahry, D. Zhao, *Adv. Energy Mater.*, **2014**, *4*, DOI 10.1002/aenm.201301725.
- [192] T. Fröschl, U. Hörmann, P. Kubiak, G. Kučerová, M. Pfanzelt, C. K. Weiss, R. J. Behm, N. Hüsing, U. Kaiser, K. Landfester, M. Wohlfahrt-Mehrens, *Chem. Soc. Rev.*, **2012**, *41*, 5313–5360.
- [193] T. Hwang, S. Lee, J. Kim, J. Kim, C. Kim, B. Shin, B. Park, *Nanoscale Res. Lett.*, **2017**, *12*, DOI 10.1186/s11671-016-1809-7.
- [194] D. Bogachuk, R. Tsuji, D. Martineau, S. Narbey, J. P. Herterich, L. Wagner, K. Suginuma, S. Ito, A. Hinsch, *Carbon N. Y.*, **2021**, *178*, 10–18.
- [195] A. Verma, D. Martineau, S. Abdolhosseinzadeh, J. Heier, F. Nüesch, *Mater. Adv.*, **2020**, *1*, 153–160.
- [196] G. Grancini, C. Roldán-Carmona, I. Zimmermann, E. Mosconi, X. Lee, D. Martineau, S. Narbey, F. Oswald, F. De Angelis, M. Graetzel, M. K. Nazeeruddin, *Nat. Commun.*, **2017**, *8*.

Chapter 2 Functionalization of Carbon Nanotubes with Nickel Cyclam for the Electrochemical Reduction of CO₂

2.1 Introduction

Catalysis for CO₂ electroreduction into energy-dense products, such as CO, formic acid, hydrocarbons and alcohols, has been extensively studied during the last 10 years as this reaction represents one of the most promising strategies for both CO₂ utilization as a carbon source and storage of intermittent renewable energy in the form of stable chemical energy.^[1] Catalysts are needed to overcome important kinetic limitations related to the multi-electron and multi-proton transfers associated with the CO₂ reduction reaction (CO₂RR). Current research focuses on both solid materials^[2-4] and homogeneous organometallic complexes.^[5,6] The former are favored industrially due to more facile product isolation and catalyst regeneration and recovery. However, molecular compounds afford the opportunity to more easily design and synthetically tune the coordination environment of the active metal center. Mechanistic studies are also facilitated in that case. To reconcile these two approaches, homogeneous catalysts can be immobilized on heterogeneous conductive supports to generate cathode materials for electrolyzers. Such heterogenized molecular systems thus combine the advantages of a solid material (easy recovery of products and catalysts, efficient electron transfer from the electrode support to the catalyst, high Turnover Numbers) with those of molecular complexes (synthetic control of the electronic properties and the coordination environment of the active sites), while suppressing deactivation processes (such as dimerization) and solubility issues associated with the latter. This class of hybrid catalysts for CO₂RR has been recently described in review articles.^[7-9]

Among various methods, a widely used and straightforward technique for immobilizing molecular catalysts is based on hydrophobic and π - π stacking interactions between a carbon-based support, generally graphite electrodes or multi-walled carbon nanotubes (MWCNTs), and the molecular catalyst, as recently reviewed.^[10] MWCNTs have the advantages of stability, high electrical conductivity and high surface area. While there have been some successes regarding heterogeneous immobilization of CO₂RR catalysts on carbon supports such as MWCNTs, these are few and limited mainly to polyaromatic macrocyclic ligands.^[11-13] For example, immobilization of a CO₂RR molecular catalyst is possible without any functionalization of the

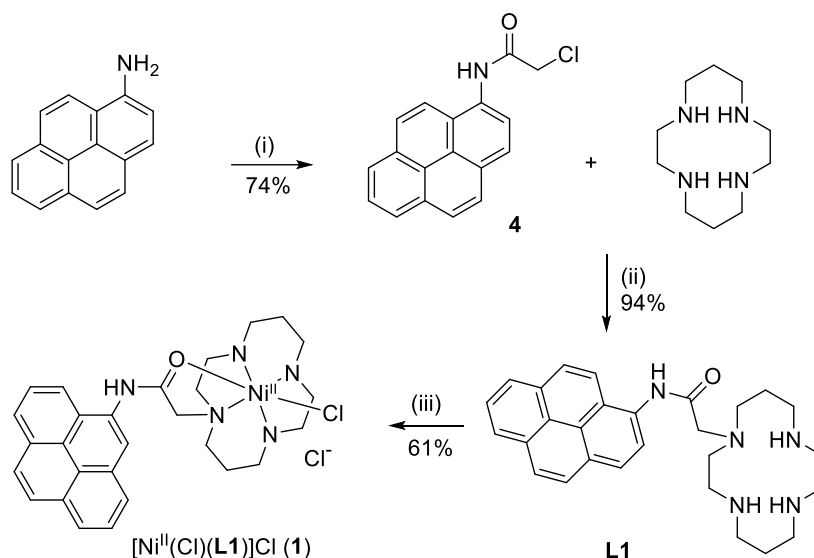
ligand when the ligand is highly conjugated as in the case of metal porphyrins and phthalocyanines.^[11–13] In contrast, when the ligand, such as bipyridine or benzene-based pincer derivatives, has a limited electronic delocalized structure, an aromatic group, most often pyrene, has to be covalently added to the ligand: the pyrene group allows tight grafting of the molecular complex on carbon electrode surfaces via π – π stacking interactions. Regarding such simple ligands functionalized with a pyrene group, the most representative reports concern bipyridine-pyrene derivatives used to immobilize a [Re(bpy)(CO)₃Cl] complex on a graphite support^[14] or a [Mn(bpy)(CO)₃Br] complex on carbon nanotubes^[15] as well as a pincer-pyrene ligand used to immobilize an Iridium complex onto a gas diffusion electrode via carbon nanotubes.^[16] The three materials displayed interesting electrochemical CO₂RR catalytic properties, however in some cases with limited activity and stability.

In order to explore other classes of ligands, in particular non-aromatic in nature, and complexes based on non-noble metals, we have investigated one of the most studied molecular catalysts for CO₂RR, [Ni(cyclam)]²⁺. To our knowledge, while the heterogenization of [Ni(cyclam)]²⁺ complex has already been proposed,^[17,18] there is no precedent for its non-covalent immobilization on a carbon-based nanostructured electrode.

For that purpose, we have synthesized an original pyrene-cyclam derivative and the corresponding Ni complex, complex **1** (**Scheme 2.1**), which was found to be a unique 6-coordinated Ni cyclam complex. We report here the electrocatalytic properties of complex **1** both in solution and after immobilization on MWCNTs. The complex proved to behave as a very selective homogeneous catalyst for CO₂ electroreduction to CO in organic solvents. Furthermore, the presence of a pyrene moiety on the ligand was exploited to readily heterogenize the complex on MWCNTs via non-covalent interactions. The novel hybrid solid electrode, obtained by deposition of the functionalized MWCNTs on a Gas Diffusion Layer (GDL), was found to be active, stable and highly selective for CO₂ electroreduction to CO in acetonitrile-water solvent.

2.2 Results

2.2.1 Complex 1 synthesis and characterization



Scheme 2.1 Synthesis of complex **1**. Conditions: (i) ClCH_2COCl , NEt_3 , CH_2Cl_2 ; (ii) K_2CO_3 , KI (cat.), MeCN ; (iii) $\text{NiCl}_2 \cdot 6\text{H}_2\text{O}$, EtOH .

In order to synthesize a $[\text{Ni}(\text{cyclam})]^{2+}$ complex bearing a pyrene group, we chose to prepare the ligand **L1**, in which one N atoms of the cyclam ring is alkylated with a substituent containing a pyrene moiety (**Scheme 2.1**), according to a previously reported procedure.^[19] However, this previous synthesis gave the product in low yields and required arduous chromatographic purification. In this work, we improved the experimental procedure, especially for the N-alkylation of the cyclam ring step, so that no chromatography purification was needed anymore, and **L1** could be easily synthesized on a large scale. The corresponding nickel complex $[\text{Ni}^{\text{II}}(\text{Cl})(\text{L1})](\text{Cl})$ (**1**) was obtained using nickel chloride hexahydrate in ethanol for metalation.

Complex **1** was isolated in the form of crystals suitable for X-ray analysis. Crystal data of all obtained structures are available in **Table A2.2**. Four different solvents, ethanol (EtOH), acetonitrile (MeCN), dichloromethane (CH_2Cl_2) and *N,N*-dimethylformamide (DMF) were used for crystallization, resulting in different crystal packings differentially stabilized by intermolecular hydrogen bonding, pi-stacking and Van der Waals interactions (**Table A2.2**). In all structures, the nickel center ion was found in a distorted octahedral coordination geometry, with a chloride ion and the oxygen atom of the amide carbonyl group occupying two ligand positions and completing the four coordinating nitrogen atoms of the cyclam ring. However, two different structures, with different configurations, were obtained, reflecting the presence of two isomers, named *trans-1* and *cis-1*. Four crystal structures of *trans-1* and two crystal structures of *cis-1* were solved (**Table A2.2 Table A2.3**). In *trans-1*, which crystallized in all solvents used, Cl and O ligands occupy the axial positions and are thus *trans* to each other with

respect to the Ni ion, while the four positions of the equatorial plane are occupied by the N atoms of the cyclam ring (**Figure 2.1a**). For the *cis-1* isomer, which crystallized in EtOH and DMF, Cl and O ligands are *cis* to each other: the equatorial plane is constituted by three N atoms of the cyclam ring (two secondary and one tertiary amines) and a Cl ligand while the apical positions are occupied by the O atom of the amide carbonyl group and the fourth N atom (one secondary amine) of the cyclam ring (**Figure 2.1b**). In the two isomers, the nickel ion, the tertiary nitrogen atom and the carbonyl oxygen atom are together part of a five-membered ring with two carbons from the dangling substituent. Each isomer is a racemic mixture of two enantiomers (only the *R,S,S,R trans-1* and the *S,S,S,S cis-1* are shown in **Figure 2.1**).

Bond lengths and angles values for all obtained crystal structures are given in **Table A2.3**. The Ni-O bond lengths are in the range of those of Ni-N (between 2.05 and 2.14 Å), while the Ni-Cl bond lengths (between 2.40 and 2.45 Å) are slightly longer. All these values are close to those of a similar octahedral [Ni(cyclam)(OH₂)(Cl)]Cl complex, previously reported by Zhanaidarova and al (Ni-O distance : 2.17 Å and Ni-Cl distance : 2.52 Å).^[18]

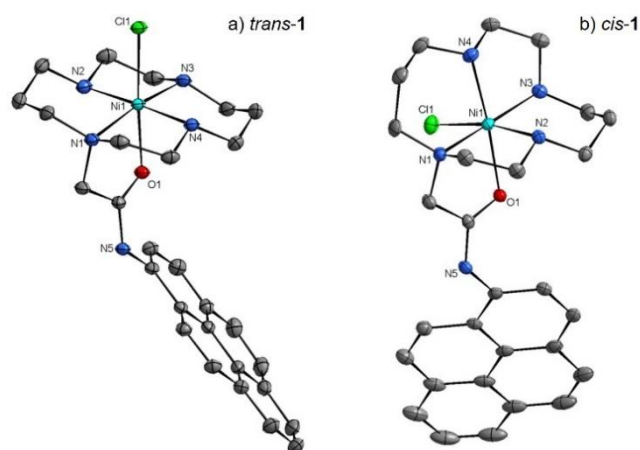


Figure 2.1 Crystal structure representation of the cation part of complex **1**. Ellipsoids are drawn with 30% probability. All hydrogen atoms are omitted for the sake of clarity. (a) *R,S,S,R trans-1* (from crystallization in MeCN); (b) *S,S,S,S cis-1* (from crystallization in DMF). Only one of the enantiomers is shown in both cases.

In the following experiments, complex **1** refers to a mixture of the two isomers. (At a later time, however, we were able to separate the two enantiomers and characterize them individually via CV, **Figure A2.4**).

The electrochemical properties of complex **1** were studied in DMF, with all potentials vs. Fc⁺/Fc⁰. **Figure 2.2** (dotted, dashed and black) shows the complex cyclic voltammograms (CVs) of complex **1** (1 mM) in DMF with 0.1 M TBAPF₆ as a supporting electrolyte on a glassy

carbon disk (3 mm diameter) as a working electrode, under an argon atmosphere, when scanned down to either -2.38, -2.62 or -3.1V. The ligand itself is redox-active due to the presence of pyrene.^[20] The first feature at -2.28 V was assigned to the one-electron reduction of Ni^{II} to Ni^I, approximately 180 mV more cathodic than for the unfunctionalized [Ni(cyclam)]²⁺ complex peaking at -2.1 V (**Figure 2.2**, red), in agreement with a much more electron-enriched Ni center in complex **1** due to the presence of extra electron-donating ligands. As a confirmation of this assignment to the metal site, this feature was absent on the CV of the unmetallated pyren-cyclam ligand, **L1** (**Figure 2.2**, blue). This signal is irreversible in all CVs even when reversing the scan immediately after the reduction peak, in contrast to that of [Ni(cyclam)]²⁺ (**Figure 2.2**). This indicates de-coordination of Cl or/and O ligands upon reduction. Quite often, a small shoulder was present at -2.1 V, likely corresponding to a very small amount of the complex without Cl/O coordination, likely in equilibrium with complex **1** in solution. A second complex irreversible feature appeared at slightly more cathodic potential (from -2.38 to -2.65 V) and proved difficult to assign. It could possibly have contributions in part from the one-electron reduction of the pyrene ring, even though the pyren-cyclam ligand, **L1**, exhibits a reversible signal in this potential region (**Figure 2.2**, blue). Finally, upon scanning down to below -3.0 V, a signal at -2.86 V was observed and assigned to Ni^I to Ni⁰ reduction. This signal is indeed absent within the CV of the unmetallated pyrene-cyclam ligand and is also present in the CV of [Ni(cyclam)]²⁺ upon scanning at a potential (- 2.55 V) allowing Ni^I to Ni⁰ conversion (**Figure 2.3**). On the oxidizing return scan, the feature at + 0.2 V, also found in the unmetallated pyren-cyclam ligand, is assigned to ligand oxidation (**Figure 2.2**). The broad signal at -0.66 V was exclusively seen after scanning down to a very negative potential, and not when the cathodic scan was reversed after the second reduction wave at - 2.62 V. This is consistent with Ni⁰ species generated at negative potentials and adsorbing on the surface of the electrode where they get oxidized to Ni^{II} at -0.66 V during the back scan. A similar situation was observed with the unfunctionalized [Ni(cyclam)]²⁺ complex when scanning down to very negative potentials (**Figure 2.3**).

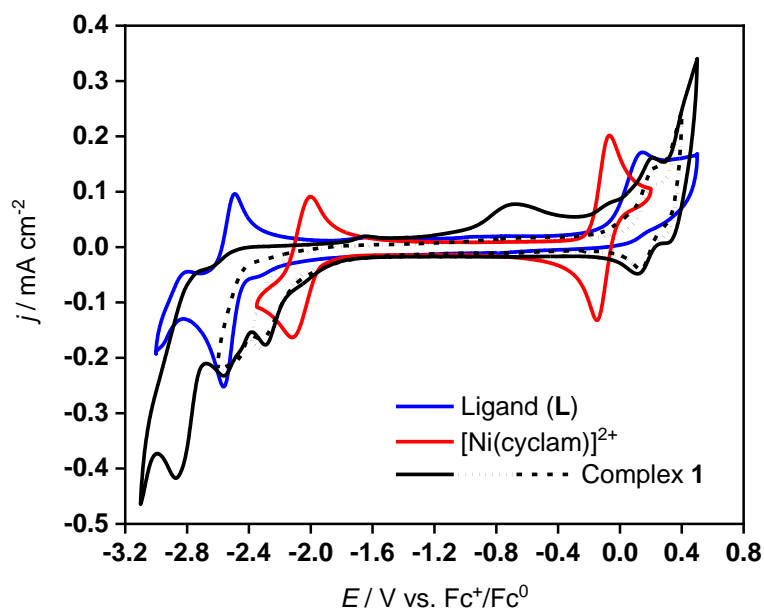


Figure 2.2 Cyclic voltammograms of complex **1**, $[\text{Ni}^{\text{II}}(\text{Cl})(\text{L}1)]^+$ (black, dashed and dotted), $[\text{Ni}(\text{cyclam})]^{2+}$ (red), ligand (**L1**, blue). Conditions: DMF with 0.1M TBAPF_6 as the electrolyte, under Ar and at room temperature. Concentrations were 1 mM for all species. Scan rate 100 mV s^{-1} .

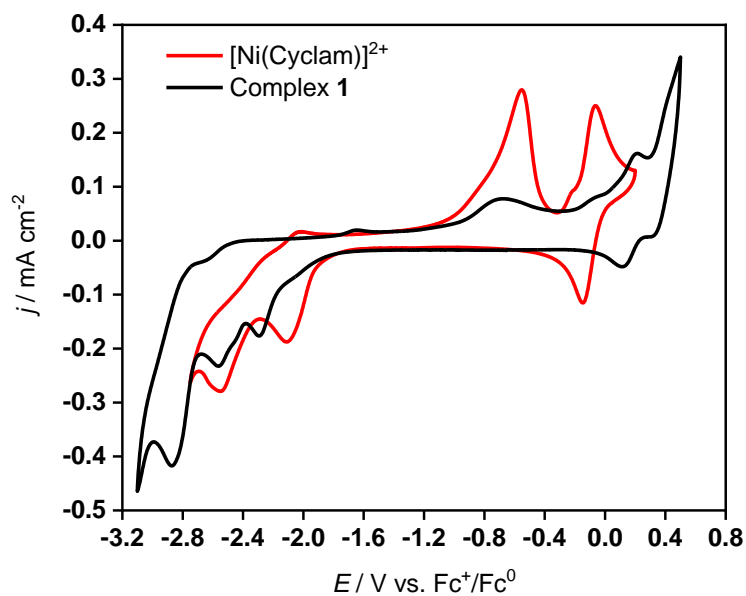


Figure 2.3 Cyclic voltammograms of 1 mM complex **1** (black) and 1 mM $[\text{Ni}(\text{Cyclam})]^{2+}$ (red). Conditions: DMF with 0.1M TBAPF_6 as the electrolyte, under Ar and at room temperature. Scan rate 100 mV s^{-1} .

As a further control of the effect of the coordination around the Ni center, we added one equivalent of AgPF₆ to the electrolyte solution in the presence of 1 mM complex **1** and stirred for one hour. After this time, the CV indicated that the first reduction from Ni^{II} to Ni^I in complex **1** was anodically shifted by about 180 mV to around -2.1V, corresponding to the unfunctionalized [Ni(cyclam)]²⁺. Conversely to [Ni(cyclam)]²⁺, however, this reduction was not reversible in complex **1**. Additionally, the second reduction feature previously observed for complex **1** and attributed to a one-electron reduction of the pyrene moiety was seemingly affected by the addition of AgPF₆, resulting in a cathodic shift of about 100 mV.

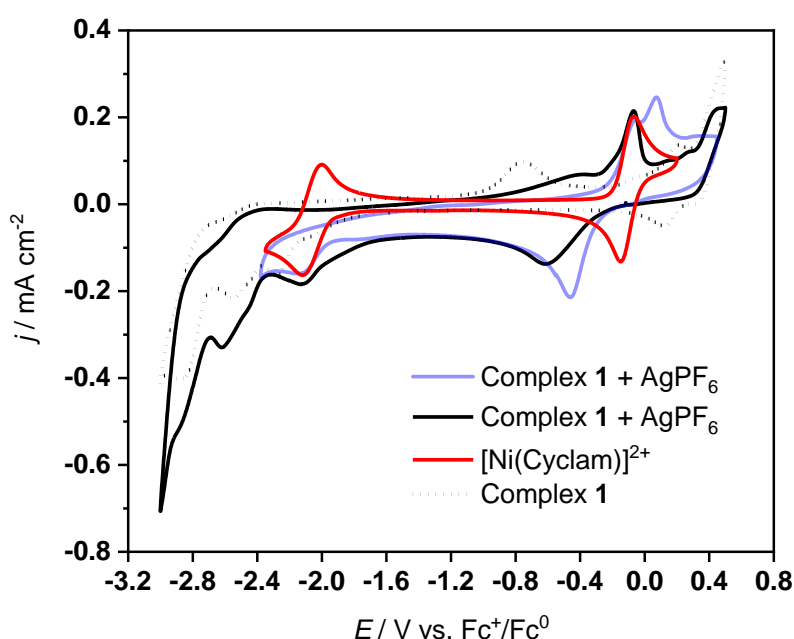


Figure 2.4 Cyclic voltammograms of 1 mM complex **1** (dotted), 1 mM [Ni(Cyclam)]²⁺ (red) and 1mM complex **1** in presence of AgPF₆ (black and mauve). Conditions: DMF with 0.1M TBAPF₆ as the electrolyte, under Ar and at room temperature. Scan rate 100 mV s⁻¹.

The cathodic peak current density (j_p) at -2.28 V varied linearly with the square root of the scan rate ($v^{1/2}$) from 0.01 to 0.5 Vs⁻¹ under Ar, consistent with diffusion-controlled processes and thus with active complex **1** remaining in solution (**Figure 2.5**). We also verified that no adsorption of the complex occurred at the surface of the GC electrode. Indeed, when, after 30 cycles of CV, the electrode was removed from the electrolyte and used in a fresh electrolyte without complex **1**, no signal corresponding to complex **1** could be observed in the CV.

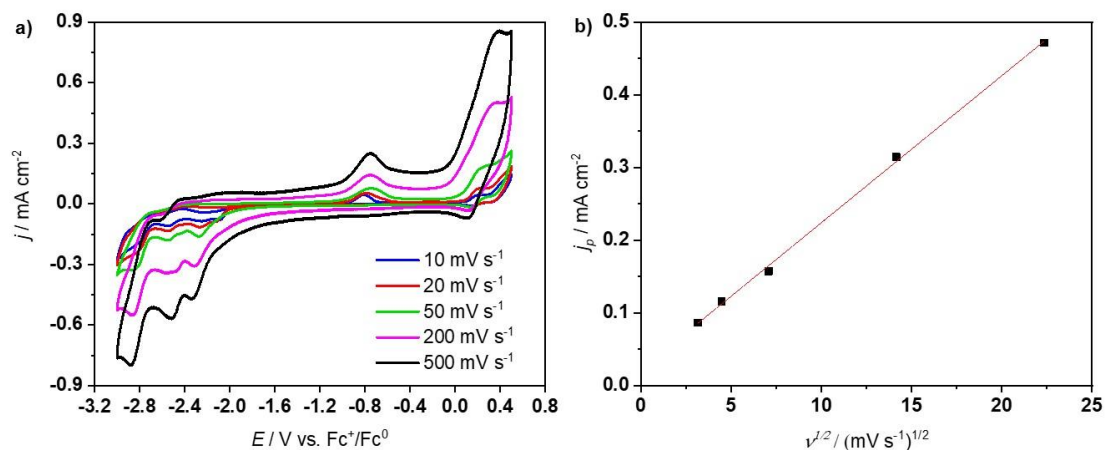


Figure 2.5 (a) CV of 1 mM complex **1** (DMF with 0.1M TBAPF₆ as the electrolyte, under Ar and at room temperature) at different scan rates and (b) plot of the cathodic peak current at -2.28 V as a function of the square root of the scan rates.

2.2.2 CO₂ reduction catalyzed by complex **1** in homogeneous conditions

Upon addition of CO₂, in the absence of a source of protons, the CV of 1 mM complex **1** (**Figure 2.6**) presented a small catalytic wave with an increase of current density and a potential at half-peak catalytic current of about -2.16 V, more anodic than that of the Ni^{II}/Ni^I signal and with an onset potential close to that of [Ni(cyclam)]²⁺. In line with previous reports on CO₂ electroreduction catalyzed by [Ni(cyclam)]²⁺, this wave is assigned to the catalytic reduction of CO₂ to CO during which reduction of Ni^{II} to Ni^I promotes de-coordination of Cl/O ligands and allows Ni^I to bind and activate CO₂ within a liberated coordination site.^[21]

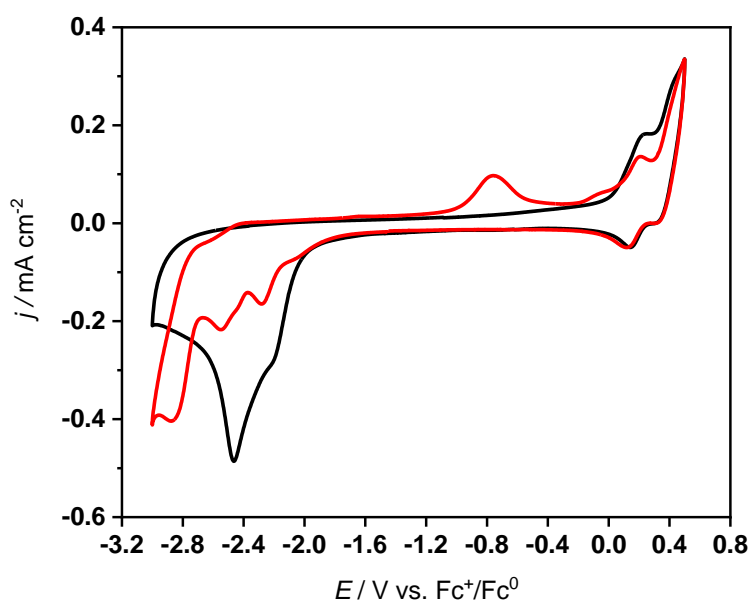


Figure 2.6 CV of complex **1** (1 mM) in Ar-saturated (red) and CO₂-saturated (black) DMF with 0.1M TBAPF₆ at room temperature. Scan rate 100 mV s⁻¹

However, given the importance of protons in the CO₂RR in general and specifically for CO₂RR catalyzed by [Ni(cyclam)]²⁺,^[22] the effect of increased concentrations of H₂O was studied by CV and bulk electrolysis. As expected, the catalytic current increased further upon addition of H₂O, from 0.4 M to 2 M (**Figure 2.7a**).

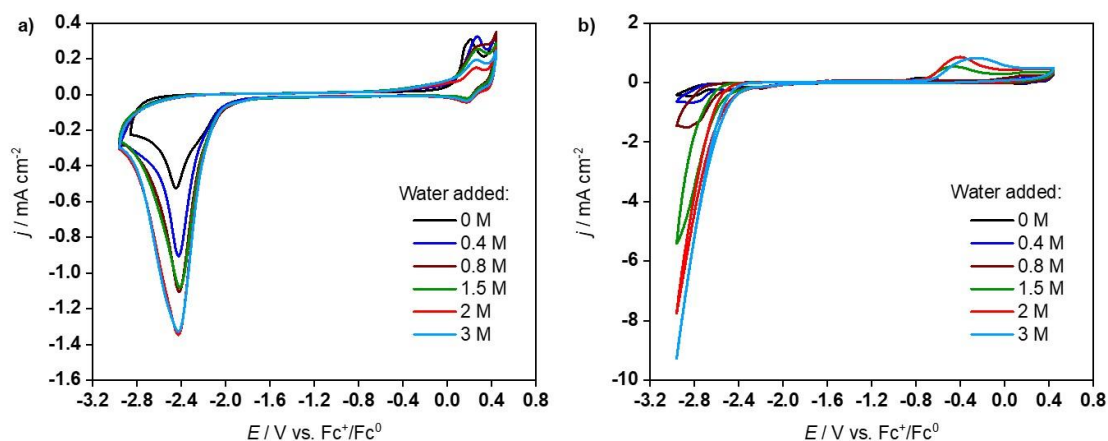


Figure 2.7 CVs of **1** (1 mM) in DMF with 0.1M TBAPF₆ and increasing concentrations of H₂O under CO₂ (a) and under Ar (b) at room temperature. Scan rate 100 mV s⁻¹. Same colors have been used for the same H₂O concentrations in both figures.

Considering a CO₂/CO reduction potential in a DMF–water solvent mixture at -1.41 V vs. Fc⁺/Fc⁰ (CO/CO₂ potential is reported to be -0.690 V vs. NHE^[23] and the Fc⁺/Fc⁰ potential is reported to be 0.720 V vs. NHE in DMF),^[24] the observed onset potential at -2.15 V corresponds to an overpotential of about 740 mV. In the absence of CO₂, a catalytic current, assigned to proton reduction to hydrogen, also increased upon increasing the concentration of H₂O (**Figure 2.7b**), however with an onset potential more cathodic than that for CO₂ reduction. This reflects the greater potential of complex **1** to catalyze the reduction of CO₂. Catalysis was similarly stimulated when using 2,2,2-Trifluoroethanol (TFE) as a proton source (**Figure A2.5**). In the following experiments, however, only H₂O was considered as the proton source.

A controlled-potential electrolysis (CPE) was then carried out at -2.39 V during which reaction products were analyzed and quantified, either by gas chromatography (for CO and H₂), by Ionic Exchange Chromatography (for HCOOH) and ¹H NMR (for CH₃OH). For that purpose, the electrochemical cell used a 1 cm² GC plate as the working electrode and the electrolyte was a solution of complex **1** (1 mM) in CO₂-saturated DMF containing 0.1 M TBAPF₆ and 2 M H₂O as a proton source. CVs obtained with such a cell reproduced nicely the above CVs (**Figure 2.8a**). After 60 minutes electrolysis (**Figure 2.8b**), CO was found as the only reaction product in the gaseous phase (faradaic yield: 96%) and no formate could be detected in the liquid phase. The catalyst proved quite robust during 1 hour electrolysis as shown from the stability of the current density, while its activity is limited as shown by the low current density (0.3 mA.cm⁻²). As a further proof of the stability of the catalyst, a CV recorded after CPE was found to be comparable to that before electrolysis, except for a small decrease in intensity (**Figure 2.8a**). The same experiment but in the absence of complex **1** did not yield any CO₂ reduction products.

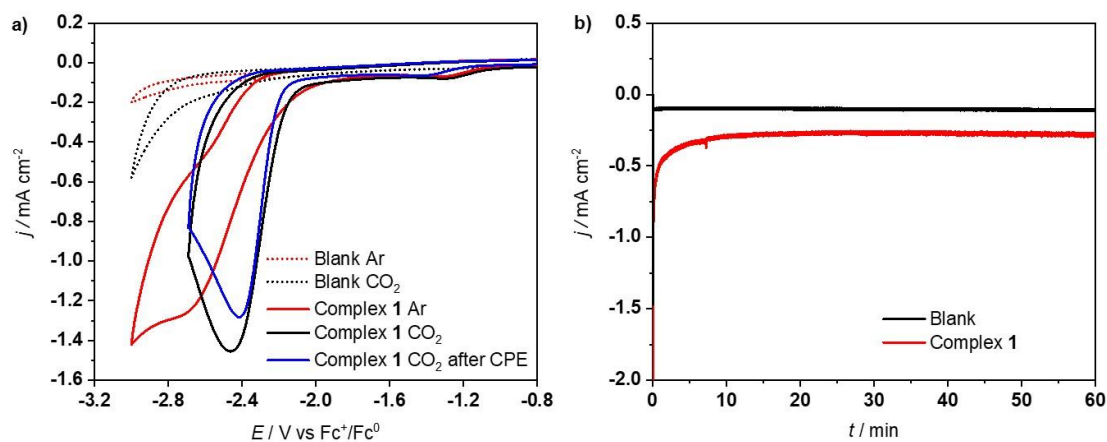


Figure 2.8 (a) CVs of **1** (1 mM) in DMF with 0.1M TBAPF₆ and H₂O 2M under CO₂ and under Ar at room temperature compared with a blank (absence of complex **1**). Scan rates 100 mV s⁻¹. (b) Controlled-potential electrolysis at -2.39 V vs. Fc⁺/Fc⁰ under the same conditions.

2.2.3 Immobilization of complex 1: preparation of the hybrid electrode, characterization, and CO₂ electroreduction

Complex **1** was physisorbed on MWCNTs through the establishment of π - π stacking interactions between the pyrene moieties and graphene motifs. In a first step, MWCNTs (2 mg) were first sonicated in ethanol in the presence of Nafion, then drop-casted on a 1 cm² surface of commercial gas diffusion layer (GDL), consisting of a carbon fibers cloth coated with a micro-porous Teflon layer embedding carbon black so as to keep electronic conductivity properties. Then the MWCNT/GDL electrode was dipped into a solution of 10 mM complex **1** in DMF, left overnight and then washed with water and acetonitrile to remove any loosely bound complexes, and finally air-dried before electrochemical experiments.

The **1**/MWCNT/GDL electrode was characterized by Scanning Electronic Microscopy (SEM) and X-ray photoelectron spectroscopy (XPS). As shown in **Figure 2.9**, a porous network of MWCNTs was observed in SEM images after functionalization. XPS analysis (survey spectrum) confirms the presence of Ni and N atoms, from complex **1**, on the surface of the electrode, together with O atoms from alcohol or carboxylic acid defects of pristine MWCNTs (**Figure 2.10** and **Table A2.1**). A Ni 2p_{3/2} signal is observed at 855.9 eV in good agreement with the presence of a Ni^{II} ion. Since there is fluoride in the deposited materials coming from Nafion with the F auger peak masking the Ni 2p signal at 861.47 eV, a control MWCNT/GDL electrode in the absence of complex **1** has been also analysed by XPS (**Figure 2.10c** and **Table A2.1**). The peak decomposition allowed to identify the signal of Ni 2p and the ratio of N/Ni is 4.5 approximately, whereas the N 1s peak was centered at 400.4 eV.

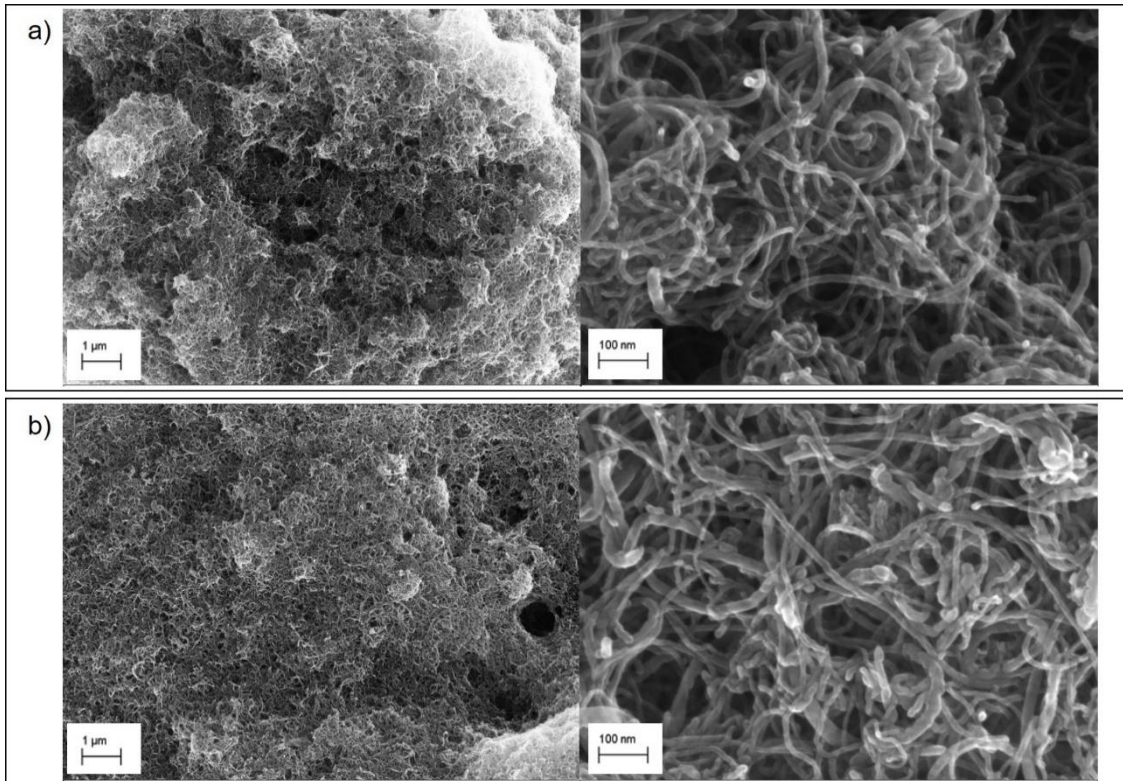


Figure 2.9 SEM images of 1/MWCNT/GDL electrode (a) before and (b) after 4h CPE.

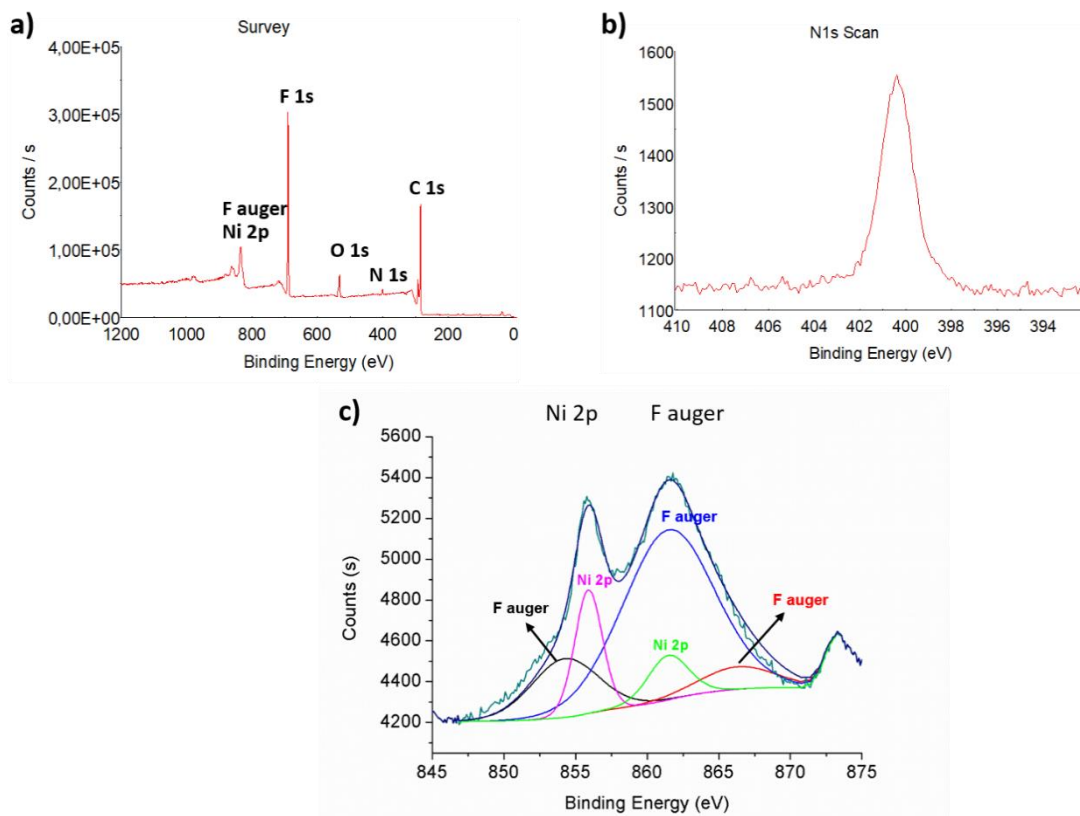


Figure 2.10 XPS survey spectrum of 1/MWCNT/GDL electrode (a), high resolution XPS spectra of N 1s (b), Ni 2p and F auger (c).

The 1/MWCNT/GDL electrode was also characterized by Cyclic Voltammetry. CVs were recorded in MeCN containing 0.1M TBAPF₆, using such 1/MWCNT/GDL electrode (**Figure 2.11a**). The high capacitive currents observed in the voltammograms are explained by the 3D structure of the working electrodes. Integration of the signal at -1.7 V vs. Fc⁺/Fc⁰ corresponding to Ni reoxidation from Ni^I to Ni^{II} allowed to determine a concentration of electroactive species for the complex of $5 \cdot 10^{-9}$ mol cm⁻² (see experimental section). Such a value is in line with previously reported values for MWCNTs functionalized with molecular Ni complexes.^[25] The intensity of that peak was directly proportional to the scan rate, thus confirming the immobilization of the nickel complex onto the electrode surface (**Figure 2.11b**).

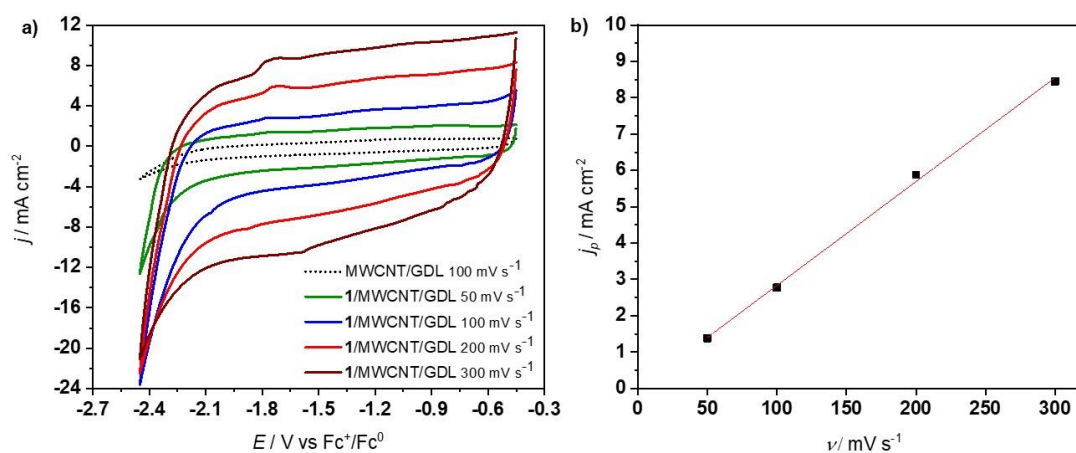


Figure 2.11 (a) CV of 1/MWCNT/GDL (acetonitrile with 0.1M TBAPF₆ as the electrolyte, under Ar and at room temperature) at different scan rates and (b) plot of the anodic peak current at -2.28 V as a function of the square root of the scan rates.

The electrochemical reduction of CO₂ using the new electrode material was carried out in MeCN containing 0.1M TBAPF₆ as the electrolyte, in the presence of 1% H₂O as a proton source, after saturation with CO₂. A linear sweep voltammogram (LSV) shows a catalytic wave occurring at more anodic potentials as compared to the MWCNT/GDL control electrode (**Figure 2.12a**).

Chronoamperometric measurements were carried out at various potentials from -2.34 to -2.74 V vs. Fc⁺/Fc⁰ for 20 min (**Figure 2.12b**). The current density proved stable in all cases. As a matter of fact, the same electrode could be used for several independent electrolysis experiments without any loss of activity. The CO₂ reduction products distribution, in terms of faradaic yields (FY), is shown in **Figure 2.12c**. CO was the major product at all potentials, with

the highest FY value (92%) obtained at -2.54 V vs. Fc^+/Fc^0 (with a current density of $6 \text{ mA}\cdot\text{cm}^{-2}$). In all cases H_2 accounted for less than 15% and no formate could be detected. As a control experiment, CPE using a MWCNT/GDL electrode was performed at -2.54 V vs. Fc^+/Fc^0 during 20 min (**Figure A2.6**). Not only the current density was much lower ($2.3 \text{ mA}\cdot\text{cm}^{-2}$) but the system was selective for H_2 production instead (FY= 83% with a FY for CO of 4%). As a further control experiment, a CPE of 1/MWCNT/GDL at -2.54 V vs. Fc^+/Fc^0 was also run under Ar. Only H_2 was produced after 20 min.

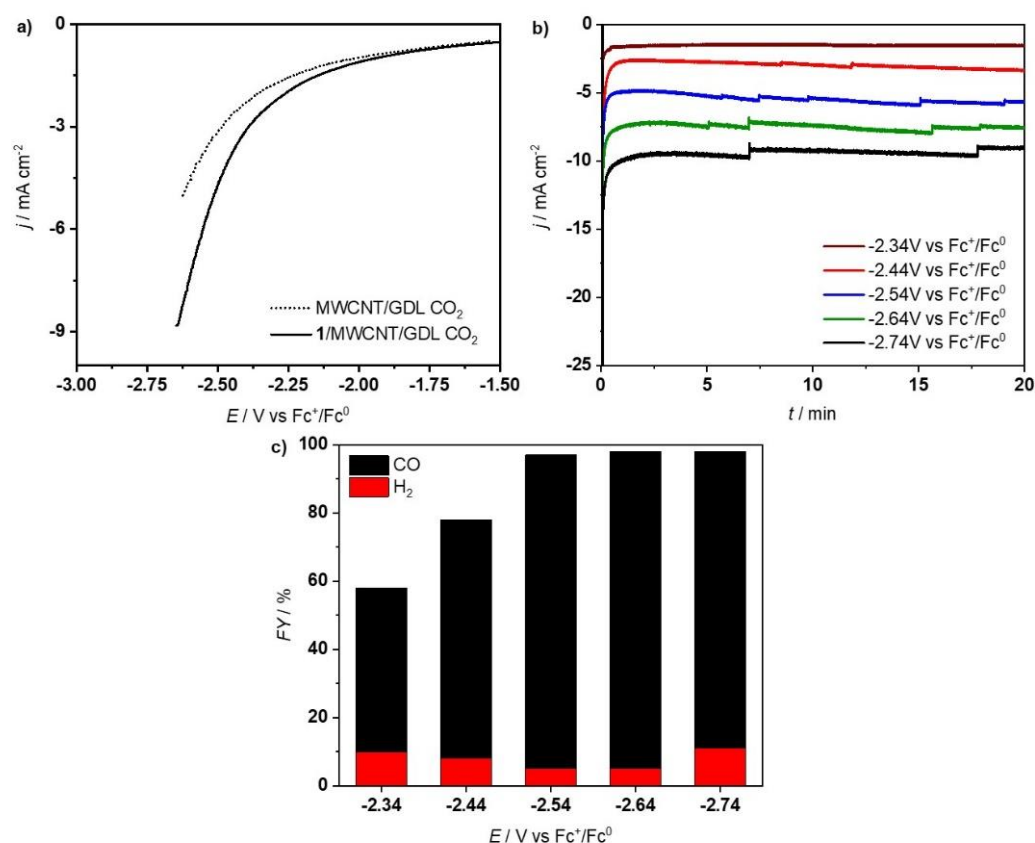


Figure 2.12 (a) LSV of 1/MWCNT/GDL (black) and MWCNT/GDL (dotted) in acetonitrile with TBAPF₆ 0.1 M and H₂O 1% under CO₂. Scan rate 10 mV s⁻¹. (b) Controlled Potential Electrolysis using 1/MWCNT/GDL as the electrode at different potentials under the same conditions. (c) Faradaic yields for CO and H₂ after 20 min electrolysis at different potentials.

A longer experiment (4h) carried out at -2.54 V vs. Fc^+/Fc^0 using the 1/MWCNT/GDL electrode under CO₂ confirmed the stability of the catalytic material as well of its selectivity with a FY for CO of more than 90% after 4h electrolysis (**Figure 2.13**). SEM analysis after 4h electrolysis showed no substantial change in the structure of the electrode (**Figure 2.9b**). XPS analysis of the sample showed the presence of Ni (**Figure 2.14**). Based on the number of electroactive sites

on the surface of the electrode ($5 \times 10^{-9} \text{ mol cm}^{-2}$), a remarkable Turnover Number for CO formation of 61460 was obtained after 4 h electrolysis, corresponding to a Turnover Frequency value of 4.27 s^{-1} .

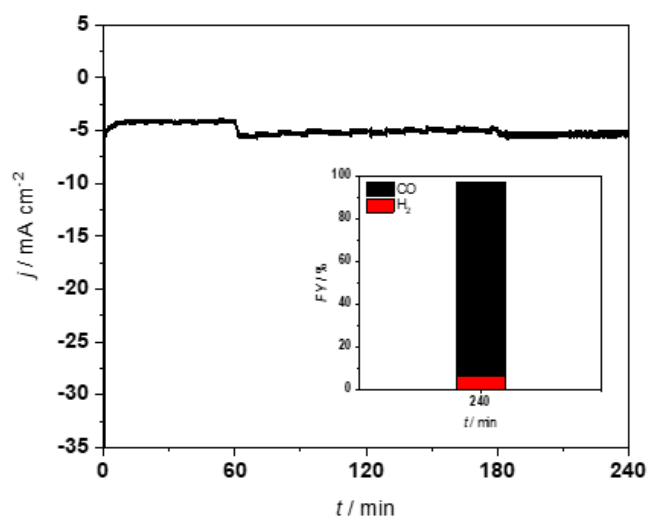


Figure 2.13 Controlled-Potential Electrolysis at -2.54 V vs. Fc^+/Fc^0 using 1-MWCNT/GDL in acetonitrile with 0.1 M TBAPF_6 and $1\% \text{ H}_2\text{O}$. Inset: Faradaic yields for CO and H₂ after 4h electrolysis.

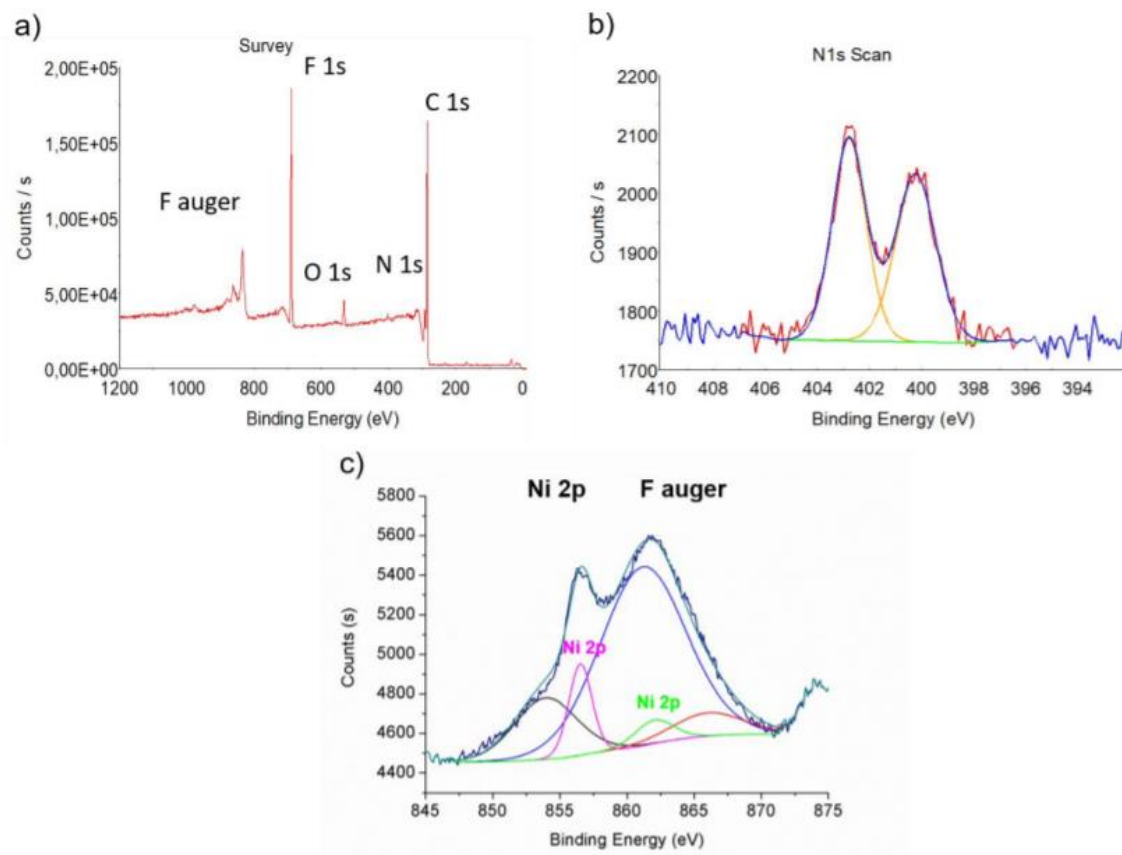


Figure 2.14 X-ray photoelectron spectra of 1/MWCNT/GDL electrode after long-term electrolysis of CO₂ in acetonitrile with 0.1M TBAPF₆ and 1% H₂O. XPS survey spectrum (a), high resolution XPS spectra of N1s (b), Ni 2p and F Auger (c).

Finally, CPE experiments were carried out at -2.14 and -2.24 V vs. Fc⁺/Fc⁰ for 20 min in MeCN with 0.1M TBAPF₆ with increased amounts of water (3% and 5%). The system became less selective for CO₂ reduction (**Figure 2.15**). When CPE was run at -2.54 V, the FY for CO was reduced to 22 and 12% for 3 v% and 5v% of water, respectively.

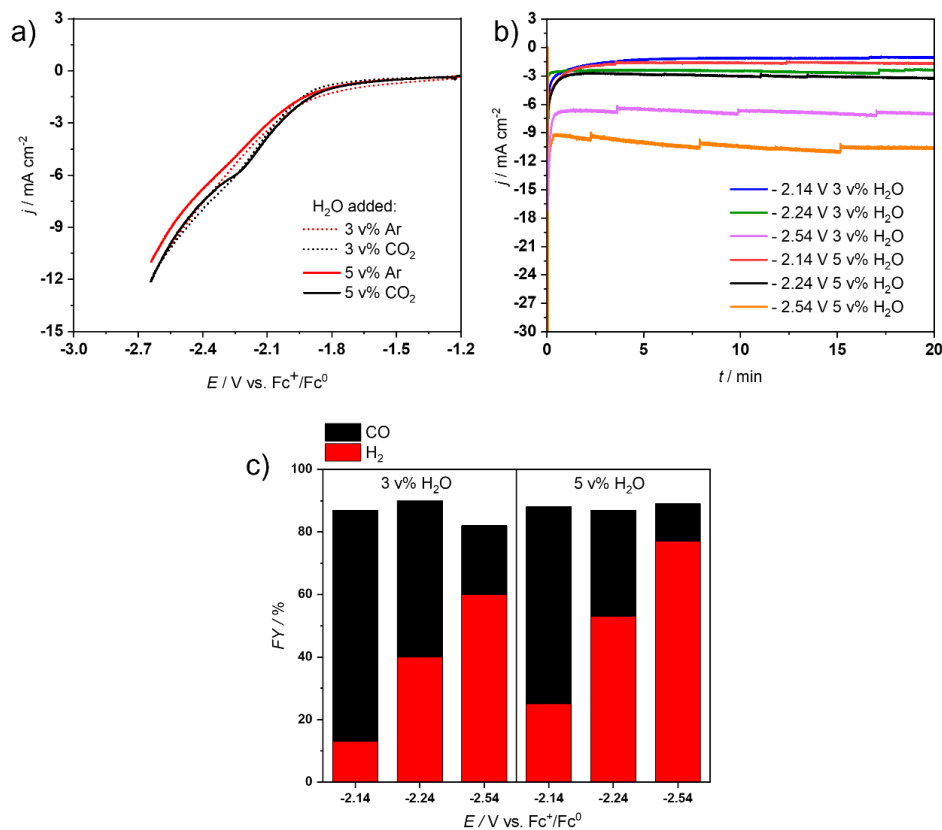


Figure 2.15 (a) LSVs of 1/MWCNT/GDL in MeCN with 3 v% (dotted) and 5 v% water (solid) with TBAPF₆ 0.1 M under CO₂ or Ar. Scan rate 10 mV s⁻¹. (b) Controlled Potential Electrolysis using 1/MWCNT/GDL at different potentials under the same conditions. (c) Faradaic yields for CO and H₂ after 20 min electrolysis at different potentials under the same conditions with 1/MWCNT/GDL.

2.2.4 CO₂ electroreduction in aqueous conditions

The electrochemical reduction of CO₂ using 1/MWCNTs/GDL was carried out in water containing 0.1M KHCO₃ as the electrolyte, under a constant flux of CO₂ (5 ml/min). The best selectivity was achieved at -0.6 and -0.8 V vs RHE (FY for CO 44 and 48% respectively), but H₂ was the major product at more negative potentials (**Figure 2.16**). This is nevertheless a quite remarkable result since at moderately cathodic potentials, thus at an overpotential of only 490 mV (being E^o CO₂/CO in water -0.11 V vs RHE at pH 7)^[26], the grafted molecular catalyst affords a 1:1 mixture of CO and H₂ at a current density of ~3 mA cm⁻². So far, relatively few molecular catalysts were shown to have the potential to catalyse the reduction of CO₂ in water.^[10]

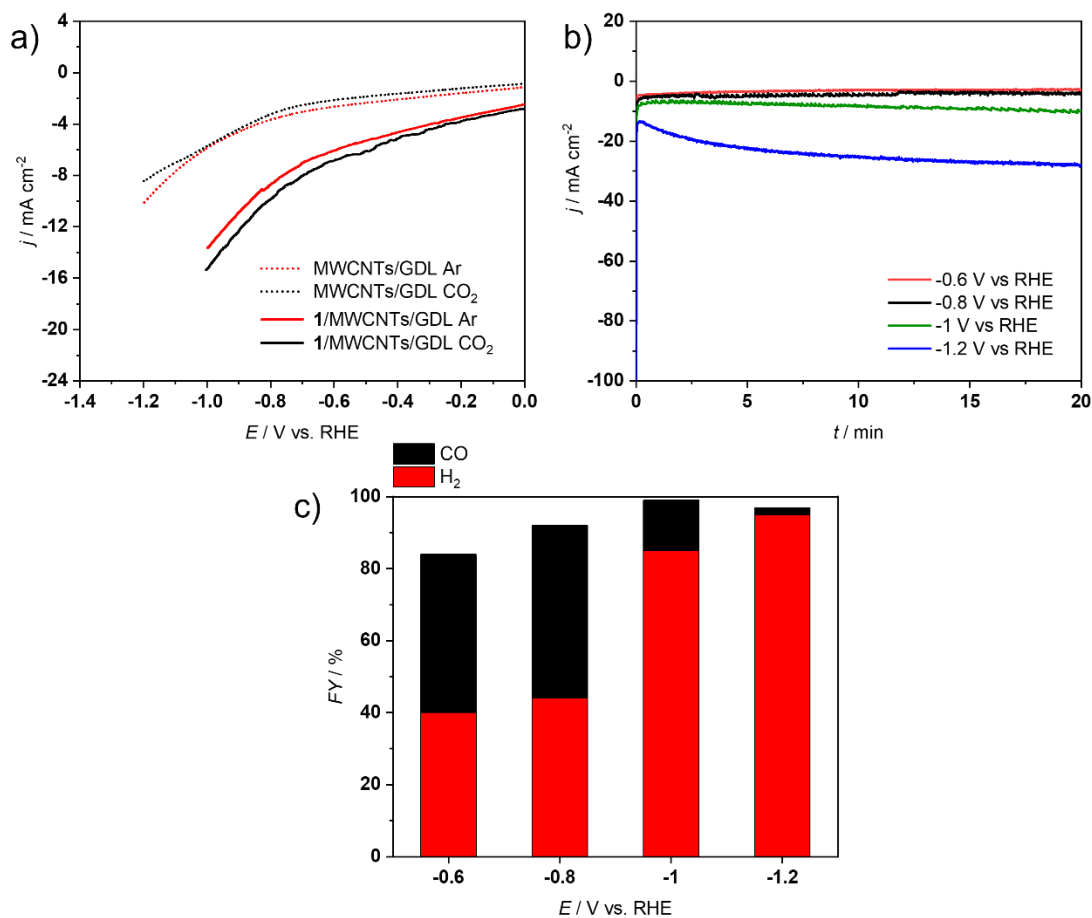


Figure 2.16 (a) LSVs of 1/MWCNT/GDL (black and red) and MWCNT/GDL (dotted) in water with KHCO₃ 0.1 M under CO₂ or Ar. Scan rate 50 mV s⁻¹. (b) Controlled Potential Electrolysis using 1/MWCNT/GDL at different potentials under the same conditions. (c) Faradaic yields for CO and H₂ after 20 min electrolysis at different potentials under the same conditions with 1/MWCNT/GDL.

2.3 Discussion

For the sake of immobilizing a [Ni(cyclam)]²⁺ complex at the surface of an electrode, a novel cyclam derivative bearing a pyrene moiety has been readily synthesized. This class of complexes have been chosen not only because [Ni(cyclam)]²⁺ is known to be a good, stable and selective molecular catalyst for CO₂ electroreduction and is based on a non-noble metal but also because, to our knowledge, there is only one precedent for carbon electrode surface modification with [Ni(cyclam)]²⁺^[18] and this hybrid material proved poorly efficient and less selective than its homogeneous counterpart. A [Ni(cyclam)]²⁺ complex modified with a carboxylic acid group was used to for grafting onto titanium(zirconium) oxide surfaces but the resulting material was only studied for its properties in photoelectron transfer.^[17]

The new complex **1** is a 6-coordinated Ni complex, in which the tetranuclear N-based coordination of the cyclam ring is completed by a chloride anion and the oxygen atom of the amide group of the dangling substituent, with two different configurations, *trans* and *cis*, with respect to the relative positions of the Cl and O ligands. Coordination to a Ni^{II} center by the oxygen atom of a pendant amide group has been recently reported in the case of substituted cyclen complexes of Ni^{II}.^[27] Complex **1** is thus the first [Ni(cyclam)]²⁺ complex carrying a pyrene substituent.

Characterization of the electrochemical properties of complex **1** in DMF/H₂O using a glassy carbon electrode has revealed the following features. First, upon one-electron reduction of Ni^{II} to Ni^I, the complex enjoys decoordination of the Cl/O ligand(s); this is very important since the Ni^I state is the active species for CO₂ binding and activation, a process that requires a free Ni coordination site. Second, catalysis for CO₂ electroreduction occurs at the Ni^{II} / Ni^I redox process, as shown by cyclic voltammetry, which indicates that the mechanism of the reaction catalyzed by complex **1** follows that of [Ni(cyclam)]²⁺.^[28] Third, as in the case of [Ni(cyclam)]²⁺ CO₂ reduction catalyzed by complex **1** is very selective for CO production (FY = 96%). Fourth, as expected, the activity is quite weak, providing only small current densities; indeed, [Ni(cyclam)]²⁺ has been shown to be poorly catalytically active when using a glassy carbon electrode, while the best activities were obtained using a mercury electrode, on which the complex adsorbs and enjoys an increased reactivity both in organic and aqueous electrolytes.^[22,28,29]

The pyrene-modified complex **1** has been immobilized on carbon nanotube-coated gas diffusion electrode using a non-covalent approach and the novel electrode, **1**/MWCNT/GDL, has been characterized electrochemically for CO₂ electroreduction. Under such a heterogenized configuration, complex **1** retained its high selectivity for CO production (FY above 90%), with H₂ accounting for less than 15%. More interestingly, it was shown to be much more active in the immobilized form than under homogeneous conditions: current densities up to 10 mA.cm⁻² could be obtained as compared to 0.3 mA.cm⁻² for a 1 mM solution of complex **1**. Finally, the derivatized electrode proved highly stable leading to impressive turnover numbers (61460 after 4 h electrolysis). This is remarkable since the electrode support is carbon-based and not mercury, so far the best electrode material for CO₂ electroreduction catalysed by [Ni(cyclam)]²⁺: this might indicate that the stable interaction between complex **1** and the carbon surface of the MWCNTs specifically favors the most reactive conformations of the complex and disfavors CO poisoning, CO desorption being the turnover-limiting step of the catalytic

cycle, as does mercury for the soluble $[\text{Ni}(\text{cyclam})]^{2+}$ complex.^[29,30] As a consequence, complex **1** is a very efficient molecular catalyst, after immobilization onto an electrode surface, reported so far for CO_2 electroreduction, as discussed below.

The only previous attempt to graft a $[\text{Ni}(\text{cyclam})]^{2+}$ complex on a solid electrode (in that case a covalent grafting onto a glassy carbon electrode) was achieved by Kubiak and coworkers, using electrooxidation of a terminal alkyne attached to the cyclam ring.^[31] This led to a cathode material which proved poorly active (with current densities below $1 \text{ mA}\cdot\text{cm}^{-2}$) and poorly selective for CO_2 reduction to CO ($\text{FY}_{\text{CO}} = 7\%$; $\text{FY}_{\text{H}_2} = 89\%$) under potential and solvent conditions comparable to those used here. The present work thus represents a great improvement regarding the utilization of solid electrodes functionalized with $[\text{Ni}(\text{cyclam})]^{2+}$. This is due in great part to the large surface area and the nanostructuring of the CNTs support which allow a greater density of electroactive species. As a matter of fact, the **1**/MWCNT/GDL electrode is also much more efficient for CO_2 reduction to CO than a glassy carbon electrode functionalized with a $[\text{Re}(\text{bpy})(\text{CO})_3\text{Cl}]$ complex using the same pyrene-dependent approach: the latter could achieve only 58 TONs during 1 hour electrolysis, after which the activity was lost.^[14] Finally, the **1**/MWCNT/GDL electrode compares well with and complements the carbon nanotube-coated gas diffusion electrode derivatized with a molecular iridium pincer dihydride catalyst, which allows high TONs of formate with high selectivity from CO_2 electroreduction in aqueous electrolytes.^[16] The latter is a reference material with respect to carbon electrodes functionalized with a molecular catalyst for CO_2 reduction. Indeed, while $[\text{Mn}(\text{bpy})(\text{CO})_3\text{Br}]$ was also attached to MWCNTs via π - π interactions of a pyrene group, present in a bpy ligand derivative, with the CNT sidewalls, the resulting material proved much less active (low current densities), less stable, less selective (giving a mixture of CO and HCOOH together with H_2 as the major product) and achieving a few thousands TONs after 8 h electrolysis under aqueous conditions.^[15]

Among the best performing pyrene-modified complexes that convert CO_2 to CO in water, a Fe triphenyl porphyrin described by Maurin and Robert^[32] was shown to operate at 480 mV overpotential. Comparable values were found employing **1**/MWCNT/GDL in aqueous medium, albeit with a lower selectivity for CO, in favor of a more pronounced hydrogen evolution. On this regard, it was observed that the alkylation of one of the N atoms of the cyclam ring could lead to decisive effects on the catalyst stability and selectivity,^[33-36] although the exact reason for such effects has not yet been completely clarified. Verifying that this effect could also occur

when [Ni(cyclam)]²⁺ is heterogenized may therefore represent a starting point for further improvements on the performance of this catalyst.

2.4 Conclusion

In this chapter, we have reported the synthesis and characterization of a novel Ni-Cyclam-pyrene complex for heterogeneous molecular CO₂ electroreduction. The first steps of the synthetic process were improved so to increase yields and avoid arduous chromatography purification. The unique 6-coordinated Ni cyclam complex is, to the best of our knowledge, the first [Ni(cyclam)]²⁺ complex carrying a pyrene substituent.

After the heterogenization on MWCNTs of the pyrene-modified complex using a non-covalent approach, the electrode was characterized electrochemically for CO₂ electroreduction. Interestingly, the complex proved to be much more active in the immobilized form than under homogeneous conditions, with Faradaic Yields for CO production above 90% and current densities up to 10 mA.cm⁻² in acetonitrile/water mixture.

Finally, the derivatized electrode proved highly stable leading to impressive turnover numbers (61460 after 4 h electrolysis). Although the hybrid electrodes did not maintain a high selectivity for CO when utilized in aqueous conditions, the present study shows that the [Ni(cyclam)]²⁺ complex can provide an excellent platform on which further improvements of hybrid electrodes can be brought.

2.5 Experimental Section

General

All starting materials were commercially available (Sigma and TCI) and were used without further purification. Solvents were purified by an MBRAUN SPS-800 Solvent Purification System. All reactions were carried out under air atmosphere unless specified. ^1H and NMR spectra were recorded on a Bruker Avance-III 300 NMR spectrometer (300 MHz) at room temperature. UV-Vis spectra were recorded using a Cary 100 UV-Vis spectrophotometer instrument (Agilent).

Synthesis of Complex **1**

2-Chloro-N-pyren-1-yl-acetamide (4). The synthesis was carried on as previously described with slight modifications.^[37] Under an Ar atmosphere, 1-aminopyrene (5.45 g, 25.1 mmol) and triethylamine (5.6 mL, 40.1 mmol) were dissolved in CH_2Cl_2 (500 mL), and chloroacetyl chloride (2.8 mL, 35.1 mmol) was added dropwise via a syringe. After 12 h of stirring under Ar, the precipitate was filtered, washed with H_2O and cold CH_2Cl_2 several times. The crude product was dried under vacuum over night to yield the product as a pale-grey powder which was used for the next step without further purification (5.49 g, 74%).

^1H NMR (CDCl_3 , 300 MHz) δ 9.01 (br s, 1H), 8.45 (d, $J = 8.3$ Hz, 1H), 8.21-8.14 (m, 4H), 8.07-7.99 (m, 4H), 4.42 (s, 2H). This spectrum is identical to the reported one.^[37]

N-Pyren-1-yl-2-(1,4,8,11-tetraazacyclotetradec-1-yl)-acetamide (L1). This ligand was synthesized according to a reported method with slight modifications.^[19] Under an Ar atmosphere, a mixture of cyclam (3.25 g, 16.2 mmol), 2-chloro-*N*-pyren-1-yl-acetamide (**4**) (940 mg, 3.2 mmol), K_2CO_3 (2.24 g, 16.2 mmol) and KI (270 mg, 1.6 mmol) in MeCN (677 mL) was heated under reflux. After 24 h, the solvent was evaporated under reduced pressure and the residue was washed with water and ether several times. The crude product was dried under vacuum overnight to yield the product as an off-white powder which was used for the next step without further purification (1.46 g, 94%).

^1H NMR (CDCl_3) δ 11.4 (br s, 1H), 8.27 (d, $J = 9.3$ Hz, 1H), 8.19-7.96 (m, 8H), 3.44 (s, 2H), 2.90 (t, $J = 5.4$ Hz, 2H), 2.80 (m, 8H), 2.42 (t, $J = 5.1$ Hz, 2H), 2.3 (t, $J = 5.1$ Hz, 2H), 2.12 (m, 2H), 1.95 (m, 2H), 1.49 (m, 2H). This spectrum is identical to the reported one.^[19]

Complex [Ni^{II}(Cl)(L1)]Cl (1). A solution of **L1** (100 mg, 0.11 mmol) in EtOH (2 mL) was added dropwise to a solution of NiCl₂·6H₂O (52 mg, 0.11 mmol) in EtOH (2 mL). The pale green solution turned immediately to orange then dark pink. After 3h at room temperature, the solvent was evaporated to dryness and the blue-pink solid was dissolved in EtOH (6 mL) and ether was allowed to slowly diffuse to this solution to give complex **1** as a pink-purple powder (78 mg, 61%).

UV-Vis [DMF]: λ nm (ϵ , M⁻¹ cm⁻¹): 543 (10.7), 389 (1880), 353 (10920), 343 (15000), 329 (10000), 277 (16300), 266 (11060).

Single crystals suitable for X-ray diffraction were obtained by slow diffusion of Et₂O into a solution of DMF containing **1** at room temperature. MeCN, EtOH and CH₂Cl₂ were also used instead of DMF giving suitable single crystals. CCDC 2021920 (*trans*-**1**, MeCN), 2021925 (*trans*-**1**, EtOH), 2021922 (*trans*-**1**, DMF), 2021923 (*trans*-**1**, DCM), 2021921 (*cis*-**1**, EtOH) and 2021924 (*cis*-**1**, DMF) contain the supplementary crystallographic data for this study.

Homogeneous Electrochemical Studies

All electrochemical experiments were performed on a VSP300 potentiostat (Bio-Logic Science Instruments SAS) and were conducted at room temperature in *N,N*-Dimethylformamide (DMF). 0.1 M tetrabutylammonium hexafluorophosphate (TBAPF₆) was used as the supporting electrolyte. The cyclic voltammetry (CV) experiments were carried out in a three electrode setup (**Figure 2.17**), with a 3 mm diameter glassy carbon (GC) electrode as a working electrode, which was polished on a polishing cloth with a 1 μ m diamond suspension (Struers), sonicated for 10 seconds, thoroughly rinsed with ethanol and dried prior to experiments. Platinum wire was used as a counter electrode and was previously flame annealed. The reference electrode was an Ag/AgCl electrode in a saturated KCl solution, equipped with a bridge to allow operation in organic solvent. All potentials were calibrated using the ferrocene/ferrocenium (Fc⁺⁰) redox couple as an internal standard, which was added in solution at the end of each measurement. In DMF, $E_{1/2}$ (Fc⁺/Fc⁰) = 0.60V vs Ag/AgCl/sat. KCl. Only the second cycle of all CVs are shown, although no difference in consecutive scans has been observed.

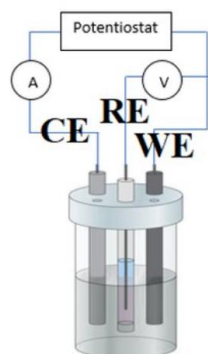


Figure 2.17 Three electrode setup used for the homogeneous electrochemical studies.

Controlled potential electrolysis (CPE) experiments were carried out in a gas-tight two-compartment electrochemical cell (**Figure 2.18**) with two ceramic-PVDF composite membranes (16 μm thickness, Xuran) separating the anodic and cathodic compartments. The working electrode was a 1 cm^2 glassy carbon plate, the counter electrode was a platinum mesh and the reference electrode was an Ag/AgCl electrode in a saturated KCl solution, equipped with a bridge to allow operation in organic solvent. Anolyte and catholyte contained DMF and 2 M of H_2O as the proton source and 0.1 M of TBAPF_6 as the electrolyte. Only in the catholyte 1 mM of complex **1** was added. Both solution compartments were saturated with CO_2 during at least 20 minutes before starting the electrolysis, but no more gas was bubbled during the electrolysis. The experiments were conducted at room temperature under stirring at the cathode side. The volume of solution held by the cell in total was 22.6 mL, with ca. 10.6 mL of total headspace volume.

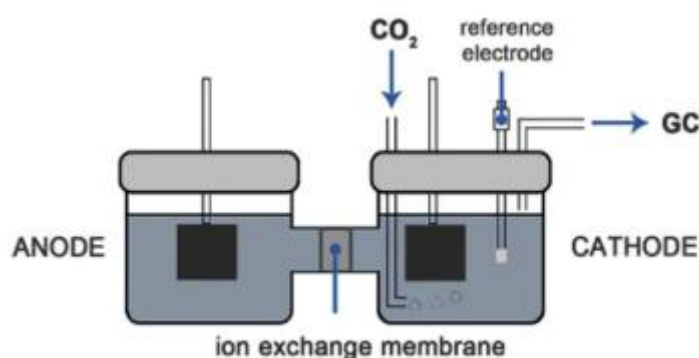


Figure 2.18 H-shape cell setup used for the heterogeneous electrochemical studies.

Gas products were quantified by gas chromatography (Model 8610C SRI Instruments) equipped with TCD and FID detectors from 50 μL aliquots of the headspace of the cathode compartments. Hydrogen (H_2) and carbon monoxide (CO) were detected by thermal

conductivity detector (TCD) and flame ionization detector (FID), respectively. Liquid products were evaluated using an ionic exchange chromatograph (Metrohm 883 Basic IC) equipped with a Metrosep A Supp 5 column and a conductivity detector.

The faradaic yields were calculated by quantifying the products in the head-space gas of the cathodic side, on the basis of Equation 1:

$$\text{Faradaic efficiency} = \frac{N \times F \times n}{Q} \times 100 \quad (1)$$

Where Q, F, and N represented the charge passed through the system (C), Faraday's constant (C mol⁻¹), and moles of H₂/CO generated, respectively. In the reaction process, 2 moles of electrons were consumed to produce 1 mole of product, therefore $n = 2$.

Electrodes preparation and characterization

The electrodes used a 3 cm x 1 cm gas diffusion layer (GDL, AVCarb GDS 3250, Fuel Cell Store) strip, which was briefly sonicated in EtOH and let dry in air before utilization. MWCNTs (Sigma) were used after acid treatment as following: the raw MWCNTs material were dispersed in H₂SO₄ (2 M), sonicated for 1 h at ambient temperature, washed repeatedly with H₂O, then EtOH and dried in a vacuum oven at 70°C overnight. This acid treated MWCNTs (2 mg) were sonicated for at least 30 min in EtOH (200 μl) containing a solution of Nafion perfluorinated resin (5 μl of a 5 wt% solution in mixture of lower aliphatic alcohols containing 5% water). The suspension was then drop-casted on the GDL (1 cm² deposit) and dried in air at 70°C for at least 30 min. Subsequently, the GDL-MWCNT electrode was immersed in a solution of complex **1** in DMF (10 mM) overnight on an orbital shaker at low speed. Finally, the electrode was dried, washed with water then acetonitrile and dried in air.

SEM images were acquired using a Hitachi S-4800 scanning electron microscope. X-ray photoelectron spectra (XPS) were collected using a Thermo Electron Escalab 250 spectrometer with a monochromated Al Kα radiation (1486.6 eV). The analyzer pass energy was 100 eV for survey spectra and 20 eV for high resolution spectra. The analysed area was 500 mm². The photoelectron take-off angle (angle between the surface and the direction in which the photoelectrons are analysed) was 90°. Curve fitting of the spectra was performed with the Thermo Electron software Advantage.

The electroactive sites were calculated through the integration of the oxidation wave in the CV scan (**Figure 2.11**) according to Equation 2:

$$\Gamma Ni = \frac{q}{nFA} \quad (2)$$

Where ΓNi is the number of electroactive sites (mol cm^{-2}), q is the charge (C) obtained from the integration of the oxidation wave, n the number of electrons in the redox process per Ni center ($n = 1$), F is the Faraday constant (96485 C mol^{-1}), and A is the geometrical electrode area (1 cm^2).^[15]

Heterogeneous Electrochemical Studies (organic medium)

Linear sweep voltammetry (LSV) was performed for each sample before CPE, first under Ar and successively under CO_2 . Gas was bubbled in the solution for at least 20 minutes before each experiment. The scan rate was 10 mV s^{-1} . CPE experiments were carried out in a gas-tight H-shape cell (**Figure 2.18**) in which cathode and reference electrode are separated from the anode by an anion exchange membrane (AMV Selemion, ACG Engineering). The solvent used was acetonitrile containing 1% of H_2O , and the electrolyte was TBAPF_6 0.1 M. The cathode used was a GDL on which MWCNs with the complex **1** were drop-casted as described above, the anode was platinum and the reference electrode was an Ag/AgCl electrode in a saturated KCl solution, equipped with a bridge to allow operation in organic solvent. All potentials were calibrated using the ferrocene/ferrocenium ($\text{Fc}^{+/0}$) redox couple as an internal standard, which was added in solution at the end of each measurement. In acetonitrile, $E_{1/2}(\text{Fc}^{+}/\text{Fc}^0) = 0.54 \text{ V}$ vs Ag/AgCl/sat. KCl. CO_2 gas was bubbled in the solution for at least 20 minutes before each experiment and no more gas was bubbled during the electrolysis. The experiments were conducted at room temperature and under stirring at the cathode side. The volume of solution held by the cell in total was 22.6 mL, with ca. 10.6 mL of total headspace volume.

The electrolysis products (hydrogen, CO and formate) were quantified in a similar manner as in the homogeneous electrochemical studies part. The faradaic yields were calculated by quantifying the products in the head-space gas of the cathodic side, on the basis of Equation 1 (see above).

The following formulas

$$TON = \frac{\text{moles of product}}{\text{moles of catalyst}} \quad (3)$$

and

$$TOF = \frac{TON}{\text{reaction time [s]}} \quad (4)$$

were used to calculate Turnover Number (TON) and Turnover Frequency (TOF) values, respectively.

Heterogeneous Electrochemical Studies (aqueous medium)

Linear sweep voltammetry (LSV) was performed for each sample before CPE, first under Ar and successively under CO₂. Gas was bubbled in the solution for at least 20 minutes before each experiment. The scan rate was 50 mV s⁻¹. CPE experiments were carried out in a gas-tight H-shape cell in which cathode and reference electrode are separated from the anode by an anion exchange membrane (AMV Selemion, ACG Engineering). The solvent used was H₂O, and the electrolyte was KHCO₃ 0.1 M. The cathode used was a GDL on which MWCNs with the complex **1** were drop-casted as described above, the anode was platinum and the reference electrode was an Ag/AgCl electrode in a saturated KCl solution. CO₂ gas was bubbled in the solution for at least 20 minutes before each experiment and a flux of CO₂ (5 mL/min) was kept during the electrolysis (only on the cathode side). The experiments were conducted at room temperature and under stirring at the cathode side.

The measured potentials vs. Ag/AgCl were converted to the reversible hydrogen electrode (RHE) scale according to the Nernst equation:

$$E_{RHE} = E_{Ag/AgCl} + 0.059 \text{ pH} + E^{\circ}_{Ag/AgCl} \quad (5)$$

where E_{RHE} is the converted potential vs. RHE, $E^{\circ}_{Ag/AgCl} = 0.1976$ at 25 °C (sat. KCl), and $E_{Ag/AgCl}$ is the experimentally measured potential against Ag/AgCl reference and the pH of a CO₂-saturated 0.1M KHCO₃ solution is ~ 6.8 (for 0.3 M KHCO₃ ~7.15 and 0.5 M KHCO₃ ~7.23).

The electrolysis products (hydrogen, CO and formate) were quantified in a similar manner as in the homogeneous electrochemical studies part. The faradaic yields were calculated by quantifying the products by gas chromatography (Model 8610C SRI Instruments) equipped with TCD and FID detectors, on the basis of Equation 1 (see above).

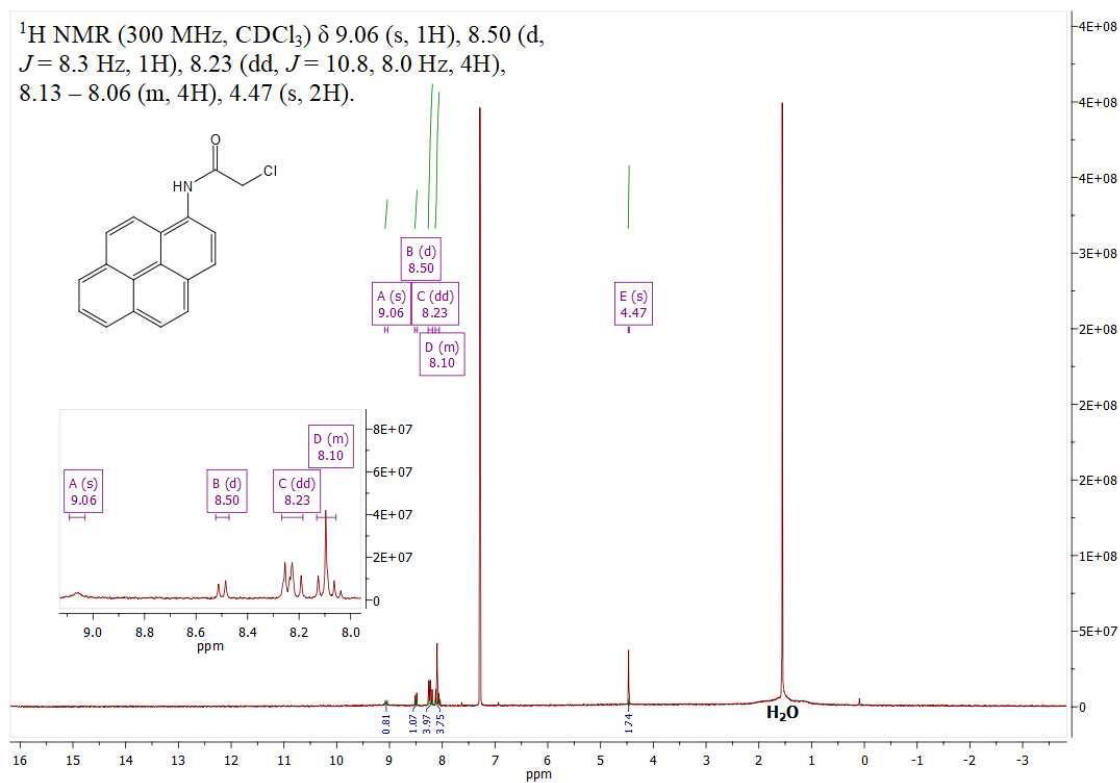
2.6 References

- [1] O. S. Bushuyev, P. De Luna, C. T. Dinh, L. Tao, G. Saur, J. van de Lagemaat, S. O. Kelley, E. H. Sargent, *Joule*, **2018**, 2, 825–832.
- [2] A. Liu, M. Gao, X. Ren, F. Meng, Y. Yang, L. Gao, Q. Yang, T. Ma, *J. Mater. Chem. A*, **2020**, 8, 3541–3562.
- [3] B. Kumar, J. P. Brian, V. Atla, S. Kumari, K. A. Bertram, R. T. White, J. M. Spurgeon, *Catal. Today*, **2016**, 270, 19–30.
- [4] D. Gao, F. Cai, G. Wang, X. Bao, *Curr. Opin. Green Sustain. Chem.*, **2017**, 3, 39–44.
- [5] R. Francke, B. Schille, M. Roemelt, *Chem. Rev.*, **2018**, 118, 4631–4701.
- [6] K. Elouarzaki, V. Kannan, V. Jose, H. S. Sabharwal, J. Lee, *Adv. Energy Mater.*, **2019**, 9, 1900090.
- [7] N. Elgrishi, M. B. Chambers, X. Wang, M. Fontecave, *Chem. Soc. Rev.*, **2017**, 46, 761–796.
- [8] C. Sun, R. Gobetto, C. Nervi, *New J. Chem.*, **2016**, 40, 5656–5661.
- [9] L. Sun, V. Reddu, A. C. Fisher, X. Wang, *Energy Environ. Sci.*, **2020**, 13, 374–403.
- [10] X. M. Hu, S. U. Pedersen, K. Daasbjerg, *Curr. Opin. Electrochem.*, **2019**, 15, 148–154.
- [11] Y. Wu, Z. Jiang, X. Lu, Y. Liang, H. Wang, *Nature*, **2019**, 575, 639–642.
- [12] X. Zhang, Z. Wu, X. Zhang, L. Li, Y. Li, H. Xu, X. Li, X. Yu, Z. Zhang, Y. Liang, H. Wang, *Nat. Commun.*, **2017**, 8, DOI 10.1038/ncomms14675.
- [13] X. Zhang, Y. Wang, M. Gu, M. Wang, Z. Zhang, W. Pan, Z. Jiang, H. Zheng, M. Lucero, H. Wang, G. E. Sterbinsky, et al., *Nat. Energy*, **2020**, 5, 684–692.
- [14] J. D. Blakemore, A. Gupta, J. J. Warren, B. S. Brunshwig, H. B. Gray, *J. Am. Chem. Soc.*, **2013**, 135, 30.
- [15] B. Reuillard, K. H. Ly, T. E. Rosser, M. F. Kuehnel, I. Zebger, E. Reisner, *J. Am. Chem. Soc.*, **2017**, 139, 14425–14435.
- [16] P. Kang, S. Zhang, T. J. Meyer, M. Brookhart, *Angew. Chemie - Int. Ed.*, **2014**, 53, 8709–8713.
- [17] G. Neri, J. J. Walsh, C. Wilson, A. Reynal, J. Y. C. Lim, X. Li, A. J. P. White, N. J. Long, J. R. Durrant, A. J. Cowan, *Phys. Chem. Chem. Phys.*, **2015**, 17, 1562–1566.
- [18] A. Zhanaidarova, C. E. Moore, M. Gembicky, C. P. Kubiak, *Chem. Commun.*, **2018**, 54, 4116–4119.
- [19] N. J. Youn, J. S. Kim, K. C. Song, S. H. Kim, S. Ahn, S. K. Chang, *Bull. Korean Chem. Soc.*, **2005**, 26, 849–851.
- [20] Y. Zhao, D. Xue, H. Qi, C. Zhang, *RSC Adv.*, **2017**, 7, 22882–22891.
- [21] J. D. Froehlich, C. P. Kubiak, *Inorg. Chem.*, **2012**, 51, 3932–3934.
- [22] J. D. Froehlich, C. P. Kubiak, *J. Am. Chem. Soc.*, **2015**, 137, 3565–3573.
- [23] C. Costentin, M. Robert, J.-M. Savéant, *Chem. Soc. Rev.*, **2013**, 42, 2423–2436.
- [24] S. Creager, *Handb. Electrochem.*, **2007**, p.101.
- [25] P. D. Tran, A. Le Goff, J. Heidkamp, B. Jusselme, N. Guillet, S. Palacin, H. Dau, M.

- Fontecave, V. Artero, *Angew. Chemie - Int. Ed.*, **2011**, *50*, 1371–1374.
- [26] M. Schreier, L. Curvat, F. Giordano, L. Steier, A. Abate, S. M. Zakeeruddin, J. Luo, M. T. Mayer, M. Grätzel, *Nat. Commun.*, **2015**, *6*, 1–6.
- [27] T. Qiu, G. P. A. Yap, J. Rosenthal, *ACS Appl. Energy Mater.*, **2019**, *2*, 8560–8569.
- [28] M. Beley, J. P. Collin, R. Ruppert, J. P. Sauvage, *J. Am. Chem. Soc.*, **1986**, *108*, 7461–7467.
- [29] Y. Wu, B. Rudshiteyn, A. Zhanaidarova, J. D. Froehlich, W. Ding, C. P. Kubiak, V. S. Batista, *ACS Catal.*, **2017**, *7*, 5282–5288.
- [30] J. Song, E. L. Klein, F. Neese, S. Ye, *Inorg. Chem.*, **2014**, *53*, 7500–7507.
- [31] A. Zhanaidarova, C. E. Moore, M. Gembicky, C. P. Kubiak, *Chem. Commun.*, **2018**, *54*, 4116–4119.
- [32] A. Maurin, M. Robert, *J. Am. Chem. Soc.*, **2016**, *138*, 2492–2495.
- [33] M. Fujihira, Y. Nakamura, Y. Hirata, U. Akiba, K. Suga, *Denki Kagaku oyobi Kogyo Butsuri Kagaku*, **1991**, *59*, 532–539.
- [34] E. Fujita, J. Haff, R. Sanzenbacher, H. Elias, *Inorg. Chem.*, **1994**, *33*, 4627–4628.
- [35] J. Costamagna, G. Ferraudi, J. Canales, J. Vargas, *Coord. Chem. Rev.*, **1996**, *148*, 221–248.
- [36] M. Aulice Scibioh, P. V Ragini, S. Rani, V. R. Vijayaraghavan, B. Viswanathan, Reduction of CO₂ by nickel (II) macrocycle catalyst at HMDE, in *Proc. Indian Acad. Sci. Chem. Sci.*, **2001**, pp. 343–350.
- [37] J. H. Kim, A. R. Hwang, S. K. Chang, *Tetrahedron Lett.*, **2004**, *45*, 7557–7561.

2.7 Appendix

Synthesis of complex 1

Figure A2.1 $^1\text{H NMR}$ (400 MHz, 25°C , CDCl_3) of 4

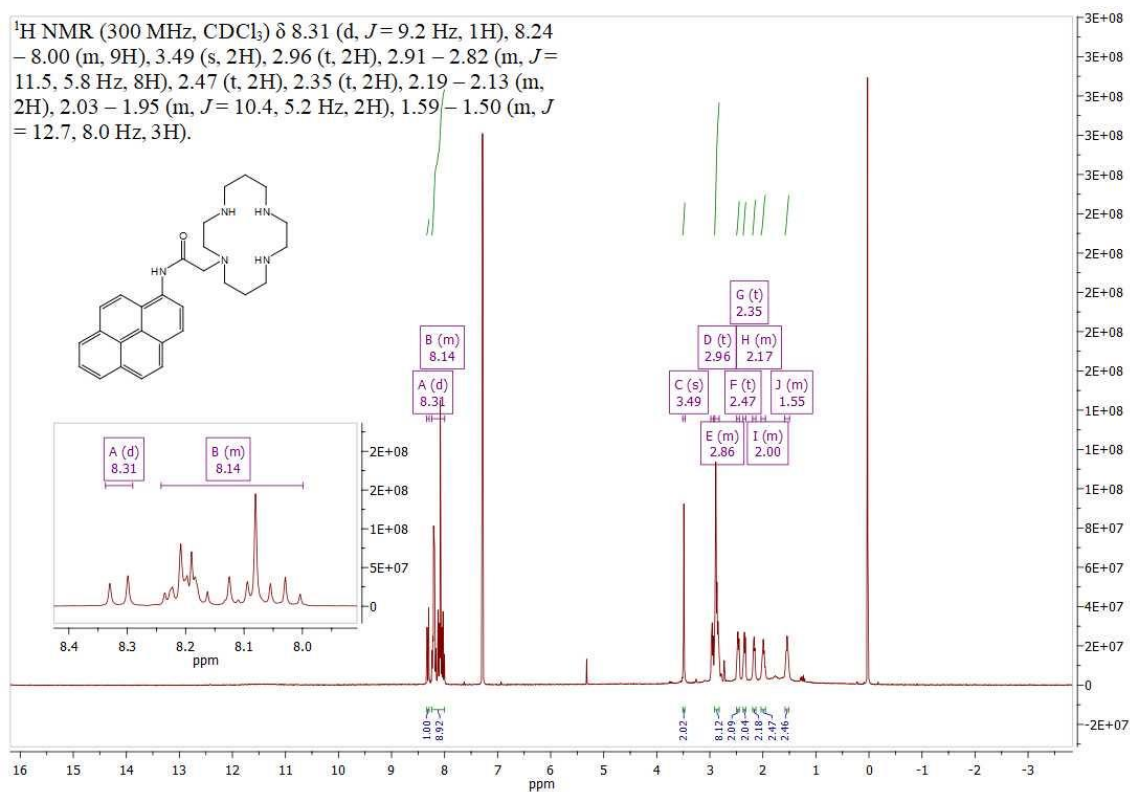


Figure A2.2 ¹H NMR (400 MHz, 25°C, CDCl₃) of L1

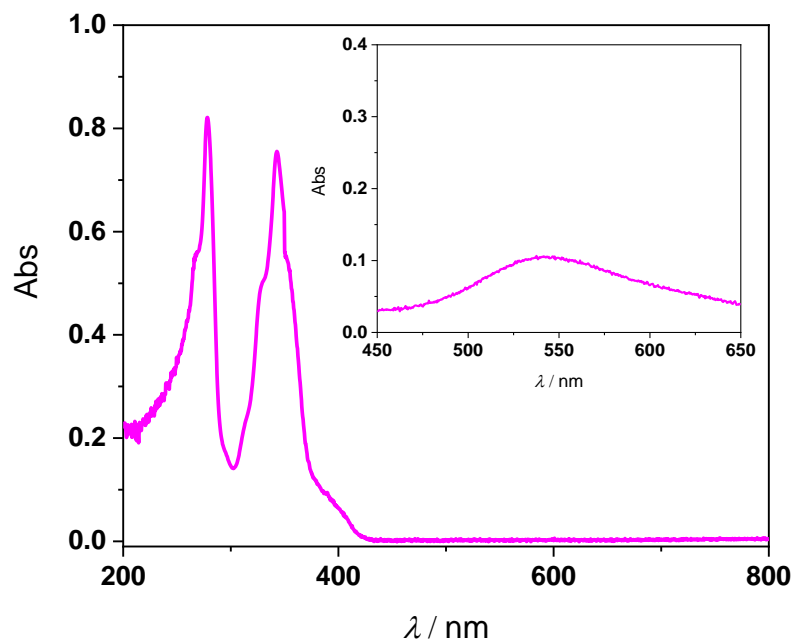


Figure A2.3 UV-Vis spectrum of complex 1 (25°C, DMF)

Homogeneous Electrochemical Studies of Complex 1

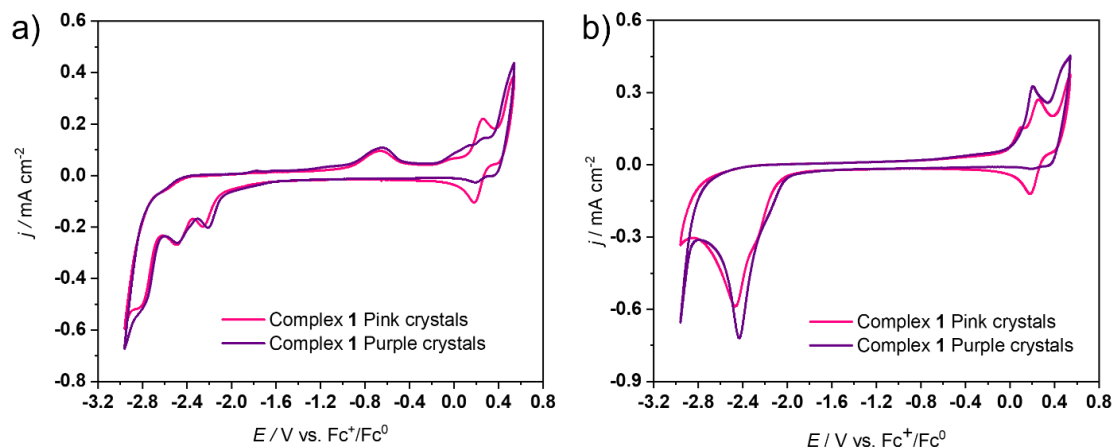


Figure A2.4 CVs of *cis*-1 (pink crystals) and *trans*-1 (purple crystals) 1 mM in DMF with 0.1M TBAPF₆ under Ar (a) and under CO₂ (b) at room temperature. Scan rate 100 mV s⁻¹.

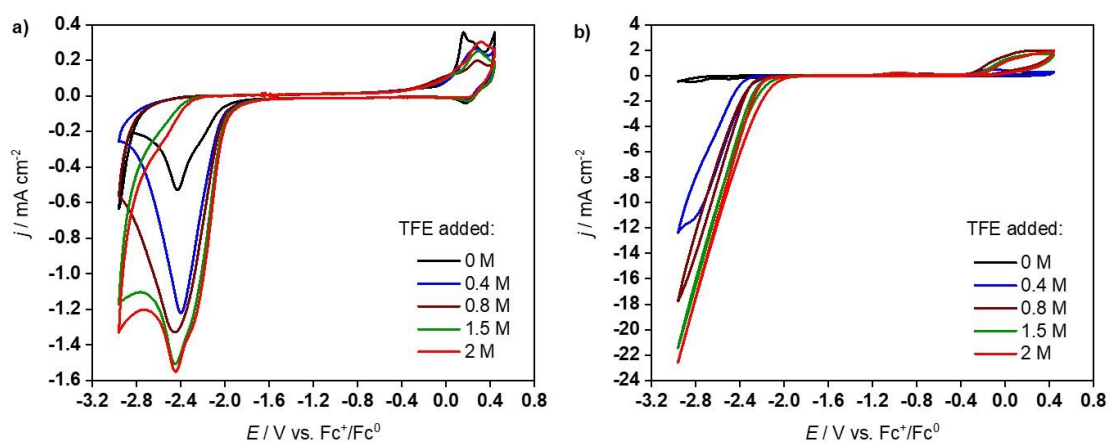


Figure A2.5 CVs of **1** (1 mM) in DMF with 0.1M TBAPF₆ and increasing concentrations of TFE under CO₂ (a) and under Ar (b) at room temperature. Scan rate 100 mV s⁻¹. Same colors have been used for the same TFE concentrations in both figures.

Heterogeneous Electrochemical Studies: 1/MWCNT/GDL electrode characterization

Table A2.1 XPS analysis of the functionalized 1/MWCNT/GDL electrode.

Name	Peak BE	FWHM eV	Area (P) CPS.eV	Atomic %
C1s	284.64	0.76	11102.59	52.13
C1s	292.07	1.23	1441.40	6.78
F1s	689.16	1.85	23178.81	29.91
N1s	400.38	1.66	824.14	2.38
O1s	532.31	2.06	3708.35	6.46
S2p	168.64	2.20	259.50	0.63
Si2p	102.25	1.68	156.49	0.79
F auger	854.26	5.45	1698.93	0.00
F auger	866.34	6.26	747.41	0.00
F auger	873.18	1.60	328.05	0.00
Ni2p3	855.90	2.28	1596.52	0.61
Ni2p3	861.47	3.36	792.95	0.32
F auger	861.48	7.53	6795.48	0.00

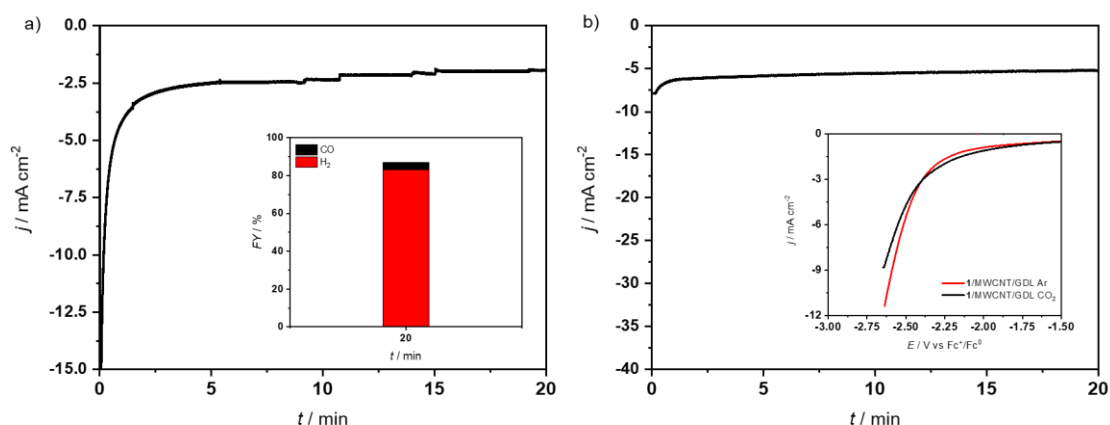
 Heterogeneous Electrochemical Studies: electroreduction of CO₂


Figure A2.6 a) Controlled-Potential Electrolysis at -2.54 V vs. Fc⁺/Fc⁰ of 1/MWCNT/GDL in acetonitrile with 0.1M TBAPF₆ and 1% H₂O under CO₂. Inset: Faradaic yields for CO and H₂ after 20 min electrolysis; b) Controlled-Potential Electrolysis at -2.54 V vs. Fc⁺/Fc⁰ of 1/MWCNT/GDL in acetonitrile with 0.1M TBAPF₆ and 1% H₂O under Ar. Inset: LSV of 1/MWCNT/GDL in acetonitrile with TBAPF₆ 0.1 M and H₂O 1% under CO₂ (black) and Ar (red). Scan rates 10 mV s⁻¹.

X-Ray crystal structure determination for complex 1

For complexes *trans-1* (MeCN) and *cis-1* (EtOH), a single crystal of each compound was selected, mounted onto a MiTeGen cryoloop and transferred into a cold nitrogen gas stream. Intensity data were collected with a Bruker Kappa APEX-II CCD diffractometer using a micro-focused Cu-K α radiation ($\lambda = 1.54178 \text{ \AA}$). Data collections were performed at 200K, with the Bruker APEXIII^[1] suite. Unit-cell parameters determinations, integrations and data reductions were carried out with SAINT^[1] program. SADABS^[2] was used for scaling and absorption corrections. The structures were solved with SHELXT^[3] and refined by full-matrix least-squares methods with SHELXL^[4] using Olex2 software package.^[5] All non-hydrogen atoms were refined anisotropically. In *cis-1* (EtOH) crystal structure, 1.5 hydrogen atoms are not represented because of a symmetry problem, but they are added in the molecular formula. These structures were deposited at the Cambridge Crystallographic Data Centre with numbers CCDC 2021920 and 2021921 respectively and can be obtained free of charge via www.ccdc.cam.ac.uk.

For complexes *trans-1* (DMF), *trans-1* (DCM) and *cis-1* (DMF), a single crystal of each compound was selected, mounted onto a MiTeGen cryoloop and transferred into a cold nitrogen gas stream. Intensity data were collected with a Bruker Kappa APEX-II CCD diffractometer using a graphite-monochromated Mo-K α radiation ($\lambda = 0.71073 \text{ \AA}$). Data collection were performed at 200K with the Bruker APEXII^[1] suite. Unit-cell parameters determination, integrations and data reductions were carried out with SAINT^[1] program. SADABS^[2] was used for scaling and absorption corrections. The structures were solved with SHELXT^[3] and refined by full-matrix least-squares methods with SHELXL^[4] using Olex2 software package^[5] or using WinGX suite^[6] for crystal *cis-1* (DMF). All non-hydrogen atoms were refined anisotropically. The *trans-1* (DMF) structure was refined as a 2-component twin with mass percentages of 67/33 around (Twin law: -100 0-10 00-1). These structures were deposited at the Cambridge Crystallographic Data Centre with numbers CCDC 2021922 to 2021924 respectively and can be obtained free of charge via www.ccdc.cam.ac.uk.

For complex *trans-1* (EtOH), a single crystal was selected, mounted onto a MiTeGen cryoloop and transferred into a cold nitrogen gas stream. Intensity data were collected with a Bruker Kappa APEX-II CCD diffractometer using a graphite-monochromated Mo-K α radiation ($\lambda = 0.71073 \text{ \AA}$). Data collection was performed at 200K with the Bruker APEXII^[1] suite. Unit-cell

parameters determination, integration and data reduction were carried out with SAINT^[1] program. SADABS^[2] was used for scaling and absorption correction. The structure was solved with SHELXT^[3] and refined by full-matrix least-squares methods with SHELXL^[4] using Olex2 software package^[5]. All non-hydrogen atoms were refined anisotropically. Molecules form large channels along the B-axis of crystal lattice. In these channels, unattributed residual electron density is present. It should be due to very disordered solvent molecules. A PLATON SQUEEZE^[7] procedure was applied on structure refinement to mask electron density of these very disordered solvent regions. Crystal was obtained with a mixture of solvents, so it is impossible to identify and quantify which ones are present in the crystal. The given chemical formula and other crystal data do not consider the unknown solvent molecules. This structure was deposited at the Cambridge Crystallographic Data Centre with number CCDC 2021925 and can be obtained free of charge via www.ccdc.cam.ac.uk.

Table A2.2 Crystallographic data for compounds *trans*-**1** and *cis*-**1**.

	<i>trans</i> - 1 (MeCN)	<i>trans</i> - 1 (EtOH)	<i>trans</i> - 1 (DMF)
CCDC deposit number	2021920	2021925	2021922
Empirical formula^a	C ₃₂ H ₄₁ N ₇ OCl ₂ Ni	C ₂₈ H ₃₅ N ₅ OCl ₂ Ni [+ solvent]	C _{30.5} H _{41.5} N _{5.5} O ₂ Cl ₂ Ni
Moiety formula	C ₂₈ H ₃₅ N ₅ OCINi ⁺ , Cl ⁻ , 2(C ₂ H ₃ N)	C ₂₈ H ₃₅ N ₅ OCINi ⁺ , Cl ⁻ , [+ solvent]	C ₂₈ H ₃₅ N ₅ OCINi ⁺ , Cl ⁻ , 0.25(H ₂ O), 0.25(C ₄ H ₁₀ O), 0.5(C ₃ H ₇ NO)
Formula weight (g/mol)	669.33	*587.22	646.80
Temperature (K)	200	200	200
Crystal system	Triclinic	Monoclinic	Orthorhombic
Space group	P-1	P2 ₁ /c	P2 ₁ 2 ₁ 2 ₁
a (Å)	11.2141(5)	14.1676(6)	14.840(5)
b (Å)	11.7279(5)	17.2428(6)	15.772(8)
c (Å)	12.4363(5)	15.5393(6)	28.055(16)
α (°)	85.021(2)	90	90
β (°)	82.258(2)	106.734(2)	90
γ (°)	88.018(2)	90	90
Volume (Å³)	1614.14(12)	3635.3(2)	6567(5)
Z	2	4	8
ρ_{calc} (g/cm³)	1.377	*1.073	1.308
Abs. coefficient μ (mm⁻¹)	2.684 (Cu Kα)	*0.704 (Mo Kα)	0.789 (Mo Kα)
F(000)	704.0	*1232.0	2728.0
Crystal size (mm³)	0.39 × 0.38 × 0.36	0.76 × 0.17 × 0.16	0.42 × 0.22 × 0.19
Wavelength λ (Å)	1.54178	0.71073	0.71073
2θ range (°)	6.214 – 133.276	3.002 – 57.818	2.962 – 54.336
Miller indexes ranges	-13 ≤ h ≤ 13, -13 ≤ k ≤ 13, -10 ≤ l ≤ 14	-18 ≤ h ≤ 19, -22 ≤ k ≤ 23, -21 ≤ l ≤ 20	-18 ≤ h ≤ 19, -20 ≤ k ≤ 20, -35 ≤ l ≤ 35
Measured reflections	36104	37215	114567
Unique reflections	5695	9525	14500
R_{int} / R_{sigma}	0.0367 / 0.0244	0.0453 / 0.0390	0.0442 / 0.0288
Reflections [I ≥ 2σ(I)]	5546	6521	11893
Restraints	0	2	62
Parameters	407	353	818
Goodness-of-fit F²	1.044	1.039	1.132
Final R indexes^{b c}	R1 = 0.0308	R1 = 0.0833	R1 = 0.0702
[all data]	wR2 = 0.0813	wR2 = 0.1285	wR2 = 0.1409
Final R indexes^{b c}	R1 = 0.0297	R1 = 0.0487	R1 = 0.0503
[I ≥ 2σ(I)]	wR2 = 0.0805)	wR2 = 0.1084	wR2 = 0.1268
Largest diff. peak/hole (e/Å³)	0.31/-0.32	1.16/-0.33	1.22/-0.37

	<i>trans</i> -1 (CH ₂ Cl ₂)	<i>cis</i> -1 (EtOH)	<i>cis</i> -1 (DMF)
CCDC deposit number	2021923	2021921	2021924
Empirical formula^a	C ₃₀ H _{39.4} N ₅ O _{1.2} Cl ₆ Ni	C ₂₉ H _{37.65} N ₅ O _{1.7} Cl ₂ Ni	C _{32.5} H _{51.5} N _{6.5} O _{5.5} Cl ₂ Ni
Moiety formula	C ₂₈ H ₃₅ N ₅ OCINi ⁺ , Cl ⁻ , 0.2(H ₂ O) 2(CH ₂ Cl ₂)	C ₂₈ H ₃₅ OCIN ₅ Ni ⁺ , Cl ⁻ , 0.2(H ₂ O), 0.5(C ₂ H ₆ O)	C ₂₈ H ₃₅ N ₅ OCINi ⁺ , Cl ⁻ , 3(H ₂ O), 1.5(C ₃ H ₇ NO)
Formula weight (g/mol)	760.67	615.35	750.91
Temperature (K)	200	200	200
Crystal system	Triclinic	Triclinic	Monoclinic
Space group	P-1	P-1	P21/c
a (Å)	11.303(3)	7.5639(2)	14.7363(6)
b (Å)	12.538(4)	9.5036(2)	21.2901(9)
c (Å)	14.076(4)	21.4966(5)	23.9216(10)
α (°)	109.237(5)	78.3510(10)	90
β (°)	108.202(5)	84.7790(10)	98.377(2)
γ (°)	94.727(6)	74.7780(10)	90
Volume (Å³)	1750.6(8)	1459.16(6)	7425.0(5)
Z	2	2	8
ρ_{calc} (g/cm³)	1.443	1.395	1.343
Abs. coefficient μ (mm⁻¹)	1.045 (Mo Kα)	2.913 (Cu Kα)	0.715 (Mo Kα)
F(000)	788.0	644.0	3184.0
Crystal size (mm³)	0.69 × 0.34 × 0.18	0.55 × 0.45 × 0.40	0.60 × 0.10 × 0.10
Wavelength λ (Å)	0.71073	1.54178	0.71073
2θ range (°)	3.806 – 61.054	8.406 – 133.254	2.572 – 52.744
Miller indexes ranges	-16 ≤ h ≤ 16, -17 ≤ k ≤ 17 -20 ≤ l ≤ 20	-8 ≤ h ≤ 8, -11 ≤ k ≤ 11, -25 ≤ l ≤ 25	-18 ≤ h ≤ 18, -26 ≤ k ≤ 26, -26 ≤ l ≤ 29
Measured reflections	101435	74728	109556
Unique reflections	10632	5153	15166
R_{int} / R_{sigma}	0.0257 / 0.0135	0.0406 / 0.0155	0.0330 / 0.0252
Reflections [I ≥ 2σ(I)]	9288	4536	12013
Restraints	6	0	9
Parameters	424	386	880
Goodness-of-fit F²	1.037	1.035	1.113
Final R indexes^{b c}	R1 = 0.0413	R1 = 0.0339	R1 = 0.0730
[all data]	wR2 = 0.0980	wR2 = 0.0788	wR2 = 0.1796
Final R indexes^{b c}	R1 = 0.0336	R1 = 0.0286	R1 = 0.0546
[I ≥ 2σ(I)]	wR2 = 0.0911	wR2 = 0.0758	wR2 = 0.1650
Largest diff. peak/hole (e/Å³)	1.31/-0.82	0.32/-0.27	1.17/-0.61

^a Including solvent molecules (if presence)

$$^b R1 = \frac{\sum ||F_o| - |F_c||}{\sum |F_o|}$$

$$^c wR2 = \sqrt{\frac{\sum (w(F_o^2 - F_c^2))}{\sum (w(F_o^2)^2)}}$$

* values not considering unidentified solvent molecules

Table A2.3 Selected bond lengths and angles in crystal structures. Distance and angles are measured with DIAMOND software.

	<i>trans</i> -1 (MeCN)		<i>trans</i> -1 (EtOH)		<i>trans</i> -1 (DMF)			
CCDC number	2021920		2021925		2021922			
Bond lengths (Å)	Ni1-C11	2.4391(4)	Ni1-C11	2.4180(7)	Ni1-C11	2.4428(17)	Ni2-C12	2.4585(19)
	Ni1-O1	2.091(1)	Ni1-O1	2.0857(18)	Ni1-O1	2.107(4)	Ni2-O2	2.113(4)
	Ni1-N1*	2.1123(13)	Ni1-N2*	2.120(2)	Ni1-N1*	2.109(5)	Ni2-N6*	2.104(5)
	Ni1-N2	2.0643(14)	Ni1-N3	2.047(2)	Ni1-N2	2.086(6)	Ni2-N7	2.071(5)
	Ni1-N3	2.0598(13)	Ni1-N4	2.070(2)	Ni1-N3	2.053(5)	Ni2-N8	2.051(5)
	Ni1-N4	2.0806(13)	Ni1-N5	2.064(3)	Ni1-N4	2.061(5)	Ni2-N9	2.066(6)
Bond angles (°)	C11-Ni1-O1	174.86(3)	C11-Ni1-O1	177.50(6)	C11-Ni1-O1	174.20(11)	C12-Ni2-O2	173.49(13)
	C11-Ni1-N1*	97.84(4)	C11-Ni1-N2*	97.49(7)	C11-Ni1-N1*	95.62(15)	C12-Ni2-N6*	96.58(15)
	C11-Ni1-N2	94.51(4)	C11-Ni1-N3	89.03(8)	C11-Ni1-N2	87.90(19)	C12-Ni2-N7	93.90(16)
	C11-Ni1-N3	91.82(4)	C11-Ni1-N4	91.22(6)	C11-Ni1-N3	92.71(16)	C12-Ni2-N8	91.66(16)
	C11-Ni1-N4	87.32(4)	C11-Ni1-N5	92.10(7)	C11-Ni1-N4	93.55(16)	C12-Ni2-N9	85.92(18)
	O1-Ni1-N1*	81.25(4)	O1-Ni1-N2*	81.19(8)	O1-Ni1-N1*	82.04(18)	O2-Ni2-N6*	81.67(17)
	O1-Ni1-N2	90.59(5)	O1-Ni1-N3	88.76(10)	O1-Ni1-N2	86.7(2)	O2-Ni2-N7	92.44(19)
	O1-Ni1-N3	89.16(5)	O1-Ni1-N4	90.12(8)	O1-Ni1-N3	89.67(19)	O2-Ni2-N8	90.27(19)
	O1-Ni1-N4	87.57(5)	O1-Ni1-N5	90.11(9)	O1-Ni1-N4	91.89(19)	O2-Ni2-N9	87.7(2)
	N1*-Ni1-N2	93.02(5)	N2*-Ni1-N3	85.64(9)	N1*-Ni1-N2	86.6(3)	N6*-Ni2-N7	92.5(2)
	N1*-Ni1-N3	170.34(5)	N2*-Ni1-N4	171.29(9)	N1*-Ni1-N3	171.7(2)	N6*-Ni2-N8	171.7(2)
	N1*-Ni1-N4	85.46(5)	N2*-Ni1-N5	93.83(10)	N1*-Ni1-N4	93.3(2)	N6*-Ni2-N9	86.6(2)
	N2-Ni1-N3	85.82(6)	N3-Ni1-N4	94.73(9)	N2-Ni1-N3	93.9(3)	N7-Ni2-N8	85.8(2)
	N2-Ni1-N4	177.77(5)	N3-Ni1-N5	178.81(11)	N2-Ni1-N4	178.5(2)	N7-Ni2-N9	179.0(2)
	N3-Ni1-N4	95.41(5)	N4-Ni1-N5	85.63(10)	N3-Ni1-N4	86.0(2)	N8-Ni2-N9	95.2(2)
		<i>trans</i> -1 (CH ₂ Cl ₂)		<i>cis</i> -1 (EtOH)		<i>cis</i> -1 (DMF)		
CCDC number	2021923		2021921		2021924			
Bond lengths (Å)	Ni1-C11	2.4426(6)	Ni1-C11	2.4083(5)	Ni1-C11	2.433(1)	Ni2-C12	2.4482(10)
	Ni1-O1	2.1029(11)	Ni1-O1	2.1189(11)	Ni1-O1	2.106(2)	Ni2-O2	2.082(2)
	Ni1-N1*	2.1123(13)	Ni1-N2*	2.1029(15)	Ni1-N1*	2.116(3)	Ni2-N6*	2.119(3)
	Ni1-N2	2.0643(14)	Ni1-N3	2.1375(15)	Ni1-N2	2.131(3)	Ni2-N7	2.107(3)
	Ni1-N3	2.0595(13)	Ni1-N4	2.0712(15)	Ni1-N3	2.078(3)	Ni2-N8	2.086(3)
	Ni1-N4	2.0806(18)	Ni1-N5	2.0841(15)	Ni1-N4	2.080(3)	Ni2-N9	2.081(3)
Bond angles (°)	C11-Ni1-O1	172.74(3)	C11-Ni1-O1	87.64(4)	C11-Ni1-O1	85.87(7)	C12-Ni2-O2	86.15(8)
	C11-Ni1-N1*	97.54(4)	C11-Ni1-N2*	94.37(4)	C11-Ni1-N1*	93.27(8)	C12-Ni2-N6*	93.23(9)
	C11-Ni1-N2	87.04(4)	C11-Ni1-N3	170.76(5)	C11-Ni1-N2	169.49(8)	C12-Ni2-N7	171.21(8)
	C11-Ni1-N3	90.75(4)	C11-Ni1-N4	90.93(5)	C11-Ni1-N3	92.73(9)	C12-Ni2-N8	92.13(9)
	C11-Ni1-N4	94.33(4)	C11-Ni1-N5	93.08(5)	C11-Ni1-N4	92.55(9)	C12-Ni2-N9	91.31(9)
	O1-Ni1-N1*	82.06(5)	O1-Ni1-N2*	81.93(5)	O1-Ni1-N1*	81.76(10)	O2-Ni2-N6*	81.73(10)
	O1-Ni1-N2	85.70(5)	O1-Ni1-N3	83.13(6)	O1-Ni1-N2	83.71(10)	O2-Ni2-N7	85.10(11)
	O1-Ni1-N3	90.00(5)	O1-Ni1-N4	99.66(5)	O1-Ni1-N3	101.19(10)	O2-Ni2-N8	100.5(1)
	O1-Ni1-N4	92.93(5)	O1-Ni1-N5	175.59(6)	O1-Ni1-N4	174.89(11)	O2-Ni2-N9	174.67(11)
	N1*-Ni1-N2	86.21(5)	N2*-Ni1-N3	84.16(6)	N1*-Ni1-N2	83.86(11)	N6*-Ni2-N7	84.60(12)
	N1*-Ni1-N3	171.42(5)	N2*-Ni1-N4	174.52(6)	N1*-Ni1-N3	173.49(11)	N6*-Ni2-N8	174.32(12)
	N1*-Ni1-N4	91.68(5)	N2*-Ni1-N5	93.68(6)	N1*-Ni1-N4	93.49(11)	N6*-Ni2-N9	93.75(12)
	N2-Ni1-N3	96.45(5)	N3-Ni1-N4	90.81(6)	N2-Ni1-N3	90.67(11)	N7-Ni2-N8	90.37(12)
	N2-Ni1-N4	177.63(5)	N3-Ni1-N5	96.11(6)	N2-Ni1-N4	97.71(12)	N7-Ni2-N9	97.33(11)
	N3-Ni1-N4	85.48(5)	N4-Ni1-N5	84.68(6)	N3-Ni1-N4	83.73(12)	N8-Ni2-N9	84.26(11)

* nitrogen atom of the tertiary amine

References

- [1] Bruker, APEX II / APEX III / SAINT. Bruker AXS Inc., Madison, Wisconsin, USA **2012**.
- [2] Bruker, SADABS. Bruker AXS Inc., Madison, Wisconsin, USA **2001**.
- [3] G. M. Sheldrick, *Act. Cryst. A*. **2015**, *71*, 3-8.
- [4] G. M. Sheldrick, *Act. Cryst. C*. **2015**, *71*, 3–8.
- [5] O.V. Dolomanov, L.J. Bourhis, R.J. Gildea, J.A.K. Howard, H. Puschmann, *J.Appl. Crystallogr.* **2009**, *42*, 339-341.
- [6] L. J. Farrugia, *J. Appl. Cryst.* **2012**, *45*, 849-854.
- [7] A. L. Spek, *Act. Cryst. C*. **2015**, *71*, 9-18

Chapter 3 Selective CO₂ electroreduction in aqueous conditions with a heterogenized C-substituted Ni cyclam catalyst

3.1 Introduction

In the previous chapter we have incorporated a molecular catalyst, **1**, derived from [Ni(cyclam)]²⁺, onto electrode surfaces by using a non-covalent approach. The so-made electrodes were found to be robust, selective for CO production and stable even after 4h of electrolysis in MeCN/water mixtures, confirming the stability of complex **1** itself and the efficiency of the heterogenization strategy. However, in fully aqueous conditions (0.1 M KHCO₃), the selectivity of the catalyst for CO₂ reduction was considerably reduced (48% FY for CO).

As already mentioned in Chapter 1, [Ni(cyclam)]²⁺ sparked the interest of electrochemists since the 80s because of its selectivity for CO₂ reduction in an aqueous electrolyte.^[1] The origin of its excellent selectivity (FY up to 99% for CO) was later on attributed to the adsorption of the catalyst on Hg electrodes during the catalytic process as high turnover numbers (TONs) and faradaic yields (FYs) were obtained only in the presence of a Hg electrode.^[2] In parallel to this, several studies observed that the presence of four H linked to the N atoms of the cyclam ring could facilitate the CO₂ reduction reaction (CO₂RR) by encouraging CO₂ chemisorption and stabilize the intermediates via H bond.^[2-4] Additionally, when C-substitutions to the cyclam ring were added in such a way that the atoms around the Ni center would adopt a flat arrangement, even better catalysts than [Ni(cyclam)]²⁺ itself could be obtained.^[5] A wise choice of the substrate/electrode and the surrounding of the metal center are therefore essential to maintain-or boost- the efficiency of the catalyst.

The only known previous attempt to heterogenize [Ni(cyclam)]²⁺ directly on carbon surfaces opted for a covalent strategy to heterogenize a series of N-substituted alkynyl cyclams on glassy carbon (GC) electrodes.^[6] The 2D surface in combination to a covalent method resulted in a monolayer of deposited catalyst which did not maintain its selectivity, even in organic medium.^[7] Successively, our efforts focused on a more suitable heterogenization strategy via

non-covalent interaction to a 3D carbon substrate (multi-walled carbon nanotubes, MWCNTs), which proved successful.^[8] Such hybrid electrodes could be employed in MeCN/water mixtures with excellent selectivity, which was however largely reduced when operating under aqueous conditions. In parallel with our attempts to perform CO₂ electroreduction with a heterogenized [Ni(Cyclam)]²⁺ in complete aqueous medium, a similar system was described by Cowan and collaborators.^[9] During a CPE at -1.4V vs Ag/AgCl using 0.5M KHCO₃ as the catholyte, the current and selectivity towards CO₂ decreased rapidly over time bringing the FY for CO to less than 50% after 30 minutes. The authors suggested that the reason for this decrease is also due to the loss of one of the 4 N-H groups on the cyclam ligand as a substitution was brought at one N atom for the addition of the grafting functionality.

For these reasons, with the aim to successfully heterogenize [Ni(cyclam)]²⁺ on a carbon substrate while maintaining its selectivity for CO₂RR in water, we decided to focus our efforts on the synthesis of a new C-substituted [Ni(cyclam)]²⁺ complex, thus avoiding modifications at N atoms.

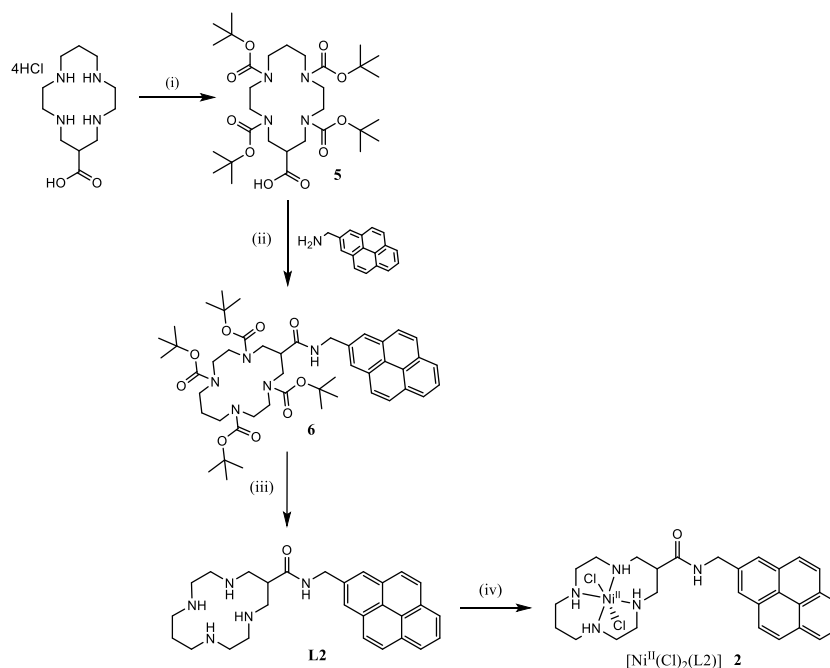
Hence, we have synthesized an original pyrene-cyclam derivative and the corresponding Ni complex, complex **2** (**Scheme 3.1**), which, as expected, was found to have similar configuration as the unfunctionalized parent [Ni(cyclam)]²⁺ complex. We report here the electrocatalytic properties of complex **2** both in solution and after immobilization on MWCNTs. The complex proved to behave as a very selective homogeneous catalyst for CO₂ electroreduction to CO in organic solvents. Furthermore, the presence of a pyrene moiety on the ligand was exploited to readily heterogenize the complex on MWCNTs via non-covalent interactions. The novel hybrid solid electrode, obtained by deposition of the functionalized MWCNTs on a Gas Diffusion Layer (GDL), was found to be active, stable and highly selective for CO₂ electroreduction to CO in acetonitrile-water solvent. Additionally, when the electrode was used in aqueous medium, the catalyst retained an excellent selectivity for CO (up to 87%), which, to our best knowledge, makes this the most selective [Ni(cyclam)]²⁺ catalyst covalently heterogenized on carbon electrodes in water.

Finally, in order to better understand (i) the influence of a longer linker on the electron transfer rates from the carbon surface to the catalyst (ii) the influence of an amide functionality on the catalytic efficiency of [Ni(cyclam)]²⁺, we proposed the synthesis of another new modified [Ni(cyclam)]²⁺ catalyst, **3** (**Scheme 3.2**), where the C-substituted cyclam ring and the pyrene moiety will be separated by a simple alkyl chain.

3.2 Results

3.2.1 Synthesis of Complex 2

The synthesis of complex **2** was designed in order to make the process scalable and as less time consuming as possible. The synthetic pathway is presented in **Scheme 3.1**.



Scheme 3.1 Synthesis of complex **2**. Conditions: (i) Boc_2O , dioxane, H_2O , RT, 72h, 83% , Na_2CO_3 ; (ii) EDC-HCl, DMAP, DCM, RT, 5h, 93%; (iii) TFA, DCM, RT, o/n, KOH, H_2O , 100%; (iv) DMF, $\text{NiCl}_2 \cdot 6\text{H}_2\text{O}$, 2h, 49%.

Starting from the commercially available hydrochloride salt of 1,4,8,11-tetraazacyclotetradecane-6-carboxylic acid, the first step (**Scheme 3.1**, (i)) involves the protection of the four secondary amines of the cyclam ring with *tert*-butoxycarbonyl (Boc) protecting groups. This step is necessary to avoid undesired side reactions taking place on the amines during the following reaction steps. Additionally, the presence of the Boc protecting groups increases the molecule solubility in organic solvents, being the salt of 1,4,8,11-tetraazacyclotetradecane-6-carboxylic acid soluble in water only. A prior study by Liolios and collaborators^[10] described the same protection reaction (with the same starting molecule) and was thus used as a guideline for the reaction.

The Boc group was added to the amine in H_2O /dioxane using di-*tert*-butyl dicarbonate (Boc_2O) in the presence of sodium carbonate. The initial addition of 5 equivalents of Na_2CO_3 to the salt

of 1,4,8,11-tetraazacyclotetradecane-6-carboxylic acid in water deprotonates the four protonated secondary amines. These can then attack the carboxylic carbon of the Boc₂O, which is added drop by drop in dioxane. The formation of a tetrahedral intermediate is followed by the loss of a carbonate which can either act as a base or decarboxylate to give CO₂ and t-butoxide, which then withdraws a proton from the protonated carbamate.

The reaction time was increased (72h) to avoid the presence of tri-substituted cyclam, which was observed when the mixture was let react less than 24h. Indeed, Liolios and collaborators let the reaction run overnight and the chromatogram obtained from RP-HPLC analysis of the reaction mixture showed the existence of two peaks, which needed to be separated for further reactions.^[10] In order to avoid purification steps, in the present synthesis, we obtained the tetraprotected cyclam in high yields by increasing the reaction time. The workup steps conveniently removed unreacted species and other water-soluble byproducts, while by acidification, the solubility of the product in water was greatly decreased, which made it possible to extract the product from the aqueous phase with polar organic solvents. The so-obtained product could be used without further purification for the successive steps.

The amide bond formation step (**Scheme 3.1**, (ii)) takes place in dichloromethane, in the presence of the carbodiimide 1-ethyl-3-(3-dimethylaminopropyl)carbodiimide (EDC) and 4-dimethylaminopyridine (DMAP). To maximize the yield, the commercially available salt 1-pyrenemethylamine hydrochloride was pretreated with a base (KOH) and then added to the reaction mixture in its deprotonated form. The acidic work-up eliminated urea byproducts and unreacted precursors, making it possible to isolate the product in excellent yields (>90%) without the need of additional purification steps.

The successive deprotection of the Boc-protected amines (**Scheme 3.1**, (iii)) was carried out with trifluoroacetic acid (TFA). The byproducts were easily removed from the mixture together with the solvent by evaporation under reduced pressure, and the product was isolated in the form of trifluoroacetate salt. The salt was treated with a base (KOH) to obtain the ligand **L2**.

The ligand was characterized via IR, ¹H NMR, ¹³C NMR (**Figure A3.11**, **Figure A3.12**, **Figure A3.14**, respectively and experimental section) and its purity was confirmed by elemental analysis and MS (Experimental section). Finally, the ligand was mixed to NiCl₂·6H₂O in DMF at room temperature to give complex **2**, which was characterized via MS and UV-Vis spectroscopy (Experimental section).

3.2.2 Homogeneous electrochemical studies of complex 2

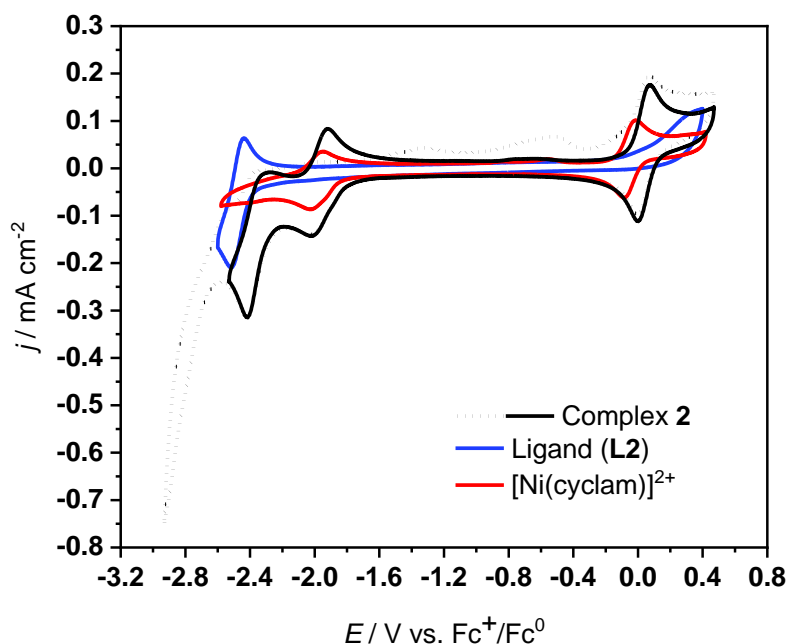


Figure 3.1 Cyclic voltammograms of complex **2**, $[\text{Ni}^{\text{II}}(\text{L}2)]^{2+}$ (black and dotted), $[\text{Ni}(\text{cyclam})]^{2+}$ (red), ligand (**L2**, blue). Conditions: DMF with 0.1M TBAPF₆ as the electrolyte, under Ar and at room temperature. Concentrations were 1 mM for all species. Scan rate 100 mV s⁻¹.

The electrochemical properties of complex **2** were studied in DMF with 0.1 M TBAPF₆ as a supporting electrolyte, with all potentials vs. Fc⁺/Fc⁰. Cyclic voltammograms (CVs) of complex **2** (1 mM) were recorded by using a glassy carbon disk (3 mm diameter) as a working electrode, under an argon atmosphere, scanning down to either -2.42 or -2.9V (**Figure 3.1**).

Two main reduction processes were identified, which showed reversibility when the scan was stopped at -2.42V. When scanning to more negative potentials, not only the two main reduction processes lost reversibility, but also two oxidation events were observed, namely at -1.31 and -0.52 V, which would not happen if the scan was reversed at less negative potentials.

The first feature was assigned to the one-electron reduction of Ni^{II} to Ni^I. This process peaks at -2 V, at approximately the same potential as the unfunctionalized $[\text{Ni}(\text{cyclam})]^{2+}$ complex (**Figure 3.1**, red), which confirms a similar metal center configuration. As a further proof of that, also the oxidation from Ni^{II} to Ni^{III} and the subsequent reduction of Ni^{III} to Ni^{II}, which

were present in the CV of the unfunctionalized [Ni(cyclam)]²⁺ complex, could be observed for complex **2**, albeit at slightly more anodic potentials.

The ligand itself is redox-active due to the presence of pyrene.^[11] The second reduction process was therefore assigned to a one-electron reduction occurring on the pyrene moiety of the ligand. This is in agreement with the CV of the unmetallated ligand, **L2** (Figure 3.1, blue), in which a reversible reduction process was observed at slightly more negative potentials (-2.5V).

Both the cathodic peak current density (j_p) at -2 V and the anodic peak current density at -1.9 V varied linearly with the square root of the scan rate ($v^{1/2}$) from 10 to 500 mV s⁻¹ under Ar, consistent with diffusion-controlled processes and thus with active complex **2** remaining in solution (Figure 3.2).

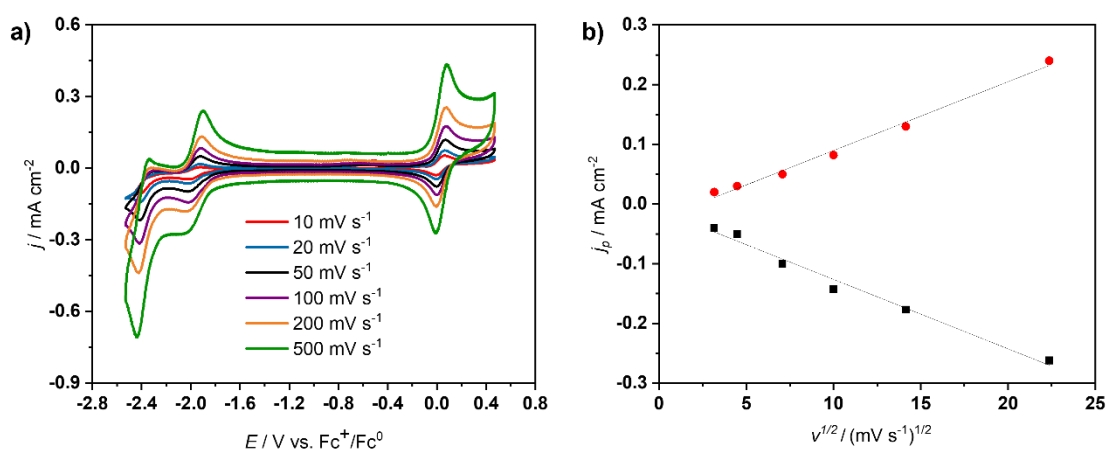


Figure 3.2 a) CV of 1 mM complex **2** (DMF with 0.1M TBAPF₆ as the electrolyte, under Ar and at room temperature) at different scan rates and b) plot of the cathodic peak current at -2 V and the anodic peak current at -1.9V as a function of the square root of the scan rates.

Upon addition of CO₂, in the absence of proton sources, the CV of 1 mM complex **2** (Figure 3.3) presented a catalytic wave with a potential at half-peak catalytic current of about -2.2 V. Upon addition of H₂O (2 M), the onset potential of the catalytic wave shifted to more anodic potentials and the current density increased, confirming the essential role of a proton source in the CO₂RR in general and specifically for CO₂RR catalyzed by [Ni(cyclam)]²⁺.^[12]

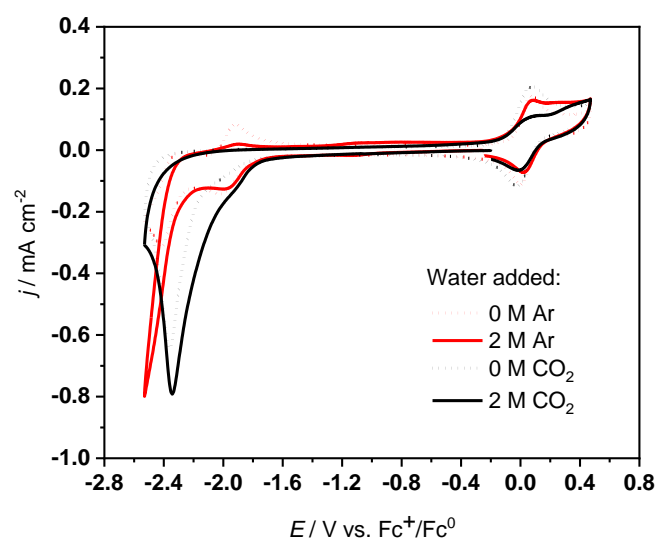


Figure 3.3 CV of complex **2** (1 mM) in Ar-saturated (red and dotted red) and CO₂-saturated (black and dotted black) DMF with 0.1M TBAPF₆ at room temperature with no H₂O added and in the presence of H₂O 2M. Scan rate 100 mV s⁻¹

Considering a CO/CO₂ reduction potential in a DMF-2M H₂O solvent mixture at - 1.41 V vs. Fc⁺/Fc⁰ (CO/CO₂ potential is reported to be - 0.690 V vs. NHE^[13] and the Fc⁺/Fc⁰ potential is reported to be 0.720 V vs. NHE in DMF),^[14] the observed onset potential at -2 V corresponds to an overpotential of about 590 mV (For complex **1**, the overpotential was of about 740 mV).

The effect of increased concentrations of H₂O was studied by CV as shown in **Figure 3.4**. Remarkably, under CO₂-saturated conditions, the potential at half-peak catalytic current shifted anodically from -2.2 V to -1.9 V for 0 to 20 v% H₂O, respectively (**Figure 3.4a**).

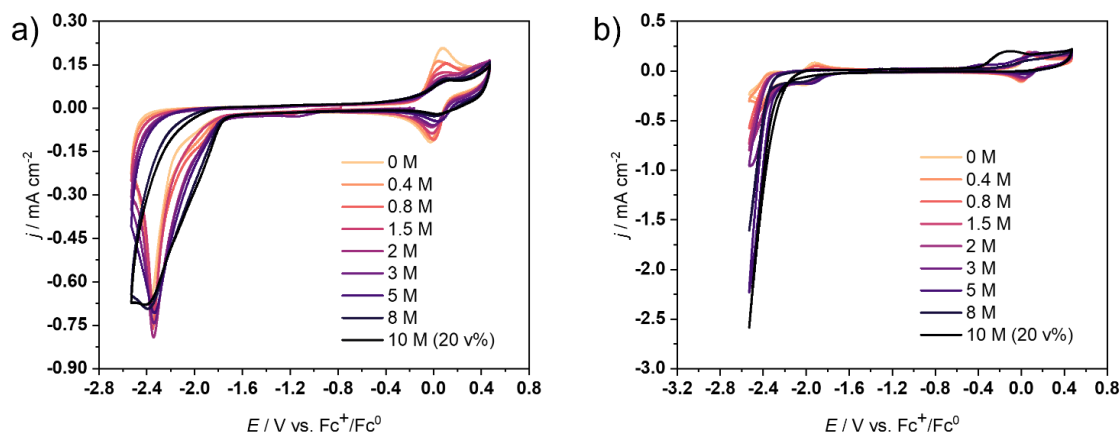


Figure 3.4 CVs of **2** (1 mM) in DMF with 0.1 M TBAPF₆ and increasing concentrations of H₂O under CO₂ (a) and under Ar (b) at room temperature. Scan rate 100 mV s⁻¹. Same colors have been used for the same H₂O concentrations in both figures.

In the absence of CO₂, a catalytic current, assigned to proton reduction to hydrogen, also increased upon increasing the concentration of H₂O (**Figure 3.4b**), however with an onset potential (-2.2 V for H₂O 20 v%) more cathodic than that for CO₂ reduction.

Controlled-potential electrolysis (CPE) was then carried out at -2.28 and -2.38 V, during which reaction products were analyzed and quantified, either by gas chromatography (for CO and H₂), by Ionic Exchange Chromatography (for HCOOH) and ¹H NMR (for CH₃OH) (**Figure 3.5**). For that purpose, the electrochemical cell used a 1 cm² GC plate as the working electrode and the electrolyte was a solution of complex **2** (1 mM) in CO₂-saturated DMF containing 0.1 M TBAPF₆ and 2 M H₂O as a proton source. The same experiment but in the absence of complex **2** (Blank, **Figure 3.5a, b**) did not yield any CO₂ reduction products. As shown from the stability of the current density, the catalyst proved to be robust. After 120 minutes electrolysis (**Figure 3.5c**), CO was found as the only reaction product in the gaseous phase (faradaic yield: 96%) and no formate could be detected in the liquid phase. As a further proof of the stability of the catalyst, a CV recorded after CPE was found to be comparable to that before electrolysis, (**Figure 3.5a**).

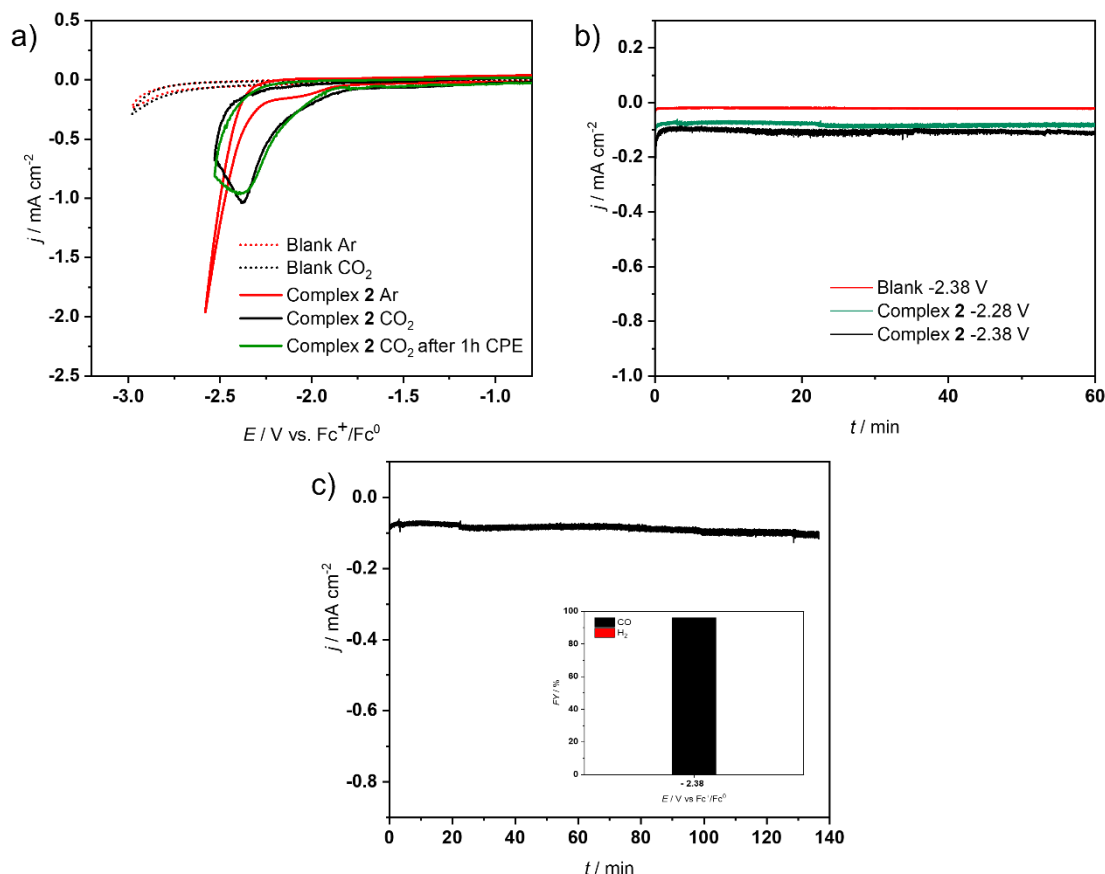


Figure 3.5 (a) CVs of **2** (1 mM) in DMF with 0.1M TBAPF₆ and H₂O 2M under CO₂ and under Ar at room temperature compared with a blank (absence of complex **2**). Scan rates 100 mV s⁻¹. (b) Controlled-potential electrolysis at -2.38 and -2.28 V vs. Fc⁺/Fc⁰ under the same conditions, in the presence of complex **2** (green, black) and at -2.38 V in the absence of complex **2** (red). (c) Controlled-Potential Electrolysis at -2.38 V vs. Fc⁺/Fc⁰ in the presence of **2** under the same conditions, and relative faradaic yields for CO and H₂ after 2h electrolysis.

3.2.3 Heterogenization of complex **2**, electrodes characterization, and CO₂ reduction

Complex **2** was physisorbed on MWCNTs through the establishment of π -stacking interactions between the pyrene moieties and graphene motifs. In a first step, MWCNTs (2 mg) were first sonicated in ethanol in the presence of Nafion, then drop-casted on a 1 cm² surface of commercial gas diffusion layer (GDL), consisting of a carbon fibers cloth coated with a micro-porous Teflon layer embedding carbon black so as to keep electronic conductivity properties. Then the MWCNT/GDL electrode was dipped into a solution of 10 mM complex **2** in methanol,

left overnight and then washed with water and acetonitrile to remove any loosely bound complexes, and finally air-dried before electrochemical experiments.

The **2**/MWCNT/GDL electrode was characterized by Scanning Electronic Microscopy (SEM) (**Figure A3.2**) and X-ray photoelectron spectroscopy (XPS) (**Figure 3.6**).

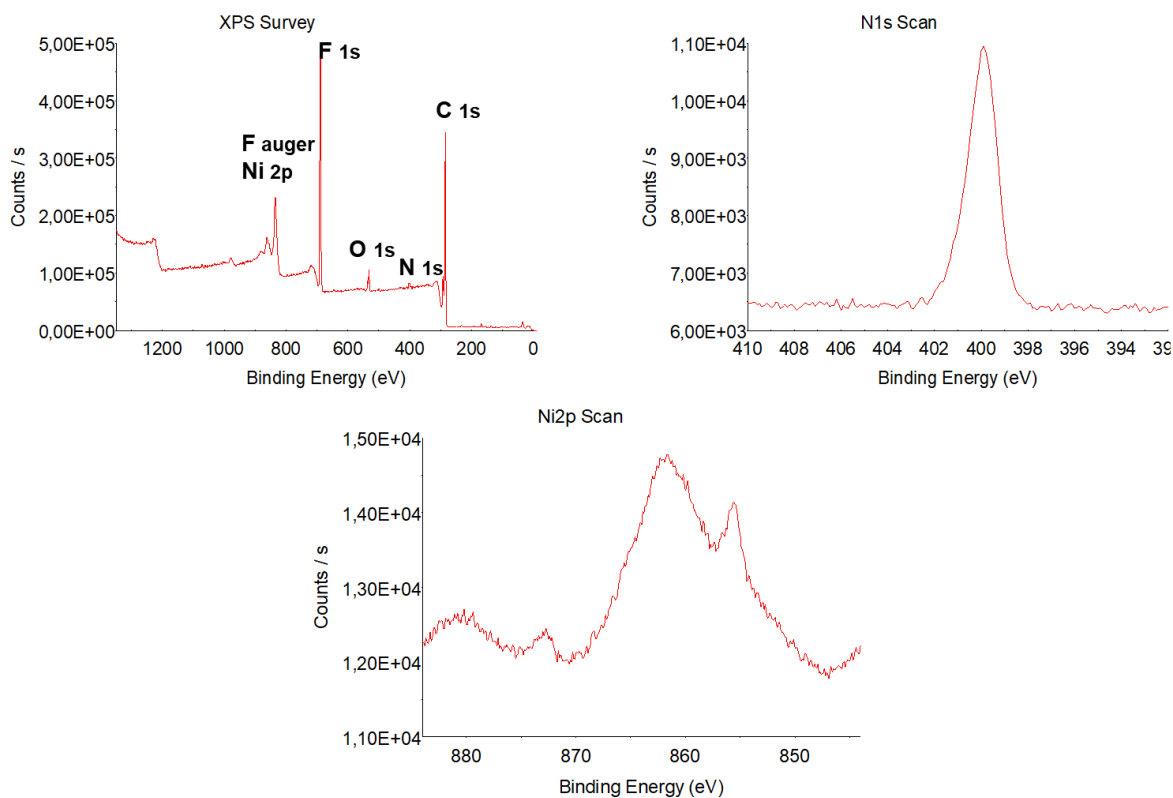


Figure 3.6 XPS survey spectrum of **2**/MWCNT/GDL electrode (a), high resolution XPS spectra of N 1s (b), Ni 2p (c).

XPS analysis (survey spectrum, **Figure 3.6a**) confirms the presence of Ni and N atoms, from complex **2**, on the surface of the electrode, together with O atoms from alcohol or carboxylic acid defects of pristine MWCNTs. N 1s peak was centered at 400.4 eV (**Figure 3.6b**). A Ni 2p_{3/2} signal is observed at 855.9 eV in good agreement with the presence of a Ni^{II} ion. Peak decomposition (as fluoride in the deposited materials coming from Nafion with the F auger peak is masking the Ni 2p signal at 861.47 eV **Figure 3.6c**) allowed to identify the signal of Ni 2p and the ratio of N/Ni was 4.5 approximately.

The **2**/MWCNT/GDL electrode was also characterized by cyclic voltammetry. CVs were recorded in acetonitrile containing 0.1M TBAPF₆, using such **2**/MWCNT/GDL electrode (**Figure 3.7**). The high capacitive currents observed in the voltammograms are explained by the

3D structure of the working electrodes. The presence of a signal at approximately -2 V vs. Fc^+/Fc^0 , which corresponds to the one-electron reduction of Ni^{II} to Ni^{I} , is in good agreement with the presence of the physisorbed catalyst. The integration of the signal (at 20 mV s^{-1}) allowed to determine a number of active sites of $4.2 \cdot 10^{-9} \text{ mol cm}^{-2}$ (see experimental section). Such a value is in line with previously reported values for MWCNTs functionalized with molecular complexes.^[15,16]

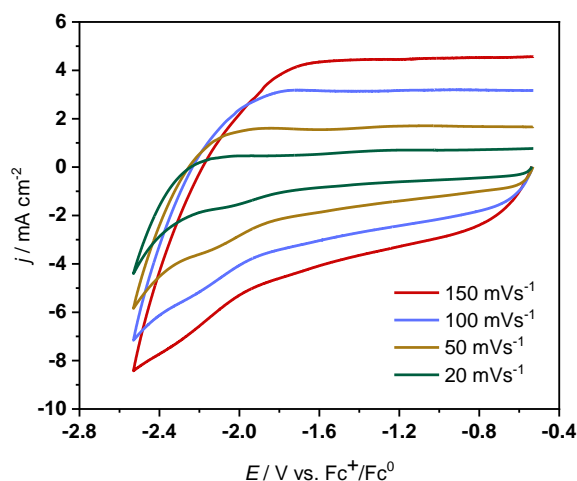


Figure 3.7 (a) CV of **2**/MWCNT/GDL (acetonitrile with 0.1M TBAPF_6 as the electrolyte, under Ar and at room temperature) at different scan rates.

The electrochemical reduction of CO_2 using the new electrode material was carried out in MeCN containing 0.1M TBAPF_6 as the electrolyte, in the presence of 1% H_2O as a proton source, after saturation with CO_2 . A linear sweep voltammogram (LSV) shows a catalytic wave occurring at more anodic potentials as compared to the MWCNT/GDL control electrode (**Figure 3.8a**).

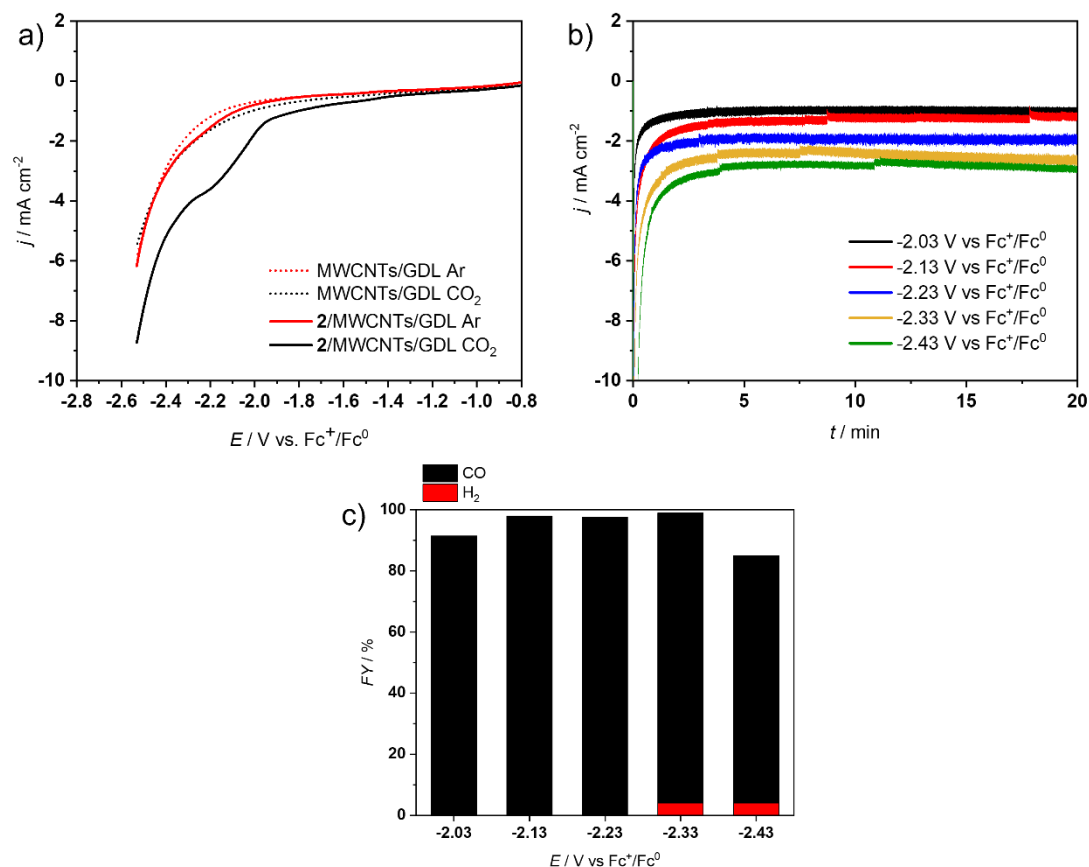


Figure 3.8 (a) LSV of 2/MWCNT/GDL (black and red) and MWCNT/GDL (dotted) in acetonitrile with TBAPF₆ 0.1 M and H₂O 1% under CO₂ or Ar. Scan rate 10 mV s⁻¹. (b) Controlled Potential Electrolysis using 2/MWCNT/GDL as the electrode at different potentials under the same conditions. (c) Faradaic yields for CO and H₂ after 20 min electrolysis at different potentials under the same conditions with 2/MWCNT/GDL.

Chronoamperometric measurements were carried out at various potentials from -2.03 to -2.43 V vs. Fc⁺/Fc⁰ for 20 min (**Figure 3.8b**). The current densities were stable at all potentials. The same electrode could be used for several independent electrolysis experiments without any loss of activity. The CO₂ reduction products distribution, in terms of faradaic yields (FY), is shown in **Figure 3.8c**. CO was the major product at all potentials, and in particular it was the only product detected between -2.03 and -2.23 V, with the best performance (FY for CO 97%) obtained at -2.23 V vs. Fc⁺/Fc⁰ (with a current density of 2 mA.cm⁻²). In all cases H₂ accounted for less than 10% and no formate could be detected. As a control experiment, CPE using a MWCNT/GDL electrode was performed at -2.13 V vs. Fc⁺/Fc⁰ during 20 min (**Figure A3.1**). Not only the current density was much lower (~ 0.8 mA.cm⁻²) but the system was selective for H₂ production instead.

A longer experiment (4h) carried out at -2.23 V vs. Fc^+/Fc^0 using the **2**/MWCNT/GDL electrode under CO_2 confirmed the stability of the catalytic material as well of its selectivity with a FY for CO of more than 90% after 4h electrolysis (**Figure 3.9**). SEM analysis after 4h electrolysis showed no substantial change in the structure of the electrode (**Figure A3.2**). Based on the amount of electroactive sites on the surface of the electrode ($4.2 \cdot 10^{-9}$ mol cm^{-2}), a Turnover Number for CO formation of 14630 was obtained after 4 h electrolysis, corresponding to a Turnover Frequency value of 1.01 s^{-1} .

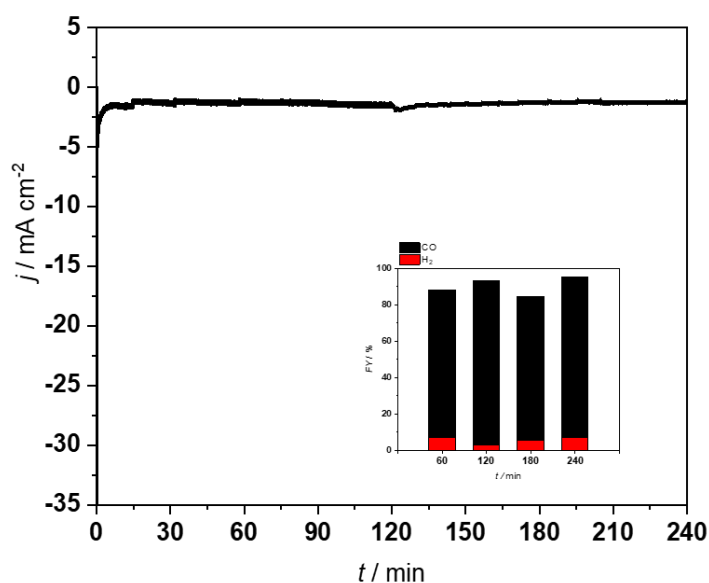


Figure 3.9 Controlled-Potential Electrolysis at -2.23 V vs. Fc^+/Fc^0 using **2**-MWCNT/GDL in acetonitrile with 0.1M TBAPF₆ and 1% H₂O. Inset: Faradaic yields for CO and H₂ during electrolysis.

A CPE experiment was carried out at -2.13 V vs. Fc^+/Fc^0 for 20 min with an increased amount of water (10 v%). The current density of the catalytic wave that was assigned to CO_2 reduction dramatically increased, as well as the onset of such wave (**Figure 3.10a**). The system tolerated the increased amount of water as demonstrated by the stability of the current density during CPE (**Figure 3.10b**), and CO was still the major product (FY for CO and H₂ of 61% and 27% , respectively).

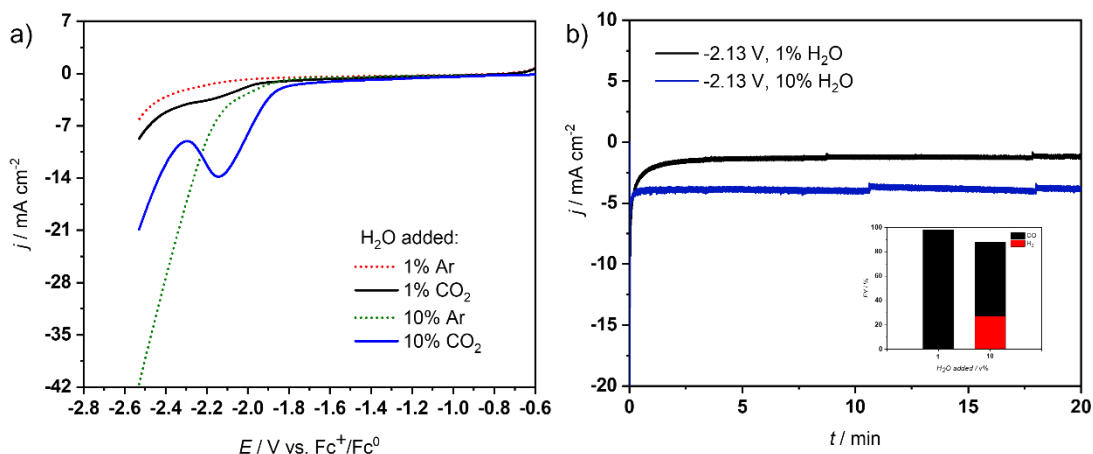


Figure 3.10 (a) LSVs of **2**/MWCNT/GDL in acetonitrile with TBAPF₆ 0.1 M and H₂O 1 v% (red, black) or 10 v% (green, blue) under CO₂ or Ar. Scan rate 10 mV s⁻¹. (b) Controlled Potential Electrolysis using **2**/MWCNT/GDL as the electrode at different potentials under the same conditions and H₂O 1% (black) or 10% (blue). Inset: faradaic yields for CO and H₂ after 20 min electrolysis at different water concentrations.

3.2.4 Electroreduction of CO₂ catalyzed by **2**/MWCNTs/GDL in water

Finally, the electrochemical reduction of CO₂ using the new electrode material was carried out in water containing 0.1M KHCO₃ as the electrolyte, under a constant flux of CO₂ (5 ml/min). A linear sweep voltammogram (LSV) shows a catalytic wave occurring at more anodic potentials as compared to the MWCNT/GDL control electrode (**Figure 3.11a**).

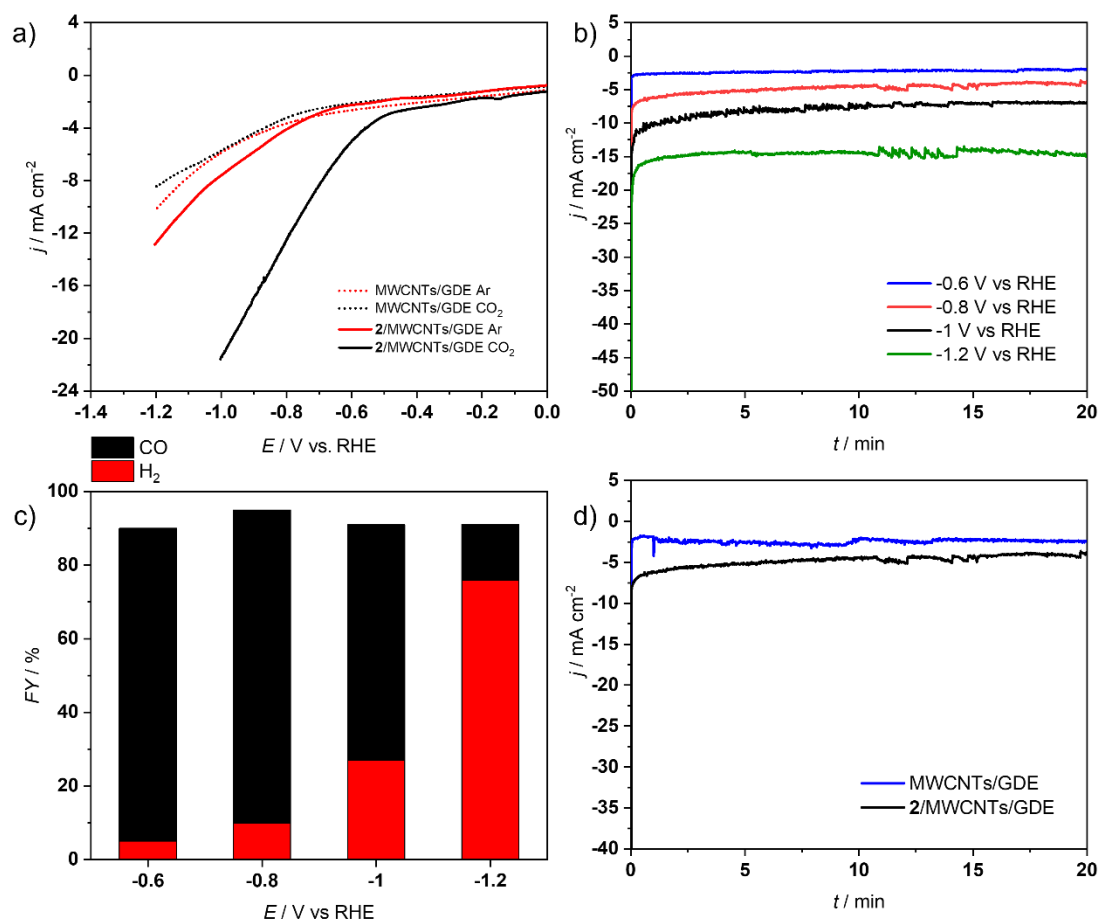


Figure 3.11 (a) LSVs of 2/MWCNT/GDL (black and red) and MWCNT/GDL (dotted) in water with KHCO_3 0.1 M under CO_2 or Ar. Scan rate 50 mV s^{-1} . (b) Controlled Potential Electrolysis using 2/MWCNT/GDL as the electrode at different potentials under the same conditions. (c) Faradaic yields for CO and H_2 after 20 min electrolysis at different potentials under the same conditions with 2/MWCNT/GDL. (d) Controlled Potential Electrolysis using 2/MWCNT/GDL (black) compared to MWCNT/GDL (blue) at -0.8 V under the same conditions.

Chronoamperometric measurements were carried out at various potentials from -0.6 to -1.2 V vs. RHE for 20 min (**Figure 3.11b**) and with a CO_2 flow rate of 5 ml/min . The current density proved stable in all cases (occasional noise in the current density signal was likely caused by the large number of gas bubbles developing at the surface of the electrode). The same electrode could be used for several independent electrolysis. The CO_2 reduction products distribution, in terms of faradaic yields (FY), is shown in **Figure 3.11c**. CO was the major product between -0.6 and -1 V , with the highest FY value (82%) obtained at both -0.6 and -0.8 V vs. RHE (with a max current density of $5 \text{ mA}\cdot\text{cm}^{-2}$). Conversely, H_2 was the major product (20% FY for CO) at -1.2 V , and in all cases no formate could be detected. As a control experiment, CPE using a MWCNT/GDL electrode was performed at -0.8 V vs. RHE during 20 min (**Figure 3.11d**). The

current density was much lower ($\sim 2.5 \text{ mA}\cdot\text{cm}^{-2}$) but almost only H₂ was produced instead (only traces of CO were detected).

During a longer experiment (4h) carried out at -0.8 V vs. RHE using the 2/MWCNT/GDL electrode, CO was the major product, despite a partial loss in selectivity with a FY for CO of 87 and 53% after 20- and 240-min electrolysis, respectively (**Figure 3.12**). This was also accompanied by a partial loss in current density (from 6 to mA cm^{-2} after 20 min CPE to 2.6 mA cm^{-2} after 240 min).

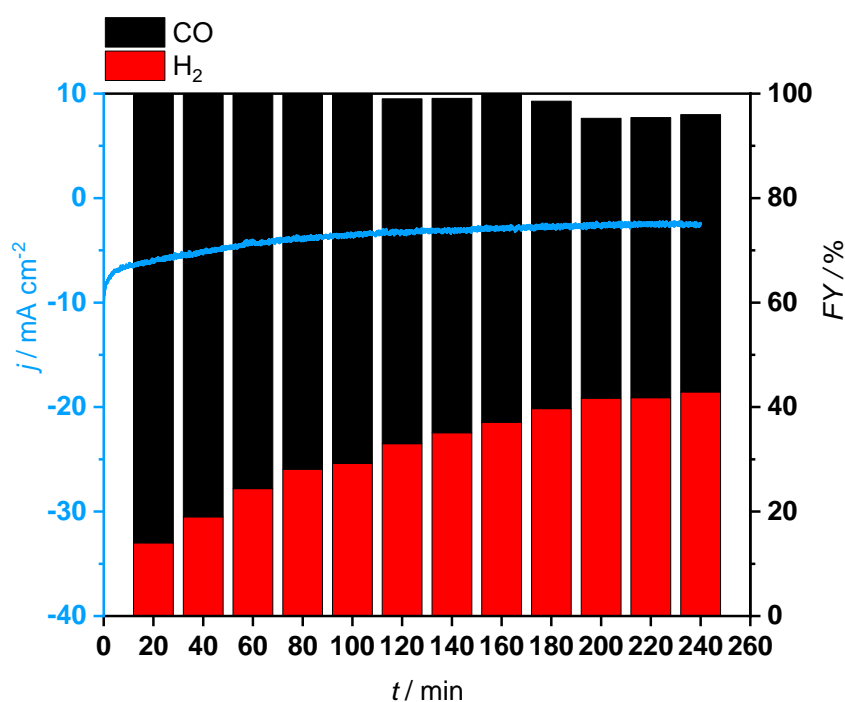


Figure 3.12 Controlled-Potential Electrolysis at -0.8 V vs. RHE using 2/MWCNT/GDL in water with 0.1M KHCO_3 and a CO_2 flow rate of 5 ml/min . Faradaic yields for CO and H₂ during the same experiment.

3.2.5 Complex 1 and complex 2: a comparison

The electrochemical properties of complex 2 are quite different from those of complex 1. In contrast to complex 1, the CV of complex 2 featured two reversible reduction processes, the first of which was assigned to the reduction of Ni^{II} to Ni^{I} . Regarding this process, for complex 1 it was approximately 180 mV more cathodic than for the unfunctionalized $[\text{Ni}(\text{cyclam})]^{2+}$ complex, and additionally it was not reversible, regardless the potential at which the scan was reversed. The difference between the CVs of complex 1 and 2 (**Figure A3.3**) thus reflects the different coordination of the metal center for the two complexes, namely that in complex 1 Ni

is hexacoordinated while it is not the case in complex 2. An additional reduction process at -2.86 V and assigned to Ni^I to Ni⁰ reduction was observed for complex 1 (**Figure A3.3**). This feature was absent in the CV of complex 2.

Both complex 1 and 2 presented, on the oxidizing return scan, a broad signal at -0.66 V which is exclusively seen after scanning down to a very negative potential (**Figure A3.3**), and not when the cathodic scan was reversed after the second reduction wave. This was also observed with the unfunctionalized [Ni(cyclam)]²⁺ complex (Chapter 2, **Figure 2.3**). Complex 2, however, presented a second broad oxidation feature at approximately -1.31V, which was not found in the CV of complex 1.

The comparison between the CVs of complex 1 and 2 under increased concentrations of H₂O in acetonitrile further underlined the differences between the two catalysts. Conversely to complex 2, the catalytic response of complex 1 under CO₂ did not change above a concentration of 3 M water (Chapter 2, **Figure 2.7**). For the same amount of water, e.g., 2M, the onset of catalytic CO₂ reduction for complex 1 was around -2.15 V, whereas it was around -2 V for complex 2 (**Figure A3.4**, inset). As previously noted, this corresponds to an overpotential of about 590 mV, while for complex 1, the overpotential was of about 740 mV. As a matter of fact, the overpotential for complex 2 is comparable to that of an iron porphyrin catalyst, Fe⁰TDHPP, one of the best molecular catalysts described so far, for which the overpotential for CO₂ reduction in DMF-2M H₂O solution was also assessed at 590 mV.^[17]

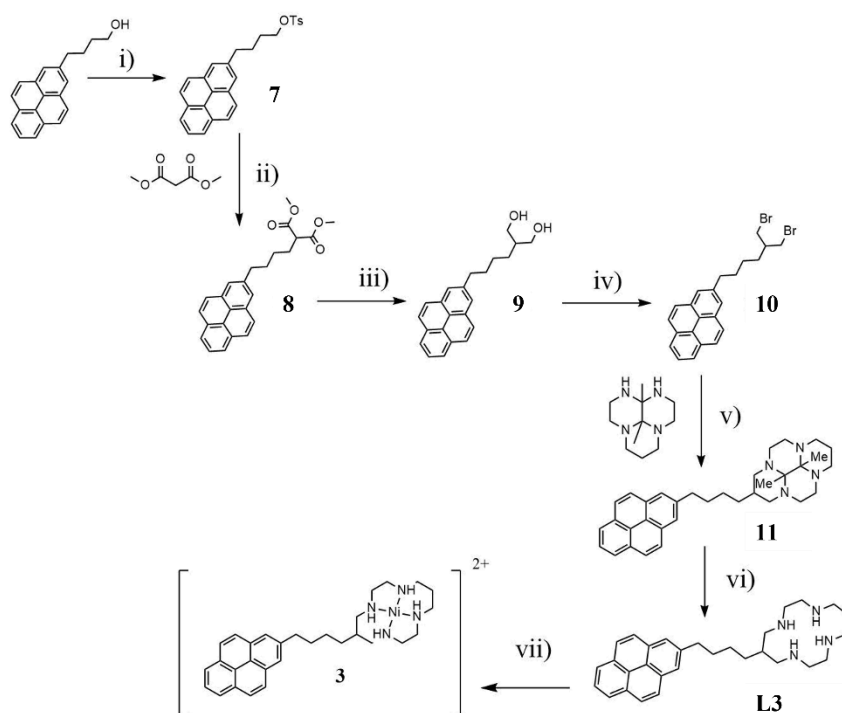
In addition, for complex 1 the catalytic wave did not shift, i.e., it did not become more anodic, as the amount of water increased (only a modest increase in current density was noticed). Conversely, in the case of complex 2, a noticeable shift in the onset of the catalytic current took place. A higher affinity of complex 1 for proton reduction compared to complex 2 could be observed from the significant difference in current density under Ar-saturated conditions. In the same conditions and in the presence of the same amount of water (2 M), the peak current density for proton reduction reached almost 8 mA cm⁻² for complex 1, while it was less than 1 mA cm⁻² for complex 2(**Figure A3.4**).

Once immobilized, the complexes showed different features, as following. The catalytic wave under CO₂ started at more negative potentials for complex 1. As a result, the window of potentials selected for the tests with this catalyst ranged from -2.34 V to -2.74 V vs Fc⁺/Fc⁰. In the case of complex 2, in accordance with the observed positive shift for Ni^{II} to Ni^I reduction in homogeneous conditions, we recorded the beginning of the catalytic wave at more anodic

potentials, which allowed us to perform the tests in a more positive potential window (-2.03 V to -2.43 V) and obtain higher current densities when CPE was run at same potentials. The positive shift for Ni^{II} to Ni^I reduction for complex **2** proved useful during CO₂ electroreduction experiments.

The differences in selectivity also proved to be in accordance with observations made in homogeneous conditions. Not only was catalyst **2** generally more selective than catalyst **1** in organic medium (with almost 100% FY for CO between -2.03 and -2.23 V), but in aqueous environment favored CO₂ reduction over proton reduction, with max 87% at -0.8 V, while the maximum selectivity of complex **1** at the same potential was 48%.

3.2.6 Synthesis of complex **3**



Scheme 3.2 Synthesis of complex **3**. Conditions: (i) Tosyl chloride, CHCl₃, RT, 6h, 83%; (ii) DMM, DMF, reflux o/n, 77%; (iii) LiAlH₄, THF, 0°C to RT 4h, 90%; (iv) PBr₃, DCM, 0°C to reflux, 12h; (synthetic steps from (iv) to (vii) are in progress).

The synthesis of complex **3** was conceived with the aim of synthesizing a ligand (**Scheme 3.2**, **L3**) in which the C-substituted cyclam ring and the pyrene functionality were separated by a simple carbon chain.

The adopted synthetic pathway begins from the commercially available 1-pyrenebutanol, which is opportunely modified to react with a protected tetramine (bis-aminal, **Scheme 3.2**, (v)) in order to form the cyclam ring. This presented some additional complexity compared to the previous syntheses because of e.g., the number of synthetic steps and the necessity for several purification steps.

The preparation of the pyrene moiety started with the commercial 4-(1-pyrenyl)butanol, which was reacted with *p*-toluenesulfonyl chloride in the presence of pyridine to afford 4-(1-Pyrenyl)butyl tosylate (**7**) in high yield (83%), with slight modifications from a previously described procedure.^[18] The successive alkylation of dimethyl malonate (DMM) with **7**, which was adapted from elsewhere,^[19] afforded **8** in good yields after chromatographic purification (77%). The reduction of the ester groups of dimethyl 2-(4-(pyren-2-yl)butyl)malonate was carried on using LiAlH₄ as the reducing agent, leading to the diol **9**. The optimization of a previously reported protocol^[20] allowed to obtain yields up to 90% after purification.

The bis-aminal was synthesized by condensation of *N,N'*-bis (2-aminoethyl)-1,3-propanediamine with butanedione, following the method initially described by Hervè and collaborators.^[21]

Our efforts are now focused on the optimization of the reaction conditions for steps (iv) to (vii) (**Scheme 3.2**).

3.3 Discussion

Starting from the observations that *N*-substituted [Ni(cyclam)]²⁺ catalysts (in both homogeneous^[22–25] and heterogeneous^[7–9] conditions) poorly catalyze the CO₂RR in aqueous conditions, we have synthesized a novel *C*-substituted cyclam derivative, **2**, carrying a pyrene moiety, in order to immobilize a [Ni(cyclam)]²⁺ catalyst on carbon electrodes while maintaining its selectivity for CO in aqueous medium.

As for **2**, the synthetic pathway leading to ligand **L2** is reported herein for the first time; the characterization results (¹H NMR, ¹³C NMR, elemental analysis, MS, IR) all agree with the desired structure. The whole synthesis of complex **2** was designed in order to make the process scalable and as less time consuming as possible. As such, no arduous purification steps were

necessary. Mass spectroscopy confirmed the attainment of complex **2**, which from UV-Vis spectroscopy in MeOH showed a broad peak at approximately 550 nm, indicative of an octahedral geometry and a high-spin, paramagnetic state, with either solvent or chloride in the axial positions.^[26] Our efforts are now focused on the preparation of suitable crystals to further support these observations via X-ray diffraction.

Characterization of the electrochemical properties of complex **2** in DMF/H₂O using a glassy carbon electrode has revealed the following features. First, the one-electron reduction of Ni^{II} to Ni^I was recorded at the same potential as the unfunctionalized [Ni(cyclam)]²⁺ complex. The reversibility of this process, as well as the presence of the reversible Ni^{II}/Ni^{III} oxidation feature, further confirm a very similar metal center coordination. Second, catalysis for CO₂ electroreduction occurs at the Ni^{II}/Ni^I redox process, as shown by cyclic voltammetry, which indicates that the mechanism of the reaction catalyzed by complex **2** follows that of [Ni(cyclam)]²⁺.^[27] Third, as in the case of [Ni(cyclam)]²⁺, CO₂ reduction catalyzed by complex **2** is nearly totally selective (FY 96%) for CO production. Fourth, although only small current densities could be attained (as expected, considering the sluggish catalytic activity of [Ni(cyclam)]²⁺ itself on glassy carbon electrodes^[2,12,27]) complex **2** demonstrated its robustness after more than 2h electrolysis.

The pyrene-modified complex **2** has been immobilized on carbon nanotube-coated gas diffusion electrode using a non-covalent approach and the novel electrode, **2**/MWCNT/GDL, was characterized electrochemically for CO₂ electroreduction. Under such a heterogenized configuration, complex **2** showed very high selectivity for CO within a 200-mV range of potentials (from -2.03 to -2.23 V vs Fc⁺/Fc⁰) with only trace amounts of H₂ detected (in MeCN with 1% H₂O as a proton source). The hybrid electrodes provided current densities up to 3 mA.cm⁻², 30 times higher than those obtained from the catalyst in homogeneous (0.1 mA.cm⁻² for a 1 mM solution of complex **2**). Under these conditions, a Turnover Number of 14630 was obtained after 4 h electrolysis. When water was added to the catholyte (up to 10 v%), a notable increase in the catalytic wave for CO₂RR was accompanied to a shift to more positive potentials (with an onset potential at -1.89 V vs Fc⁺/Fc⁰).

Hence, **2**/MWCNT/GDL was also characterized for CO₂ electroreduction under aqueous conditions (0.1 M KHCO₃). Remarkably, current density proved stable in all cases within a range of potentials from -0.6 to -1.2 V vs. RHE for 20 min, and CO was the major product between -0.6 and -1 V, with the highest FY value (82%) obtained at both -0.6 and -0.8V vs. RHE (with a max current density of 5 mA.cm⁻²). When a longer experiment (4h) was carried

out using the **2**/MWCNT/GDL electrode, CO was the major product, despite a partial loss in selectivity and current density.

With these results, we have reached several important milestones in the development and utilization of $[\text{Ni}(\text{cyclam})]^{2+}$ as heterogenized molecular catalyst, as follows.

We have synthesized the first C-substituted $[\text{Ni}(\text{cyclam})]^{2+}$ catalyst bearing a pyrene moiety; with this, we obtained the most selective $[\text{Ni}(\text{cyclam})]^{2+}$ catalyst noncovalently heterogenized on carbon electrodes, with unprecedented high selectivity, up to 87% FY for CO, in water. Only two previous attempts for CO₂ electroreduction with a heterogenized $[\text{Ni}(\text{cyclam})]^{2+}$ in complete aqueous medium were described. Saravanakumar et al.^[28] reported impressive FY (up to 92%) for CO for a immobilized $[\text{Ni}(\text{cyclam})]^{2+}$; in this case, however, the hybrid electrode was fabricated by introducing the catalyst in a polyallylamine polymer via axial coordination of a pyridine moiety to the Ni center, and the lack of characterization and electrochemical information for the so-made hybrid electrode make these results of somehow difficult interpretation. More recently, Cowan and collaborators^[9] directly heterogenized a N-substituted pyrene-cyclam on gas diffusion electrode (GDE) via the noncovalent strategy, however the selectivity in water was less than 60% and it decreased rapidly over the course of 2h to less than 30%. The authors attribute the initial lack of selectivity primarily to the fact that the catalyst was substituted on the N atom on the cyclam ring.

On this regard, the comparison between our previously studied N-substituted $[\text{Ni}(\text{cyclam})]^{2+}$ pyrene catalyst^[8], **1**, and the new C-substituted one described herein, allowed us to provide experimental proof that substitution of N atoms in the cyclam ring leads to lower selectivity for CO when $[\text{Ni}(\text{cyclam})]^{2+}$ is immobilized on carbon electrodes (this phenomenon was proven only in homogeneous conditions).^[22–25]

Among the best heterogenized catalysts for CO₂RR in water via pyrene strategy, a molecular iridium pincer dihydride catalyst immobilized on carbon nanotube-coated GDEs allowed high TONs of formate with high selectivity in aqueous electrolyte.^[29] A pyrene-appended iron triphenyl porphyrin deposited on carbon nanotubes showed excellent selectivity for CO at 480 mV overpotential.^[16] The activity of the immobilized complex **2** has proven to be comparable to the aforementioned examples, and its performances exceed those of more recent ones, such as a pyrene-substituted $[\text{Mn}(\text{bpy})(\text{CO})_3\text{Br}]$,^[15] anchored on MWCNTs, or a pyrene-substituted rhenium^I diimine complex,^[30] which showed activity in H₂O, with CO as the primary reduction product, albeit at modest (65%) FY after 1h of CPE.

Although the present results are encouraging, the partial decrease in selectivity and current density observed during the 4h experiments have yet to be properly addressed. It is not yet possible to establish with certainty whether this phenomenon is due in part, or totally, to catalyst desorption during the electrolytic process, or whether catalyst deactivation (especially observed for homogeneous [Ni(cyclam)]²⁺ at GC electrodes^[31]) may play an important role.

Finally, another synthetic pathway for ligand **L3** and complex **3** was proposed. In this synthesis, the generation of the cyclam macrocycle will take advantage of a template strategy to “direct and protect” a linear tetramine, a method introduced by Hervé and coworkers^[21] for the first time, and widely exploited since, for the synthesis of tetraazamacrocycles.

Here, the objective was to synthesize a C-substituted [Ni(cyclam)]²⁺, in which the cyclam ring and the pyrene functionality were separated by a simple carbon chain, for the following reasons. First, the ligand would not present a functionality between the two moieties that could hinder the stability of the complex (e.g., in acid environment); Second, comparison between **2** and **3** could provide us information on the influence of the amide group on the catalytic efficiency of [Ni(cyclam)]²⁺, which, to the best of our knowledge, was never addressed before; Third, we expect that the presence of a 4-C chain between pyrene and cyclam, i.e., a relatively long chain with greater flexibility, would positively influence the electron transfer process, as already demonstrated for heterogenized ferrocene on diamond and graphitic surfaces.^[32,33]

3.4 Conclusion

In this chapter, we have reported the synthesis and characterization of a novel C-substituted Ni-Cyclam-pyrene complex in order to immobilize a [Ni(cyclam)]²⁺ catalyst on carbon electrodes while maintaining its selectivity for CO in aqueous medium.

The synthetic pathway, which was reported herein for the first time, was designed in order to make the process scalable and as less time consuming as possible. The redox properties of such complex were investigated under homogeneous conditions and a very similar metal center configuration to the parent [Ni(cyclam)]²⁺ was confirmed.

After the heterogenization on MWCNTs of the pyrene-modified complex using a non-covalent approach, the electrode was characterized electrochemically for CO₂ electroreduction. The complex proved to be extremely selective and stable in acetonitrile/water mixture, with

Chapter 3

Faradaic Yields for CO production above 98% and high turnover numbers (14630 after 4 h electrolysis).

When tested in aqueous conditions, the hybrid electrodes maintained the selectivity for CO with the highest FY value (82%) obtained at -0.8 V vs. RHE (current density 6 mA cm⁻²) after 20 min. Although a partial loss of selectivity and current density after 4h CPE, CO remained the major product. These unprecedented results also provided the experimental proof that substitution of N atoms in the cyclam ring leads to lower selectivity for CO when [Ni(cyclam)]²⁺ is immobilized on carbon electrodes.

3.5 Experimental Section

General

All starting materials were commercially available (Sigma, Acros Organics, Alfa Aesar and TCI) and were used without further purification. 1,4,8,11-tetraazacyclotetradecane-6-carboxylic acid was purchased from Chematech. Diethylether (Et₂O), tetrahydrofuran (THF), toluene and dichloromethane (DCM) were dried with an MBraun solvent purification system and stored under argon. All reactions were carried out under Ar atmosphere unless specified. Flash chromatography was performed using silica gel Silica Flash® 40-63 micron (230- 400 mesh). TLC detection was accomplished by irradiation with a UV lamp at 265 or 313 nm. Organic solutions were concentrated under reduced pressure on a Büchi rotary evaporator. Yields refer to purified compounds, unless otherwise stated. Melting points were determined on a Büchi B-545 device.

¹H and ¹³C NMR spectra were recorded on a 400 MHz NMR JEOL spectrometer (500 and 101 MHz for ¹H and ¹³C respectively), at room temperature unless specified, and are referenced either to tetramethylsilane (TMS) peak (at δ 0 ppm), or internally referenced to residual solvent signals, CDCl₃ referenced at δ 7.26 and 77.16 ppm.

Data for ¹H is reported as follows: chemical shift (δ ppm), multiplicity (s = singlet, d = doublet, t = triplet, q = quartet, m = multiplet), coupling constant (Hz), integration and assignment. Data for ¹³C are reported in terms of chemical shift, multiplicity (s = singlet, d = doublet, t = triplet, q = quartet, m = multiplet), coupling constant (Hz) and no special nomenclature is used for equivalent carbons.

UV-Vis spectra were recorded using a Agilent Cary 100 UV-Vis spectrophotometer. IR spectra were recorded on a Perkin Elmer Spectrum 65 FT IR Spectrometer and are reported in terms of frequency of absorption (cm⁻¹).

High-resolution mass spectra were obtained using ESI ionization on a Bruker Maxis Impact mass spectrometer.

Synthesis of Complex 2

1,4,8,11-tetrakis(tert-butoxycarbonyl)-1,4,8,11-tetraazacyclotetradecane-6-carboxylic acid (5): This protocol is modified from prior disclosed conditions.^[10] 1,4,8,11-tetraazacyclotetradecane-6-carboxylic acid (0.1 g, 0.26 mmol) and Na₂CO₃ (0.138 g, 1.30 mmol, 5.1 eq) were dissolved in H₂O (2.50 mL) and the solution was stirred for 10 minutes. Boc₂O (0.268 g, 1.23 mmol, 4.8 eq) in dioxane (2.50 mL) was added to this solution dropwise, and the reaction mixture was stirred at room temperature and monitored by TLC (R_f 0.5, EtOAc). After 72h, the solution was concentrated under vacuum to remove the dioxane. The aqueous phase was first extracted with Et₂O, then acidified with H₂SO₄ 3M to pH 1.0–2.0. The aqueous phase was then extracted with Et₂O/EtOAc (1:3). The organic layer was collected, washed twice with brine and water, dried over MgSO₄, and finally evaporated under vacuum. The product was obtained as a white solid with a glassy texture and was used without need of further purification. (0.137 g, yield 83%). Melting point 69°C.

IR (neat, ATR) $\tilde{\nu}$ /cm⁻¹: 3000, 2950, 2800, 1700, 1490, 1480, 1400

¹H NMR (400 MHz, CDCl₃, 55°C) δ 1.46 (s, 36H), 1.69-1.84 (m, 3H), 2.90 (t, 1H), 3.13-3.31 (m, 4H) 3.33-3.54 (m, 8H), 3.56-3.66 (m, 4H).

¹³C NMR (101 MHz, CDCl₃, 55°C) δ 175.73 (s), 155.81 (s), 80.62 (s), 80.05 (s), 77.44 (s), 77.08 (s), 76.81 (d, *J* = 32.0 Hz), 67.07 (s), 49.75 – 46.23 (m), 49.75 – 45.54 (m), 53.58 – 46.23 (m), 45.04 (s), 28.43 (d, *J* = 9.0 Hz).

1-Pyrenemethylamine: 1-Pyrenemethylamine hydrochloride (0.1 g, 0.38 mmol) was stirred in CH₂Cl₂ (10 mL) and KOH 2M (10 mL) for 2 hours. The organic layer was then collected, dried over MgSO₄ and finally evaporated under vacuum to leave the deprotected amine in quantitative yield (0.9 g, yield 100%). Melting point 172-173°C.

IR (neat, ATR) $\tilde{\nu}$ /cm⁻¹: 3000, 2861, 2500, 1586, 1495

¹H NMR (400 MHz, CDCl₃) δ 4.61 (s, 2H), 7.99-8.07 (m, 4H), 8.14-8.20 (ddd, *J* = 13.3, 8.4, 5.0 Hz 4H), 8.35 (d, *J* = 9.2 Hz, 1H).

Tetra-tert-butyl 6-((pyren-2-ylmethyl)carbamoyl)-1,4,8,11-tetraazacyclotetradecane-1,4,8,11 tetracarboxylate (6): This protocol was modified from prior disclosed conditions.^[34] A flame-dried round-bottomed flask was degassed, flushed with argon, and charged with 2mL

DCM, EDC-HCl (1-(3 dimethylaminopropyl)-3-ethylcarbodiimide hydrochloride, 0.039g, 0.2 mmol, 1.3 eq), and DMAP (0.21 mmol, 1.4 eq, 0.026g). The reaction flask was cooled to zero degrees in an ice bath. **5** (0.1 g, 0.15 mmol) was dissolved in 1 mL DCM and added to the previous mixture. After five minutes of stirring, 1-pyrenemethylamine (0.036g, 0.15 mmol, 1 eq) was dissolved in 1 mL DCM and added to the mixture. The ice bath was removed, the reaction was monitored via TLC (R_f 0.5, EtOAc:hexane 50:50) and allowed to stir overnight at RT. The reaction was then quenched with 4 mL 1M HCl and the organics separated. The aqueous layer was extracted three times with CHCl₃. All the organic layers were combined and dried over MgSO₄ and evaporated under vacuum. The crude product (0.12g ,93%) was used for the next step without purification. Melting point 114-115°C.

IR (neat, ATR) $\tilde{\nu}$ /cm⁻¹: 3000, 2900, 1700, 1550, 1475, 1300

¹H NMR (400 MHz, CDCl₃) δ 8.29 (d, J = 9.3 Hz, 1H), 8.15 (ddd, J = 13.0, 7.7, 3.6 Hz, 4H), 8.08 – 7.91 (m, 4H), 5.12 (d, J = 5.1 Hz, 2H), 3.63 (d, J = 6.4 Hz, 4H), 3.55 – 3.32 (m, 9H), 3.22 (dd, J = 32.0, 9.9 Hz, 4H), 2.94 – 2.72 (m, 1H), 1.77 (dt, J = 13.4, 6.6 Hz, 2H), 1.38 (d, J = 19.6 Hz, 36H).

HR-MS (ESI) exact mass calculated for [M+H]⁺ (C₄₈H₆₈N₅O₉) 858.49; found 858.50.

N-(pyren-2-ylmethyl)-1,4,8,11-tetraazacyclotetradecane-6-carboxamide (L2): The procedure was modified from previously described conditions^[35]. In a round-bottom flask, **6** (0.2g, 0.23 mmol), TFA (1.48g, 13.5 mmol, 56 eq) and 5 mL DCM were stirred under argon overnight at room temperature. Successively, the mixture was evaporated under vacuum. The orange solid that remained was dissolved in 0.5 mL water. KOH 2M was added until pH was 11-12. The mixture was stirred for 30 minutes, then the aqueous layer was extracted with CHCl₃ (three times). The organic layer was washed with water once, then dried over MgSO₄ and evaporated under vacuum to yield an off-white powder (0.1 g, 100% yield). Melting point 189-190°C.

IR (neat, ATR) $\tilde{\nu}$ /cm⁻¹: 3259, 3192, 3033, 2198, 2869, 2807, 1631, 1461, 1120, 839.

¹H NMR (400 MHz, CDCl₃) δ 10.19 (s, 1H), 8.32 (d, J = 9.2 Hz, 1H), 8.24 – 8.12 (m, 4H), 8.09 – 7.98 (m, 4H), 5.19 (d, J = 5.2 Hz, 2H), 3.12 (dd, J = 11.2, 4.3 Hz, 2H), 2.80 (dd, J = 11.3, 2.3 Hz, 2H), 2.65 – 2.33 (m, 9H), 2.12 (dt, J = 18.2, 7.0 Hz, 4H), 1.53 – 1.43 (m, 2H).

^{13}C NMR (101 MHz, CDCl_3) δ 174.18 (s), 132.60 (s), 131.43 (s), 130.99 (d, $J = 14.5$ Hz), 128.86 (s), 128.04 (s), 127.49 (d, $J = 8.1$ Hz), 126.80 (s), 126.19 (s), 125.56 – 125.00 (m), 124.95 (s), 123.14 (s), 51.69 (s), 50.66 (s), 49.03 (d, $J = 18.1$ Hz), 45.52 (s), 41.50 (s), 29.33 (s).

HR-MS (ESI) exact mass calculated for $[\text{M}+\text{H}]^+$ ($\text{C}_{28}\text{H}_{36}\text{N}_5\text{O}$) 458.28; found: 458.29.

Complex $[\text{Ni}^{\text{II}}(\text{Cl})_2(\text{L2})]^0$ (2): L2 (0.071 g, 0.16 mmol) and $\text{NiCl}_2 \cdot 6\text{H}_2\text{O}$ (0.037 g, 0.16 mmol) were mixed in 2 mL DMF. The solution turned pink after 10 minutes. After stirring 2h at room temperature, a pink precipitate formed. The precipitate was recuperated, washed with Et_2O , and dried under vacuum. (44.5 mg, 49 %).

UV-Vis [MeOH]: λ nm (ϵ , $\text{M}^{-1} \text{cm}^{-1}$): 543 (10.7), 389 (1880), 353 (10920), 343 (15000), 329 (10000), 277 (16300), 266 (11060), 241(32600), 232 (22120).

^1H NMR gave broad, unresolved peaks, typical of a paramagnetic complex.

HR-MS (ESI) exact mass calculated for $[\text{M}+\text{H}]^+$ ($\text{C}_{28}\text{H}_{35}\text{ClN}_5\text{NiO}$) 550.19; found 550.19.

Synthesis of Complex 3

4-(pyren-2-yl)butyl benzenesulfonate (7): This protocol was modified from prior disclosed conditions.^[18] To a solution of 4-(1-pyrenyl)butanol (0.1 g, 0.36 mmol) in dry chloroform (1 mL) at 0°C , were added first pyridine (0.058 g, 0.73 mmol, 2 eq) and then p-toluenesulfonyl chloride (0.1 g, 0.55 mmol, 1.5 eq) dropwise. After 30 minutes, the ice bath was removed and the reaction was monitored via TLC (R_f 0.7, EtOAc:Hexane 3:1). The mixture was stirred overnight at room temperature. The reaction mixture was then diluted with diethyl ether (3.3mL) and washed with HCl 10% (x2), H_2O , NaHCO_3 5% (x2), H_2O , and brine. The organic layer was recuperated, dried over MgSO_4 and evaporated under vacuum to give an oily residue. Crystallization in hexane:EtOAc (2:1 v/v) yielded the product as a pale yellow powder (0.12 g, 77%). Melting point $91\text{-}92^\circ\text{C}$.

IR (neat, ATR) $\tilde{\nu}/\text{cm}^{-1}$: 3043, 2966, 2932, 2860, 1600, 1441, 1347, 1168, 915, 857.

^1H NMR (400 MHz, CDCl_3) δ 8.23 – 8.12 (m, 3H), 8.09 (dd, $J = 9.6, 2.1$ Hz, 2H), 8.05 – 7.95 (m, 3H), 7.76 (ddd, $J = 16.5, 8.1, 2.1$ Hz, 3H), 7.23 (s, 2H), 4.15 – 4.02 (m, 2H), 3.31 (t, $J = 7.4$ Hz, 2H), 2.35 (s, 3H), 1.97 – 1.70 (m, 4H).

¹³C NMR (101 MHz, CDCl₃) δ 144.80 (s), 135.96 (s), 133.28 (s), 131.57 (s), 131.02 (s), 130.00 (d, J = 15.0 Hz), 128.74 (s), 127.99 (s), 127.73 – 127.23 (m), 126.87 (s), 126.02 (s), 125.10 (dd, J = 16.9, 14.0 Hz), 123.32 (s), 70.50 (s), 32.83 (s), 28.90 (s), 27.62 (s), 21.69 (s).

Dimethyl 2-(4-(pyren-2-yl)butyl)malonate (8): This protocol was modified from prior disclosed conditions.^[19] Dimethyl malonate (0.046 g, 0.35 mmol, 1.5 eq) was added to a suspension of NaH 60% (0.098 g, 0.245 mmol, 1.05 eq) in DMF (0.5 mL). The mixture was stirred for 30 min at room temperature, then **7** (0.1 g, 0.23 mmol) in 0.5 mL DMF was added dropwise. The reaction mixture was heated at 85°C and monitored via TLC (R_f 0.5, toluene). After 15h, the reaction was brought to room temperature and 1 mL H₂O was added. The mixture was extracted with EtOAc (x3) and the organic layer was washed with brine, then dried over MgSO₄ and finally evaporated under reduced pressure to give the crude product in the form of an off-white solid, which was purified by chromatography on silica gel eluting with toluene to give the pure product as a white solid (0.06g, 66%). Melting point 80-81°C.

IR (neat, ATR) $\tilde{\nu}$ /cm⁻¹: 3038, 2922, 2860, 1727, 1432, 1250, 1199, 1167, 1139, 847, 711.

¹H NMR (400 MHz, CDCl₃) δ 8.25 (d, J = 9.3 Hz, 1H), 8.20 – 8.08 (m, 4H), 8.06 – 7.94 (m, 3H), 7.85 (d, J = 7.8 Hz, 1H), 3.72 (s, 6H), 3.37 (dt, J = 15.7, 7.7 Hz, 3H), 2.09 – 1.81 (m, 4H), 1.51 (dd, J = 15.5, 7.5 Hz, 2H).

¹³C NMR (101 MHz, CDCl₃) δ 170.01 (s), 136.69 (s), 131.59 (s), 131.06 (s), 129.97 (s), 128.73 (s), 127.65 (s), 127.37 (d, J = 2.2 Hz), 126.74 (s), 125.95 (s), 125.34 – 124.72 (m), 123.49 (s), 52.62 (s), 51.78 (s), 33.36 (s), 31.49 (s), 28.89 (s), 27.59 (s).

HR-MS (ESI) exact mass calculated for [M+H]⁺ (C₂₅H₂₅O₄) 389.17; found 389.17.

2-(4-(pyren-2-yl)butyl)propane-1,3-diol (9): This protocol was modified from prior disclosed conditions^[20]. To a cooled mechanically stirred suspension of powdered LiAlH₄ (0.089g, 2.3 mmol, 4.1 eq) in anhydrous THF (2 mL) was added **8** (0.22 g, 0.57 mmol) in anhydrous THF (2 mL) dropwise. After 30 minutes the ice bath was removed and the reaction mixture was stirred at room temperature overnight. After completion of the reaction as indicated by TLC (R_f 0.5, EtOAc), Et₂O (2mL) was added, and the mixture was cooled with an ice bath. H₂O (0.08mL) was slowly added, then NaOH 2M (0.08mL) and water (0.24mL). The mixture was stirred at room temperature for 15 minutes, then MgSO₄ was added, and the reaction mixture was filtered through celite and the residue was washed profusely with ethyl acetate. The filtrate

Chapter 3

was washed with brine, dried over MgSO₄ and concentrated in vacuo and the resulting crude diol was purified by column chromatography on silica gel, using ethyl acetate to afford the product as a white solid. (0.135g, 72%) Melting point 80-81°C

IR (neat, ATR) $\tilde{\nu}$ /cm⁻¹: 3297, 3043, 2923, 2855, 1064, 1040, 1014, 841.

¹H NMR (400 MHz, CDCl₃) δ 8.27 (d, J = 9.2 Hz, 1H), 8.16 (dd, J = 7.4, 2.9 Hz, 4H), 8.07 – 7.95 (m, 3H), 7.86 (d, J = 7.7 Hz, 1H), 3.90 – 3.75 (m, 2H), 3.75 – 3.57 (m, 2H), 3.46 – 3.26 (m, 2H), 2.07 (t, J = 5.0 Hz, 2H), 1.94 – 1.83 (m, 2H), 1.79 (ddd, J = 10.3, 7.0, 3.4 Hz, 1H), 1.35 (dd, J = 15.7, 6.9 Hz, 2H).

¹³C NMR (101 MHz, CDCl₃) δ 137.00 (s), 131.60 (s), 131.07 (s), 129.93 (s), 128.75 (s), 127.67 (s), 127.37 (d, J = 5.5 Hz), 126.72 (s), 125.95 (s), 125.23 (d, J = 5.0 Hz), 125.12 – 124.72 (m), 123.56 (s), 66.76 (s), 42.20 (s), 33.58 (s), 32.24 (s), 27.79 (s), 27.50 (s).

HR-MS (ESI) exact mass calculated for [M+H]⁺ (C₂₃H₂₅O₂) 333.1849; found 333.1869.

9a,9b-dimethyloctahydro-1,3a,6a,9-tetra-azaphenalene (Bis-aminal) : the synthesis was carried on according to a reported method with slight modifications.^[21] A cooled solution of 0.29 g (3.41 mmol, 1 eq) of butanedione in 3 ml of acetonitrile is slowly added dropwise to a solution of 0.55 g (3.41 mmol) of N,N'-bis (2-aminoethyl)-1,3-propanediamine in 3.8 ml of acetonitrile at -10°C. The mixture is stirred vigorously and maintained at this temperature for two hours. After this time, the solvent is evaporated at the same temperature, leaving a light yellow solid which is subsequently purified by crystallization in hexane to give an off-white solid (0.66 g, 92%). Melting point 82-83°C

IR (neat, ATR) $\tilde{\nu}$ /cm⁻¹: 3226, 2492, 2811, 1501, 1390

¹³C NMR (101 MHz, CDCl₃) δ 73.52 (s), 68.31 (s), 51.36 (s), 49.21 (s), 46.86 (s), 45.86 (s), 42.27 (s), 39.42 (s), 23.85 (s), 18.53 (s), 10.96 (s).

Homogeneous Electrochemical Studies

All electrochemical experiments were performed on a VSP300 potentiostat (Bio-Logic Science Instruments SAS) and were conducted at room temperature in N,N-Dimethylformamide (DMF). 0.1 M tetrabutylammonium hexafluorophosphate (TBAPF₆) was used as the supporting electrolyte. The cyclic voltammetry (CV) experiments were carried out in a three-electrode setup (Chapter 2, **Figure 2.17**), with a 3 mm diameter glassy carbon (GC) electrode as a

working electrode, which was polished on a polishing cloth with a 1 μm diamond suspension (Struers), sonicated for 10 seconds, thoroughly rinsed with ethanol and dried prior to experiments. Platinum wire was used as a counter electrode and was previously flame annealed. The reference electrode was an Ag/AgCl electrode in a saturated KCl solution, equipped with a bridge to allow operation in organic solvent. All potentials were calibrated using the ferrocene/ferrocenium ($\text{Fc}^{+/0}$) redox couple as an internal standard, which was added in solution at the end of each measurement. In DMF, $E_{1/2}(\text{Fc}^{+}/\text{Fc}^0) = 0.60\text{V}$ vs Ag/AgCl/sat. KCl. Only the second cycle of all CVs are shown, although no difference in consecutive scans has been observed.

Controlled potential electrolysis (CPE) experiments were carried out in a gas-tight two-compartment electrochemical cell (Chapter 2, **Figure 2.18**) with two ceramic-PVDF composite membranes (16 μm thickness, Xuran) separating the anodic and cathodic compartments. The working electrode was a 1 cm^2 glassy carbon plate, the counter electrode was a platinum mesh and the reference electrode was an Ag/AgCl electrode in a saturated KCl solution, equipped with a bridge to allow operation in organic solvent. Anolyte and catholyte contained DMF and 2 M of H_2O as the proton source and 0.1 M of TBAPF_6 as the electrolyte. Only in the catholyte 1 mM of complex **1** was added. Both solution compartments were saturated with CO_2 during at least 20 minutes before starting the electrolysis, but no more gas was bubbled during the electrolysis. The experiments were conducted at room temperature under stirring at the cathode side. The volume of solution held by the cell in total was 22.6 mL, with ca. 10.6 mL of total headspace volume.

Gas products were quantified by gas chromatography (Model 8610C SRI Instruments) equipped with TCD and FID detectors from 50 μL aliquots of the headspace of the cathode compartments. Hydrogen (H_2) and carbon monoxide (CO) were detected by thermal conductivity detector (TCD) and flame ionization detector (FID), respectively. Liquid products were evaluated using an ionic exchange chromatograph (Metrohm 883 Basic IC) equipped with a Metrosep A Supp 5 column and a conductivity detector.

The faradaic yields were calculated by quantifying the products in the head-space gas of the cathodic side, on the basis of Equation 1:

$$\text{Faradaic efficiency} = \frac{N \times F \times n}{Q} \times 100 \quad (1)$$

Where Q, F, and N represented the charge passed through the system (C), Faraday's constant (C mol^{-1}), and moles of H_2/CO generated, respectively. In the reaction process, 2 moles of electrons were consumed to produce 1 mole of product, therefore $n = 2$.

Electrodes preparation and characterization

The electrodes used a 3 cm x 1 cm gas diffusion layer (GDL, AVCarb GDS 3250, Fuel Cell Store) strip, which was briefly sonicated in EtOH and let dry in air before utilization. MWCNTs (Sigma) were used after acid treatment as following: the raw MWCNTs material were dispersed in H₂SO₄ (2 M), sonicated for 1 h at ambient temperature, washed repeatedly with H₂O, then EtOH and dried in a vacuum oven at 70°C overnight. This acid treated MWCNTs (2 mg) were sonicated for at least 30 min in EtOH (200 μl) containing a solution of Nafion perfluorinated resin (5 μl of a 5 wt% solution in mixture of lower aliphatic alcohols containing 5% water). The suspension was then drop-casted on the GDL (1 cm² deposit) and dried in air at 70°C for at least 30 min. Subsequently, the GDL-MWCNT electrode was immersed in a solution of complex **1** in DMF (10 mM) overnight on an orbital shaker at low speed. Finally, the electrode was dried, washed with water then acetonitrile and dried in air.

SEM images were acquired using a Hitachi S-4800 scanning electron microscope. X-ray photoelectron spectra (XPS) were collected using a Thermo Electron Escalab 250 spectrometer with a monochromated Al Kα radiation (1486.6 eV). The analyzer pass energy was 100 eV for survey spectra and 20 eV for high resolution spectra. The analysed area was 500 mm². The photoelectron take-off angle (angle between the surface and the direction in which the photoelectrons are analysed) was 90°. Curve fitting of the spectra was performed with the Thermo Electron software Avantage. The electroactive sites were calculated through the integration of the oxidation wave in the CV scan (Figure S9) according to Equation 2:

$$\Gamma Ni = \frac{q}{nFA} \quad (2)$$

Where ΓNi is the number of electroactive sites (mol cm⁻²), q is the charge (C) obtained from the integration of the oxidation wave, n the number of electrons in the redox process per Ni center ($n = 1$), F is the Faraday constant (96485 C mol⁻¹), and A is the geometrical electrode area (1 cm²).^[15]

Heterogeneous Electrochemical Studies (organic solvent)

Linear sweep voltammetry (LSV) was performed for each sample before CPE, first under Ar and successively under CO₂. Gas was bubbled in the solution for at least 20 minutes before each experiment. The scan rate was 10 mV s⁻¹. CPE experiments were carried out in a gas-tight H-shape cell (Chapter 2, **Figure 2.18**) in which cathode and reference electrode are separated from the anode by an anion exchange membrane (AMV Selemion, ACG Engineering). The solvent used was acetonitrile containing 1% of H₂O, and the electrolyte was TBAPF₆ 0.1 M. The cathode used was a GDL on which MWCNs with the complex **1** were drop-casted as

described above, the anode was platinum and the reference electrode was an Ag/AgCl electrode in a saturated KCl solution, equipped with a bridge to allow operation in organic solvent. All potentials were calibrated using the ferrocene/ferrocenium (Fc⁺⁰) redox couple as an internal standard, which was added in solution at the end of each measurement. In acetonitrile, E_{1/2} (Fc⁺/Fc⁰) = 0.54V vs Ag/AgCl/sat. KCl. CO₂ gas was bubbled in the solution for at least 20 minutes before each experiment and no more gas was bubbled during the electrolysis. The experiments were conducted at room temperature and under stirring at the cathode side. The volume of solution held by the cell in total was 22.6 mL, with ca. 10.6 mL of total headspace volume.

The electrolysis products (hydrogen, CO and formate) were quantified in a similar manner as in the homogeneous electrochemical studies part. The faradaic yields were calculated by quantifying the products in the head-space gas of the cathodic side, on the basis of Equation 1 (see above).

The following formulas

$$TON = \frac{\text{moles of product}}{\text{moles of catalyst}} \quad (3)$$

and

$$TOF = \frac{TON}{\text{reaction time [s]}} \quad (4)$$

were used to calculate Turnover Number (TON) and Turnover Frequency (TOF) values, respectively.

Heterogeneous Electrochemical Studies (water)

Linear sweep voltammetry (LSV) was performed for each sample before CPE, first under Ar and successively under CO₂. Gas was bubbled in the solution for at least 20 minutes before each experiment. The scan rate was 50 mV s⁻¹. CPE experiments were carried out in a gas-tight H-shape cell in which cathode and reference electrode are separated from the anode by an anion exchange membrane (AMV Selemion, ACG Engineering). The solvent used was H₂O, and the electrolyte was KHCO₃ 0.1 M. The cathode used was a GDL on which MWCNs with the complex **1** were drop-casted as described above, the anode was platinum and the reference electrode was an Ag/AgCl electrode in a saturated KCl solution. CO₂ gas was bubbled in the solution for at least 20 minutes before each experiment and a flux of CO₂ (5 mL/min) was kept during the electrolysis only on the cathode side. The experiments were conducted at room temperature and under stirring at the cathode side.

Chapter 3

The measured potentials vs. Ag/AgCl were converted to the reversible hydrogen electrode (RHE) scale according to the Nernst equation:

$$E_{RHE} = E_{Ag/AgCl} + 0.059 \text{ pH} + E^{\circ}_{Ag/AgCl} \quad (5)$$

where E_{RHE} is the converted potential vs. RHE, $E^{\circ}_{Ag/AgCl} = 0.1976$ at 25 °C (sat. KCl), and $E_{Ag/AgCl}$ is the experimentally measured potential against Ag/AgCl reference and the pH of a CO₂-saturated 0.1M KHCO₃ solution is ~ 6.8 (for 0.3 M KHCO₃ ~7.15 and 0.5 M KHCO₃ ~7.23).

The electrolysis products (hydrogen, CO and formate) were quantified in a similar manner as in the homogeneous electrochemical studies part. The faradaic yields were calculated by quantifying the products by gas chromatography (Model 8610C SRI Instruments) equipped with TCD and FID detectors, on the basis of Equation 1 (see above).

3.6 References

- [1] M. Beley, J. P. Collin, R. Ruppert, J. P. Sauvage, *J. Chem. Soc. - Ser. Chem. Commun.*, **1984**, 2, 1315–1316.
- [2] Y. Wu, B. Rudshiteyn, A. Zhanaidarova, J. D. Froehlich, W. Ding, C. P. Kubiak, V. S. Batista, *ACS Catal.*, **2017**, 7, 5282–5288.
- [3] A. Zhanaidarova, C. E. Moore, M. Gembicky, C. P. Kubiak, *Chem. Commun.*, **2018**, 54, 4116–4119.
- [4] X. Zhao, Y. Liu, *J. Am. Chem. Soc.*, **2020**, 142, 5773–5777.
- [5] J. Schneider, H. Jia, K. Kobirow, D. E. Cabelli, J. T. Muckerman, E. Fujita, *Energy Environ. Sci.*, **2012**, 5, 9502–9510.
- [6] A. Zhanaidarova, C. E. Moore, M. Gembicky, C. P. Kubiak, *Chem. Commun.*, **2018**, 54, 4116–4119.
- [7] A. Zhanaidarova, C. E. Moore, M. Gembicky, C. P. Kubiak, *Chem. Commun.*, **2018**, 54, 4116–4119.
- [8] S. Pugliese, N. T. Huan, J. Forte, D. Grammatico, S. Zanna, B. L. Su, Y. Li, M. Fontecave, *ChemSusChem*, **2020**, 13, 6449–6456.
- [9] F. Greenwell, G. Neri, V. Piercy, A. J. Cowan, *Electrochim. Acta*, **2021**, 392, 139015.
- [10] C. C. Liolios, C. Zikos, E. Fragozeorgi, D. Benaki, M. Pelecanou, I. Pirmettis, N. Ioannidis, Y. Sanakis, C. P. Raptopoulou, V. Psycharis, A. Terzis, et al., *Eur. J. Inorg. Chem.*, **2012**, 2012, 2877–2888.
- [11] Y. Zhao, D. Xue, H. Qi, C. Zhang, *RSC Adv.*, **2017**, 7, 22882–22891.
- [12] J. D. Froehlich, C. P. Kubiak, *J. Am. Chem. Soc.*, **2015**, 137, 3565–3573.
- [13] C. Costentin, M. Robert, J.-M. Savéant, *Chem. Soc. Rev.*, **2013**, 42, 2423–2436.
- [14] S. Creager, *Handb. Electrochem.*, **2007**, p.101.
- [15] B. Reuillard, K. H. Ly, T. E. Rosser, M. F. Kuehnel, I. Zebger, E. Reisner, *J. Am. Chem. Soc.*, **2017**, 139, 14425–14435.
- [16] A. Maurin, M. Robert, *J. Am. Chem. Soc.*, **2016**, 138, 2492–2495.
- [17] C. Costentin, M. Robert, J. M. Savéant, *Chem. Soc. Rev.*, **2013**, 42, 2423–2436.
- [18] F. M. Winnik, M. A. Winnik, S. Tazuke, C. K. Ober, *Macromolecules*, **1987**, 20, 38–44.
- [19] E. Brenna, F. Cannavale, M. Crotti, V. De Vitis, F. G. Gatti, G. Migliazza, F. Molinari, F. Parmeggiani, D. Romano, S. Santangelo, *ChemCatChem*, **2016**, 8, 3796–3803.
- [20] B. V. Subba Reddy, H. Kumar, P. Borkar, J. S. Yadav, B. Sridhar, *European J. Org. Chem.*, **2013**, 2013, 1993–1999.
- [21] G. Hervé, H. Bernard, N. Le Bris, J. J. Yaouanc, H. Handel, L. Toupet, *Tetrahedron Lett.*, **1998**, 39, 6861–6864.
- [22] M. Fujihira, Y. Nakamura, Y. Hirata, U. Akiba, K. Suga, *Denki Kagaku oyobi Kogyo Butsuri Kagaku*, **1991**, 59, 532–539.
- [23] E. Fujita, J. Haff, R. Sanzenbacher, H. Elias, *Inorg. Chem.*, **1994**, 33, 4627–4628.
- [24] J. Costamagna, G. Ferraudi, J. Canales, J. Vargas, *Coord. Chem. Rev.*, **1996**, 148, 221–248.

- [25] M. Aulice Scibioh, P. V Ragini, S. Rani, V. R. Vijayaraghavan, B. Viswanathan, *Proc. Indian Acad. Sci. Chem. Sci.*, **2001**, pp. 343–350.
- [26] T. D. Cook, S. F. Tyler, C. M. McGuire, M. Zeller, P. E. Fanwick, D. H. Evans, D. G. Peters, T. Ren, *ACS Omega*, **2017**, *2*, 3966–3976.
- [27] M. Beley, J. P. Collin, R. Ruppert, J. P. Sauvage, *J. Am. Chem. Soc.*, **1986**, *108*, 7461–7467.
- [28] D. Saravanakumar, J. Song, N. Jung, H. Jirimali, W. Shin, *ChemSusChem*, **2012**, *5*, 634–636.
- [29] P. Kang, S. Zhang, T. J. Meyer, M. Brookhart, *Angew. Chemie Int. Ed.*, **2014**, *53*, 8709–8713.
- [30] S. Sinha, A. Sonea, W. Shen, S. S. Hanson, J. J. Warren, *Inorg. Chem.*, **2019**, *58*, 10454–10461.
- [31] J. D. Froehlich, C. P. Kubiak, *Inorg. Chem.*, **2012**, *51*, 3932–3934.
- [32] D. Dhar, C. G. McKenas, C. W. Huang, J. M. Atkin, J. L. Dempsey, M. R. Lockett, *ACS Appl. Energy Mater.*, **2020**, *3*, 8038–8047.
- [33] R. E. Ruther, Q. Cui, R. J. Hamers, *J. Am. Chem. Soc.*, **2013**, *135*, 5751–5761.
- [34] D. C. Miller, G. J. Choi, H. S. Orbe, R. R. Knowles, *J. Am. Chem. Soc.*, **2015**, *137*, 13492–13495.
- [35] S. J. Krivickas, E. Tamanini, M. H. Todd, M. Watkinson, *J. Org. Chem.*, **2007**, *72*, 8280–8289.

3.7 Appendix

Complex 2 Heterogeneous CO₂ reduction

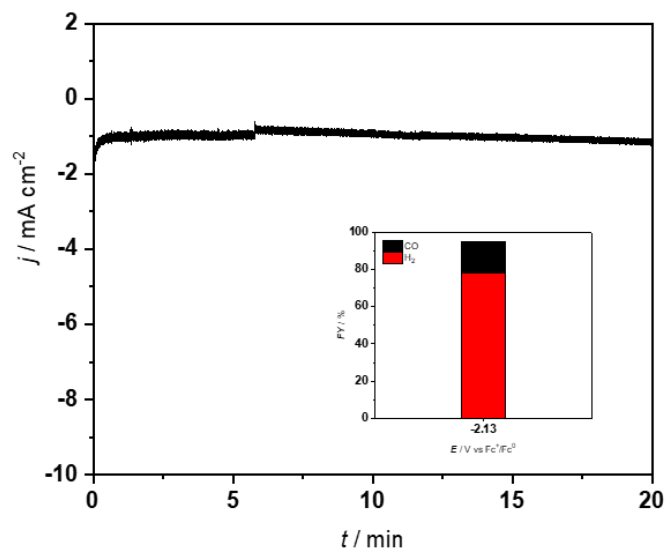


Figure A3.1 Controlled-Potential Electrolysis at -2.13V vs. Fc⁺/Fc⁰ using MWCNT/GDL in acetonitrile with 0.1M TBAPF₆ and 1% H₂O. Inset: Faradaic yields for CO and H₂ after 20min electrolysis.

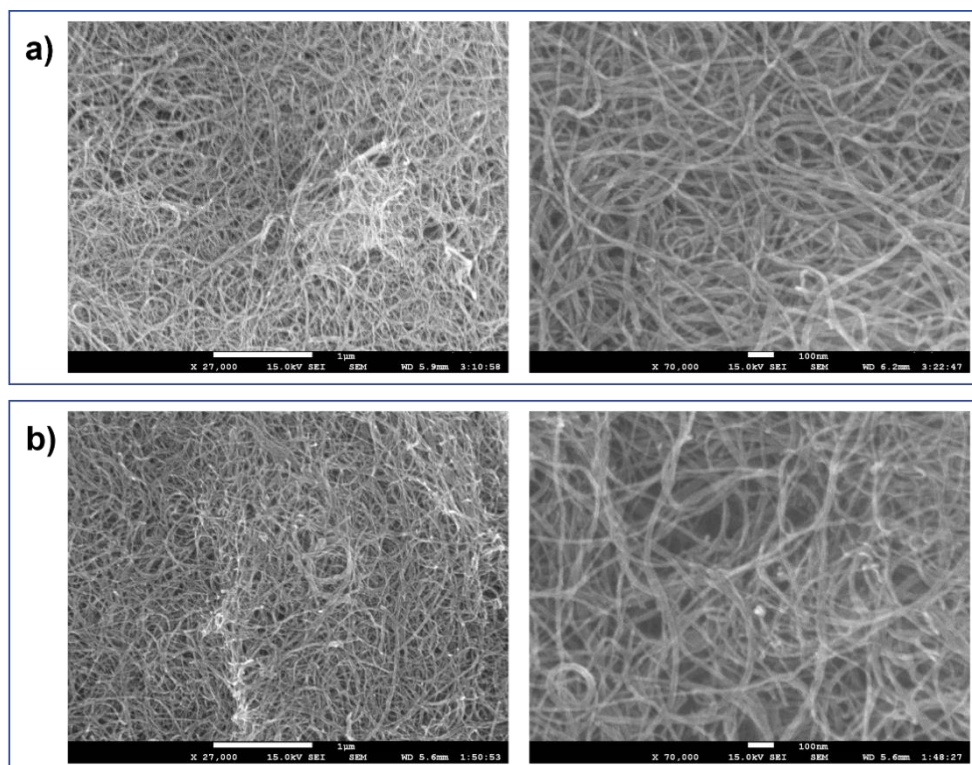


Figure A3.2 SEM images of 2/MWCNTs/GDL electrode a) before and b) after 4h electrolysis.

Complex 1 and complex 2: comparison

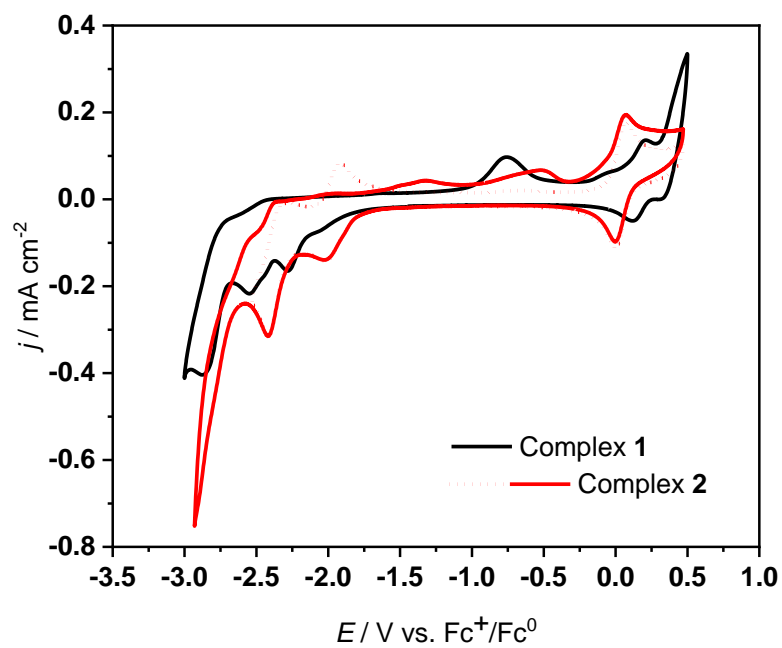


Figure A3.3 Comparison of CVs of 1 mM complex 2 and complex 1 (DMF with 0.1M TBAPF₆, under Ar and at room temperature, scan rate 100 mV s⁻¹).

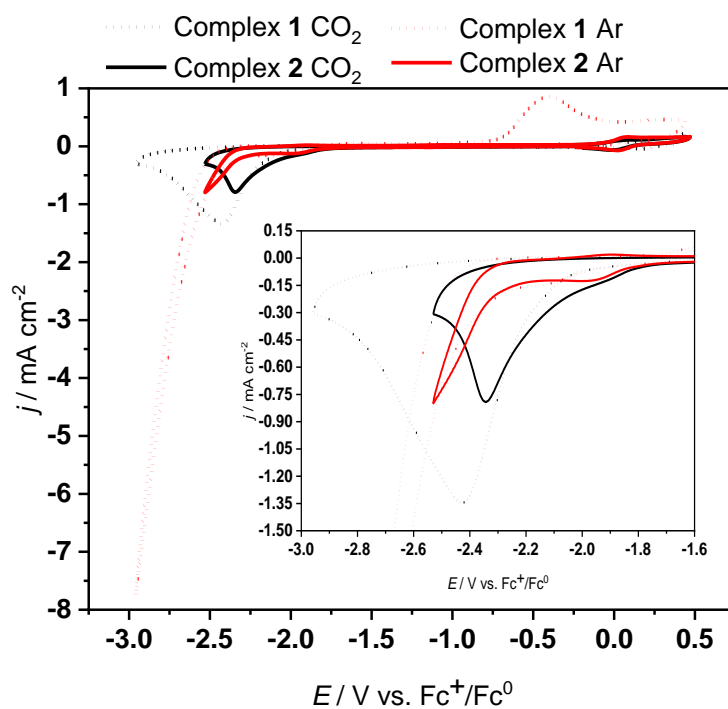


Figure A3.4 Comparison of CVs of 1 mM complex **2** and complex **1** (DMF with 0.1M TBAPF_6 and H_2O 2M, under Ar or CO_2 and at room temperature, scan rate 100 mV s^{-1}).

Synthesis of complex 2

1,4,8,11-tetrakis(tert-butoxycarbonyl)-1,4,8,11-tetraazacyclotetradecane-6-carboxylic acid (5)

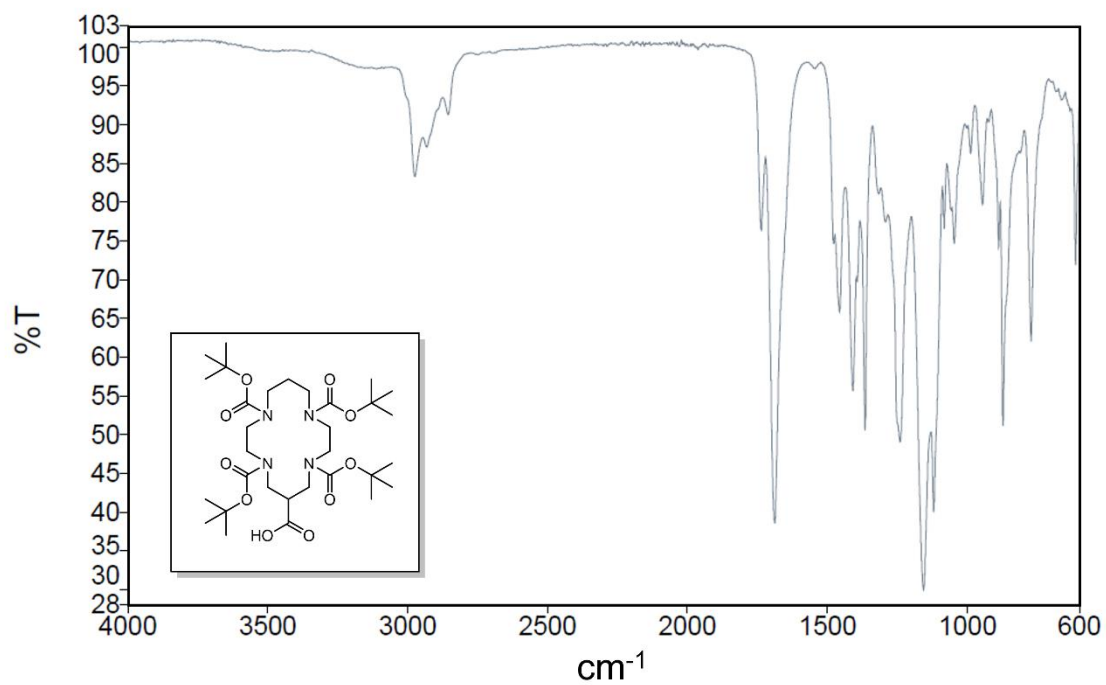


Figure A3.5 FT-IR spectrum of 5 (powder)

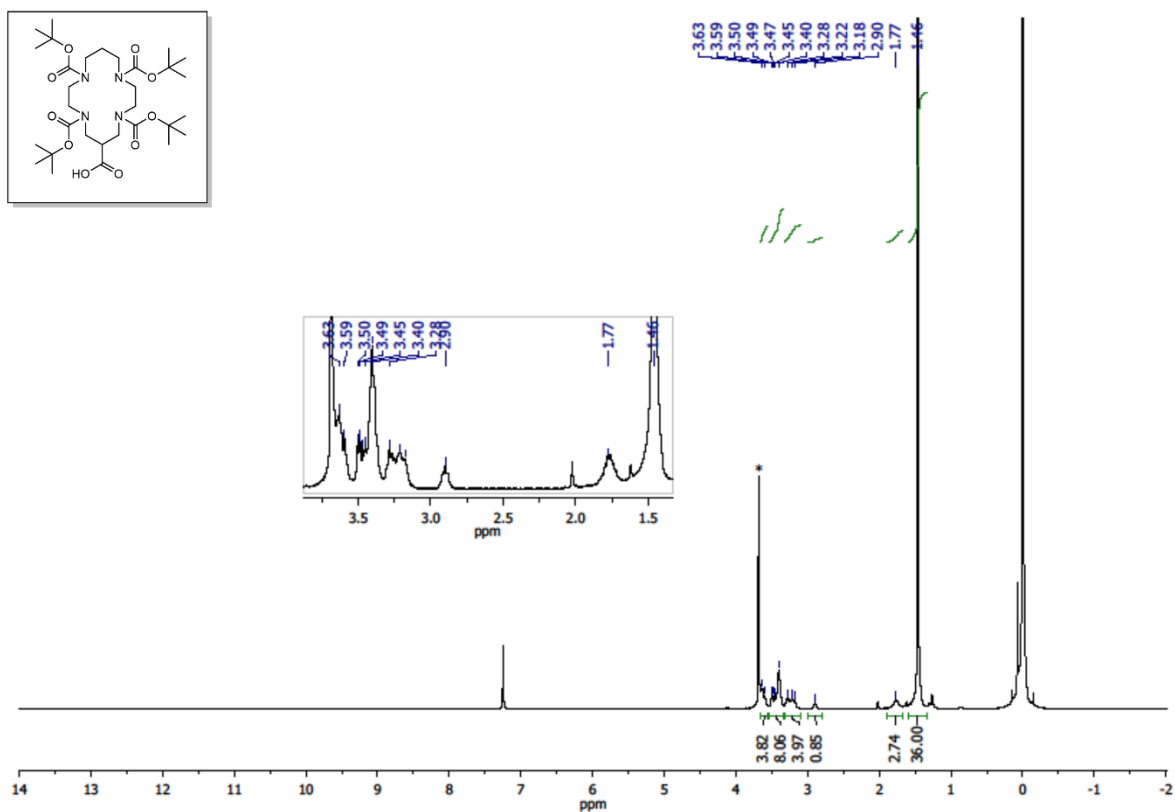


Figure A3.6 ¹H NMR (400 MHz, 50 °C, CDCl₃) of 5

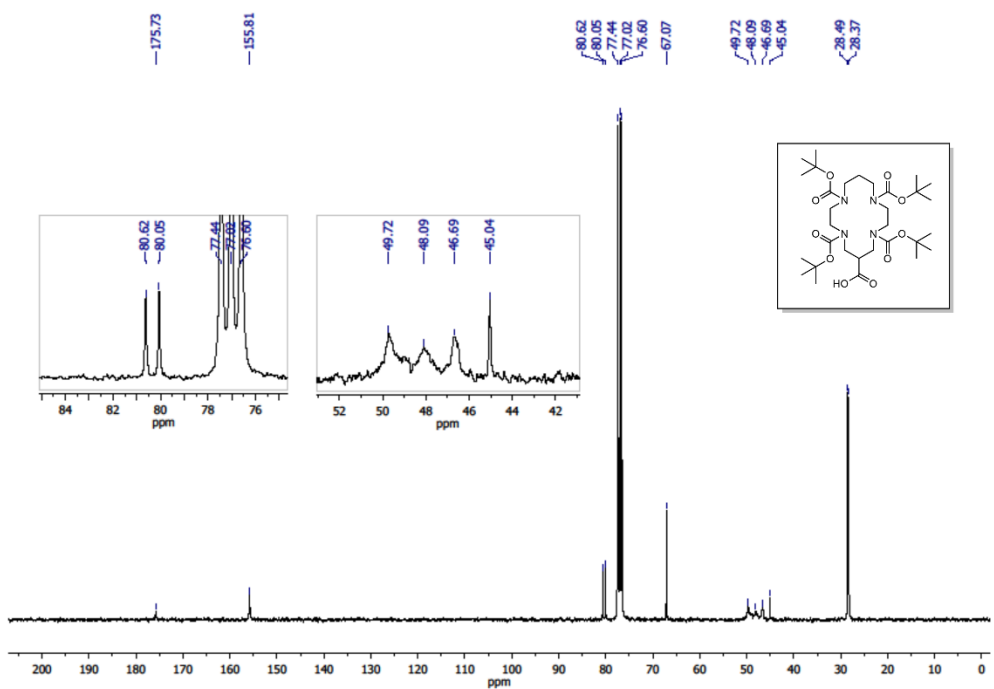


Figure A3.7 ¹³C NMR (101 MHz, 55 °C, CDCl₃) of 5.

1-Pyrenemethylamine

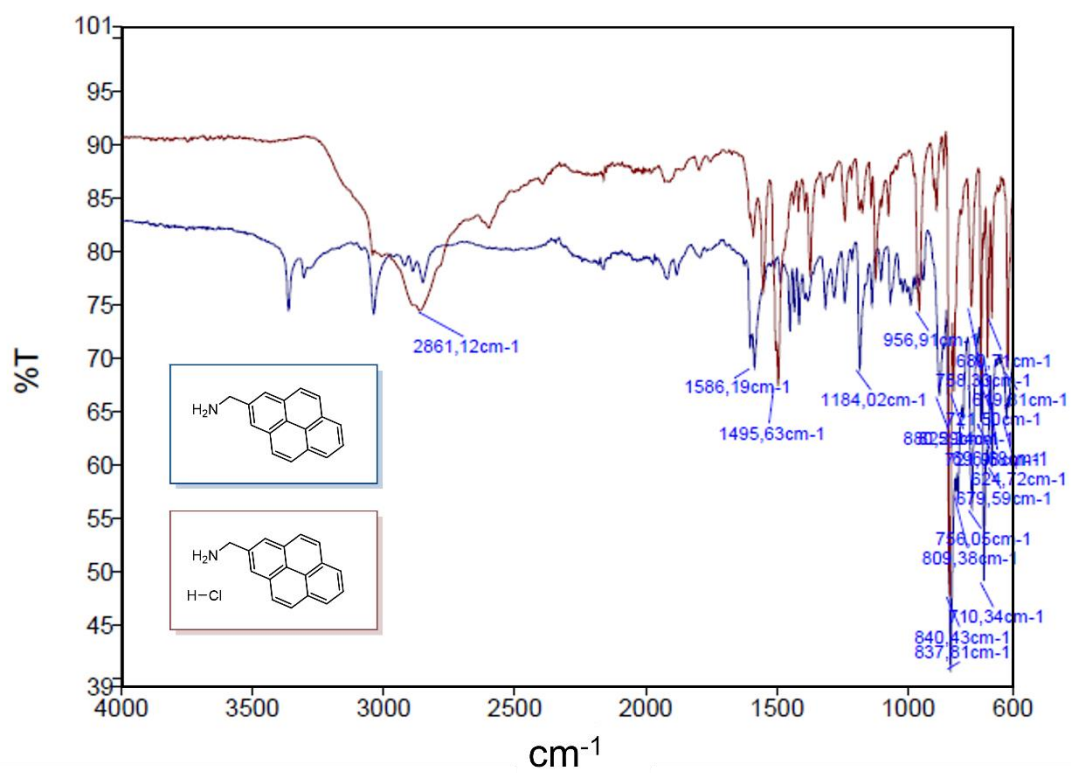


Figure A3.8 FT-IR spectrum of 1-pyrenemethylamine (blue) and its hydrochloride salt (brown) (powders).

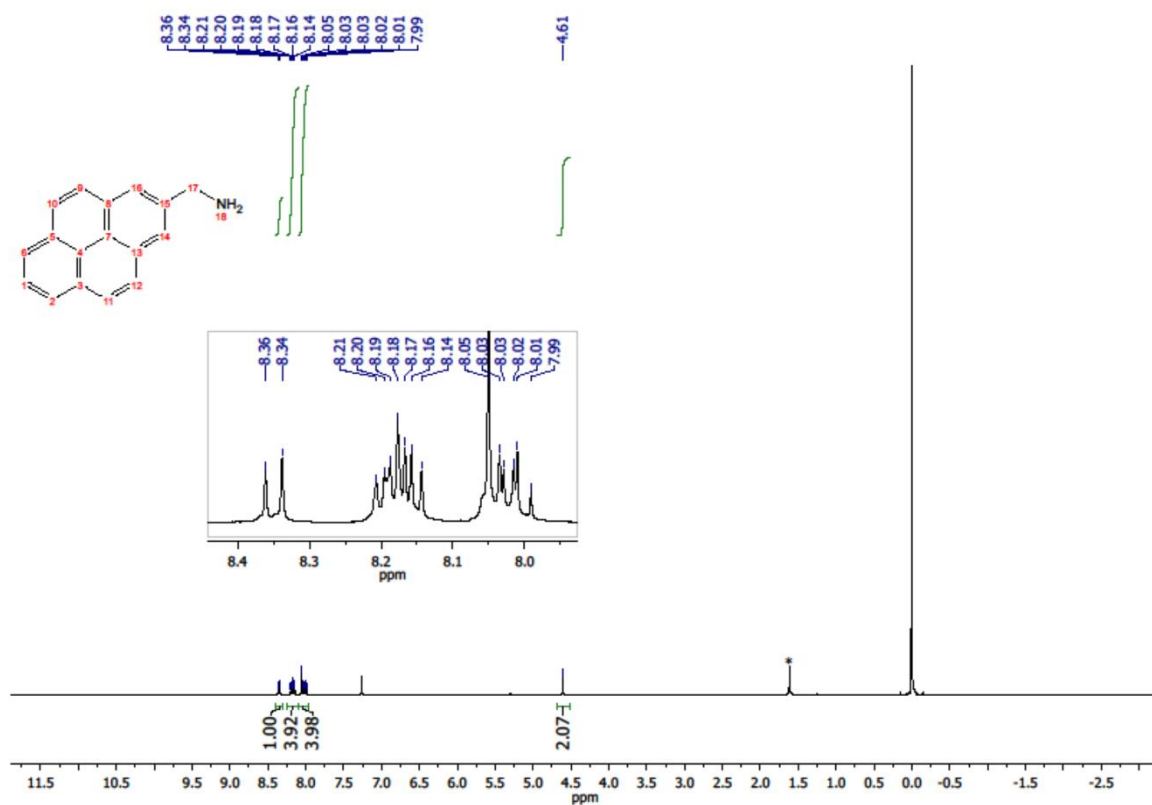


Figure A3.9 ¹H NMR (400 MHz, 25°C, CDCl₃) of 1-Pyrenemethylamine

Tetra-tert-butyl 6-((pyren-2-ylmethyl)carbamoyl)-1,4,8,11-tetraazacyclotetradecane-1,4,8,11-tetracarboxylate (6)

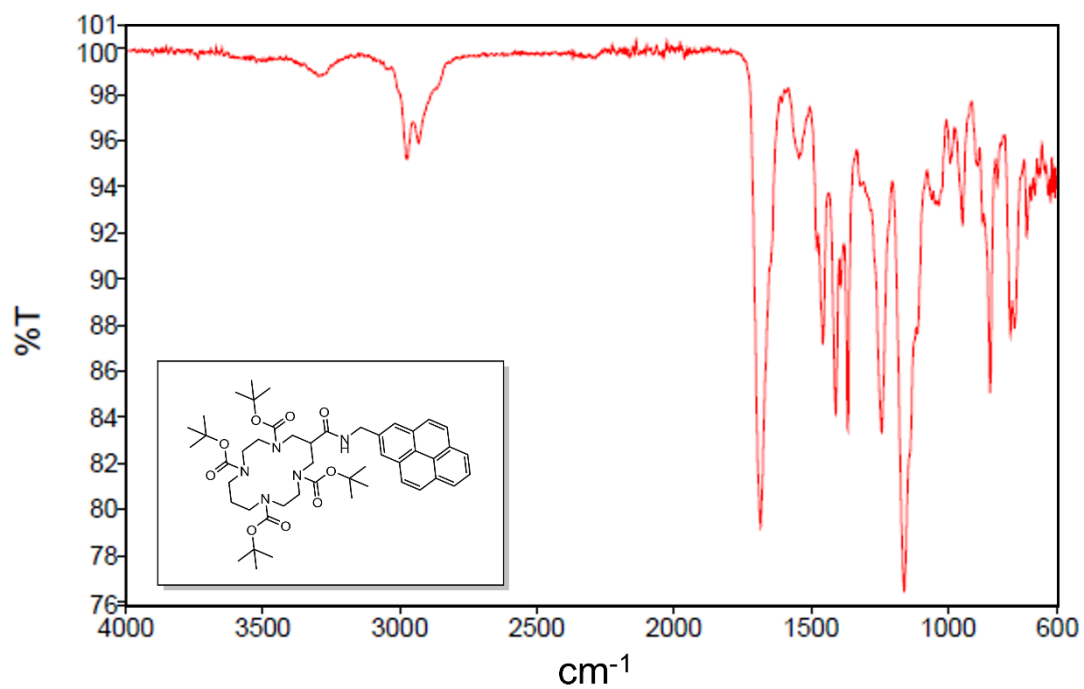


Figure A3.10 FT-IR spectrum of **6** (powder)

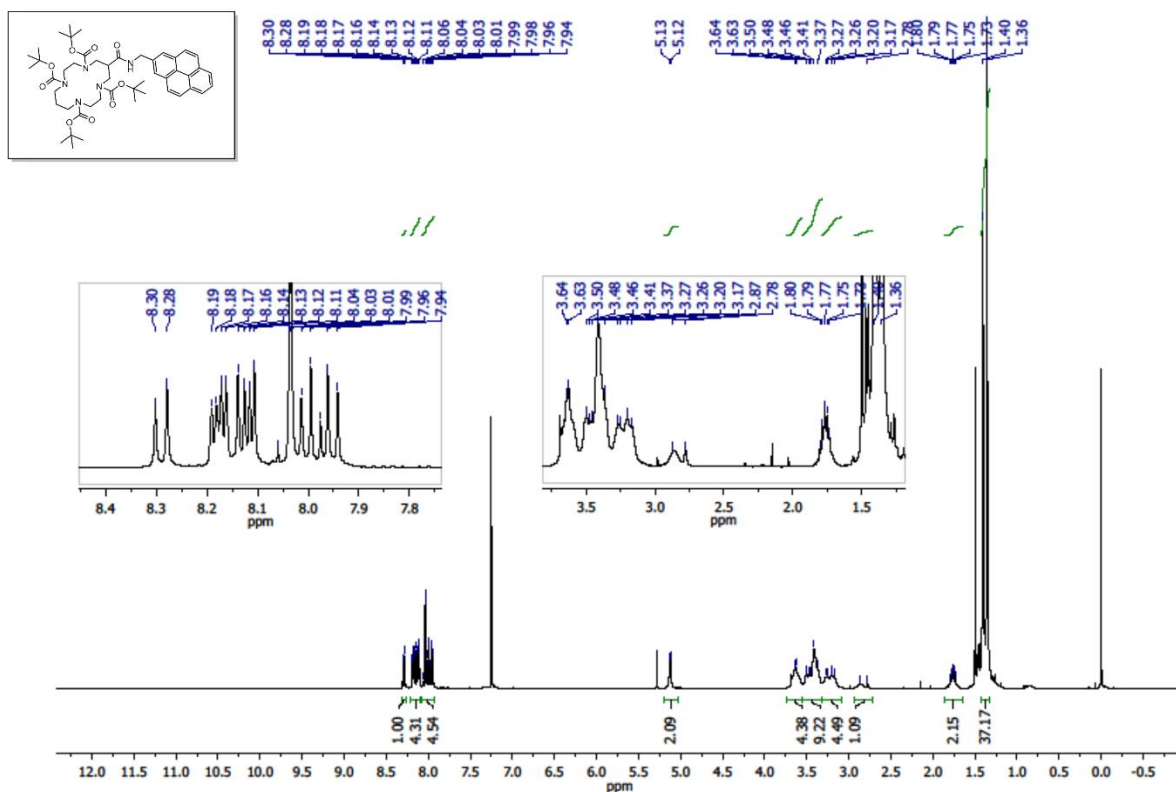


Figure A3.11 ¹H NMR (400 MHz, 50°C, CDCl₃) of **6**

N-(pyren-2-ylmethyl)-1,4,8,11-tetraazacyclotetradecane-6-carboxamide (**L2**)

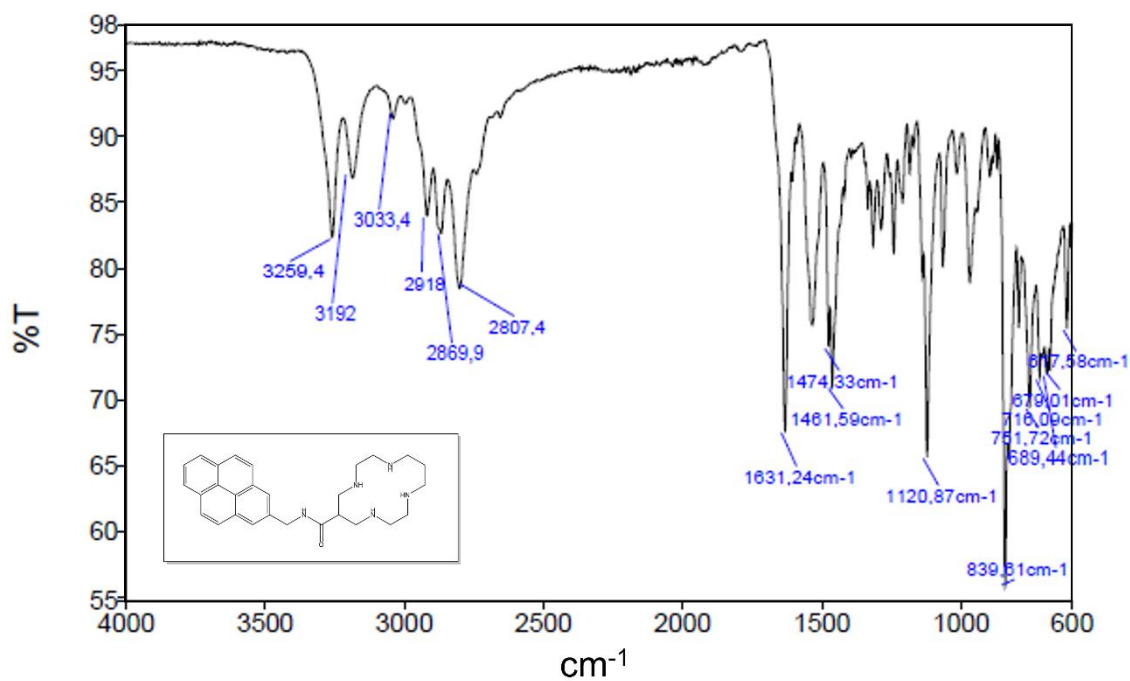


Figure A3.12 FT-IR spectrum of **L2** (powder)

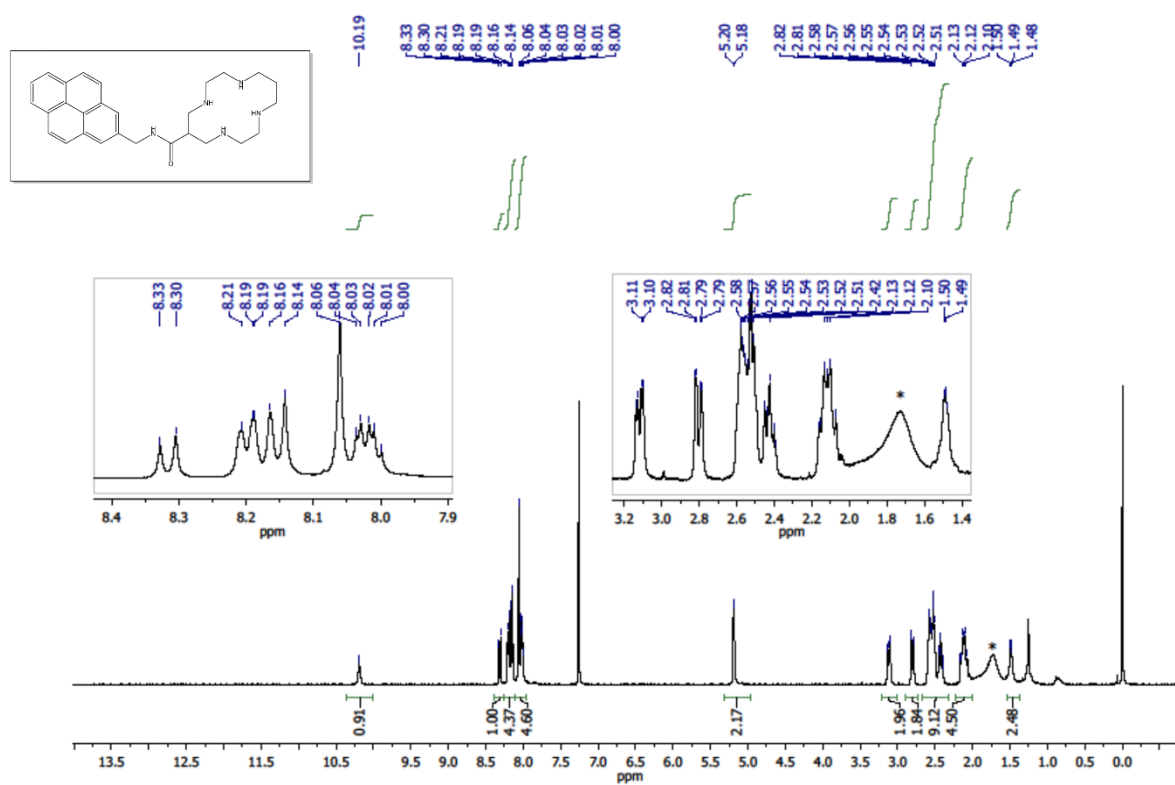


Figure A3.13 ^1H NMR (400 MHz, 25°C, CDCl_3) of L2

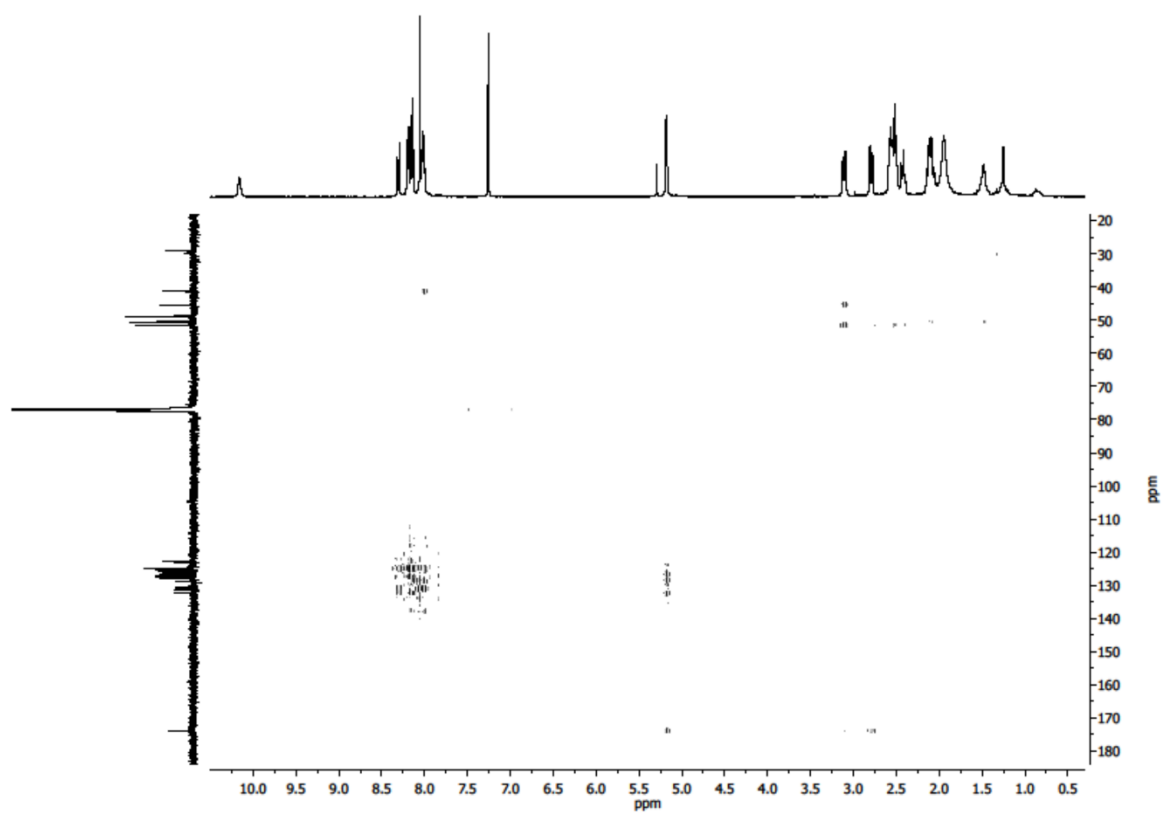


Figure A3.14 2D HMBC NMR (101 MHz, 400 MHz, 25°C, CDCl₃) of **L2**

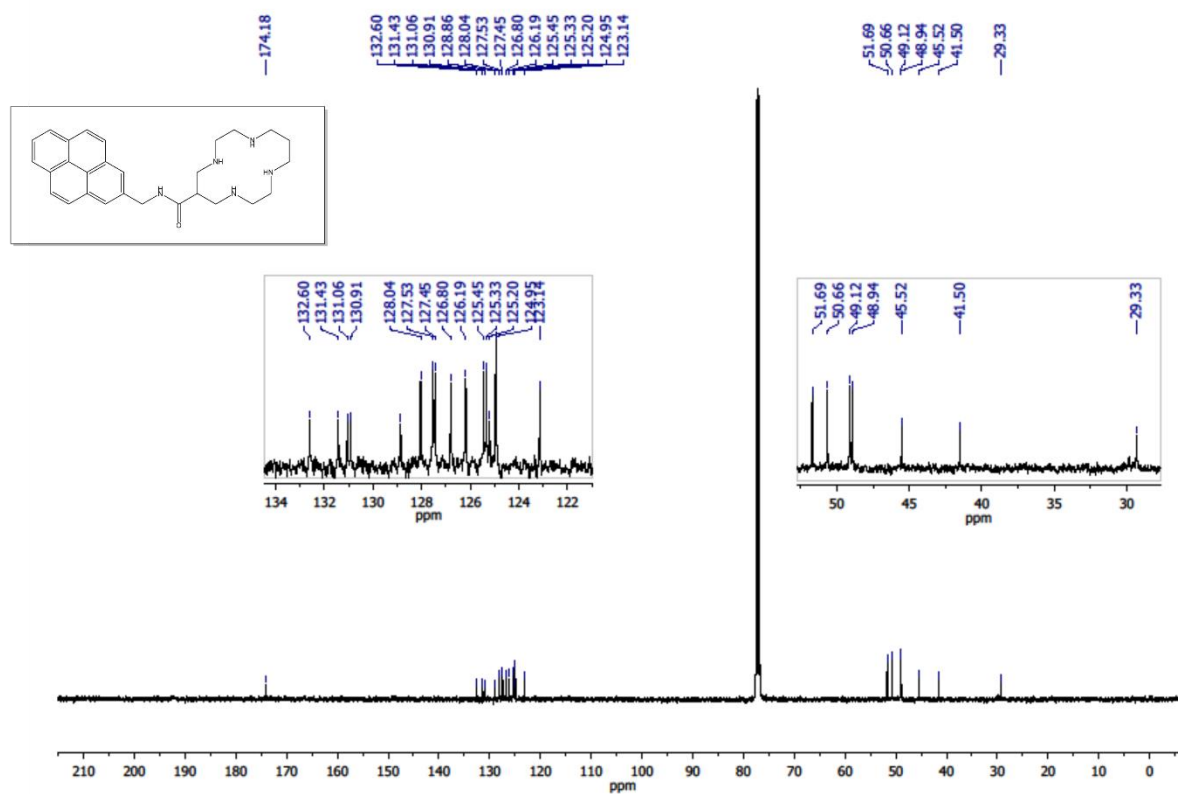


Figure A3.15 ^{13}C NMR (101 MHz, 25 °C, CDCl_3) of L2.

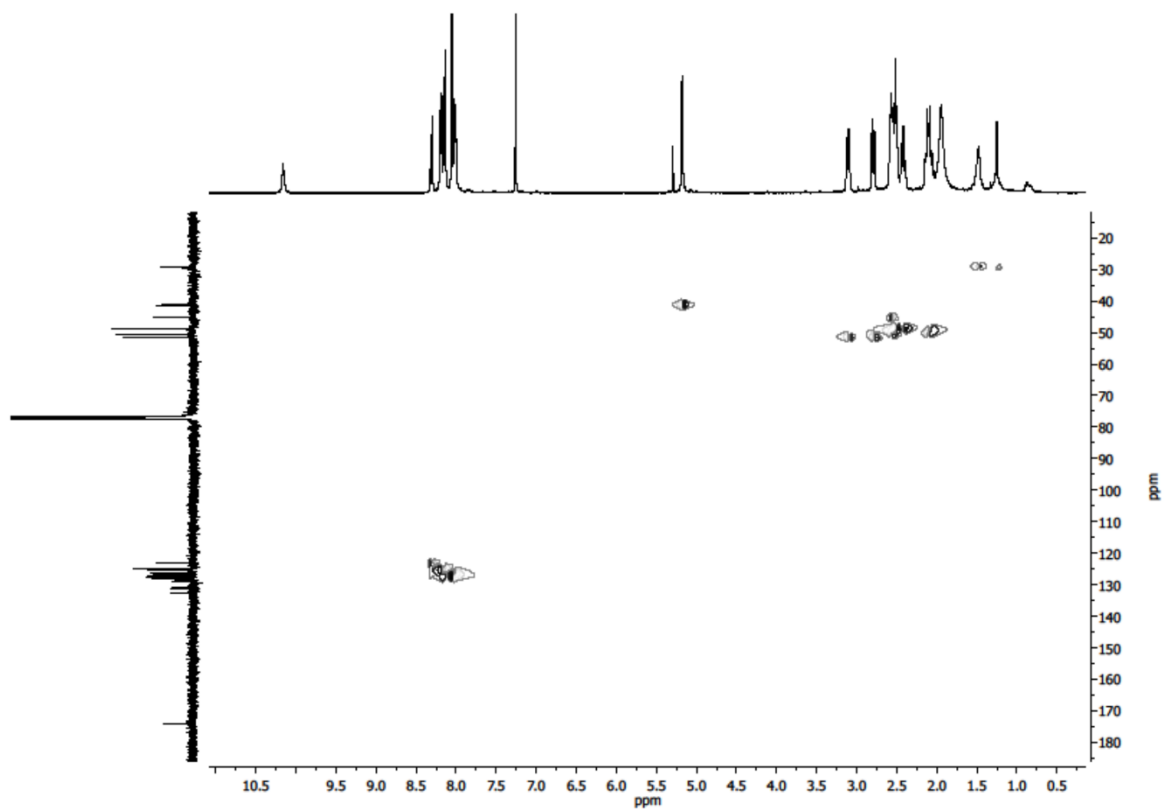
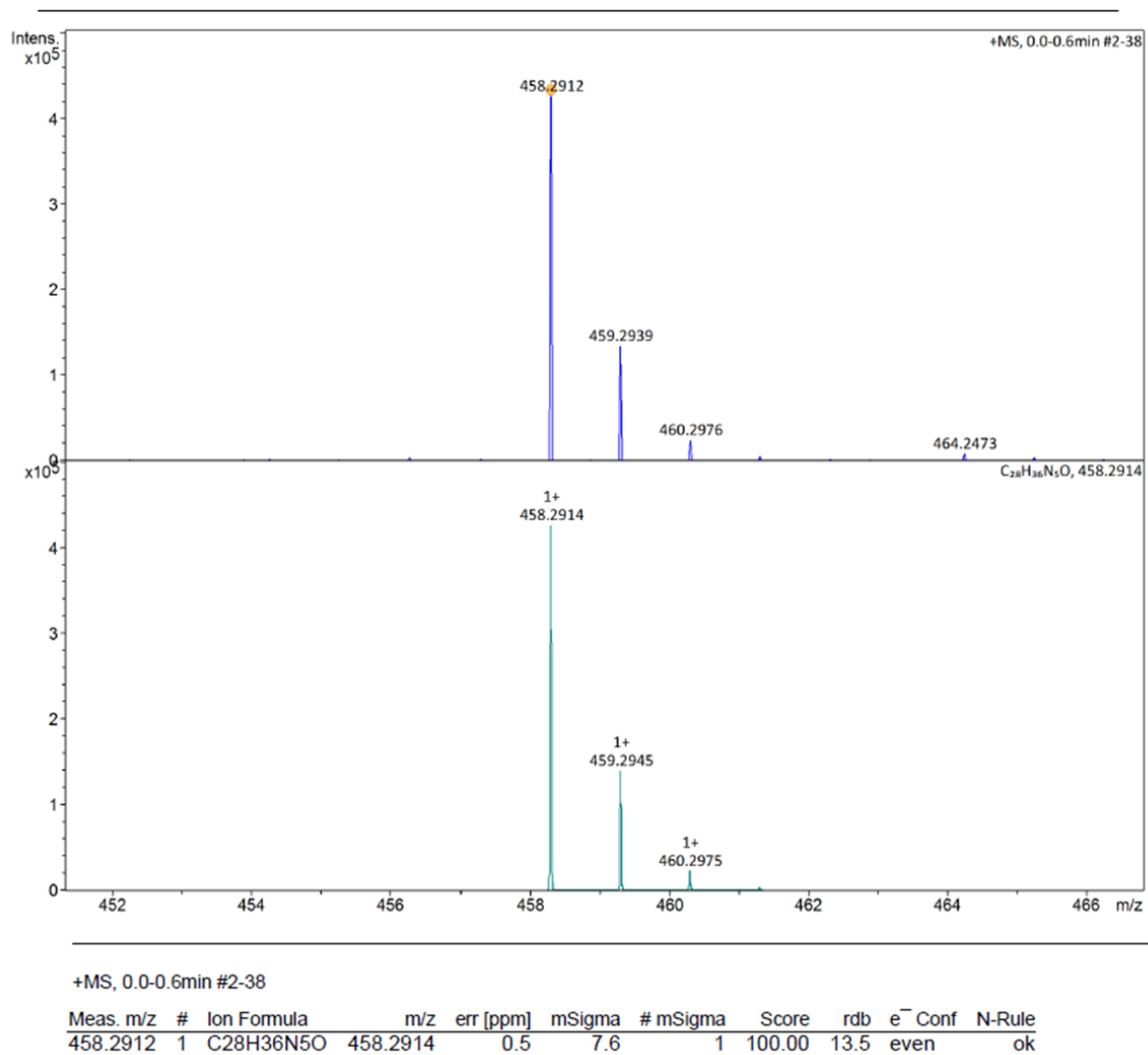


Figure A3.16 2D HSQC NMR (101 MHz, 400 MHz, 25°C, CDCl₃) of **L2**

**Figure A3.17** MS (ESI) report for L2

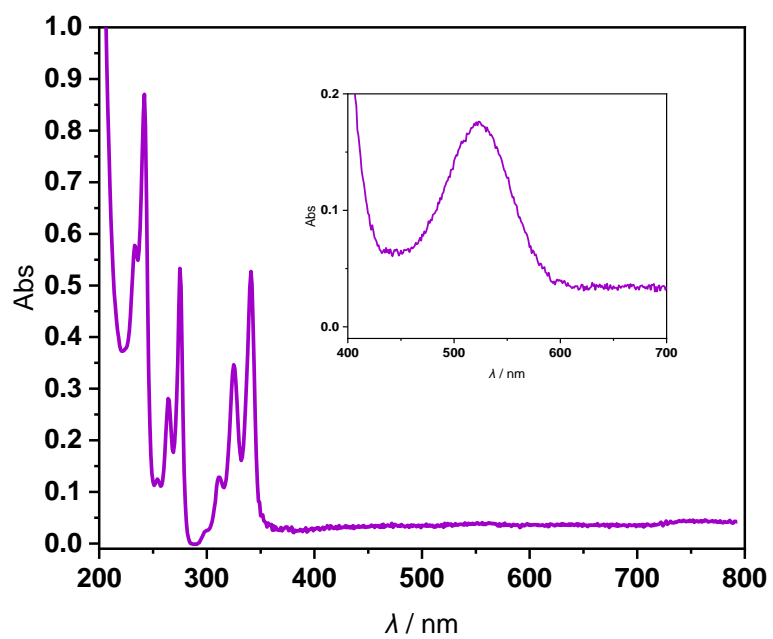


Figure A3.18 UV-Vis spectrum of complex 2 (25°C, MeOH)

Synthesis of complex **3**

4-(pyren-2-yl)butyl benzenesulfonate (**7**)

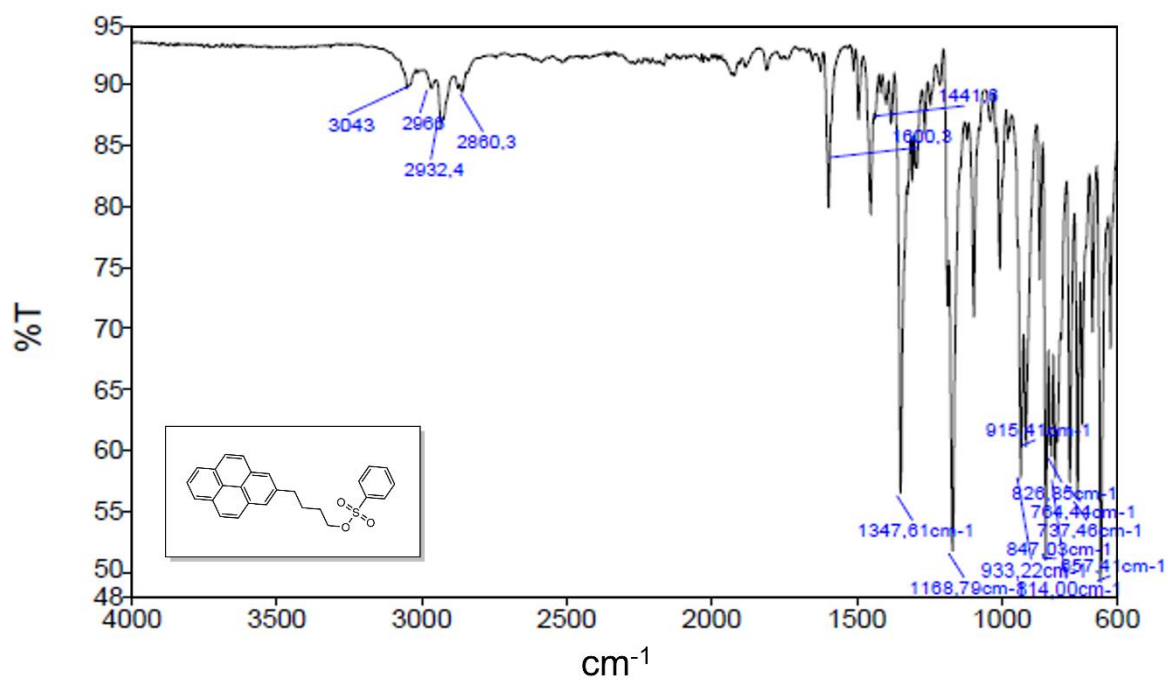


Figure A3.19 FT-IR spectrum of **7** (powder)

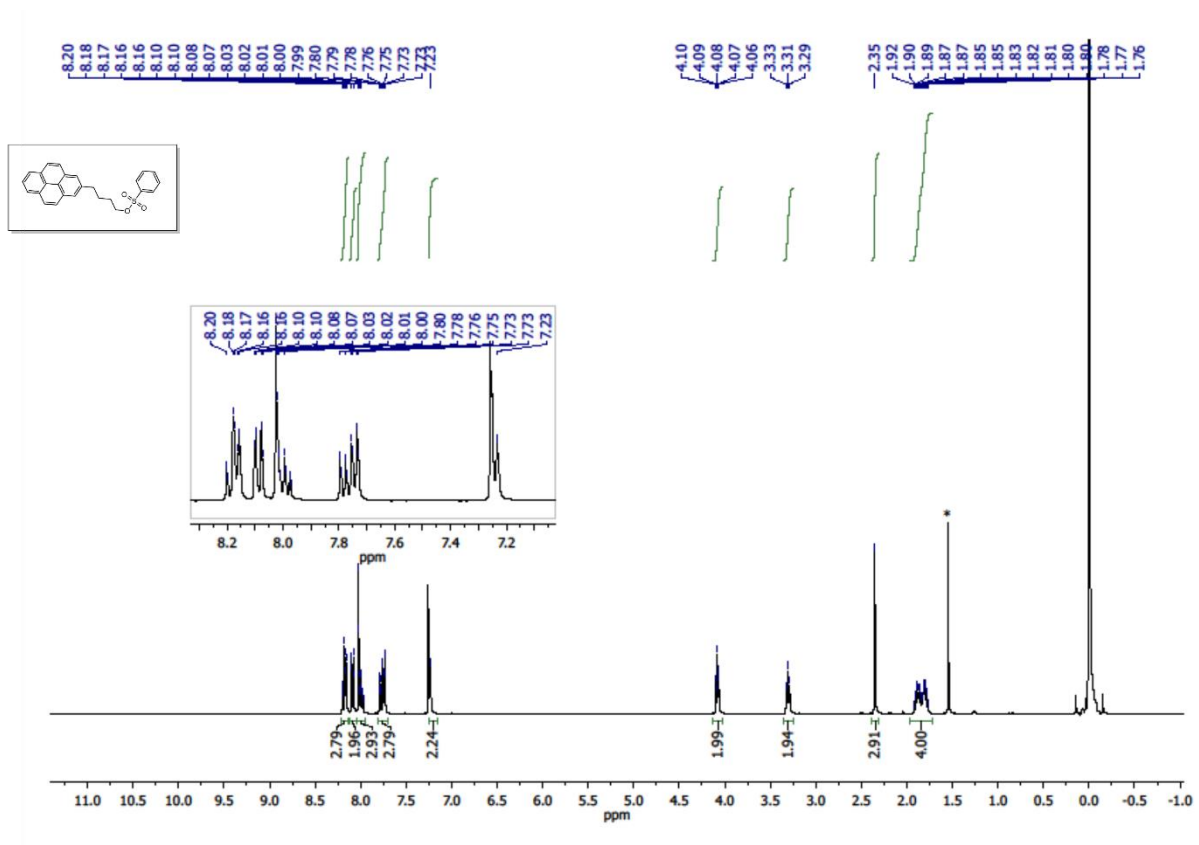


Figure A3.20 ¹H NMR (400 MHz, 25°C, CDCl₃) of 7

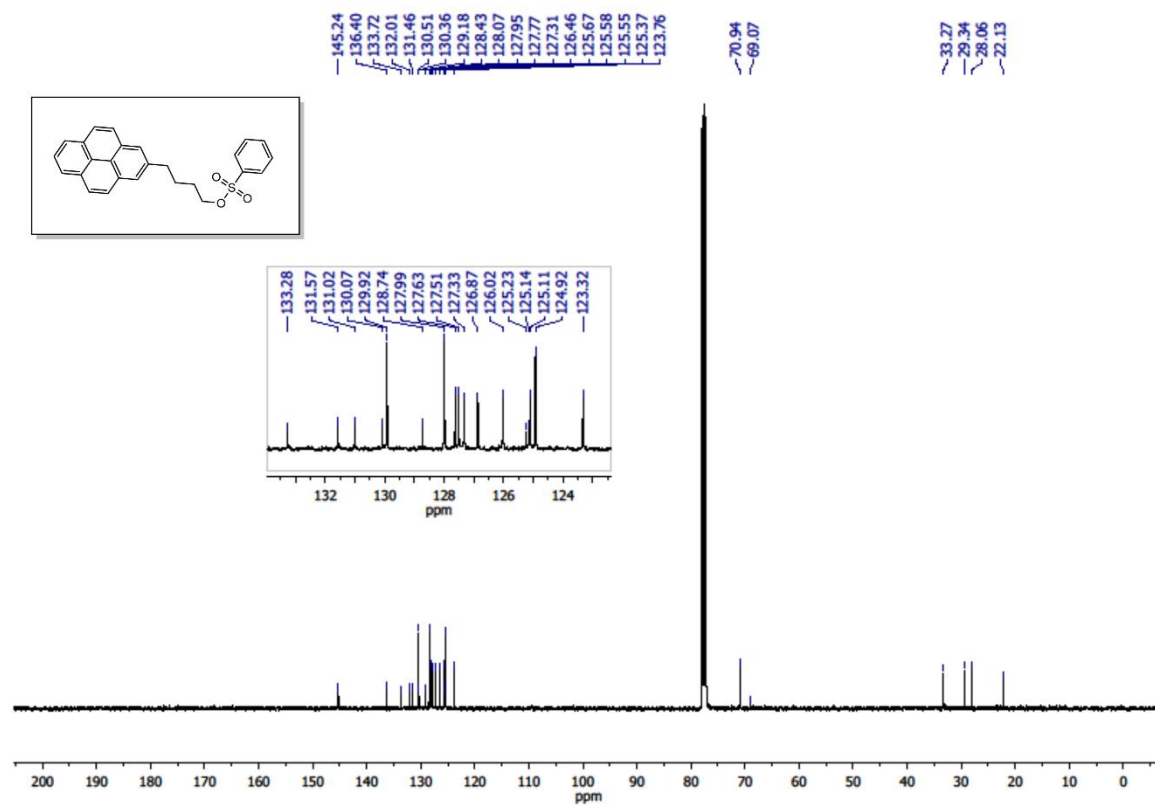


Figure A3.21 ^{13}C NMR (101 MHz, 25 °C, CDCl_3) of 7.

Dimethyl 2-(4-(pyren-2-yl)butyl)malonate (**8**)

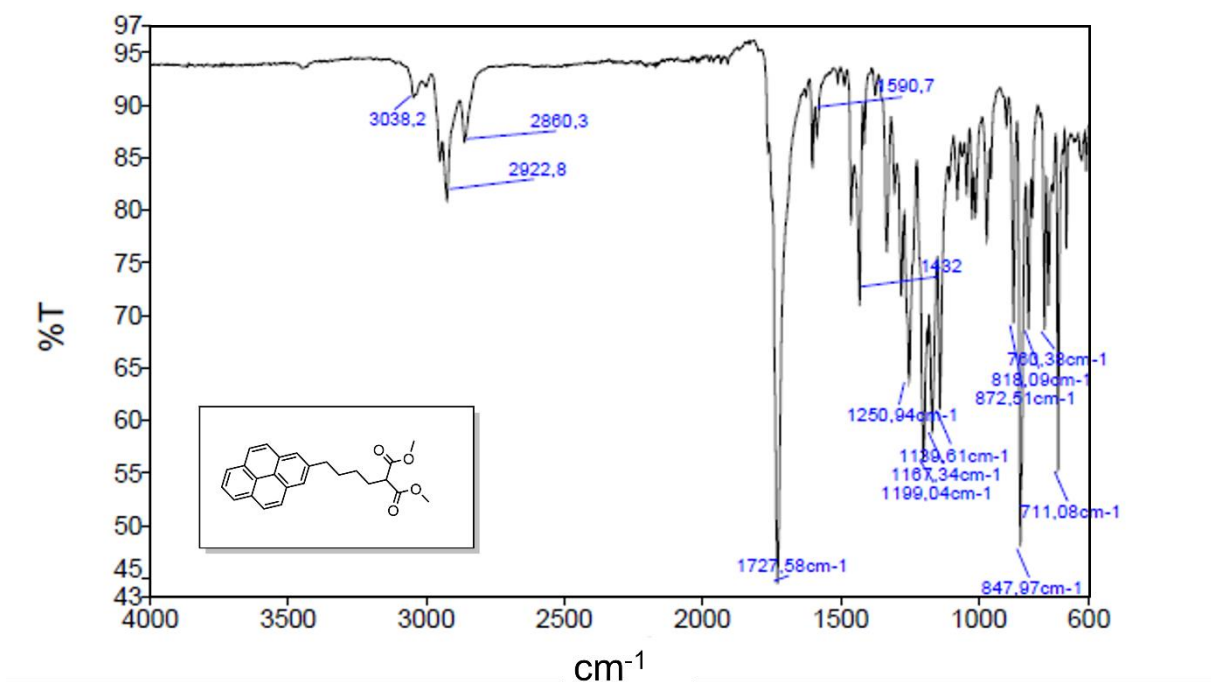


Figure A3.22 FT-IR spectrum of **8** (powder)

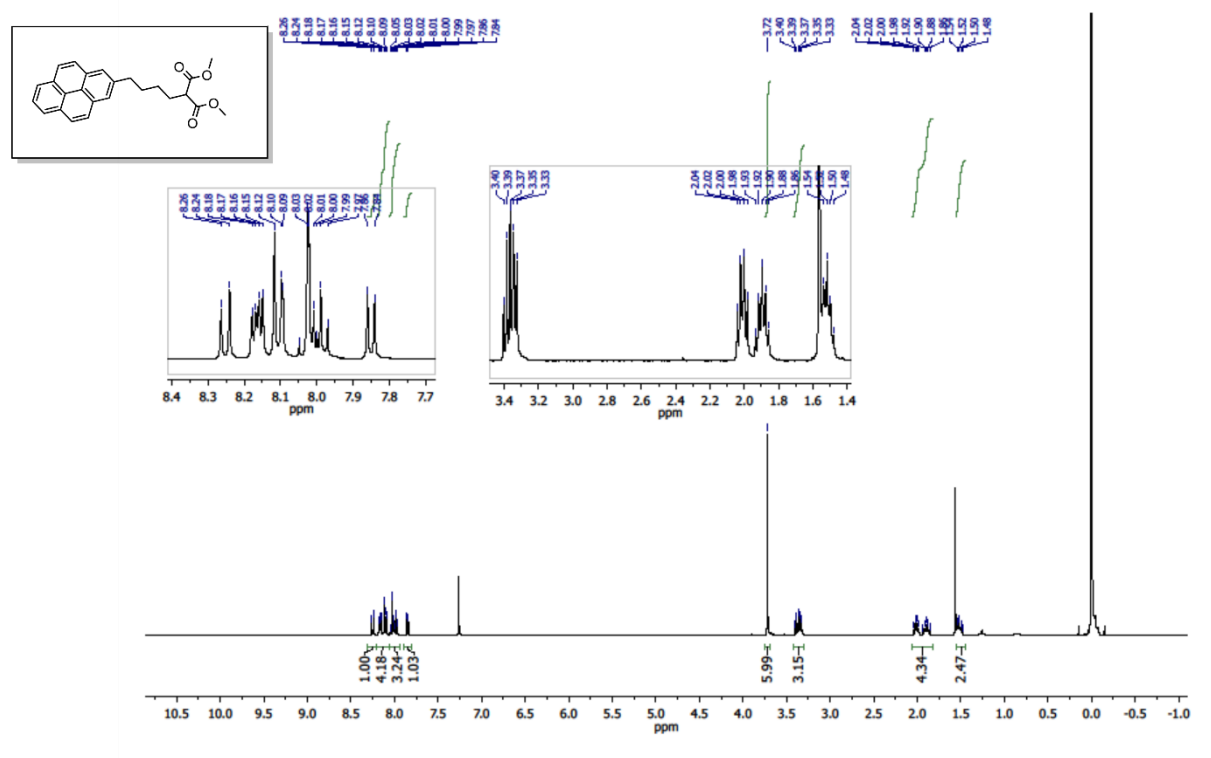


Figure A3.23 ¹H NMR (400 MHz, 25°C, CDCl₃) of **8**.

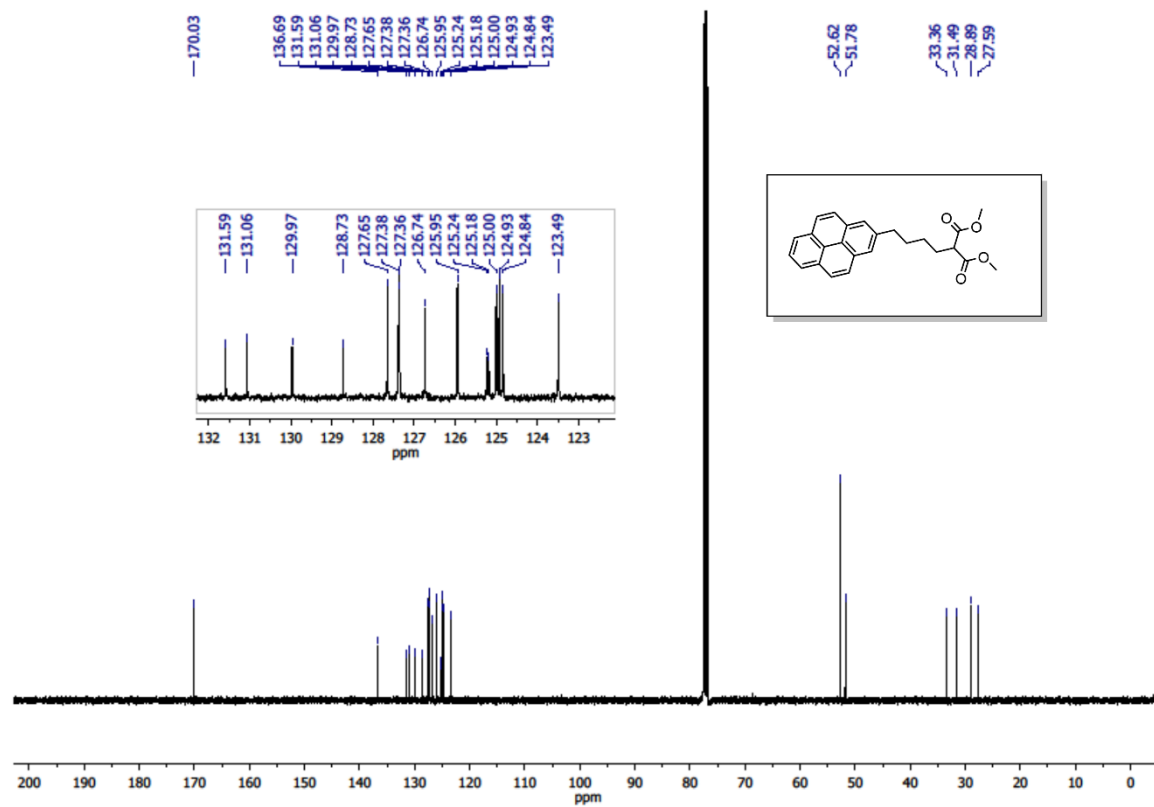


Figure A3.24 ^{13}C NMR (101 MHz, 25 °C, CDCl_3) of **8**.

2-(4-(pyren-2-yl)butyl)propane-1,3-diol (**9**)

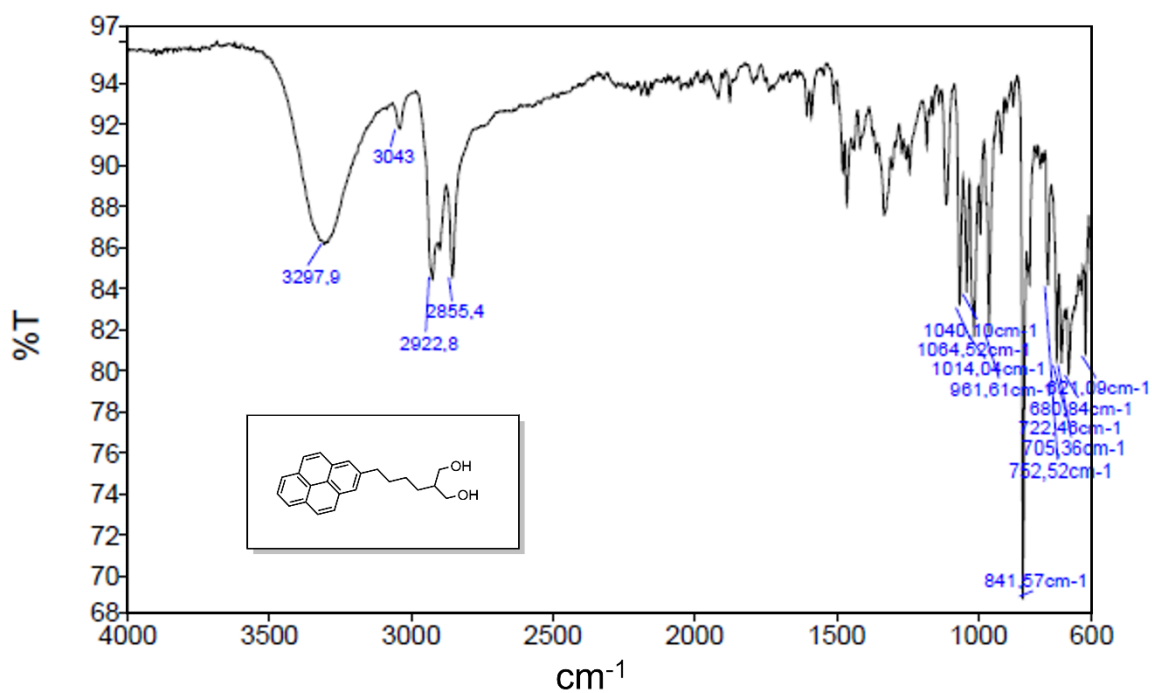


Figure A3.25 FT-IR spectrum of **9** (powder)

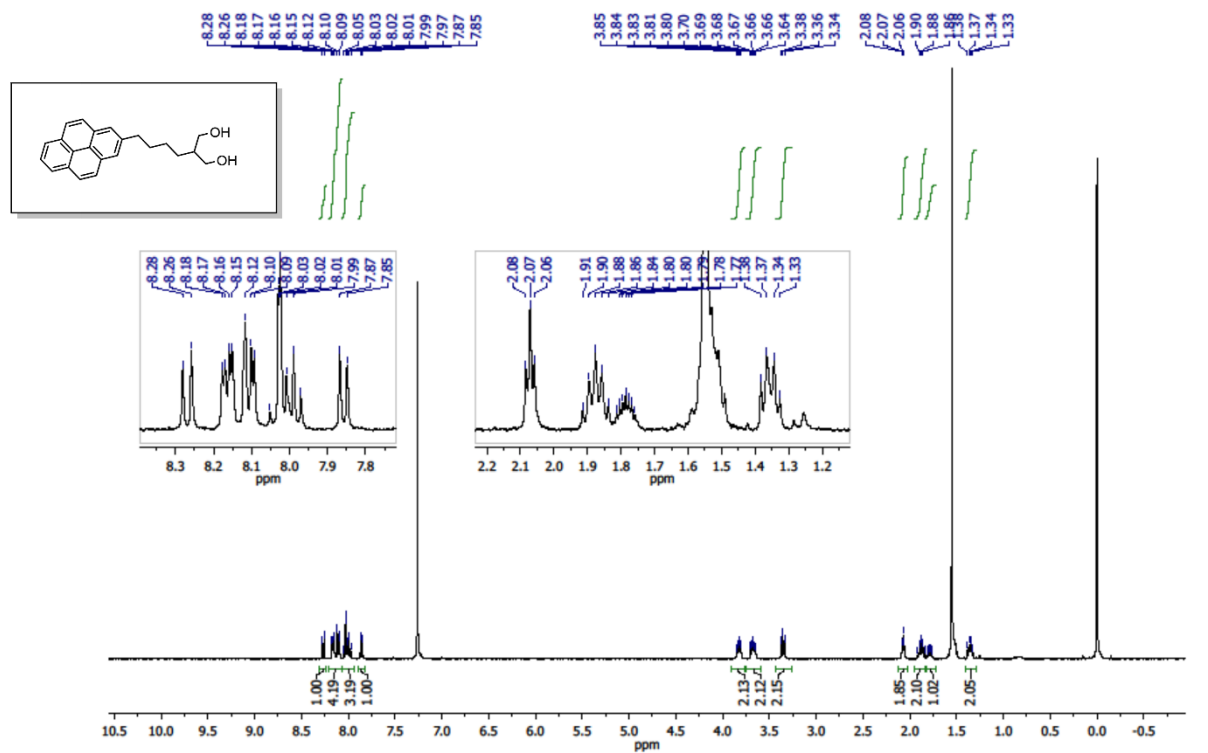


Figure A3.26 ¹H NMR (400 MHz, 25°C, CDCl₃) of **9**

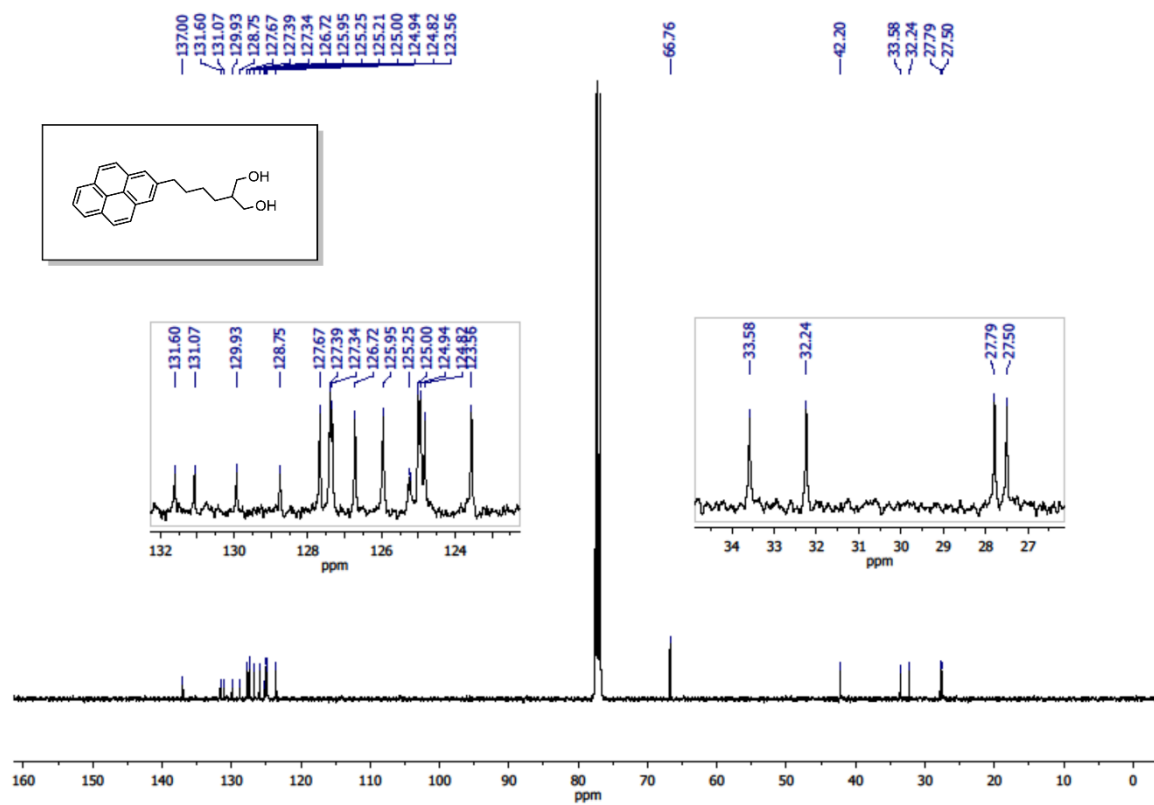
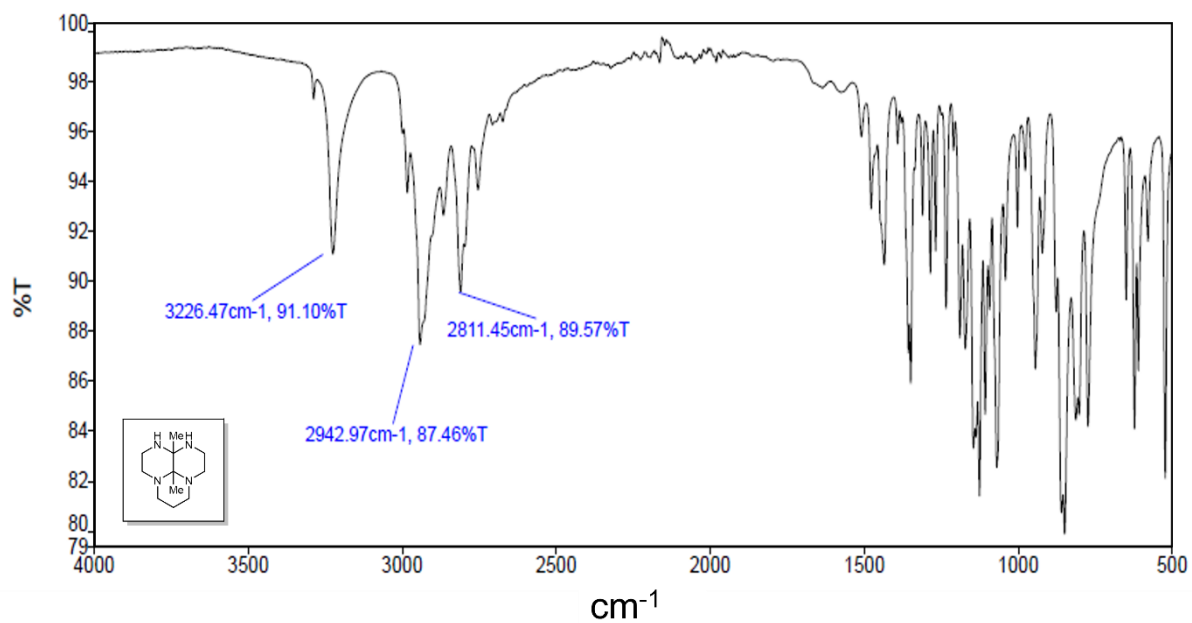
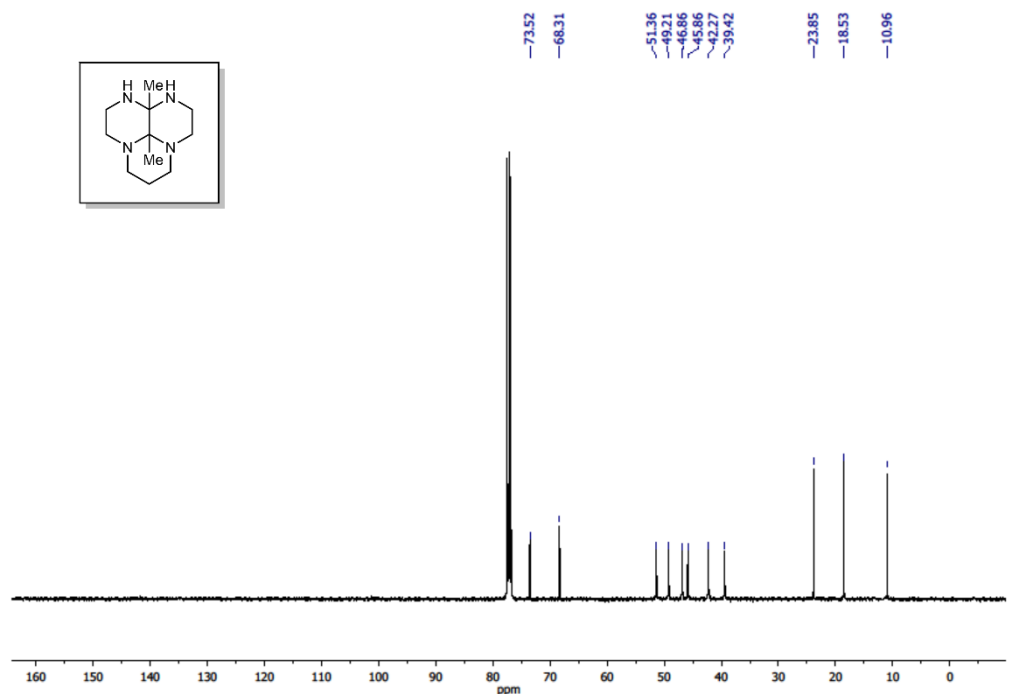


Figure A3.27 ¹³C NMR (101 MHz, 25 °C, CDCl₃) of **9**.

9a,9b-dimethyloctahydro-1,3a,6a,9-tetra-azaphenalene (Bis-aminal)**Figure A3.28** FT-IR spectrum of bis-aminal (powder)**Figure A3.29** ^{13}C NMR (101 MHz, 25 °C, CDCl_3) of bis-aminal.

Chapter 4 Increasing the performance of mesoscopic printable perovskite solar cells by modifying the meso-TiO₂ layer morphology

4.1 Introduction

Since the pioneering work of Miyasaka and collaborators^[1] where metal halide perovskite materials were first used as dyes and loaded on mesoporous TiO₂ photoanodes in liquid dye-sensitized solar cells (DSSCs), the architectures of perovskite solar cells (PSCs) have undergone substantial advancements.^[2] Because of their cost-effective and simple fabrication procedure,^[3] hole transporting material (HTM)-free solar cells are today among the most investigated designs for PSCs.

Efforts have been made to enhance the performance of HTM-free PSCs, which, as the name itself suggests, do not include HTMs, and thus are generally constituted of a perovskite layer, an electron transporting material (ETL), and two electrodes. The main advancements for the development of such devices account exploring different counter electrodes (e.g. Au^[4] or carbon as a low-cost alternative^[5]) or modifying the design of the device, which resulted in mesoporous architectures, where the perovskite layer is deposited over a mesoporous TiO₂ layer, or planar ones, in which the mesoporous TiO₂ layer is absent.

Among the mesoporous designs, the monolithic architecture possesses the highest potential for large-size and commercial-scale production.^[6] In monolithic PSCs, all the layers can be screen printed and stacked, and the perovskite is then infiltrated into the device at the end, via drop-casting or inkjet printing^[7] techniques. An additional spacer layer (mainly ZrO₂) is normally present between the counter electrode and the meso-TiO₂ layer. Although the story of these devices is rather recent,^[3] several attempts have already been made in order to optimize the stacked ensemble. Han and collaborators^[8] were the first to propose a carbon/graphite electrode in 2013, initially achieving a power conversion efficiency (PCE) of 6.7%. Later on, the same group increased the efficiency to 10.6% by the use of TiO₂ nanosheets.^[9] The development of the perovskite precursor brought in 2017 to obtain a PCE of 15.6%,^[10] the current record for this type of PSCs.

As the majority of the attempts to increase the PCE have been focusing on the amelioration of the carbon electrodes^[11–13] or the perovskite precursors,^[14–16] likewise, the optimization of the meso-TiO₂ layer as ETL, as a crucial component of PSCs, should be addressed. As a selective contact to extract electrons as well as scaffold to sustain the perovskite, the ETL significantly affects the device performance.^[17] Hence, modifications of the meso-TiO₂ layer, such as W-doping,^[18] were proposed. It must be noted, however, that strategies like doping/modification with additional materials, especially metals, have so far promoted only small increments in the PCE, while at the same time accounting for expensive modifications, which somehow do not follow the principle of using abundant and environmentally friendly materials, which is at the base of this type of PSCs. More effective and at the same time economical solutions are needed to keep this kind of design among the most relevant for the industrial field.

A feasible solution may be found in the manipulation of the morphology of TiO₂. It is now widely demonstrated that morphological changes in the ETL are able to greatly increase the efficiency of DSSCs and PSCs.^[19] For monolithic PSCs, Han's group^[20] found the best size of nanoparticles that managed to take the efficiency of the cell up to 13.41%, and Yu et al.^[21] prepared a composite nanostructured TiO₂ consisting of size blended nanoparticles and nanoarrays, achieving a maximum efficiency of 13.5%. These excellent results strengthen the idea that satisfactory PCEs can be obtained by modifying the ETL morphology, without largely affecting the economical and scalability aspects of the manufacturing process.

With this mindset, in the present work, we modified the morphology of the meso-TiO₂ scaffold to increase the PCE of mesoscopic fully printable carbon-based PSCs. We initially synthesized and fully characterized a range of mesoporous TiO₂ nanomaterials with different morphological features and we introduced them into the stacked devices. Successively, we have adopted an even more viable strategy by introducing different degrees of porosity into state-of-the-art nanoparticle based TiO₂ scaffolds. This was accomplished by using polymer beads as sacrificial templates. All the so-made ETLs have then been characterized and introduced into the final devices for the determination of the photovoltaic parameters.

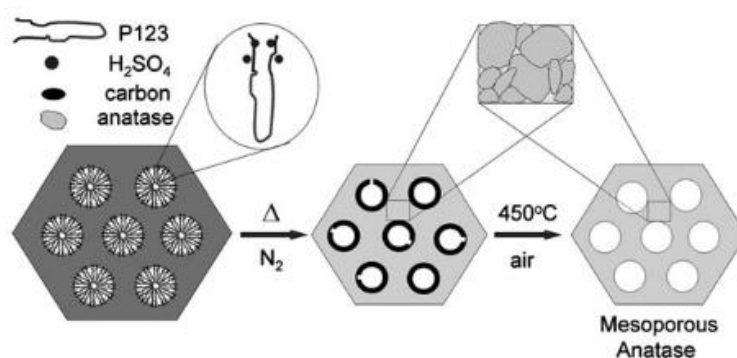
Among all the ETL architectures tested, the introduction of polymeric nanospheres as scaffolds for the generation of increased porosity has proved the most effective approach, leading to an increase of the PCE of the PSCs, with maximum efficiencies up to 14.2%, the best achieved so

far from the simple modification of the TiO₂ mesoporous layer of mesoscopic carbon-based solar cells. To the best of our knowledge, this is also the first time that materials like inverse-opal TiO₂ or polymeric nanospheres as sacrificial scaffolds are employed with monolithic PSCs.

4.2 Results and Discussion

4.2.1 Synthesis of mesoporous TiO₂ materials

The synthesis of TiO₂ anatase nanoparticles with ordered mesoporous channels (referred to as material **1**) was carried on following a previously described procedure.^[22] The synthetic pathway for this material is depicted in **Scheme 4.1**.



Scheme 4.1 Synthetic process for crystalline anatase nanoparticles, **1**.^[22]

The first step of the synthesis accounted for an ethanolic evaporation-induced self-assembly (EISA) process in which titanium isopropoxide (TIPO) was used as the precursor. The template was provided by the commercial amphiphilic triblock copolymer Pluronic P123. Concentrated H₂SO₄ and HCl were used as acid catalysts.

In the second step, the calcination under N₂ at 550°C allowed the carbonization of the surfactant template, which could then support the TiO₂ framework during the high temperature crystallization. Once the crystalline framework was formed, the amorphous carbon inside the mesoporous channels could be burned out in air at 450°C for 6 h, leaving the anatase nanoparticles, **1**, in the form of a white powder.

The material was characterized by X-ray diffraction (XRD), nitrogen physisorption, scanning electron microscopy (SEM) and transmission electron microscopy (TEM). The wide-angle

XRD pattern showed well-resolved diffraction peaks (**Figure 4.1**), all of which could be attributed to the anatase phase reflections according to card number 21-1272 of the Joint Committee on Powder Diffraction Standards (JCPDS).^[22] The absence of other diffraction peaks suggested the presence of a pure anatase phase.

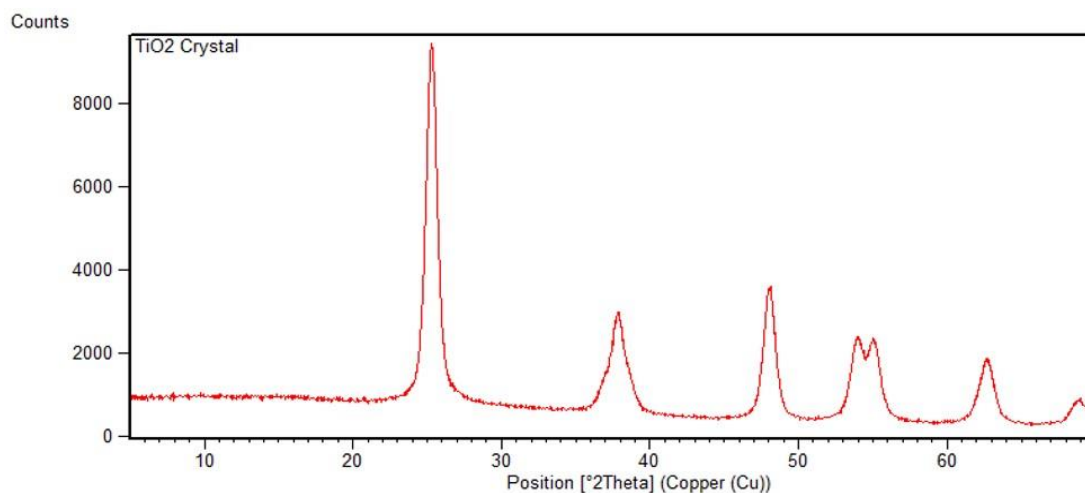


Figure 4.1 wide-angle X-ray diffraction XRD pattern for sample **1**.

The nitrogen physisorption isotherm for **1** showed a typical type-IV curve with a final saturation plateau, indicative of a mesoporous material (**Figure 4.2a**). Additionally, the type H1 hysteresis loop suggested a narrow range of uniform mesopores. The pore size distribution was assessed from the adsorption data using the Barrett–Joyner–Halenda (BJH) method (**Figure 4.2b**). The material presented a narrow pore width distribution with a maximum around 16-18 nm and total pore volume 0.337 cm³/g (BJH adsorption). The surface area was calculated using the Brunauer–Emmett–Teller (BET) method to be 92 m²/g.

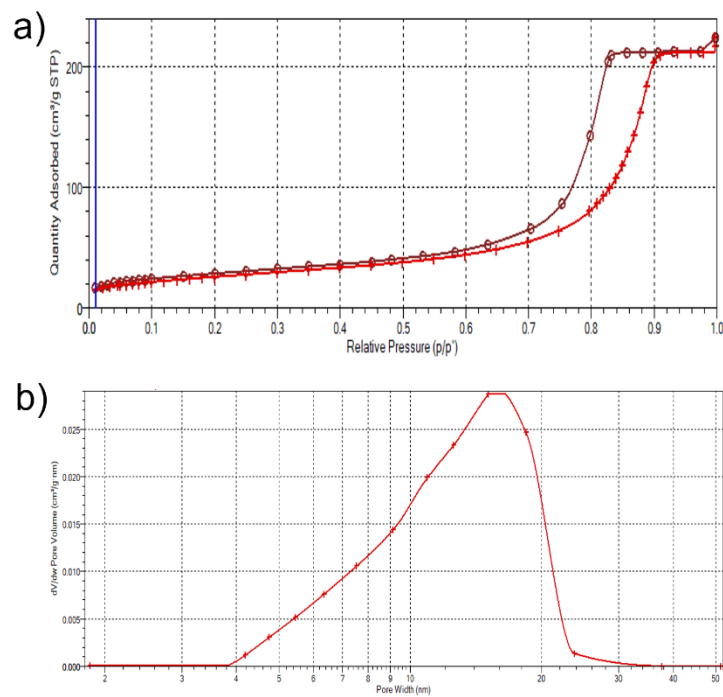


Figure 4.2 N₂ pysisorption isotherm (a) and pore size distribution (b) BJH adsorption for sample 1.

Finally, the morphology of sample **1** was inspected by means of TEM and SEM. **Figure 4.3a** revealed a very homogeneous mesoporous material made of well-defined anatase nanoparticles with random orientation (**Figure 4.3b** and c) and average diameter of 13 nm. No ordered 2D hexagonal structure was observed.

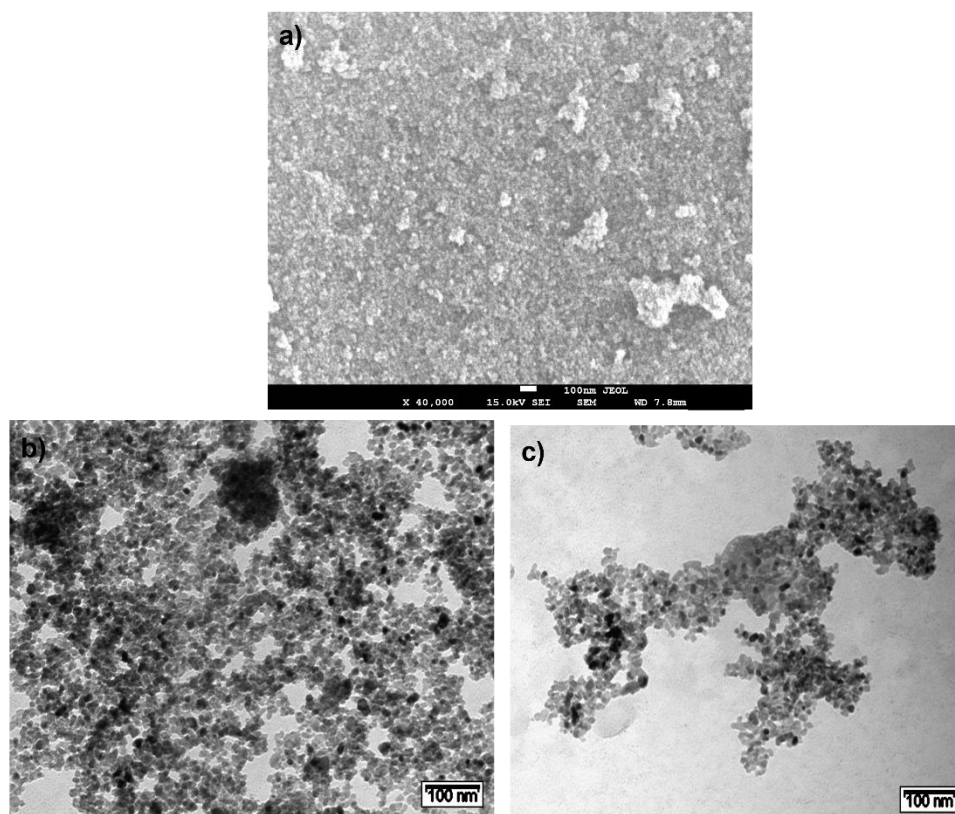
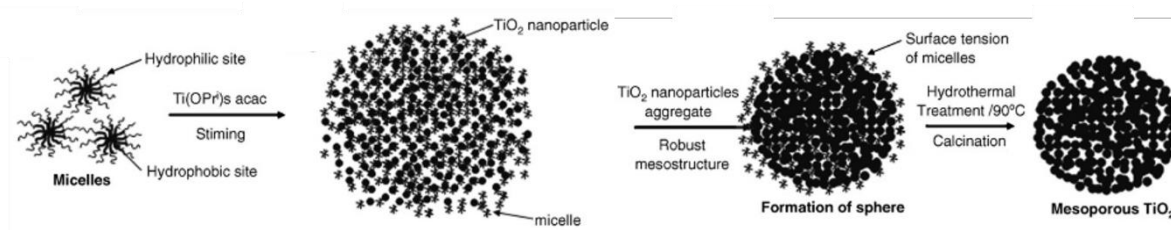


Figure 4.3 SEM (a) and TEM (b, c) images for material **1**.

Spherical-shaped TiO_2 anatase nanoparticles (**2**) were synthesized via hydrothermal treatment as previously reported.^[23] In this sol-gel approach in aqueous solution, the triblock copolymer P123 was used to form the micelles that will direct the formation of the TiO_2 nanoparticles; H_2SO_4 was used to create an acidic environment and TIPO (mixed with acetylacetonate) was used as the precursor. Thus, in the first step, the precursor $\text{Ti}(\text{OPr}^i)_3\text{acac}$ produced by mixing 2,4-pentanedione and TIPO in a 1:1 molar ratio was dissolved in presence of the surfactant and the acid. Hydrolysis and condensation of the titanium precursor led to the growth TiO_2 nanoparticles, which slowly aggregated in a spherical shape. Finally, the hydrothermal treatment and the calcination determine the generation of the anatase phase and the removal of the surfactant, providing **2** as a white powder. The synthesis pathway for material **2** is depicted in **Scheme 4.2**.



Scheme 4.2 Synthesis pathway for the formation of spherical-shaped TiO_2 nanoparticles (**2**).^[23]

The material was characterized by XRD, nitrogen physisorption, TEM and SEM. The wide-angle XRD pattern showed nine diffraction peaks (**Figure 4.4**), all of which could be attributed to the anatase phase reflections according to the JCPDS card number 21-1272.^[22] The peaks, which were not very well defined, suggested that the obtained material has a small crystallite size. The absence of other diffraction peaks suggested the presence of a pure anatase phase.

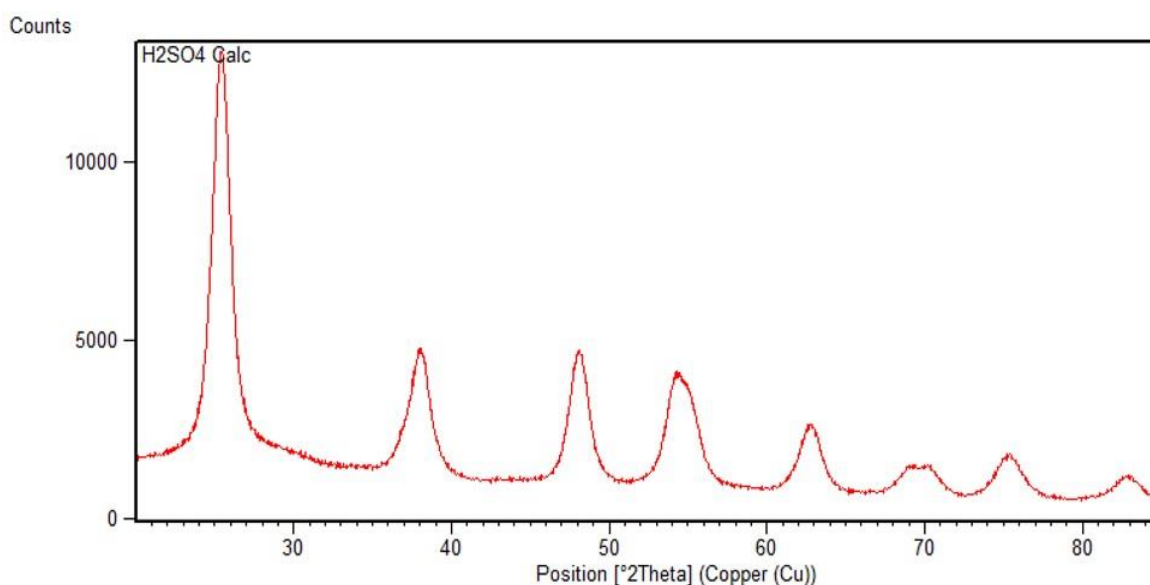


Figure 4.4 wide-angle X-ray diffraction XRD pattern for sample **2**.

The nitrogen physisorption isotherm for **2** (**Figure 4.5a**) showed a type-IV curve with a final saturation plateau, indicative of a mesoporous material. The hysteresis loop was identified like a type H2(a), suggesting more complex pore structures in which network effects are important. The quite steep desorption branch could be attributed either to pore-blocking/percolation in a narrow range of pore necks or to cavitation-induced evaporation.^[24]

The pore size distribution was assessed from the adsorption data using the BJH method (**Figure 4.5b**). The material presented a pore width distribution with a maximum between 3-8 nm and total pore volume 0.3 cm³/g (BJH adsorption). The calculated BET surface area reached a very high value of 220 m²/g.

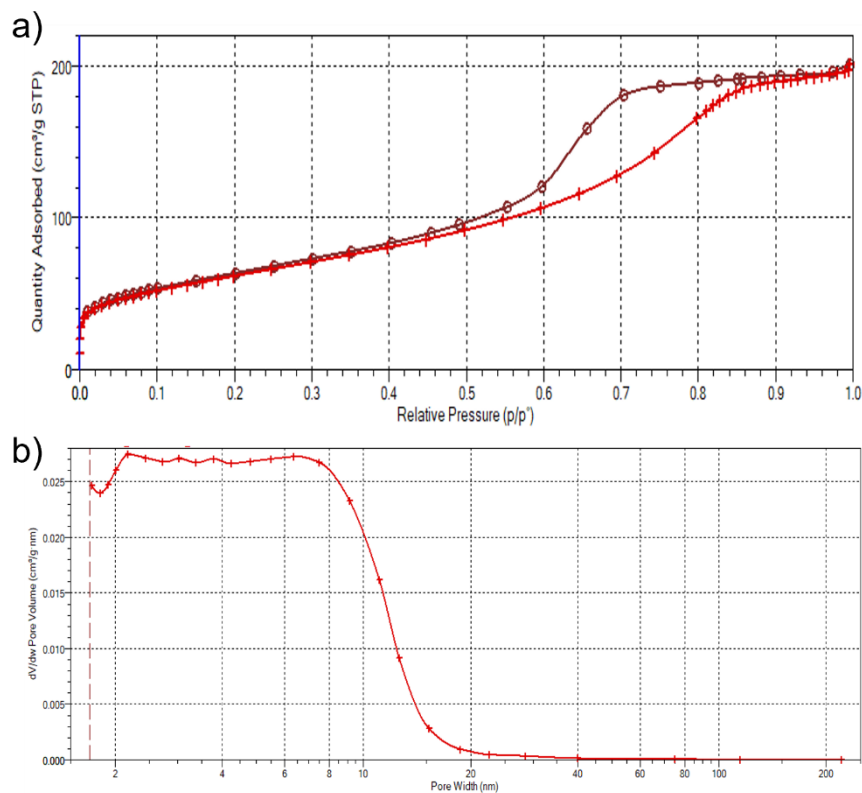


Figure 4.5 N₂ pysisorption isotherm (a) and pore size distribution (b) BJH adsorption for sample 2.

The SEM images for material 2 showed the spherical morphology of the particles (**Figure 4.6a** and b) with different diameters ranging from 500 nm to 2-3 micrometers. The spheres were made of interconnected TiO₂ nanoparticles of a mean diameter of 7 nm, as indicated by the TEM images (**Figure 4.6c**)

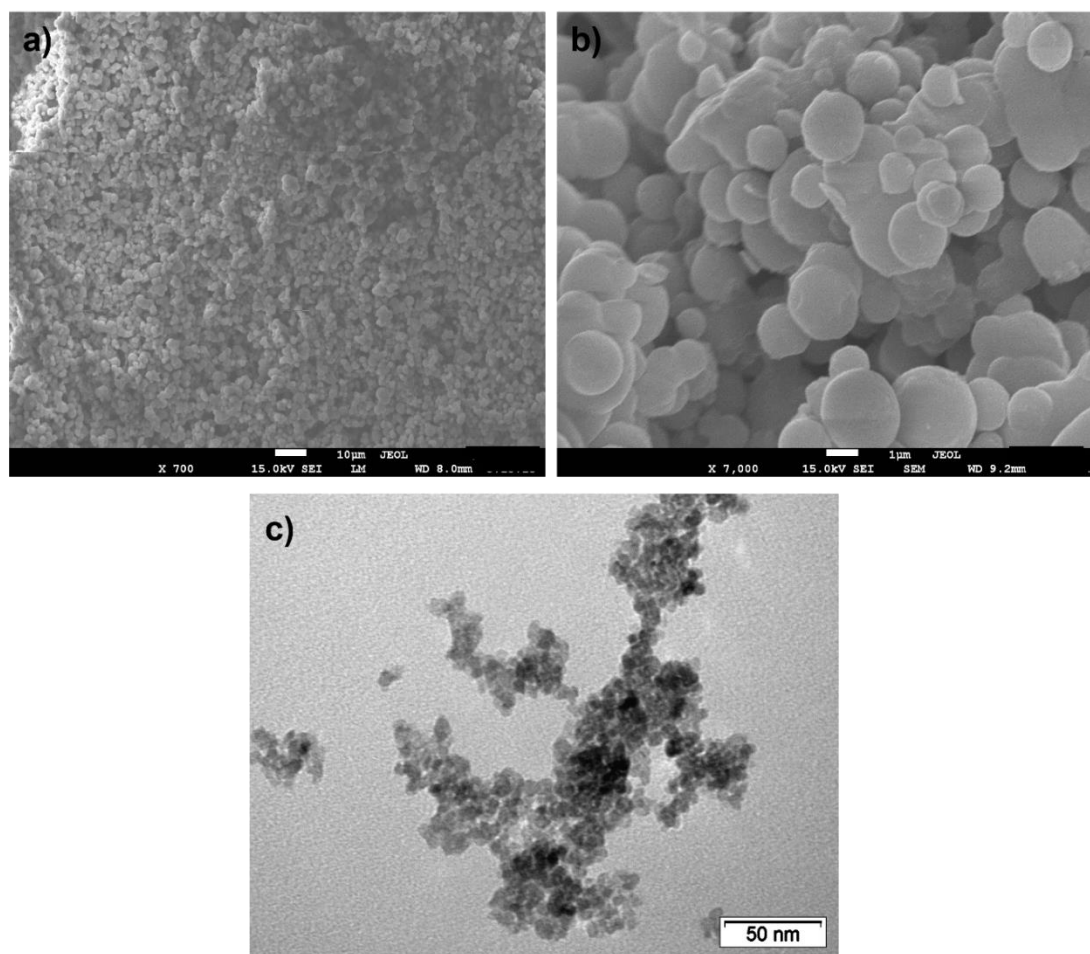


Figure 4.6 SEM (a,b) and TEM (c) images for material 2.

4.2.2 Synthesis of polymeric nanospheres and inverse-opal TiO₂

The synthesis of polystyrene (PS) nanospheres was performed (with modifications) by taking into account a previous report by Liu et al.^[25] Thanks to this synthesis process in aqueous solution, it was possible to fabricate highly monodisperse PS spheres using potassium persulfate (KPS) as the initiator and sodium dodecyl sulfate (SDS) as emulsifier. In a typical polymerization procedure, SDS was dissolved in water, then KPS was added, and the temperature was raised to 80°C. Under mild mechanical stirring at about 200 rpm, a mixture of styrene and 1-butanol was slowly dropped into the system and the polymerization was carried on at 85°C for around 20h.

The so-formed nanospheres were analyzed by SEM and dynamic light scattering (DLS), to investigate the morphology and the dispersity of the particles, respectively. SEM images (**Figure 4.7a**) showed that the spherical morphology was attained, with homogeneous, well-

defined spheres. DLS analysis confirmed the homogeneity of the dispersion with a sharp distribution curve (**Figure 4.7b**) from which the calculated mean diameter was ~ 270 nm.

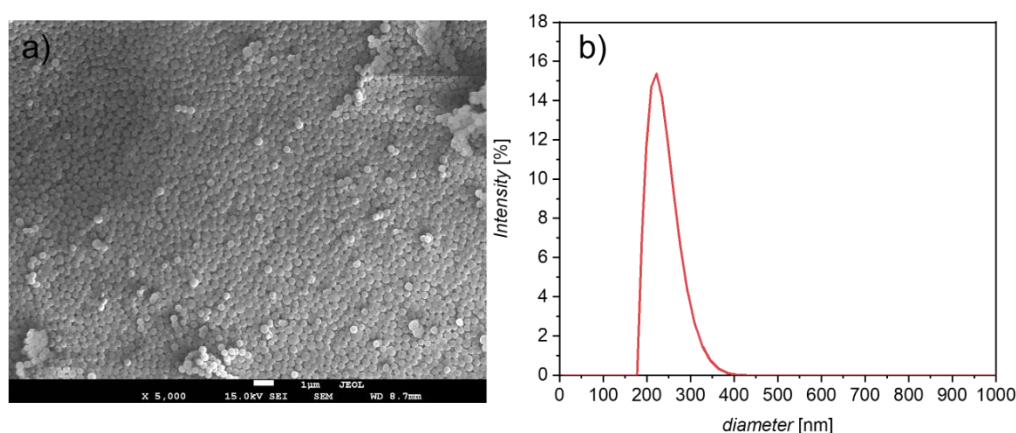


Figure 4.7 a) SEM image of PS nanospheres and b) DLS analysis (mean diameter 270 nm).

By modifying the concentration of styrene precursor, initiator, or emulsifier, it was possible to obtain more (or less) monodispersity and a different mean diameter for the final PS nanospheres. Thus, it was possible to obtain smaller nanospheres (with mean diameter around 72 nm) by increasing the concentration of SDS used during the synthesis (while keeping all the other parameters constant). In the following study, however, only the above described 270 nm PS nanospheres were used.

The synthesis of a polymer from styrene and acrylic acid was carried on following a previously reported procedure.^[26] In this synthesis, the soap-free emulsion polymerization of styrene and acrylic acid generates a statistical copolymer, i.e. polystyrene-*statistical*-polyacrylic acid (PS-*s*-PAA), in which the sequential distribution of the monomeric units follows statistical laws. Thus, the arrangement of monomeric units tends toward alternation, or clustering of alike units, or exhibits no ordering tendency at all.^[27] The polymerization was carried on in aqueous conditions and ammonium persulfate (APS) was employed as initiator.

The so-formed nanospheres were analyzed by SEM and DLS, to investigate the morphology and the dispersity of the particles, respectively. SEM images (**Figure 4.8a**) showed that the spherical morphology was attained, with homogeneous, well-defined spheres. DLS analysis confirmed the homogeneity of the dispersion with a sharp distribution curve (**Figure 4.8b**) from which the calculated mean diameter was ~ 290 nm.

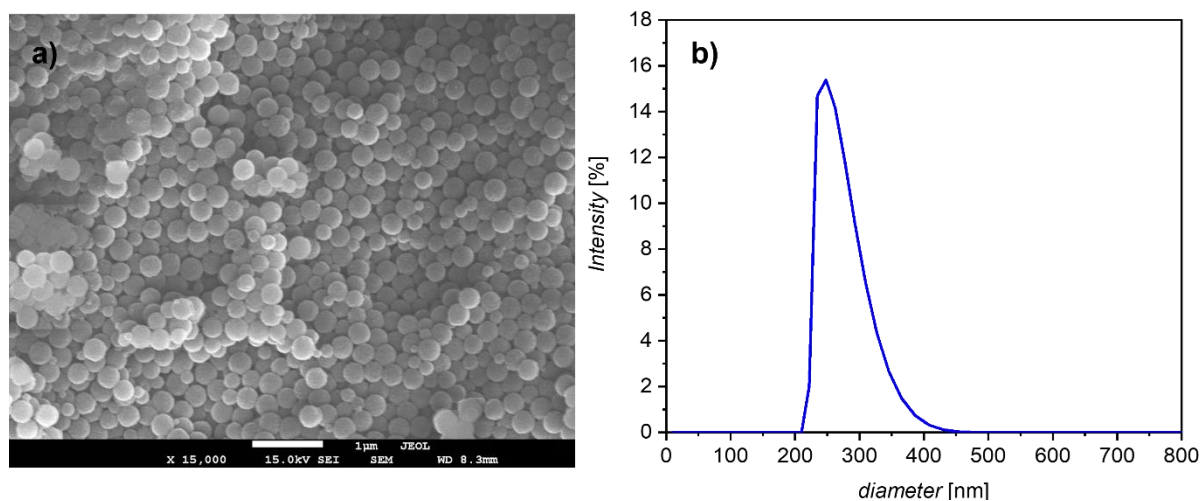


Figure 4.8 a) SEM image of PS-*s*-PAA nanospheres and b) DLS analysis (mean diameter 290 nm).

Finally, inverse-opal TiO₂ materials (IO-TiO₂) were prepared (in collaboration with Thomas Lourdu Madanu, UNamur) following a previously reported co-assembly procedure with modifications.^[28] Briefly, pre-synthesized TiO₂ nanoparticles were mixed to a known concentration of 300 nm PS nanospheres in aqueous suspension. A suitable (highly hydrophilic) surface was then immersed vertically in a beaker containing the mixture and left undisturbed in an oven at 40°C for several days. The process afforded the evaporation-induced deposition of highly ordered templating colloids and metal oxide nanoparticles. The calcination at high temperatures afforded their crystallization to the anatase phase and their cohesion to form the inverse opal structure, while the polymeric scaffold was removed.

SEM images of the so-made IO-TiO₂ materials showed the ordered and defect-free nature of the assembled films (**Figure 4.9a**). The optical properties of such periodic material could also be observed by naked eye (**Figure 4.9b**).

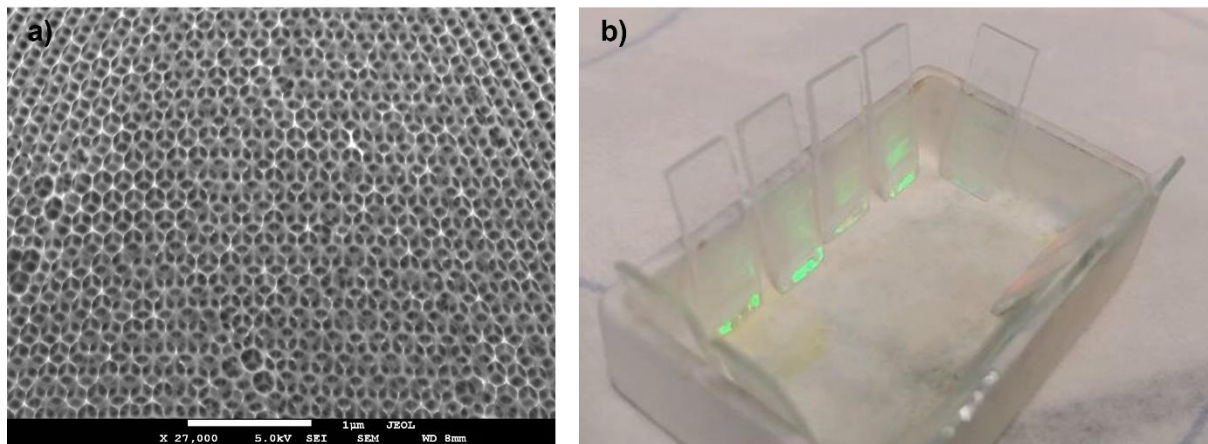


Figure 4.9 a) SEM image of IO-TiO₂ material and b) picture of several glass substrates on which IO-TiO₂ was deposited (green reflex).

4.2.3 Fabrication of perovskite solar cells with modified mesoscopic TiO₂ layer

The architecture of the PSCs used in this is depicted in **Figure 4.10**.

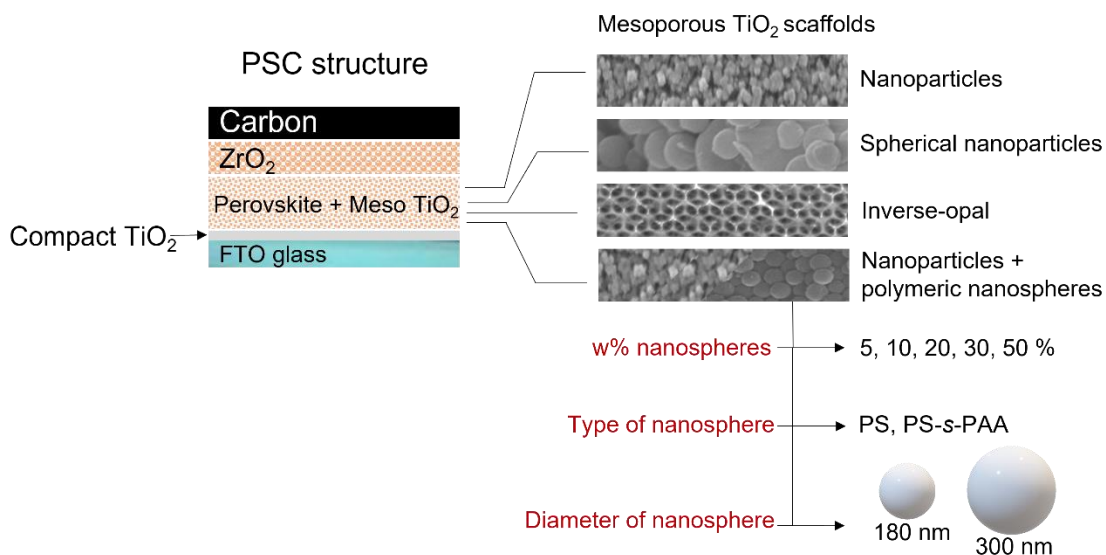


Figure 4.10 Architecture of the PSCs used in this work, with a focus on the different mesoporous TiO₂ scaffolds tested as ETL.

The structure consists of a fluorine-doped tin oxide (FTO) glass substrate on which a compact layer of TiO₂ is deposited. This compact layer maximized the contact between the FTO and the mesoporous titanium dioxide (meso-TiO₂) layer, which serves as ETL. A layer of zirconium

dioxide (ZrO₂) acting as a spacer layer separates the ETL from a carbon-based electrode, consisting primarily of graphite flakes and carbon black nanoparticles.

The three layers (m-TiO₂/ZrO₂/C) cell stack is fabricated by successive deposition of each individual layer via screen printing on top of the compact TiO₂ layer. To do so, the materials are incorporated in a mixture of ethyl cellulose (ETHOCEL™), as a binder, and terpineol, as a solvent, which possesses the necessary viscosity to be screen-printed. After each layer is printed, a firing step eliminates the components of the paste, leaving the material ready for the successive layer deposition.

The ensemble is infiltrated with a perovskite precursor solution via inkjet printing from the carbon top-layer, which penetrates through the pores and crystallizes into the perovskite photoabsorber (within the mesostructured TiO₂ scaffold mainly) upon the removal of the solvent (e.g. by annealing). The carbon electrode features high conductivity and contributes to hindering the moisture ingress into the PSC, which confers to the cell high stability in normal conditions. The so-made fresh PSCs are then aged for seven days under controlled humidity (75% RH) and temperature (42 °C) conditions before being tested.

As it is often used for the preparation of printable PSCs, the Ti-nanoxide T165/SP m-TiO₂ paste produced by Solaronix SA was considered as a reference. This paste is composed of highly dispersed anatase titania nanoparticles obtained by hydrothermal synthesis. The range of size for the nanoparticles is about 15-20 nm. The reference ETL layer fabricated with such paste is homogeneous, with an average thickness of 600 nm (**Figure A4.1**). BET surface area was estimated to be around 100 m²/g and pore size is comparable to the nanoparticles size, i.e., about 20 nm in diameter.

To test the influence of different meso-TiO₂ scaffolds on the efficiency of printable PSCs, we prepared several modified PSCs containing TiO₂ materials with different morphologies, namely material **1**, material **2** and IO-TiO₂ previously described (**Figure 4.10**). With the only exception of the IO-TiO₂ material, which was synthesized *in situ* on the compact-TiO₂ layer, all the pastes were prepared as analogues of the Ti-nanoxide T165/SP (more details on the preparation of the screen-print pastes are provided in the experimental section).

Additionally, we have modified the reference Ti-nanoxide T165/SP paste by introducing polymeric nanospheres as sacrificial scaffolds for the generation of additional non-ordered porosity. Hence, different pastes were fabricated by varying the weight ratio between nanospheres and TiO₂ particles (from 5% to 50%), the mean diameter of the nanospheres (~300 nm or ~180 nm), and the nature of the polymer (PS, PS-*s*-PAA) (**Figure 4.10**). More specifically, ETLs having the following configurations were prepared:

- Reference TiO₂ + PS nanospheres (~300 nm), weight ratios 5, 10, 20, 30, 50%;
- Reference TiO₂ + PS nanospheres (~180 nm), weight ratios 10, 20, 30, 50%;
- Reference TiO₂ + PS-*s*-PAA nanospheres (~300 nm), weight ratio 10, 20, 30, 50%

Thus, giving a total of 13 different samples. While the nanospheres of around 300 nm were synthesized and characterized as described above, the PS nanospheres of ~180 nm were kindly provided by Prof. Billon group (UPPA, France) and their morphology and mean diameter were characterized once received (**Figure A4.3**).

During the firing step, the polymeric nanospheres were eliminated together with the paste solvent and binder, leaving different degrees of porosity. The overall performance of the so-made PSCs was then investigated.

While for TiO₂ materials this is not a concern, it is crucial for the nanospheres to be stable within the screen-print paste for a long period of time. Depending on the polymer, certain solvents can readily attack the nanospheres, making them swell or, in the worse cases, dissolving them. We therefore tested the stability of the nanospheres in a mixture of terpineol and ETHOCELTM (i.e., the main constituents of the screen-print pastes used). Both PS and PS-*s*-PAA retained their shape and remained stable even several months after their introduction into the paste. On the contrary, nanospheres of other polymers, e.g., polymethyl methacrylate, started to swell after few hours.

4.2.4 Photovoltaic parameters and characterization of the modified perovskite solar cells

Because only one effective charge separation interface is present in monolithic, fully printable carbon-based PSCs (TiO₂/perovskite), the mesoporous TiO₂ scaffold, which acts as electron extractor as well as scaffold to sustain the perovskite, has the potential to significantly affect

the device performance. As such, an ideal meso-TiO₂ layer should be robust, chemically inert, and stable under a wide range of temperatures; most importantly, the scaffold should present a high surface area to maximize the contact with the perovskite and thus optimize the charge separation. At the same time, however, large pore size would enable a better perovskite filling and growth of bigger crystal domains, which would improve current densities and light absorption efficiency. The trade-off between the requirements of high specific surface area and suitable large pore size in the meso-TiO₂ layer can be optimized via morphological changes, which represent a simple and effective option to increase the PCE of these devices without affecting too much manufacturing costs and large-scale fabrication, i.e., the main strengths of this type of cells.

The reference meso-TiO₂ layer is constituted of stacked anatase nanoparticles of around 20 nm diameter, without a particular organization. As such, the only porosity is given by the hollow space created between the nanoparticles once the layer is deposited. Therefore, by initially replacing the reference TiO₂ material with three titanium dioxide materials that we synthesized, namely **1**, **2**, and IO-TiO₂, we hoped to understand if the anatase nanoparticles, once organized in well-defined mesostructures, could better accommodate perovskite crystals, supporting their growth and/or increasing the contact with them. Material **1**, **2**, and IO-TiO₂ possess anatase nanoparticles of similar sizes, however their arrangement generated ordered mesoporous channels for **1**, spherical domains for **2**, and inverse opal structure for **3**.

To investigate the change of photovoltaic parameters resulted from the introduction of modified meso-TiO₂ scaffolds, current-voltage (*J-V*) scans were measured under a solar simulator providing 100 mW cm⁻², AM 1.5G illumination. The short-circuit current density (*J_{sc}*), open-circuit voltage (*V_{oc}*), fill factor (*FF*) and power-conversion efficiency (*PCE*) were obtained as a result of reverse and forward voltage sweeps (from 1 to -0.3 V, scan rate of 5 mV s⁻¹) using the prepared PSCs. For each modified meso-TiO₂ layer, an average of 5 devices were tested.

Table 4.1 J-V parameters obtained from reverse and forward voltage sweeps of the prepared PSCs with m-TiO₂ made of **1**, **2**, or IO-TiO₂. Maximum values (average values of at least 5 different devices between brackets).

Sample	V _{oc} [V]	FF	J _{sc} [mAcm ⁻²]	PCE [%]
reference	0.983 (0.934)	0.705 (0.627)	20.746 (17.962)	13.46 (10.627)
Material 1	0.987 (0.740)	0.664 (0.495)	9.16 (7.05)	4.10 (2.86)
Material 2	0.858 (0.749)	0.53 (0.606)	6.97 (4.29)	3.05 (1.71)
IO-TiO ₂	0.887 (0.828)	0.535 (0.436)	5.08 (2.68)	1.98 (1.27)

The photovoltaic parameters of the cells with material **1**, **2**, and IO-TiO₂ as ETLs are presented in **Table 4.1**. In general, none of the modified PSCs performed better than the reference. Between the three different materials, material **1** gave the best results, though far less satisfactory than the reference performance. In particular, the maximum values of V_{oc} and FF were close to those of the reference, but the current densities and consequently the PCE were less than half of the reference values. The lowest PCE was obtained with PSCs having IO-TiO₂ as meso-TiO₂ material.

The open circuit voltage value is generally an indicator of the level of recombination at the interfaces; a high V_{oc} suggests that the recombination within the perovskite crystals or at the interface TiO₂/perovskite is minimized. Thus, since all the PSCs presented an average V_{oc} , it can be argued that the penetration of the perovskite within the materials was successful, perovskite crystals formed, and they were in good contact with the meso-TiO₂ scaffold. As for the current densities, the J_{sc} value generally indicates the ease of photoelectron transfer throughout the bulk and it is therefore attributed to a good contact between Perovskite/TiO₂, good layer architecture (thickness, defects), good coverage of the c-TiO₂, all of which would prevent charge accumulation. The poor values of J_{sc} in the materials tested (in the best case, for material **1**, less than half of the reference value) seem to indicate a general difficulty for the charges to be delivered at the electrodes; this could be due to scarce contact between the m-TiO₂ layer and the compact TiO₂ layer, defects within the m-TiO₂ layer itself, or excessive thickness of the layer.

In an attempt to understand the reason for their low efficiency, we observed the IO-TiO₂ ETL layers via SEM before and after being incorporated into the final devices. **Figure 4.11a** shows the IO-TiO₂ material synthesized on top of the Compact TiO₂ layer on FTO glass. It is evident from this image that (i) The IO material does not form a uniform layer, rather it presents several cracks throughout all the surface; (ii) each portion of IO material is barely in contact with the underlying compact-TiO₂ layer and (iii) the IO layer is around 2.5 μm thick, around 4 times more than the reference layer (which optimized thickness is 600 nm). When introduced in the final device (i.e., when the successive ZrO₂ and carbon layers were printed on top), while some portions of the layer maintained their integrity (**Figure 4.11b**), some others broke and formed flakes that mixed with the paste of the successive layers. **Figure 4.11c** shows that the ZrO₂ and carbon layers have filled the cracks in the IO layer, thus getting to touch the compact TiO₂ layer.

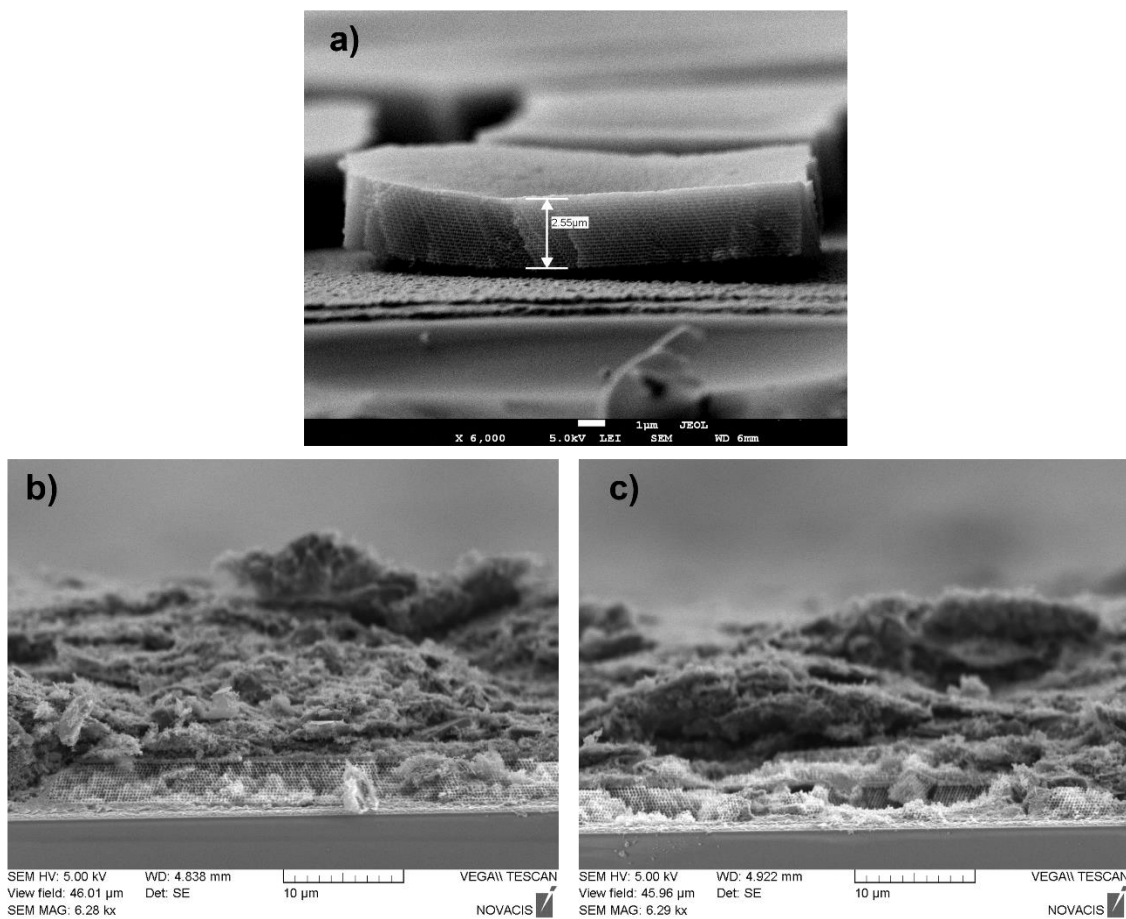


Figure 4.11 SEM cross sections of a) IO-TiO₂ synthesized on FTO+ compact TiO₂ before the print of the successive layers; b,c) IO-TiO₂ synthesized on FTO+ compact TiO₂ after the screen print of the successive layers (ZrO₂, Carbon).

Similarly, by analyzing the cross-section of the meso-TiO₂ layer obtained with material **1** (**Figure A4.2**), we observed that, despite the fact that the material had maintained its porosity, the layer was very thick (>6 μm, 10 times thicker than the reference) and poorly homogeneous, which could be the consequence of aggregation of TiO₂ nanoparticles.

Previous studies on the morphological optimization of the ETL layer in printable monolithic carbon based PSCs have employed TiO₂ nanosheets,^[9] or focused on tuning of the anatase nanoparticles dimension to maximize the PCE.^[20,30] The introduction of materials **1**, **2**, and IO-TiO₂ thus represents a novelty for PSCs with this architecture. A similar material to **2**, based on spherical TiO₂ aggregates, was previously employed in mesoscopic PSCs (with Au electrodes and HTM) and afforded a PCE of 18.41%.^[31,32] Inverse opals TiO₂ materials have been widely tested in other PSCs architectures^[33–35]; they brought excellent improvements, above all, thanks to their periodic structure, which gives them optical properties such as the slow photon, resonance, and scattering^[36]. For this reason, inverse opals are considered as very promising materials to develop the third generation of solar cells based on photonic crystals.^[37] Despite this, the IO synthesis is generally complex and difficult to scale up. IO for ETLs are generally made according to spin coating processes^[33–35,38] that lead to defect-rich inverse opals, and thus hinder the optical effects, which are generated by the periodicity of the structure.^[28] Our synthesis technique, on the other hand, does not involve spin coating, can be easily scaled up and has proved to form very homogeneous and optically active inverse opals.^[28,29] When applied to PSCs, however, the synthesis process has not proved to be the most suitable one, as extremely smooth surfaces are necessary for a good adhesion of the IO film. As the FTO substrate generally exhibit irregularities, the resulting IO tended to detach from it.

The excellent results when introduced in other PSCs architectures demonstrate that the materials synthesized in this study have the potential to work as very efficient ETLs in monolithic PSCs. Our studies represent therefore a first step towards the generation of efficient meso-scaffolds with these materials. A first optimization that could already bring to impressive increases in PCEs should focus on reducing the thickness of the layers.

The results obtained with the materials led us to consider another strategy of easier implementation, in which we directly modified the reference meso-TiO₂ (the thickness of which was already optimized is Solaronix SA for the screen-print of PSCs). In this approach, we introduced polymeric nanospheres in the Ti-nanoxide T165/SP paste. As stated before, a

rationalized introduction of cavities in the mesoporous TiO₂ could improve the crystallization of perovskite. The cavities should help the formation of larger crystals, which in turn would enhance light harvesting and decrease electron-hole recombination. Besides this, the idea of introducing a sacrificial template seemed suitable, as the process does not add additional fabrication steps other than the preparation of the nanospheres and their incorporation in the m-TiO₂ paste. The introduction of polymer scaffolds to modify the morphology of the layer was previously described for mesoscopic PSCs,^[39] however, to the best of our knowledge, it was never tested on monolithic printed PSCs.

One word must be added concerning the commercial availability of polymeric nanospheres and their production process. Today, many companies can provide nanobeads of different nature, diameter, and with modifications, such as fluorescent dyes or organic functionalizations embedded on the surface of the nanosphere. Polymeric nanospheres find most applications in the biomedical field, as drug delivery systems, protein carriers, and so on.^[40] In this field, for obvious reasons, the nanospheres need to be purified prior to use. The decontamination process makes them very expensive, as the cleaning needs to be done with specific techniques, which are more complicated as the diameter of the bead decreases (100 nm, 600 €/g on average). For other applications, such as the use of nanospheres as sacrificial scaffold, the purification is not necessary, as the beads are going to be fired away together with the impurities. For our studies we thus have optimized the synthesis of PS and PS-*s*-PAA nanospheres, obtaining suitable monodisperse beads, without increasing the PSC manufacturing cost with the purchase of expensive products.

As in the previous cases, *J-V* curves and photovoltaic parameters were obtained by reverse and forward voltage sweeps (from 1 to -0.3 V, scan rate of 5 mV s⁻¹) under a solar simulator providing 100 mW cm⁻², AM 1.5G illumination. The response of at least 5 different cells for every m-TiO₂ configuration were recorded.

Figure 4.12 and **Figure 4.13** present the photovoltaic parameters obtained when incorporating either PS or PS-*s*-PAA nanospheres (~300 nm) with different weight ratios from 0 to 50%, where 0% indicates no nanospheres, i.e., the reference, and 5, 10, 20, 30, 50 % is the weight of nanospheres added (compared to that of TiO₂, which was kept constant).

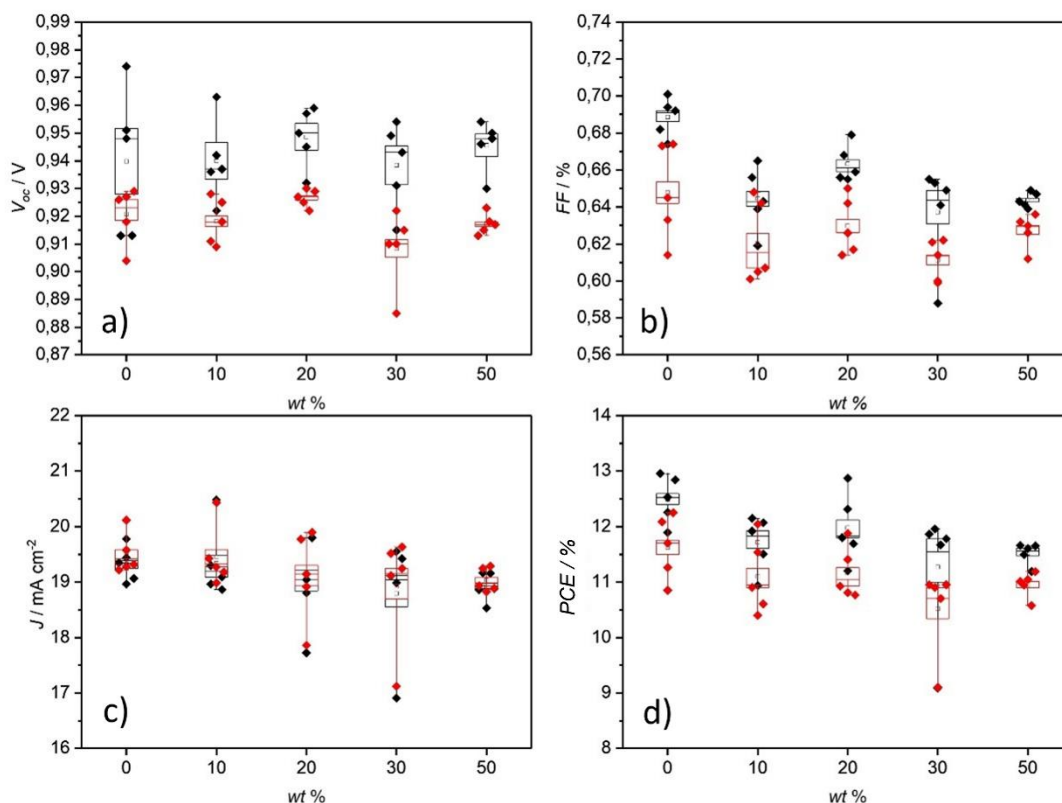


Figure 4.12 J - V parameters obtained from reverse (black) and forward (red) scans of the PSCs made by adding different wt% of ~ 300 nm PS- s -PAA nanospheres within the meso- TiO_2 layer.

The difference between the two types of polymeric nanospheres is that PS- s -PAA present carboxylic acid functionalities on the surface of the beads, which may interact with TiO_2 nanoparticles and facilitate their coordination around the nanospheres, possibly making the layer more homogeneous. The results, however, indicate that best performances are obtained by pastes containing PS nanospheres. More generally, regardless of the type of bead, increase in their weight percentage decreases the performance. This trend is very marked for the PS nanospheres, while it is less evident for the PS- s -PAA ones. Thus, the worst performances were given for both pastes with 50 wt% beads.

The best performance was obtained with the pastes containing 5 and 10 wt% of PS nanospheres. The latter slightly exceeds the reference in terms of V_{oc} and J_{sc} for both forward and reverse scans, thus giving a better average PCE (12.2% vs 12% for the reference). The paste containing 5% PS nanospheres presents much better V_{oc} than the reference in the reverse scan (0.97 vs 0.94V, respectively) and also in the forward scan (0.94 vs 0.92V). J_{sc} increased, with results very similar to the paste containing 10% PS nanospheres, but unlike this one, the FF for the forward scan increased significantly, exceeding that of the reference (0.66 vs 0.64 respectively).

In total, these improvements resulted in the best performing cell (compared to the reference) with a max PCE of 13.6% (and an average of 12.7%).

As the primary effect of added porosity is the growth of bigger perovskite crystals and reduction of grain boundaries (which limit the recombination pathways), the most affected parameter should be the V_{oc} , as it was observed. However, as the wt% of nanospheres grows, defects in the layer grow as well. Disruptions in the homogeneity of the layer can decrease the contact at the interface c-TiO₂/m-TiO₂, mainly impacting FF and J_{sc} . This could explain the observed decrease of such parameters, due to internal resistance.

The performance increase for the 5 wt% PS nanospheres cell is well illustrated on the J - V curves (**Figure 4.14**), where almost no hysteresis could be observed. It was proven that the meso-TiO₂ can have a significant impact on the suppression of the hysteresis, due to its assistance on the extraction of the photogenerated current and the capacitive charges.^[41]

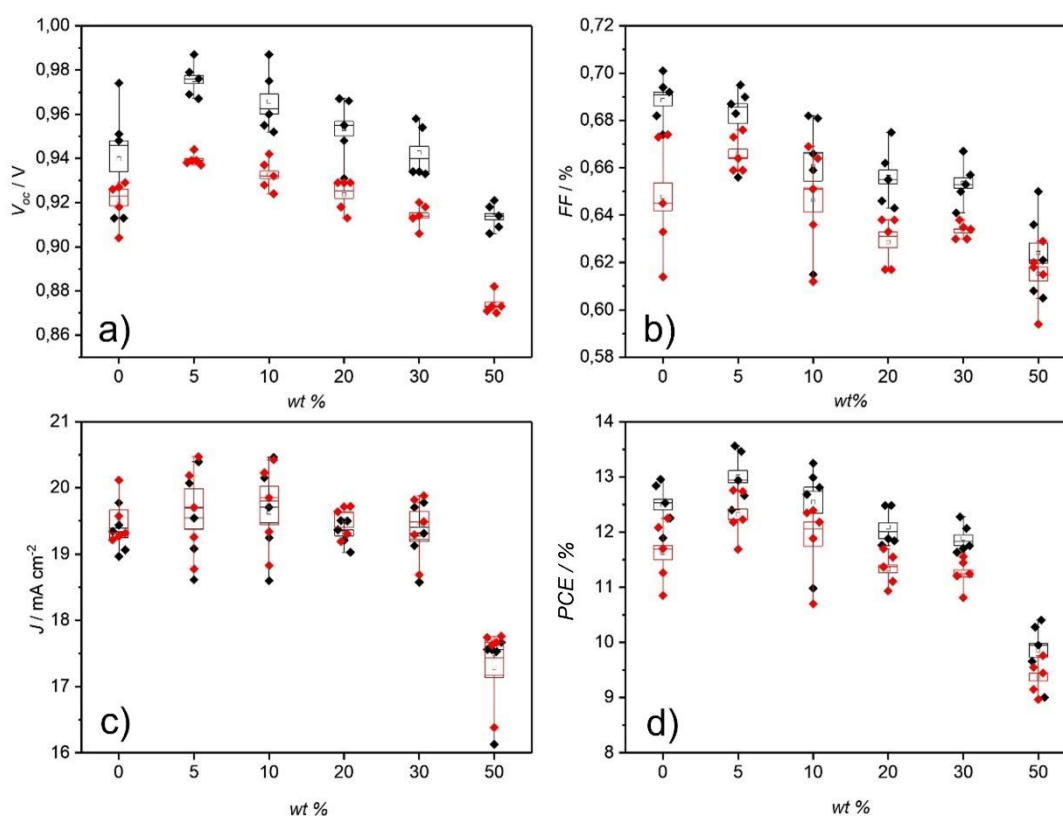


Figure 4.13 J - V parameters obtained from reverse (black) and forward (red) scans of the PSCs made by adding different wt% of ~300 nm PS nanospheres within the meso-TiO₂ layer.

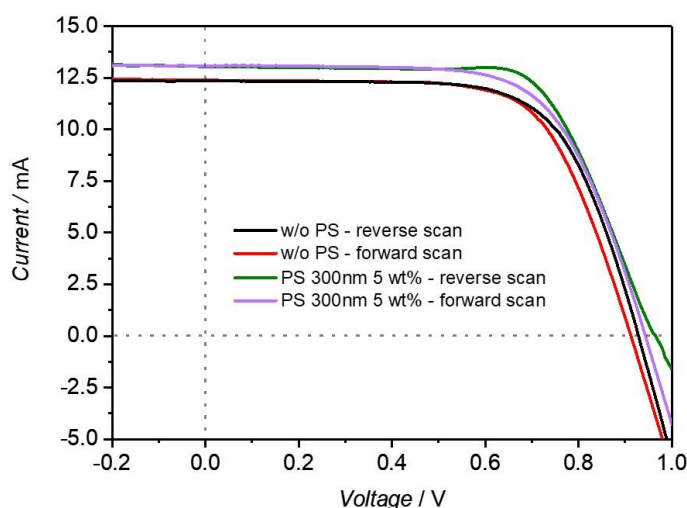


Figure 4.14 J - V curves of the champion PSCs, based on the reference TiO_2 nanoparticles + 5 wt% 300 nm-sized PS nanospheres in forward and reverse scan directions (compared to the bare reference).

The photovoltaic parameters of pastes made by introducing smaller (~ 180 nm) nanospheres (**Figure 4.15**) display enhanced dispersion of results (especially for the V_{oc} , **Figure 4.15a**). Because of this, no specific trends could be observed for V_{oc} and FF values (**Figure 4.15a** and **b**). Interestingly, however, the current densities proved to be higher than the reference for all the modified pastes, with the best performances provided by higher nanospheres wt% (**Figure 4.15c**). Nonetheless, the average PCEs were comparable to the reference in all cases (**Figure 4.15d**). Only in two isolated measures, the sample with highest wt% of nanospheres presented a higher PCE than the reference (as a result of a very high V_{oc}). It must also be noted that this series of samples presents the highest PCEs among all the tested ones (12.8 % for the reference), with the maximum PCE value reached by the 50 wt% of PS ~ 180 nm paste with a remarkable 14.2%. This value is today among the highest results obtained by printable monolithic PSCs when addressing the modification of the meso- TiO_2 layer.^[17] Despite the impossibility of finding the optimal added quantity of nanospheres, the excellent results obtained are a proof of the validity of the strategy; the very high PCE is in fact a consequence of an exceptional V_{oc} (> 0.99 V), which could relate the performance increase to good pore filling and formation of larger perovskite crystals.

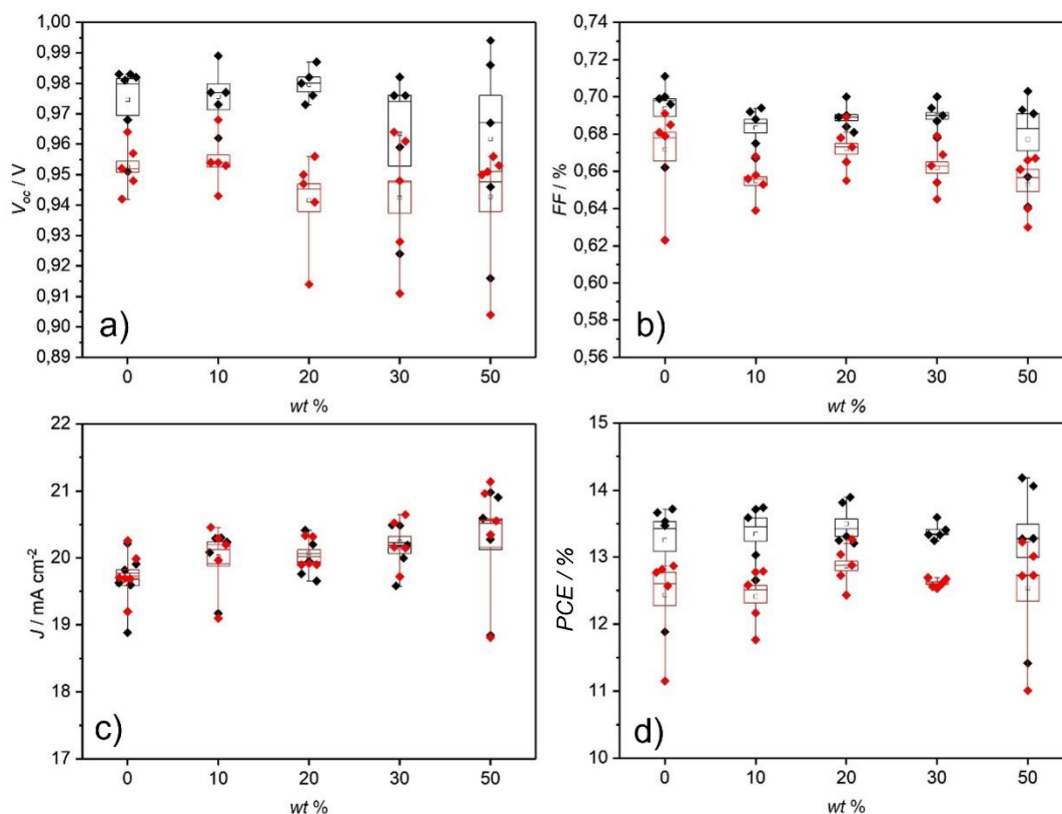


Figure 4.15 J - V parameters obtained from reverse (black) and forward (red) scans of the PSCs made by adding different wt% of ~ 180 nm PS nanospheres within the m-TiO₂ layer.

To better understand the observed trends in relation to the morphology of the ETLs, the meso-TiO₂ layers were characterized by SEM. The difference between the surface of the reference in the absence of nanospheres (**Figure A4.1**) and after the elimination of the polymeric mold (**Figure 4.16**) is evident, with the presence of additional, disordered pores. SEM images of non-fired samples show a clear difference between samples made with 300 or 180 nm nanospheres. While, in the first case, the distribution of the nanospheres on the surface of the m-TiO₂ layer is rather homogeneous (**Figure 4.16a**), in the second case the beads form evident clusters that can reach several μm of diameter (**Figure 4.16b**), which makes their distribution within the layer highly inhomogeneous. As a consequence, the fired 300 nm samples show a more uniform pores distribution (**Figure 4.16c**); conversely, the 180 nm samples are characterized by poorly distributed pores, with areas having fewer pores than others. Pore sizes are also very different. In some cases, the clusters generated by the agglomeration of the nanospheres create micrometer-range cavities that make the surface of the layer bumpy and uneven (**Figure 4.16d**).

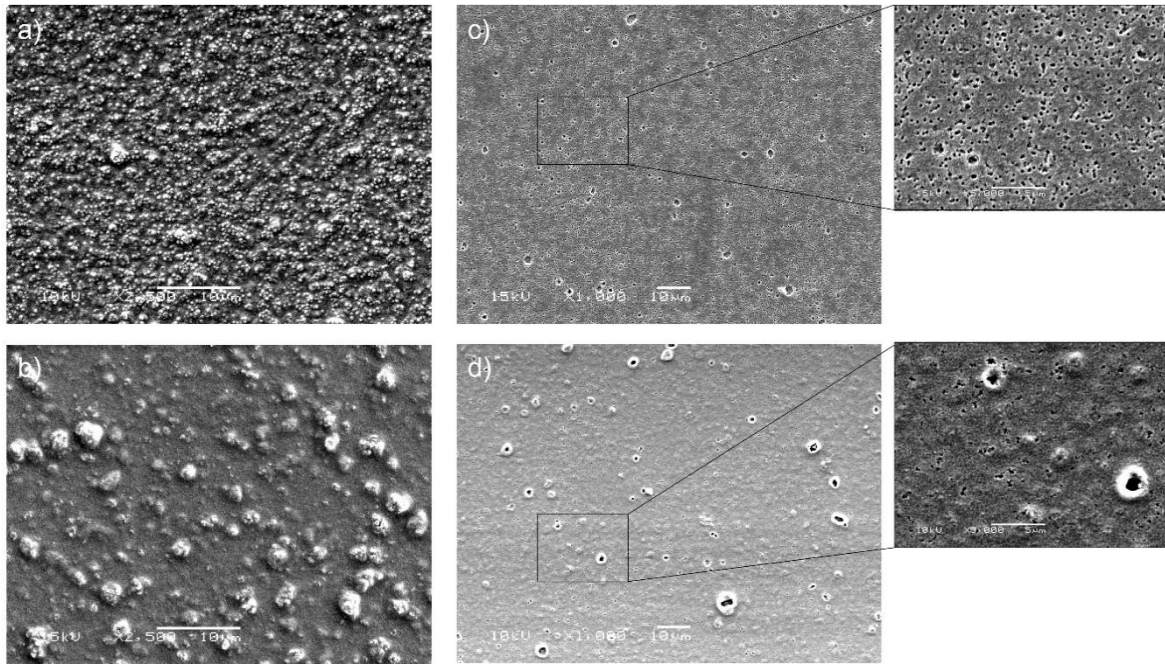


Figure 4.16 Meso-TiO₂ layers for the sample PS-*s*-PAA 300 nm 20 wt % a) before and c) after firing. Meso-TiO₂ layers for PS 180 nm 20 wt % b) before and d) after firing.

The thickness of the layer does not appear to be greatly affected by the presence of the additional porosity, unless big nanosphere aggregates are present (**Figure 4.17**). SEM cross-section images for the 300 nm nanospheres samples confirm what was previously observed concerning the homogeneity of the beads dispersion. In fact, the difference between the samples containing 20 and 50 wt% of nanospheres is visible, and since increase in the amount of nanospheres (and therefore cavities) is well distributed, the layer is homogeneous and the thickness is almost the same in both cases (**Figure 4.17a** and **b**). The presence of clusters disrupting the homogeneity of the layer is confirmed for samples containing 180 nm nanospheres. The formation of aggregates of several tens of nanospheres is evident, regardless of their weight percentage in the paste (**Figure 4.17c** and **d**).

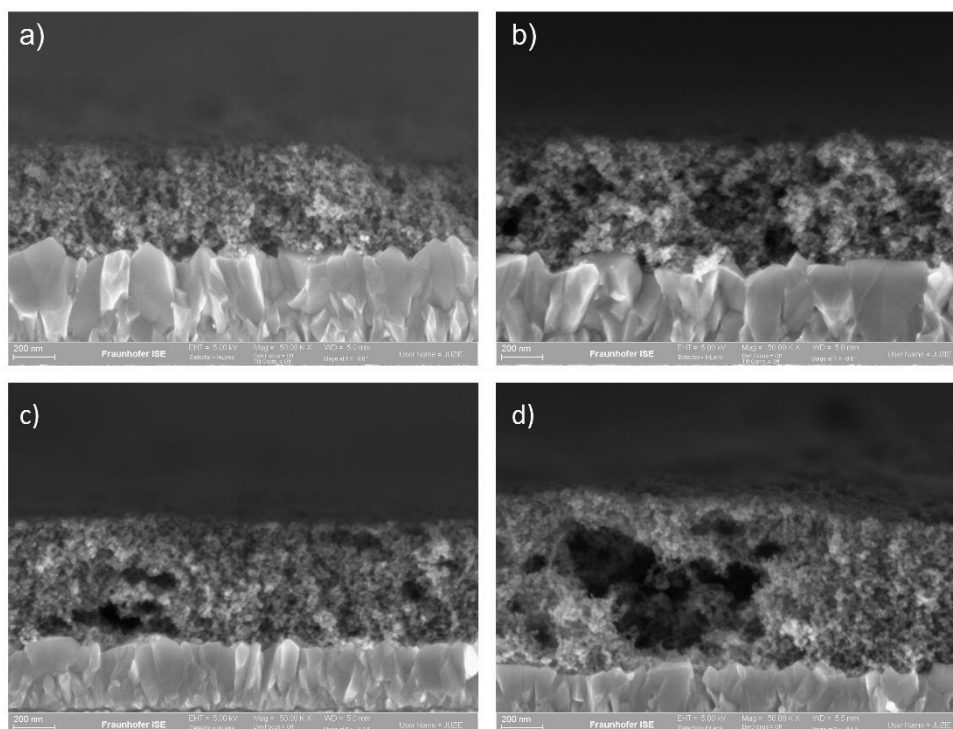


Figure 4.17 SEM cross sections of meso-TiO₂ layer for PS-*s*-PAA 300 nm a) 20 wt % and b) 50 wt % ; meso-TiO₂ layer for PS 180 nm a) 20 wt % and b) 50 wt %.

While the SEM observations provided useful information for the interpretation of the photovoltaic parameters trends, it was still not clear how the pastes containing 180 nm beads, despite their homogeneity being compromised by the clusters, still maintained acceptable performances, in some cases (V_{oc} and J_{sc} , **Figure 4.15**) even better than the reference. In an attempt to elucidate the phenomena related to this efficiency, we performed electrochemical impedance spectroscopy (EIS) on the samples containing 180 nm PS 10wt% and compared them to the reference.

EIS is a useful method to investigate the charge recombination and transfer processes in PSCs. **Figure 4.18** shows the Nyquist plots for three reference samples and three PSCs based on m-TiO₂ layers with 10 wt% 180 nm-sized PS nanospheres. One semicircle at high frequencies and one transmission line/semicircle at low frequencies can be observed in both cases. Fitting the data with an equivalent circuit would not be possible without further analysis; nonetheless, it is possible to compare the results to few previous studies presenting Nyquist plots with the same cell architecture.

Thus, the small semicircle has been generally attributed to transfer resistance at the interface ETL/perovskite. As the semicircle for the 180 nm samples is smaller, this indicates less

resistance at these interfaces, suggesting that photoelectron transfer processes are facilitated; thus, the presence of additional porosity might have contributed to better pore filling, the contact between perovskite and TiO_2 being maintained, even ameliorated. The line/big semicircle at low frequency represents the interfacial and/or bulk recombination, i.e., the recombination impedance of the cell. This semicircle becomes somehow smaller for the 180 nm PS beads samples, indicating an increased probability of recombination of electrons and holes. This could be attributed to the observed disruptions within the layer, where the TiO_2 scaffold layer thickness increased; the thicker the TiO_2 scaffold layer, the longer the distance the carriers need to travel, hence the probability of recombination. In other words, the EIS results might indicate that, while an excellent contact between the interface ELS/perovskite could be obtained, the presence of disorder within the layer (especially areas of different thickness) could increase recombination events.

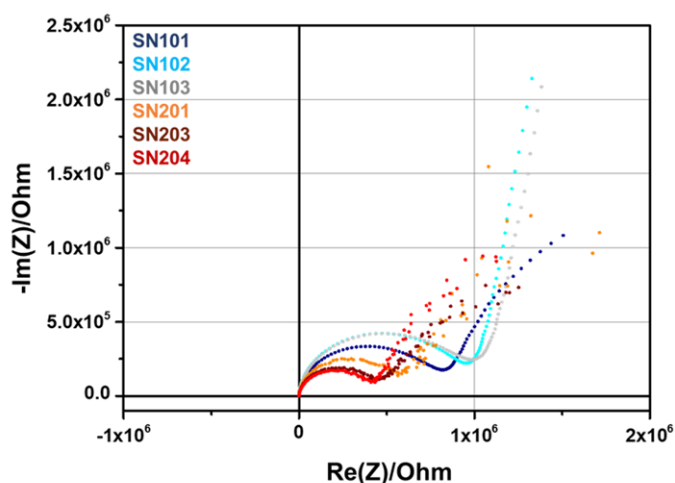


Figure 4.18 Nyquist plots of PSCs based on reference cells (SN101 to 103), vs. $m\text{-TiO}_2$ layers with with 10 wt% 180 nm-sized PS nanospheres (SN201 to 204).

Our initial efforts confirmed that improving the PCE of monolithic PSCs through the use of polymeric scaffolds in the ETL can lead to excellent improvements. It is obviously necessary to further optimize of this strategy, in particular with additional characterizations of the layers and the identification of the best size and quantity of beads, taking into account the trade-off between the growth of bigger perovskite crystals and the generation of additional defects.

An explanation for the different levels of nanospheres aggregation (and therefore, PCEs) observed can be given considering the nature of the beads and the manufacture of the pastes.

Once the spheres are synthesized, their suspension can be dried, forming a powder, in which the beads tend to aggregate. While the cohesion strength is minimal between nanoparticles of quite large diameter (≥ 300 nm), for smaller diameters, (≤ 200 nm), the nanoparticles tend to form very strong and compact aggregates that are very difficult to separate, once formed. This was further confirmed by beads manufacturers, which strongly discourage drying suspended nanoparticles with small diameter on their products sheets, to avoid such effect.^[42,43] The pastes made herein used dry beads powders for the fabrication of the PSCs. It is reasonable then to conclude that, as observed by SEM, while the bigger nanospheres could be integrated in the paste without suffering big aggregation effects, the smaller nanospheres would be irreversibly aggregated at the moment of their addition to the paste, resulting in clusters. Hence, our current efforts focus on the synthesis and direct incorporation of the beads into the paste (without a drying step) so to maintain the dispersion of the beads and the homogeneity of the resulting paste.

4.3 Conclusion

The manufacturing process of monolithic, fully printable carbon-based PSCs makes this type of devices among the most competitive photovoltaic devices present nowadays on the market, with high potential for scalability and applications in future low-cost technologies. Despite this, PCEs of these devices (15.6% at its best^[10]) is still lower than conventional PSCs, which generally feature expensive (Au) electrodes and organic HTMs, and for which the best certified PCE has been recently increased up to 23.7%.^[44] Efforts to increase the PCE of monolithic printable PSCs are therefore necessary to maintain their competitiveness. When a strategy is proposed, however, it is important to bear in mind the principles of cost-effectiveness that represent the strength of these solar cells: unless the PCE is dramatically increased, any modification should avoid increases in the manufacturing ease and cost of the device.

With this mindset, in the present work, we started from already commercialized mesoscopic fully printable carbon-based PSCs and we modified the morphology of the meso-TiO₂ scaffold to increase the PCE of these cells. We initially synthesized and fully characterized a range of mesoporous TiO₂ nanomaterials, namely **1**, **2** and IO-TiO₂, with different morphological features and we introduced them into the stacked devices. The materials brought to poor PCEs in our devices; their use in other PSCs architectures, however, proved very effective. Even if

appropriate adjustments are still needed, our studies represent a first step towards the generation of efficient meso-scaffolds for printable monolithic PSCs with these materials.

We successively adopted an even more viable strategy by introducing different degrees of porosity into state-of-the-art nanoparticle based TiO₂ scaffolds by using polymer beads as sacrificial templates. All the so-made ETLs have then been characterized and introduced into the final devices for the determination of the photovoltaic parameters. By varying the polymer nature, diameter of the nanosphere and polymer/TiO₂ weight ratio, we have obtained an optimal ETL layer based on the addition of 5 wt% of 300 nm PS nanospheres, which showed better V_{oc} , FF and J_{sc} than the reference, and for which the max PCE reached 13.6% (with an average of 12.7%).

Additionally, with the use of smaller nanospheres (~180 nm), we could reach maximum efficiencies up to 14.2%, the best achieved so far from the simple modification of the TiO₂ mesoporous layer of mesoscopic carbon-based solar cells. To the best of our knowledge, this is also the first time that materials like inverse-opal TiO₂ or polymeric nanospheres as sacrificial scaffolds are employed with monolithic PSCs.

While further studies are needed to better identify the optimal size and quantity of beads compared to TiO₂ nanoparticles, these results represent the first confirmation of a strategy that has the potential to afford excellent PCE enhancements with minimum impact on the manufacturing process of printable monolithic carbon-based PSCs, a front runner on the market for its competitive low cost.

4.4 Experimental section

General

All chemicals were purchased from commercial sources and used as received. Pluronic P123 (Poly(ethylene glycol)-*block*-poly(propylene glycol)-*block*-poly(ethylene glycol), P123), titanium isopropoxide (TIPO), Styrene, Potassium persulfate (KPS) and sodium dodecylsulfate (SDS), ammonium persulfate (APS) and acrylic acid of analytical reagent grade were purchased from Sigma-Aldrich. The monodispersed polystyrene (PS) nanospheres of ~175 nm diameter used in this work were kindly provided from prof. Billon's bio-inspired materials group in UPPA, France.

The hydrophilization of the substrates for the synthesis of the inverse-opal TiO₂ materials was carried on using a QUORUM Q150T ES Sputter coater (plasma mode). The monodispersed PS nanospheres of ~300 nm diameter used for the fabrication of this material were purchased from Sigma-Aldrich.

For the materials characterization, scanning electron microscope (SEM) images were obtained from a JEOL 7500F microscope operating at 15kV with EDX detector incorporated, while transmission electron microscope (TEM) images were recorded on a TECNAI T20 and T10 microscopes working under 200 kV and 100 kV. Powdery X-ray diffraction was used to investigate the crystallinity and identify crystalline phases with a Panalytical X'Pert PRO diffractometer (Cu K α radiation, Bragg-Brentano geometry, sealed tube operated at 45 mA 30 kV X'Celerator linear detector). The nitrogen physisorption analysis was performed with ASAP 2420 using a platinum resistance device and liquid nitrogen as an adsorbed molecule to detect the porosity. The surface areas of the materials were calculated with the Brunauer–Emmett–Teller (BET) equation, and their pore-size distributions were determined by using the Barrett–Joyner–Halenda (BJH) formula from the adsorption branch.

Fluorine-doped tin oxide glass substrates TCO22-7/LI (sheet resistance 7 Ω /sq.), silver paste Elcosil SG/SP, titania paste Ti-nanoxide T165/SP, zirconia paste Zr-nanoxide ZT/SP, carbon graphite paste Elcocarb B/SP and methylammonium lead iodide perovskite solution with 5-ammonium valeric acid additive (5-AVAI) were provided by Solaronix SA. Titanium

diisopropoxide bis (acetylacetonate) (75% in isopropanol), Hellmanex, isopropanol, ETHOCEL™ and terpineol were purchased from Sigma-Aldrich.

The current-density and voltage curves of aged devices were measured with a source meter (Keithley 2400) at a scan rate of 5 mV/s using a class A solar simulator providing 100 mW/cm², AM 1.5G illumination. The infiltration of the perovskite ink was done using an inkjet printer PixDro LP50, with a spatial resolution tuned to match the wished perovskite volume onto the cell. The optimal resolution was obtained with 350 x 350 dpi. Scanning Electron Microscopy (SEM) images were obtained with a SEM Tescan Vega Serie. We thank Dmitry Bogachuk (Fraunhofer Institute for Solar Energy Systems) and Frédéric Oswald (CEA) for the additional SEM images.

Synthesis of TiO₂ mesoporous materials

TiO₂ anatase nanoparticles with mesoporous channels (1). P123 (5 g), ethanol (15 g), HCl (7 g) and 2.3 g of a solution of H₂SO₄ 44% wt were mixed in a round bottom flask equipped with Graham condenser, temperature control and oil bath. The mixture was successively heated at 40°C and stirred for 3 h. After that, 15 g of TIPO were added under vigorous stirring, and the mixture was kept at 40°C under stirring for 20 h. The solution was then poured into a crystallization dish and kept at 40°C under 50-60 % relative humidity conditions for two days. The membranes formed were let dry in an oven at 100°C for two days. The products were initially calcinated under N₂ at 550°C for 3 h (temperature increase 2°C/min), and subsequently in air at 450°C for 6 h. The material obtained was in the form of a white powder.

Spherical-shaped TiO₂ anatase nanoparticles (2). 4 g of P123 were dissolved in 100 ml water at 40°C. After the surfactant dissolved, 1.5 g of concentrated sulfuric acid were added. 11.76 g of TIPO were mixed to 4.14 g of 2,4-pentanedione and then added slowly to the previous mixture under vigorous stirring. The solution was heated at 55°C and let for 2 h without stirring. After this time, the solution was transferred to an autoclave and underwent hydrothermal treatment at 90°C for 10 h. After the hydrothermal treatment, the formed product was filtered and washed with water and ethanol (2 times each). Successively, the product was calcinated in air at 300°C (temperature increase 1°C/min) for 4 h. The material obtained was in the form of a white powder.

Synthesis of polymeric nanospheres and inverse opal TiO₂

Polystyrene nanospheres ~300 nm (PS). Styrene is previously washed with 0.1 M NaOH (x2) and water (x2) in a separation funnel (to eliminate the stabilizing agent). In a 2-neck round bottom flask (250 mL) equipped with stirring bar and oil bath SDS is added in 100 mL H₂O (N₂ is previously bubbled for around 30 min to eliminate the free oxygen before adding the SDS). When SDS is dissolved, KPS is added and the temperature is raised to 80°C under Ar. Successively, styrene and 1-butanol are added drop by drop through a dripping funnel while stirring. Stirring is fixed to 200 rpm at 80°C for 1h, then the temperature is raised to 85°C for 20h. After this time the reaction is quenched (when necessary, the spheres were washed with milliQ water three times by centrifugation and the solvent was replaced with milliQ water).

Polystyrene-*stat*-Polyacrylic acid nanospheres ~300 nm (PS-*s*-PAA). Styrene is previously washed with 0.1 M NaOH (x2) and water (x2) in a separation funnel (to eliminate the stabilizing agent). In a 2-neck round bottom flask (250 mL) equipped with stirring bar and oil bath, 10 g styrene are added together with 0.5g acrylic acid and 120g H₂O. N₂ is bubbled for around 30 min. After this time, the mixture is heated to 75°C and a solution of APS (0.2g) in 10 g H₂O is added. The mixture is stirred under N₂ for 10 hours. After this time, the reaction is quenched (when necessary, the spheres were washed with milliQ water three times by centrifugation and the solvent was replaced with milliQ water).

Inverse opal TiO₂ (IO-TiO₂) (collaboration with Thomas Lourdu Madanu, UNamur). TiO₂ nanoparticles of <10 nm diameter were previously prepared as described elsewhere.^[28] A known concentration of PS nanospheres (0.1 wt %) was mixed to a 8 mL suspension of the TiO₂ nanoparticles (40 µL per mL of the final suspension) in a 10 mL beaker. The suspension was sonicated for 5 minutes. Successively, the hydrophilic glass substrates were immersed in the suspension, immobilized in a vertical position, and left in a oven at 40°C for several days, until complete evaporation of the aqueous suspension. (In this phase, the substrates should not be touched or moved, in order to avoid the disruption of the highly ordered PS scaffold film onto the suspended substrate). Once completely dry, the substrates were calcinated at 500°C (temperature increase 1°C/min) for 2h.

Preparation of the m-TiO₂ ETL screen print pastes using material 1 and 2

Chapter 4

Experimental m-TiO₂ pastes were prepared as analogues of Ti-nanoxide T165/SP manufactured by Solaronix SA. 1.8 g of dry TiO₂ powders of **1** or **2** were finely grated in a mortar. 5g of terpineol were added slowly, until no aggregates were visible at naked eye. The dispersion was transferred into a beaker and put to sonication for at least 30 minutes. Successively, an ultrasonication probe (2 minutes at 20% Amplitude, pulses of 2 sec on 2 sec off) was used. 5g of ETHOCEL™ 7 in terpineol were added (if some aggregates were forming at this point, the ultrasonication probe was used again until the dispersion was homogeneous). The final paste was mixed thoroughly on a 3-roll mill at max speed for 5 minutes.

Preparation of the m-TiO₂ ETL screen print pastes by incorporation of polymeric nanospheres

Experimental m-TiO₂ pastes were prepared as analogues of Ti-nanoxide T165/SP manufactured by Solaronix SA, with the addition of a specific quantity and type of polymeric nanosphere, as follows.

A certain amount of nanospheres powder (5, 10, 20, 30, or 50 wt% of TiO₂) was finely grated in a mortar. 5g of terpineol were added slowly, until no aggregates were visible at naked eye. The dispersion was transferred into a beaker and put to sonication for at least 30 minutes. Successively, an ultrasonication probe (2 minutes at 20% Amplitude, pulses of 2 sec on 2 sec off) was used. 5g of ETHOCEL™ 7 in terpineol were added (if some aggregates were forming at this point, the ultrasonication probe was used again until the dispersion was homogeneous), followed by 10 g of Paste Ti nanoxide (18.4 wt% TiO₂) Solaronix. The final paste was mixed thoroughly on a 3-roll mill at max speed for 5 minutes.

Preparation of the m-TiO₂ ETL layer using IO-TiO₂

The experimental m-TiO₂ ETL layer using IO-TiO₂ was prepared as described above (IO-TiO₂ synthesis), by using a FTO substrate on which the compact TiO₂ layer was previously deposited.

Fabrication of the solar cells

Devices were fabricated on 10x10 cm² plates of FTO-coated glass. First, a laser pattern defined cathode and anode areas with an automated fiber laser. After that, the substrate was subjected to sequential cleaning steps in 1% aqueous solution of Hellmanex, acetone, and isopropanol respectively (20 min each) in an ultrasonic bath and subsequently dried in air. The thin compact titania layer (c-TiO₂) was grown by spray-pyrolysis on a hot-plate set to 550°C, using a glass

mask to protect the contact areas. A volume of 20 mL of titanium diisopropoxide bis (acetylacetonate) diluted in absolute ethanol (1:160) was sprayed with oxygen as a carrier gas, and warming was prolonged for 30 min before allowing the sample to cool down.

An array of 18 electrodes was subsequently defined by screen-printing silver contacts, followed by m-TiO₂, ZrO₂ and finally carbon paste, using a 100e40, 165e30, 90e48, and 43e80 mesh stencil, respectively (the number of strands is per cm). Each screen-printed layer was allowed to dwell for 10 min before drying at 120°C for 10 min, followed by a firing step at 500°C (or 400°C for carbon) for 30 min, after a 30 min ramp. The perovskite precursor solution was deposited by inkjet, selectively on the active solar cells areas, with a 10µL droplet volume.

The wet samples were then annealed at 50°C for 10 min, to allow the perovskite crystallization in the porous electrodes structure. Finally, the solar cells were individualized by cutting the glass substrate into the corresponding solar cells. The resulting devices were submitted to heat and damp treatment at 42°C and 75% R.H. for 135 h before being tested.^[45]

4.5 References

- [1] A. Kojima, K. Teshima, Y. Shirai, T. Miyasaka, *J. Am. Chem. Soc.*, **2009**, *131*, 6050–6051.
- [2] P. Roy, N. Kumar Sinha, S. Tiwari, A. Khare, *Sol. Energy*, **2020**, *198*, 665–688.
- [3] S. M. Abdulrahim, Z. Ahmad, J. Bahadra, N. J. Al-Thani, *Nanomaterials*, **2020**, *10*, 1–23.
- [4] L. Etgar, P. Gao, Z. Xue, Q. Peng, A. K. Chandiran, B. Liu, M. K. Nazeeruddin, M. Grätzel, *J. Am. Chem. Soc.*, **2012**, *134*, 17396–17399.
- [5] Y. Lv, Y. Jin, W. Cai, Z. Zhang, X. Zhou, H. Chen, *J. Alloys Compd.*, **2020**, *821*, 153272.
- [6] H. Chen, S. Yang, *Adv. Mater.*, **2017**, *29*, 1603994.
- [7] A. Verma, D. Martineau, S. Abdolhosseinzadeh, J. Heier, F. Nüesch, *Mater. Adv.*, **2020**, *1*, 153–160.
- [8] Z. Ku, Y. Rong, M. Xu, T. Liu, H. Han, *Sci Rep*, **2013**, 3132.
- [9] Y. Rong, Z. Ku, A. Mei, T. Liu, M. Xu, S. Ko, X. Li, H. Han, *J. Phys. Chem. Lett.*, **2014**, *5*, 2160–2164.
- [10] Y. Rong, X. Hou, Y. Hu, A. Mei, L. Liu, P. Wang, H. Han, *Nat. Commun.*, **2017**, *8*, 1–8.
- [11] D. Bogachuk, R. Tsuji, D. Martineau, S. Narbey, J. P. Herterich, L. Wagner, K. Suginuma, S. Ito, A. Hinsch, *Carbon N. Y.*, **2021**, *178*, 10–18.
- [12] Z. Li, S. A. Kulkarni, P. P. Boix, E. Shi, A. Cao, K. Fu, S. K. Batabyal, J. Zhang, Q. Xiong, L. H. Wong, N. Mathews, et al., *ACS Nano*, **2014**, *8*, 6797–6804.
- [13] Z. Wei, H. Chen, K. Yan, X. Zheng, S. Yang, *J. Mater. Chem. A*, **2015**, *3*, 24226–24231.
- [14] X. Hou, Y. Hu, H. Liu, A. Mei, X. Li, M. Duan, G. Zhang, Y. Rong, H. Han, *J. Mater. Chem. A*, **2017**, *5*, 73–78.
- [15] Y. Sheng, Y. Hu, A. Mei, P. Jiang, X. Hou, M. Duan, L. Hong, Y. Guan, Y. Rong, Y. Xiong, H. Han, *J. Mater. Chem. A*, **2016**, *4*, 16731–16736.
- [16] X. Li, M. Tschumi, H. Han, S. S. Babkair, R. A. Alzubaydi, A. A. Ansari, S. S. Habib, M. K. Nazeeruddin, S. M. Zakeeruddin, M. Grätzel, *Energy Technol.*, **2015**, *3*, 551–555.
- [17] M. Duan, Y. Hu, A. Mei, Y. Rong, H. Han, *Mater. Today Energy*, **2018**, *7*, 221–231.
- [18] Y. Xiao, N. Cheng, K. K. Kondamareddy, C. Wang, P. Liu, S. Guo, X. Z. Zhao, *J. Power Sources*, **2017**, *342*, 489–494.
- [19] C. Zhen, T. Wu, R. Chen, L. Wang, G. Liu, H.-M. Cheng, *ACS Sustain. Chem. Eng.*, **2019**, *7*, 4586–4618.
- [20] Y. Yang, K. Ri, A. Mei, L. Liu, M. Hu, T. Liu, X. Li, H. Han, *J. Mater. Chem. A*, **2015**, *3*, 9103–9107.
- [21] Z. Yu, F. Qi, P. Liu, S. You, K. K. Kondamareddy, C. Wang, N. Cheng, S. Bai, W. Liu, S. Guo, X. Z. Zhao, *Nanoscale*, **2016**, *8*, 5847–5851.
- [22] R. Zhang, B. Tu, D. Zhao, *Chem. - A Eur. J.*, **2010**, *16*, 9977–9981.
- [23] D. S. Kim, S. Y. Kwak, *Appl. Catal. A Gen.*, **2007**, *323*, 110–118.
- [24] M. Thommes, K. Kaneko, A. V Neimark, J. P. Olivier, F. Rodriguez-Reinoso, J.

- Rouquerol, K. S. W. Sing, *Pure Appl. Chem.*, **2015**, 87, 1051–1069.
- [25] K. Liu, Z. Wang, *Front. Chem. China*, **2007**, 2, 17–20.
- [26] W. Sun, S. Zhou, B. You, L. Wu, *Chem. Mater.*, **2012**, 24, 3800–3810.
- [27] A. D. Jenkins, K. L. Loening, *Compr. Polym. Sci. Suppl.*, **1989**, 13–54.
- [28] K. R. Phillips, T. Shirman, E. Shirman, A. V Shneidman, T. M. Kay, J. Aizenberg, *Adv. Mater.*, **2018**, 30, 1706329.
- [29] B. Hatton, L. Mishchenko, S. Davis, K. H. Sandhage, J. Aizenberg, *Proc. Natl. Acad. Sci. U. S. A.*, **2010**, 107, 10354–10359.
- [30] Z. hui Liu, S. Bi, G. liang Hou, C. zhan Ying, X. jia Su, *J. Power Sources*, **2019**, 430, 12–19.
- [31] I. S. Yang, J. S. You, S. Do Sung, C. W. Chung, J. Kim, W. I. Lee, *Nano Energy*, **2016**, 20, 272–282.
- [32] Y. Huang, J. Zhu, Y. Ding, S. Chen, C. Zhang, S. Dai, *ACS Appl. Mater. Interfaces*, **2016**, 8, 8162–8167.
- [33] X. Chen, S. Yang, Y. C. Zheng, Y. Chen, Y. Hou, X. H. Yang, H. G. Yang, *Adv. Sci.*, **2015**, 2, 1–6.
- [34] A. Maho, M. Lobet, N. Daem, P. Piron, G. Spronck, J. Loicq, R. Cloots, P. Colson, C. Henrist, J. Dewalque, *ACS Appl. Energy Mater.*, **2021**, 4, 1108–1119.
- [35] S. J. Ha, J. H. Heo, S. H. Im, J. H. Moon, *J. Mater. Chem. A*, **2017**, 5, 1972–1977.
- [36] M. Lobet, P. Piron, J. Dewalque, A. Maho, O. Deparis, C. Henrist, J. Loicq, *Opt. Express*, **2019**, 27, 32308.
- [37] J. Liu, M. Yao, L. Shen, *J. Mater. Chem. C*, **2019**, 7, 3121–3145.
- [38] H. Lu, B. Gu, S. Fang, *Sustain. Energy Fuels*, **2021**, 5, 880–885.
- [39] T. Hwang, S. Lee, J. Kim, J. Kim, C. Kim, B. Shin, B. Park, *Nanoscale Res. Lett.*, **2017**, 12, DOI 10.1186/s11671-016-1809-7.
- [40] A. Krishna Sailaja, *Drug Des. Intellect. Prop. Int. J.*, **2018**, 2, DOI 10.32474/ddipij.2018.02.000140.
- [41] H. S. Kim, N. G. Park, *J. Phys. Chem. Lett.*, **2014**, 5, 2927–2934.
- [42] Bangs Laboratories, *Tech Notes*, **2008**, 1–3. (www.bangslabs.com)
- [43] Bangs Laboratories, *Tech Notes*, **2013**, 1–16. (www.bangslabs.com)
- [44] H. S. Kim, A. Hagfeldt, N. G. Park, *Chem. Commun.*, **2019**, 55, 1192–1200.
- [45] S. G. Hashmi, D. Martineau, M. I. Dar, T. T. T. Myllymäki, T. Sarikka, V. Ulla, S. M. Zakeeruddin, M. Grätzel, *J. Mater. Chem. A*, **2017**, 5, 12060–12067.

4.6 Appendix

Characterization of the reference m-TiO₂ ETL (Nanoxide T/SP m-TiO₂ paste produced by Solaronix SA)

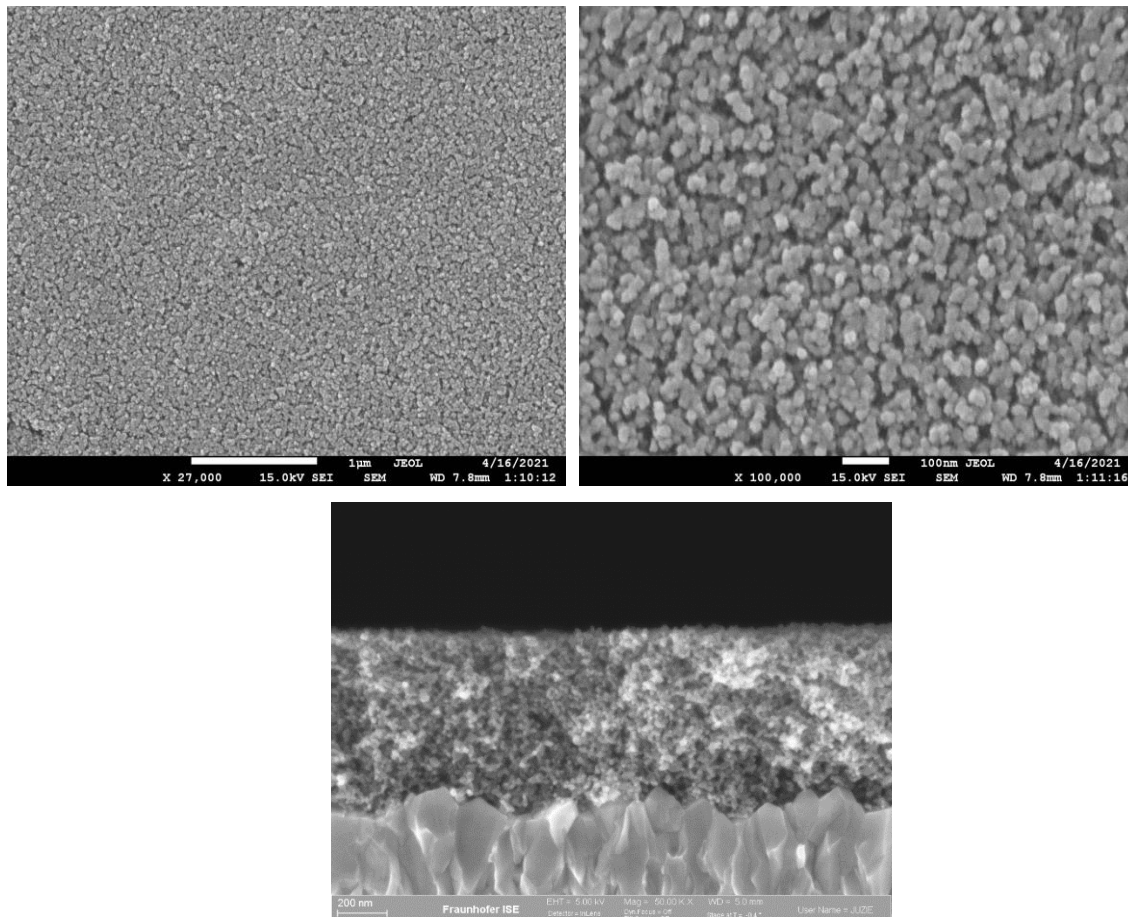


Figure A4.1 SEM images of the m-TiO₂ layer made with the reference TiO₂ nanoparticles (Nanoxide T/SP m-TiO₂ produced by Solaronix SA). Above, top view; Below, cross-section view.

Characterization of the m-TiO₂ ETL made with material 1

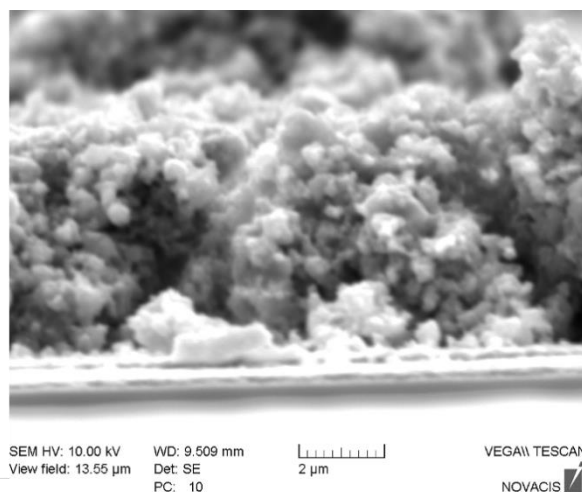


Figure A4.2 SEM image of the m-TiO₂ layer made with material **1**. Cross-section view.

Characterization of PS nanospheres (UPPA)

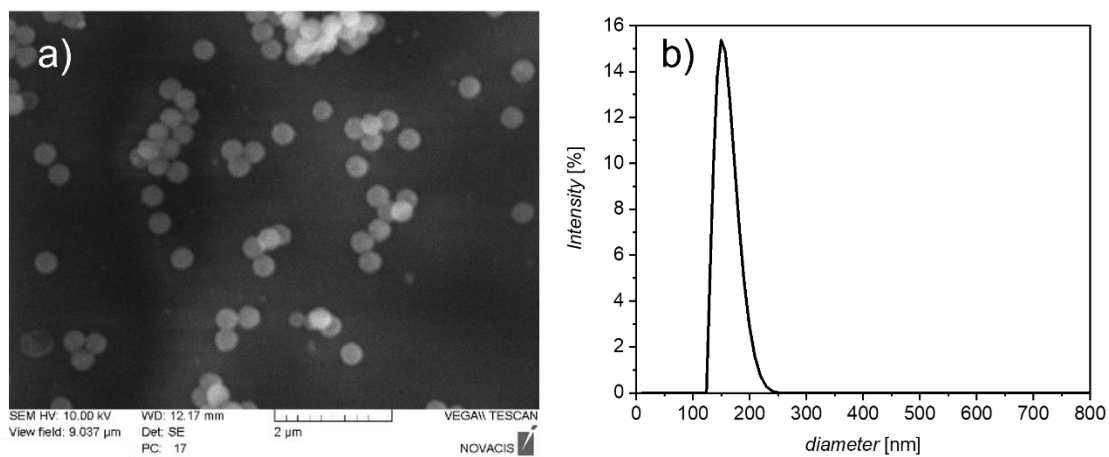


Figure A4.3 a) SEM image of PS nanospheres and b) DLS analysis (mean diameter 175 nm).

Chapter 5 Conclusions and future perspectives

The heterogenization of molecular catalysts has proven, over the years, to be an excellent strategy for the creation of efficient and industrially relevant electrodes for the CO₂ reduction reaction (CO₂RR).^[1-3] More efficient and selective systems, together with more advanced analytical methods, have allowed the recent implementation of molecular catalysts into flow cells and electrolyzers that could operate at large current densities, giving rise to exciting new perspectives.^[4,5]

Among these molecular catalysts, one in particular, [Ni(cyclam)]²⁺, attracted our attention for its history of “ups and downs”, starting with its discovery as an exceptional homogeneous CO₂ reduction catalyst in aqueous conditions.^[6] The initial enthusiasm of the scientific community somewhat faded when it was understood that the activity of [Ni(cyclam)]²⁺ was the result of a series of complex interactions concerning the configuration of the catalyst, its deactivation, but above all, its exclusive interaction with mercury electrodes: it was thought that in the absence of Hg, [Ni(cyclam)]²⁺ could not represent a valid catalyst for the electroreduction of CO₂.^[7,8] After more than twenty years from its discovery, in parallel to computational and experimental studies aimed at elucidating the catalysis mechanism, [Ni(cyclam)]²⁺ started to be utilized with glassy carbon electrodes besides Hg^[9,10]; the relatively few attempts regarding its heterogenization, however, generally gave poor results.^[11,12]

As the first objective of this PhD project was to synthesize new CO₂-reducing molecular catalysts and integrate them into nanostructured porous scaffolds, we decided to take up the [Ni(cyclam)]²⁺ challenge. We thus asked ourselves if noncovalent heterogenization could work as a strategy to reach levels of catalytic activity comparable to those obtained by this catalyst when used in homogeneous systems in the presence of Hg.

In a first study, we therefore synthesized the first [Ni(cyclam)]²⁺ with a pyrene functionalization for its immobilization on the surface of multi-walled carbon nanotubes (MWCTs). We obtained a unique 6-coordinated Ni cyclam complex (**1**), which we first characterized in homogeneous conditions. We then heterogenized such complex on porous, carbon-based electrodes, and characterized such system electrochemically for CO₂ electroreduction. The complex proved to be much more active in the immobilized form than under homogeneous conditions, with

Faradaic Yields (FY) for CO production above 90% and current densities up to 10 mA cm⁻² in acetonitrile/water mixture. Although the hybrid electrodes did not maintain a high selectivity for CO when utilized in aqueous conditions, this research proved to be a success, in the fact that for the first time it was possible to obtain excellent turnover numbers with a heterogenized [Ni(cyclam)]²⁺, thus confirming the validity of the strategy and encouraging us to search for improvements to this promising hybrid system.

Consequently, among other aspects, we individuated (i) the quite negative working overpotentials and (ii) the poor selectivity of the catalyst in water as the most crucial issues to tackle. These two phenomena are closely related to the environment surrounding the Ni center, and molecular catalysts have the powerful advantage that their primary and secondary coordination spheres can be tuned by manipulating the chelating environment.

We have thus synthesized another [Ni(cyclam)]²⁺ catalyst, complex **2**, this time with a pyrene moiety coordinated to a carbon atom of the cyclam macrocycle, in light of the observations that N-substituted [Ni(cyclam)]²⁺ catalysts (in both homogeneous^[13-16] and heterogeneous conditions^[11]) poorly catalyze the CO₂RR in aqueous medium.

The objective of obtaining a similar metal center configuration to the parent [Ni(cyclam)]²⁺ (and thus also reducing the overpotential for the Ni^{II} to Ni^I reduction process) was confirmed by characterization in homogeneous conditions; after the heterogenization of such complex on MWCNTs, we performed electrochemical tests under the same conditions as **1**, and we found that the selectivity had improved. Moreover, when tested in aqueous conditions, the new complex maintained its selectivity for CO with the highest FY value (87%) obtained at -0.8 V vs. RHE. Although a partial loss of selectivity and current density after 4h CPE, CO remained the major product.

With these results, we obtained the experimental proof that substitution of N atoms in the cyclam ring leads to lower selectivity for CO when [Ni(cyclam)]²⁺ is immobilized on carbon electrodes. Besides that, to the best of our knowledge, our complex has proven to be the most selective [Ni(cyclam)]²⁺ catalyst covalently heterogenized on carbon electrodes in water. While this allowed us to give an answer to our initial question, at the same time it paved the way for many other challenges and ideas for possible future improvements.

Further studies under the heterogeneous conditions need to be carried on. It should be understood if the catalytic mechanism follows exactly the same pathway as in the homogeneous case, or if the substrate could bring any effect to the selectivity and activity of the catalyst.

Finally, it could be possible to further optimize few secondary aspects, as follows. First, starting from the complex synthesis, C-substitutions to the cyclam ring could be added in such a way that the atoms around the Ni center would adopt a flat arrangement (this was demonstrated to afford even better catalysts than $[\text{Ni}(\text{cyclam})]^{2+}$ itself in homogeneous conditions^[10,14]). Secondly, the distance of the catalyst and its position in space relatively to the substrate (e.g., longer or shorter chain) should be investigated, to see what effects it entails in relation to electronic exchanges.

It is for this reason, among others, that we have begun the synthesis of a third pyrene-modified $[\text{Ni}(\text{cyclam})]^{2+}$ complex, where the C-substituted cyclam ring and the pyrene moiety will be separated by a 4-C alkyl chain.

To date, the excellent properties of MWCNTs remain almost undisputable, but one could think of another substrate, especially optimized to avoid the desorption of the catalyst on the long run, and maximize mass transport phenomena. With their multiple levels of porosity, conductive hierarchical materials could represent a valid alternative. At the same time, a more accurate study concerning the optimal loading of the catalyst, which for reasons of time could not be done during the project, should also be carried on.

Within the framework of the eSCALED project, the second objective of this PhD was to collaborate with the Swiss company Solaronix to improve the performance of the perovskite solar cells that will be used in the eSCALED final device. This represented a great opportunity, and at the same time a great challenge, as we would try to ameliorate devices which are already optimized and commercialized. By analyzing the architecture of such cells, i.e., fully printable, monolithic, carbon-based PSCs, we observed that relatively few efforts to optimize the mesoporous TiO_2 scaffold were described^[17–19] (despite its paramount importance), compared to the carbon electrodes^[20–22] or the perovskite precursors.^[23–25] Hence, we decided to modify the electron transporting layer (ETL) morphology, without largely affecting the economical and scalability aspects of the manufacturing process.

We initially chose three materials that, for their morphological structure, represented good candidates to replace the reference TiO₂ layer. Hence, we synthesized and fully characterized material **1**, **2**, and IO-TiO₂, which possessed anatase nanoparticles of similar sizes, however their arrangement generated ordered mesoporous channels for **1**, spherical domains for **2**, and inverse opal structure for **3**. With our surprise, all these materials performed poorly in the stacked devices. The excellent results when introduced in other PSCs architectures,^[26–28] however, demonstrated that the materials synthesized in this study have the potential to work as very efficient ETLs in monolithic PSCs. Our studies represent therefore a first step towards the generation of efficient meso-scaffolds with these materials. A first optimization that could already bring to improvements in PCEs should focus on reducing the thickness of the layers.

The results obtained with the materials led us to consider another strategy of easier implementation, in which we directly modified the reference meso-TiO₂ by the introduction of polymeric nanospheres. The polymer bead acted as a scaffold, creating additional porosity. The introduction of polymer scaffolds to modify the morphology of the layer was previously described for mesoscopic PSCs,^[29] however, to the best of our knowledge, it was never tested on monolithic printed PSCs. For our studies, we have optimized the synthesis of polystyrene (PS) and polystyrene-*stat*-polyacrylic acid (Ps-*s*-PAA) nanospheres, obtaining suitable monodisperse beads, without increasing the PSC manufacturing cost with the purchase of expensive products.

By varying the polymer nature, diameter of the nanospheres and polymer/TiO₂ weight ratio, we have found that (i) PS nanospheres represent an optimal candidate for this application, because of their stability, ease of synthesis with good diameter tunability and monodispersity; (ii) a trade-off between the creation of cavities that could host bigger perovskite crystals and the generation of additional layer defects implies that an optimal amount of beads must be found, depending on their diameter; (iii) in the case of 300 nm nanospheres, the best performances were given by 5 wt% of PS, with an average of 12.7% PCE; (iv) special attention must be paid when handling smaller nanospheres, as they can generate irreversible aggregates and thus disrupt the homogeneity of the layer. Nonetheless, the maximum PCE among all the devices tested in this work was attained with a sample containing 50 wt% of ~180 nm beads, with a stunning 14.2%, which is today among the highest results obtained by printable monolithic PSCs when addressing the modification of the meso-TiO₂ layer.^[30]

This work opens up numerous perspectives: it is first of all necessary to further optimize of this strategy, in particular with additional characterizations of the layers, in order to understand the effect of such beads within the ETL and especially the influence of the cavities on perovskite deposition and evolution of the crystallization process. Additional tests aiming at the identification of the best size and quantity of beads are essential. Smaller diameters (50-100 nm) could be tested, however with the precaution of maintaining the dispersion of the beads and the absence of aggregates in the resulting paste.

Once a good performance is obtained, it would be essential to analyze the cells via X-ray diffraction, to assess the crystallinity of the material and the dimension of the crystals. Among others, also UV–Vis absorption of the scaffold layer infiltrated with perovskite could provide useful information to verify if the modification brought to an increment of optical absorption.

This PhD might have come to an end, however, in scientific research, the word end does not exist. I sincerely hope that these results will travel, grow, evolve, and somehow manage to contribute to both the fields of CO₂ electroreduction and perovskite solar cells. Above all, I can not wait to see the work of all of us in a single artificial leaf signed eSCALED.

5.1 References

- [1] B. Zhang, L. Sun, *Chem. Soc. Rev.*, **2019**, *48*, 2216–2264.
- [2] C. Sun, R. Gobetto, C. Nervi, *New J. Chem.*, **2016**, *40*, 5656–5661.
- [3] L. Rotundo, R. Gobetto, C. Nervi, *Curr. Opin. Green Sustain. Chem.*, **2021**, *31*, 100509.
- [4] Y. Wu, Z. Jiang, X. Lu, Y. Liang, H. Wang, *Nature*, **2019**, *575*, 639–642.
- [5] S. Ren, D. Joulié, D. Salvatore, K. Torbensen, M. Wang, M. Robert, C. P. Berlinguette, *Science (80-.)*, **2019**, *365*, 367–369.
- [6] M. Beley, J. P. Collin, R. Ruppert, J. P. Sauvage, *J. Chem. Soc. - Ser. Chem. Commun.*, **1984**, *2*, 1315–1316.
- [7] Y. Wu, B. Rudshiteyn, A. Zhanaidarova, J. D. Froehlich, W. Ding, C. P. Kubiak, V. S. Batista, *ACS Catal.*, **2017**, *7*, 5282–5288.
- [8] M. Fujihira, Y. Hirata, K. Suga, *J. Electroanal. Chem. Interfacial Electrochem.*, **1990**, *292*, 199–215.
- [9] J. D. Froehlich, C. P. Kubiak, *Inorg. Chem.*, **2012**, *51*, 3932–3934.
- [10] T. D. Cook, S. F. Tyler, C. M. McGuire, M. Zeller, P. E. Fanwick, D. H. Evans, D. G. Peters, T. Ren, *ACS Omega*, **2017**, *2*, 3966–3976.
- [11] A. Zhanaidarova, C. E. Moore, M. Gembicky, C. P. Kubiak, *Chem. Commun.*, **2018**, *54*, 4116–4119.
- [12] G. Neri, J. J. Walsh, C. Wilson, A. Reynal, J. Y. C. Lim, X. Li, A. J. P. White, N. J. Long, J. R. Durrant, A. J. Cowan, *Phys. Chem. Chem. Phys.*, **2015**, *17*, 1562–1566.
- [13] M. Fujihira, Y. Nakamura, Y. Hirata, U. Akiba, K. Suga, *Denki Kagaku oyobi Kogyo Butsuri Kagaku*, **1991**, *59*, 532–539.
- [14] E. Fujita, J. Haff, R. Sanzenbacher, H. Elias, *Inorg. Chem.*, **1994**, *33*, 4627–4628.
- [15] J. Costamagna, G. Ferraudi, J. Canales, J. Vargas, *Coord. Chem. Rev.*, **1996**, *148*, 221–248.
- [16] M. Aulice Scibioh, P. V Ragini, S. Rani, V. R. Vijayaraghavan, B. Viswanathan, Reduction of CO₂ by nickel (II) macrocycle catalyst at HMDE, in *Proc. Indian Acad. Sci. Chem. Sci.*, **2001**, pp. 343–350.
- [17] L. Etgar, P. Gao, Z. Xue, Q. Peng, A. K. Chandiran, B. Liu, M. K. Nazeeruddin, M. Grätzel, *J. Am. Chem. Soc.*, **2012**, *134*, 17396–17399.
- [18] Z. hui Liu, S. Bi, G. liang Hou, C. zhan Ying, X. jia Su, *J. Power Sources*, **2019**, *430*, 12–19.
- [19] Y. Xiao, N. Cheng, K. K. Kondamareddy, C. Wang, P. Liu, S. Guo, X. Z. Zhao, *J. Power Sources*, **2017**, *342*, 489–494.
- [20] D. Bogachuk, R. Tsuji, D. Martineau, S. Narbey, J. P. Herterich, L. Wagner, K.

- Suginuma, S. Ito, A. Hinsch, *Carbon N. Y.*, **2021**, *178*, 10–18.
- [21] Z. Li, S. A. Kulkarni, P. P. Boix, E. Shi, A. Cao, K. Fu, S. K. Batabyal, J. Zhang, Q. Xiong, L. H. Wong, N. Mathews, et al., *ACS Nano*, **2014**, *8*, 6797–6804.
- [22] Z. Wei, H. Chen, K. Yan, X. Zheng, S. Yang, *J. Mater. Chem. A*, **2015**, *3*, 24226–24231.
- [23] X. Hou, Y. Hu, H. Liu, A. Mei, X. Li, M. Duan, G. Zhang, Y. Rong, H. Han, *J. Mater. Chem. A*, **2017**, *5*, 73–78.
- [24] Y. Sheng, Y. Hu, A. Mei, P. Jiang, X. Hou, M. Duan, L. Hong, Y. Guan, Y. Rong, Y. Xiong, H. Han, *J. Mater. Chem. A*, **2016**, *4*, 16731–16736.
- [25] X. Li, M. Tschumi, H. Han, S. S. Babkair, R. A. Alzubaydi, A. A. Ansari, S. S. Habib, M. K. Nazeeruddin, S. M. Zakeeruddin, M. Grätzel, *Energy Technol.*, **2015**, *3*, 551–555.
- [26] I. S. Yang, J. S. You, S. Do Sung, C. W. Chung, J. Kim, W. I. Lee, *Nano Energy*, **2016**, *20*, 272–282.
- [27] S. J. Ha, J. H. Heo, S. H. Im, J. H. Moon, *J. Mater. Chem. A*, **2017**, *5*, 1972–1977.
- [28] A. Maho, M. Lobet, N. Daem, P. Piron, G. Spronck, J. Loicq, R. Cloots, P. Colson, C. Henrist, J. Dewalque, *ACS Appl. Energy Mater.*, **2021**, *4*, 1108–1119.
- [29] T. Hwang, S. Lee, J. Kim, J. Kim, C. Kim, B. Shin, B. Park, *Nanoscale Res. Lett.*, **2017**, *12*, DOI 10.1186/s11671-016-1809-7.
- [30] M. Duan, Y. Hu, A. Mei, Y. Rong, H. Han, *Mater. Today Energy*, **2018**, *7*, 221–231.